Imperial College of Science, Technology and Medicine
Department of Physics

Topology on Almost Any Lattice

Topological Order and Invariants with Structural Disorder

Peru d'Ornellas

Submitted in part fulfilment of the requirements for the degree of
Doctor of Philosophy in Physics of Imperial College of Science,
Technology and Medicine, January 2024

Abstract

We study the relationship between topological phases of matter, both topological insulators (TIs) and topologically ordered magnets, and the geometry of the lattices on which they are constructed.

In the case of TIs, we consider the Chern number, which is central to our understanding of non-interacting topological phases of matter. Such phases are generally highly robust to disorder, whereas the Chern number depends on translational symmetry to be well-defined. We consider several real-space formulations of the Chern number, showing how they are constructed, discussing their relative limitations and providing a novel physical interpretation for the real-space Chern number as a localised measurement of the Hall conductivity.

Next, we study many-body topological order, focussing on Kitaev's honeycomb quantum spin liquid. We show that Kitaev's Hamiltonian can be constructed and exactly solved on almost any tri-coordinated lattice. Two complications arise in the non-crystalline case, namely the problems of assigning bond labels and finding the ground state flux sector. We present solutions to both these problems and calculate the phase diagram on a general lattice. We show that a robust gapped quantum spin liquid ground state emerges with spontaneously broken time reversal symmetry, and discuss the stability of the system against bond-strength disorder.

Finally, we consider an extension of the Honeycomb model that includes the Heisenberg couplings present in candidate Kitaev materials. Here we consider the effect of geometric frustration, constructing the Kitaev-Heisenberg model on a non-bipartite lattice. In doing so, we frustrate antiferromagnetic order and find two valence bond solid phases that have no analogue on the honeycomb model. Triplon excitations are investigated in these phases, where we find that the interplay of an external magnetic field with the Kitaev couplings leads to a bosonic analogue of the quantum Hall effect, with a rich phase diagram of topological triplon bands.

Acknowledgements

First and foremost, I would like to thank my supervisors Derek Lee and Ryan Barnett for introducing me to the topic, for always finding time to talk through a problem for as long as was necessary, and for providing me with countless ideas, tools and tricks for understanding the concepts presented in this thesis. Without their guidance, none of what I have achieved over the last few years could have been possible.

I am also immensely grateful to Johannes Knolle, who has provided me with an academic second home, and introduced me to a wealth of new ideas that I could not have otherwise found. The months I spent at the Technical University of Munich were profoundly inspiring, and I returned each time to London with a greater love for physics than when I left.

Throughout my PhD I have benefitted from a number of collaborations, most notably that with Gino Cassella and Tom Hodson, with whom I undertook much of the initial work on the Kitaev model. I am indebted to Krishnan Ganesh, with whom I have learnt much of what I know, to George Smith who has shown me many things that he knows, and to Josef Willsher who exposed me to many things I would rather not have known. I have benefitted enormously from discussions with Anton Markov, Joseph Sykes, Charles Stahl, Adolfo Grushin, Johannes Hauschild, Natasha Perkins, Kirill Shtengel, Julien Vidal, Jonas Habel, Valentin Leeb, GiBaik Sim, Frank Schindler, Mathieu Dos Santos, Alex Mook, Markus Drescher, Thivan Gunawardana, Henry Davenport, Andres Perez-Fadon, Wonjune Choi, Peng Rao, Yu-Jie Liu and Avedis Neehus. In particular, I would like to thank Krishnan, Josef and Anton for their careful proofreading of the thesis.

Outside of physics, my sanity has been sustained by Kalvin, Lauren, Suzana, Mattea, Matt, Eden, Phoebe, Andy, Rebecca, Fredrika, Alex, Gabriel, Jackie, Milan, Halvard, Chris, Felix, Isobel, Jack, Lizzy and many more. Without them, an alternative career path as a tropical alcoholic would have been a lot more tempting.

And finally, this thesis is dedicated to my parents, Laure and Juan, for always supporting my love of science, despite the fact that most of it makes no sense and probably isn't real anyway.

The work in this thesis was supported by the Engineering and Physical Sciences Research Council, grant number: EP/R513052/1

Declaration

I certify that this thesis, and the research contained within are the product of my own work, except where specific reference is made to the work of others. Any work that was undertaken collaboratively is stated in the text and acknowledgements.

Copyright

The copyright of this thesis rests with the author. Unless otherwise indicated, its contents are licensed under a Creative Commons Attribution-Non Commercial 4.0 International Licence (CC BY-NC). Under this licence, you may copy and redistribute the material in any medium or format. You may also create and distribute modified versions of the work.

This is on the condition that: you credit the author and do not use it, or any derivative works, for a commercial purpose. When reusing or sharing this work, ensure you make the licence terms clear to others by naming the licence and linking to the licence text. Where a work has been adapted, you should indicate that the work has been changed and describe those changes.

Please seek permission from the copyright holder for uses of this work that are not included in this licence or permitted under UK Copyright Law.

Contents

1 Introduction **1**

1.1 Universality . . . 3

1.1.1 The Integer Quantum Hall Effect . . . 5

1.1.2 The TKNN Invariant and the Chern Number . . . 8

1.2 Magnetism, Frustration and Fractionalisation . . . 10

1.2.1 Classical Frustration . . . 11

1.2.2 The Classical Kitaev Honeycomb Model . . . 14

1.2.3 A Quantum Spin Liquid . . . 16

1.3 Thesis Outline . . . 20

1.4 Publications . . . 23

2 Chern Number and Topological Insulators **24**

2.1 Abelian Berry Phase and the Chern Number . . . 25

2.1.1 A Discrete Brillouin Zone . . . 25

2.1.1.1 Berry Flux . . . 26

2.1.1.2 Chern Number . . . 27

2.1.2 Topology of a General Hamiltonian . . . 28

2.1.2.1 Berry Curvature . . . 30

2.1.2.2 Chern Number . . . 31

2.1.3 An Example – The Two-Level System . . . 31

2.1.3.1 Chern Number . . . 33

2.1.4 Final Notes . . . 34

2.1.4.1 Smoothly Deforming the Hamiltonian . . . 34

2.1.4.2 The Bulk-Boundary Correspondence . . . 34

2.1.4.3 Chern Number and Globally Smooth Gauges . . . 35

2.2 The Qi-Wu-Zhang Model . . . 35

2.2.1 Strip Geometry and Edge Modes . . . 36

2.2.2 The Amorphous QWZ Model . . . 38

3 Local Chern Markers **42**

3.1 The Bott and Chern Markers . . . 43
3.1.1 The Chern Marker . . . 46
3.1.2 Some Examples . . . 47
3.1.2.1 Are These Markers Purely Topological? . . . 49
3.2 Kitaev's Local Marker . . . 50
3.2.1 Relation to the Chern Number . . . 52
3.2.2 Kitaev's Marker in a Finite System . . . 55
3.2.3 Numerical Examples . . . 57
3.3 A Physical Interpretation . . . 59
3.3.1 Electric Fields . . . 60
3.3.2 Current Operators . . . 61
3.3.3 Kato Dynamics . . . 62
3.3.3.1 Adiabatic EM Fields . . . 63
3.3.3.2 Adiabatic Current . . . 63
3.3.4 Marker Derivation . . . 63

4 The Amorphous Kitaev Model **68**

4.1 Kitaev's Honeycomb Model . . . 70
4.1.1 Spins to Fermions to Majoranas . . . 71
4.1.2 Gauge Transformations and Fluxes . . . 73
4.1.3 Time Reversal Symmetry . . . 75
4.1.4 Solving the Hamiltonian . . . 76
4.1.5 The Ground-State Phase Diagram . . . 77
4.1.5.1 The Gapped A Phases . . . 79
4.1.5.2 From the Gapless to the gapped B Phase . . . 79
4.1.6 The Chern Number . . . 80
4.2 The Amorphous Kitaev Model . . . 82
4.2.1 Setting up the Model – Bond Colouring . . . 83
4.2.2 Fluxes on an Amorphous Lattice . . . 84
4.2.3 The Ground State Flux Sector . . . 86
4.2.3.1 Cycles and the Ground State Energy . . . 86
4.2.3.2 Finite Size Effects . . . 90
4.2.3.3 Numerics . . . 91
4.2.4 The Ground-State Phase Diagram . . . 93
4.2.5 Accounting for Bond Disorder . . . 94

5 The Kitaev-Heisenberg Model on the Star Lattice **97**
5.1 The Ground-State Phase Diagram . . . 99
5.1.1 Isometries of the Phase Diagram . . . 102
5.2 A Majorana Parton Mean Field Study . . . 104
5.3 Triplon Excitations in the VBS . . . 108

6 Conclusion and Outlook **112**
6.1 Local Markers . . . 112
6.2 The Amorphous Kitaev Model . . . 113
6.3 Triplons and the Kitaev-Heisenberg Model . . . 115

Bibliography **116**

A Voronoi Lattices **130**
A.1 Lloyd's Algorithm . . . 130
References . . . 131

B Time-Evolution and Current Under Kato Dynamics **133**
B.1 Adiabatic Time-Evolution Operator . . . 133
B.2 Adiabatic Current Operators . . . 134
B.2.1 Two-Point Flow Operator . . . 134
B.2.2 Adiabatic Current . . . 135
References . . . 138

C Tait Colourings and the Four-Colour Theorem **139**
C.1 4-Face Colouring to a 3-Edge Colouring . . . 140
C.2 3-Edge Colouring to a 4-Face Colouring . . . 141
References . . . 142

D Diagonalising Quadratic Hamiltonians **144**
D.1 The Majorana Case . . . 144
D.1.1 Correlation Values . . . 146
D.2 Triplons and the Bosonic Case . . . 147
D.2.1 Construction of the Hamiltonian . . . 147
D.2.2 Bosonic Bogoliubov-de Gennes Method . . . 149
D.2.3 Bosonic Chern Number . . . 151
References . . . 152

List of Figures

1.1 Illustration of an electron in a smooth potential compared to an electron in tight-binding. . . . 2

1.2 Illustration of a spin-averaging procedure and real space renormalisation step. Diagram of theory space, with a set of stable fixed points. . . . 4

1.3 Hall conductivity as a function of applied magnetic field. A Corbino disc geometry with a sketch of successive states within a Landau level. . . . 5

1.4 Density of states and energy of landau levels for both a clean and disordered quantum Hall sample on a ring geometry. . . . 7

1.5 Illustration of the space of all non-interacting Hamiltonians, classified by their Chern numbers. . . . 9

1.6 Ground state of the spin-$\frac{1}{2}$ Heisenberg model on the honeycomb, triangular and star lattice. . . . 11

1.7 Ground state configuration for three clusters of n-spins, kagome lattice and pyrochlore lattice. . . . 12

1.8 Ground state degeneracy in the Kagome antiferromagnet. . . . 13

1.9 Bond colouring for the honeycomb Kitaev model and classical ground state configuration. . . . 14

1.10 Diagram of bond operators and their corresponding gauge fluxes in the Kitaev honeycomb model. . . . 19

2.1 A grid of states parametrised by a discrete parameter. . . . 27

2.2 Colourmap of a local gauge transformation. . . . 29

2.3 A single band of the QWZ model plotted on the Bloch sphere. . . . 35

2.4 Band structure of the QWZ model. . . . 37

2.5 QWZ bands in open boundaries. . . . 38

2.6 Hopping operators for the amorphous QWZ model, shown on the Bloch sphere. 39

2.7 Energies of the amorphous QWZ model in open and periodic boundary conditions, revealing the presence of edge modes. . . . 41

3.1 Bott index and Chern marker for a sample of amorphous QWZ model. . . . 48

3.2 Effect of lattice-only distortion on the Chern marker or Bott index. . . . 49

3.3 Partition of the plane into three regions used to construct Kitaev's local Chern number. . . . 50
3.4 Decomposition of the plane into four quadrants. . . . 53
3.5 Two examples of the vanishing of Kitaev's local marker in a finite system. . . . 55
3.6 The restricted Kitaev marker, suitable for use in finite systems. . . . 56
3.7 Example of the Kitaev marker for an amorphous QWZ system in periodic and open boundaries. . . . 58
3.8 Effect of a topological phase transition on Kitaev's local marker. . . . 58
3.9 Effect of increasing disorder on Kitaev's marker. . . . 59
3.10 Electric field and potential used to calculate a local Hall conductivity. . . . 60
3.11 Local current operator used to calculate a local Hall conductivity. . . . 61
3.12 A schematic for local Hall measurement. . . . 64

4.1 Honeycomb lattice, bond labelling and plaquette operators used in the Kitaev honeycomb model. . . . 70
4.2 A depiction of the three steps in transforming the spin Hamiltonian into a quadratic Majorana Hamiltonian. . . . 73
4.3 A depiction of a gauge transformation. . . . 74
4.4 Creation of fluxes and depiction of global fluxes. . . . 76
4.5 The Honeycomb model phase diagram, shown as a function of the three J^α parameters. . . . 78
4.6 The effect of a magnetic field on the band structure of the Majorana Hamiltonian in the B phase. . . . 79
4.7 Bound states in the non-Abelian phase. . . . 81
4.8 An example of the procedure for flipping a set of fluxes, the Peterson snark and examples of the loop structure formed by considering only two sets of bonds. . . . 83
4.9 An example of the procedure for flipping a set of fluxes. . . . 85
4.10 Decomposing the flux through a complex region into its constituent plaquettes. . . . 89
4.11 The effect of twisted boundaries on system crossing fluxes. . . . 91
4.12 Energy and gap of every flux sector for a system with 16 plaquettes. Plot of energy and fermion gap scaling with system size. . . . 92
4.13 Ground-state phase diagram calculated for an example amorphous lattice with 800 sites. . . . 93
4.14 Kitaev Chern marker, edge mode and density of states for an amorphous Kitaev system with ~ 8000 vertices. . . . 94
4.15 The effect of bond disorder on the amorphous Kitaev model. . . . 95

5.1 Star lattice with bond colouring and the Kitaev-Heisenberg tuning parameter. . . . 99

5.2 The full Kitaev-Heisenberg phase diagram, shown for both the honeycomb model and the star lattice model. 100
5.3 iDMRG results for the star lattice KH model. 101
5.4 The four-unit-cell transformation on the star lattice. 103
5.5 Majorana MFT results for the star lattice KH model. 105
5.6 Majorana fermion band structure calculated for the chiral QSL phase within a parton MFT for a strip-geometry 107
5.7 Transformation from the spin-half Star lattice model to a kagome triplon system. 108
5.8 Triplon mean field results – band structure, Chern numbers and edge modes. . . 110

A.1 A Voronoi partition calculated in periodic boundaries. 131
A.2 One step of Lloyd's algorithm. 132
A.3 The effect of successive iterations of Lloyd's algorithm on a Voronoi lattice. . . . 132

C.1 A 3-edge colouring on a tri-coordinated graph, transformed into a valid 4-colouring of the faces. 140
C.2 Colouring an arbitrary lattice via two paths. 142

Chapter 1

Introduction

In 1928, just two years after Erwin Schrödinger published his famous wave equation, Felix Bloch proposed a new method for calculating the electronic properties of solids [1]. By this point, the idea that electrons in atoms arranged themselves into a hierarchy of discrete orbitals was well-established. Bloch proposed that, rather than starting with a free electron and considering how its motion might be affected by the material's potential, the properties might be better understood by starting with a set of electronic states $|\phi_n(\mathbf{R}_i)\rangle$, each corresponding to the n^{th} orbital on the atom at position $\mathbf{R}_i$. Here, a wavefunction could be constructed by taking a linear combination of these orbitals. Next, the Hamiltonian operator, given by

$$H = \frac{\mathbf{p}^2}{2m} + V \tag{1.1}$$

would be rewritten in terms of these states. By exploiting the translational symmetry in crystalline materials and considering only the lowest energy s orbital, Bloch was able to solve the periodic Schrödinger equation and the technique – known as the LCAO (linear combination of atomic orbitals), or tight-binding method – paved the way for the development of band theory.

In practice, this was a spectacularly complex procedure to perform rigorously. To re-express the Hamiltonian in terms of orbitals, one had to evaluate an enormous number of integrals of the form $\langle\phi_n(\mathbf{R}_i)|H|\phi_m(\mathbf{R}_j)\rangle$ – one for each pair of orbitals separated by each lattice translation. Thus, finding the exact form of the Hamiltonian was in most cases an impossible task. Rather, the utility of this method became apparent when one accepted this impossibility and just guessed the form of H [2, 3].[1] With just a few assumptions one could simplify the Hamiltonian to the point that it only depended on a small number of parameters. For example, one would expect the coupling between two orbitals to vanish unless they were sufficiently close as to overlap. Furthermore, by studying the symmetries in a crystalline material, one finds many couplings that must be equivalent. Thus, the game became one of adjusting this small number of parameters until the tight-binding model matches the properties found in experiment.

This tight-binding picture is a radically different world for an electron to live in, in comparison to the original form of Schrödinger's Hamiltonian (Eqn. 1.1). In Schrödinger's story, the electron exists as a wave in a fundamentally smooth world, where the potential defines a landscape through which the electron roams. However, in Bloch's story the collective properties of the electrons emerge from the overlap between a discrete lattice of orbitals. Here the landscape

[1] In [2], Slater and Koster provide a detailed account of the many complications involved with performing a rigorous LCAO calculation.

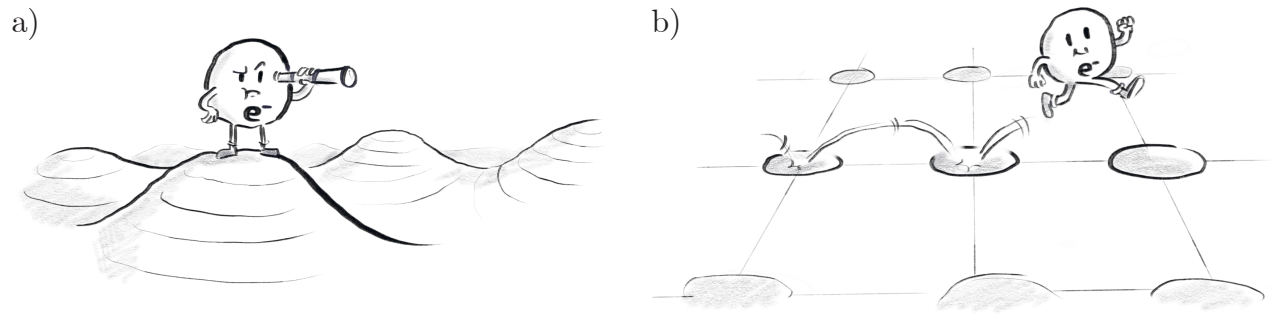


Figure 1.1: **(a)** An electron whose dynamics follows Eqn. 1.1, exploring a smooth potential. **(b)** An electron in tight binding hopping between a set of discrete sites on a lattice. *Illustration by Krishnan Ganesh.*

is more akin to an archipelago, with electrons that hop from island to island as in Fig. 1.1. Constructing a model in this formalism is a completely different procedure to that of Schrödinger, since we must start by asking: *What is the geometry of the lattice?* Only then can we decide the values of the couplings between lattice sites and build a Hamiltonian. Here, the geometry of the lattice has a fundamental role in deciding what kind of Hamiltonians we can build.

Of course, the tight binding method is just one of a huge variety of approximations that have been used to understand how electrons behave in materials. However, it is not the only context where the lattice geometry turns out to be absolutely central in determining what kinds of Hamiltonians can exist, and thus what kind of collective phases may emerge. In a crystalline material, the lattice structure determines the shape of the Brillouin zone, as well as the position of high symmetry points. Thus, the band structure that emerges is strongly constrained by the shape of the lattice [4, 5]. In many magnetic materials, the role of lattice geometry arguably becomes even more important. Here the electron-electron repulsion is sufficiently strong that electrons become immobilised on each site. An effective description of the material treats each electron as completely fixed to a point on the lattice, and electrons interact only by realigning their spin and internal degrees of freedom in response to the state of a neighbour [6, 7].

In condensed matter, the process of learning a new model can often feel similar to learning a board game: One starts by looking at the board, studying its symmetries and defects, and then progresses to learning the rules and finally playing the game. A natural question to ask is: *How does the game depend on the shape of the board?* The equivalent question for a physicist is: *How does the microscopic structure of a material determine the types of collective phases that can emerge?* For a given Hamiltonian, on a given lattice, we can ask how the phase changes when we alter the character of the lattice, for example adding in holes or defects, altering its connectivity, changing its symmetries or even completely disordering the lattice and destroying all spatial symmetries. In modelling a real system, we may also consider the effect of a disordered potential, applying an energy penalty to occupying certain regions over others. Over the last hundred years, this question has yielded an enormous variety of answers. In some contexts, one finds that nothing really changes. Many properties in condensed matter are remarkably insensitive to the microscopic details – that is, they are shared by an enormous variety of systems living on an enormous variety of lattices. Two famous examples of this phenomenon are that of universality, which we give a brief introduction to in §1.1 and band topology, which we describe in §1.1.1. On the other hand there are cases – notably that of frustrated magnetism – where the details of the lattice geometry are paramount in determining the properties of the system, which we shall discuss in §1.2.

1.1 Universality

The search for universal properties, i.e. those that are insensitive to the microscopic details of matter, is an old one. At the atomic level the world is spectacularly complex, with an enormous number of constituent particles interacting with one another in ways that are chaotic and poorly understood. Yet, by the time we reach the macroscopic scale, most of these complexities have been averaged away, and familiar physics emerges. One of the remarkable aspects of this averaging is that different microscopic systems converge to the same macroscopic behaviour. For example, despite enormous variation in chemical composition, all liquids have similar bulk properties, and follow almost identical equations of motion, *more is the same*.

One of the great successes in understanding this universality was developed in the mid 20th century, starting with the work of Ginzburg and Landau [8], and then further developed by a generation of physicists, most notably Ken Wilson [9] who introduced the concept of the renormalisation group (RG). Let us briefly sketch the central idea using the Ising model as an example,[2] although a thorough discussion is beyond the scope of this thesis, and can be found in Refs. [11, 12].

We start with a set of classical spins $\{s_i = \pm 1\}$ arranged on a lattice, interacting according to a general Hamiltonian, for example the Ising Hamiltonian,

$$H = -B\sum_j s_j - J\sum_{\langle jk\rangle} s_j s_k, \tag{1.2}$$

where $\langle jk\rangle$ indicates the sum is over nearest-neighbour pairs of spins. The parameters J and B define the strength of the nearest neighbour coupling and the applied magnetic field respectively. Rather than working with individual spins, which can only take two values ± 1, Ginzburg and Landau suggested constructing a smoothly varying local order parameter $m(\mathbf{x})$ by dividing up these spins into blocks and averaging over each block as seen in Fig. 1.2a. In this language, the partition function, originally a sum over all states of the system, would be rewritten as a path integral over all possible configurations of $m(\mathbf{x})$, weighted by the number of states that corresponded to each configuration of $m(\mathbf{x})$

$$\mathcal{Z} = \sum_{\{s_i\}} e^{-\beta E(s_i)} \to \int \mathcal{D}m \sum_{\{s_i\}|m(\mathbf{x})} e^{-\beta E(s_i)}. \tag{1.3}$$

The sum on the right-hand side is arbitrarily difficult, however – as with tight binding a few decades earlier – the key insight was that we didn't have to evaluate it at all. Rather, we could just wrap the quantity up as some unknown free energy

$$\sum_{\{s_i\}|m(\mathbf{x})} e^{-\beta E(s_i)} = e^{-\beta F(m)}, \tag{1.4}$$

and make a guess as to the form of the free energy by including only coefficients that are consistent with the symmetries of the system. For example, in an Ising model with no external field the system has spin-flip symmetry so must remain invariant under $m \to -m$. Thus, odd

[2] Of course, an exact solution to the classical Ising model was famously proposed by Onsager [10]. Here, we use the model as a simple model with which to illustrate the much deeper notion of universality.

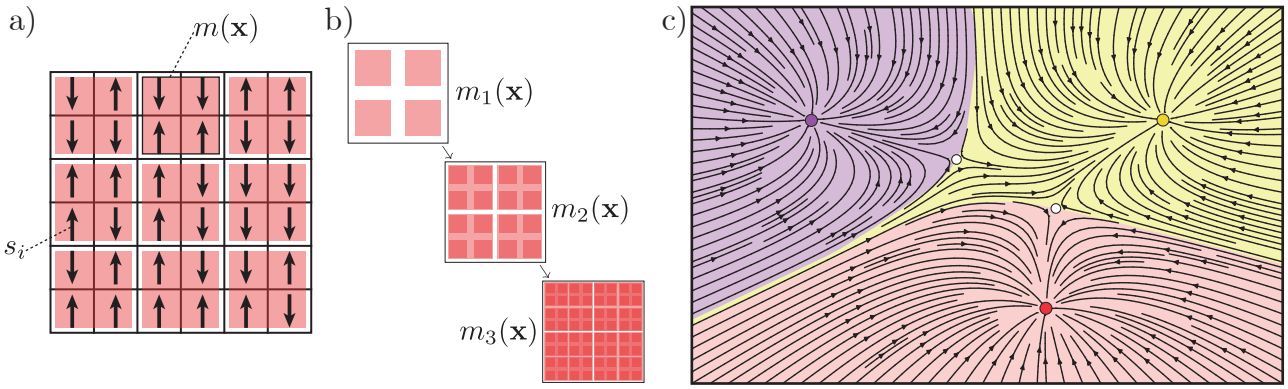


Figure 1.2: **(a)** In the first step of coarse graining, an averaged magnetisation parameter $m(\mathbf{x})$ is constructed by choosing and averaging over set of spins s_i, each set is indicated with a red box. **(b)** A real space rescaling can be performed by averaging over successively larger chunks of spins, leading to a set of successively more coarse-grained order parameters $m_i(\mathbf{x})$. **(c)** A heuristic diagram of a parameter space for $F(m)$, where arrows indicate the flow under RG. In each region, the theory flows to one corresponding fixed point, indicated with a circle, which defines the long-range properties of the model.

powers of m are forbidden,

$$F(m) = \int d^d x \left[\gamma(\nabla m)^2 + \alpha_2 m^2 + \alpha_4 m^4 + ...\right]. \tag{1.5}$$

In doing this, we have parametrised every possible effective theory for our model with a (possibly infinite) set of prefactors, $\{\gamma, \alpha_n\}$. The next insight came by considering how an effective theory might change under a *rescaling transformation*. There are several ways that this transformation may be formulated, for example one might consider a real-space method, where $m(\mathbf{x})$ is redefined by choosing some larger block size and averaging $m(\mathbf{x})$ over this area, effectively zooming out and setting a limit to how finely-resolved the fluctuations in the model can be, shown in Fig. 1.2b. Equivalently, one can consider integrating out the high momentum modes that correspond to the unwanted small-scale fluctuations, imposing a momentum cut-off in the partition function. Parametrising this scaling with τ, we find that the coefficients of the free energy pick up a τ-dependence and the rescaling process generates a flow in parameter space $\{\gamma, \alpha_n\} \to \{\gamma(\tau), \alpha_n(\tau)\}$, known as renormalisation flow.

Under this transformation, the points where the free energy functional is static correspond to fixed points where the effective theory becomes scale-invariant, since any dependence on scale implies that the model will change under τ. For each set of symmetries, and dimensionality of the system, the flow generated under RG will look different and have a different set of fixed points. Remarkably, in many cases there turns out to be only a finite number of these fixed points, an illustration is shown in Fig. 1.2c. Fixed points can be characterised by their stability under small perturbations. A stable fixed point, where perturbations decay under RG flow, represents a phase of matter (shown with the coloured circles in Fig. 1.2c). Such stable points act as a basin of attraction where, under RG flow, many microscopically different systems that start from different points in parameter space flow to the same fixed point and thus have the same long-range properties. An unstable fixed point is one where small perturbations flow away from the point. Such points lie at the boundaries between the basins of different stable fixed points and represent phase transitions (shown with the white circles in Fig. 1.2c). Thus, the whole of

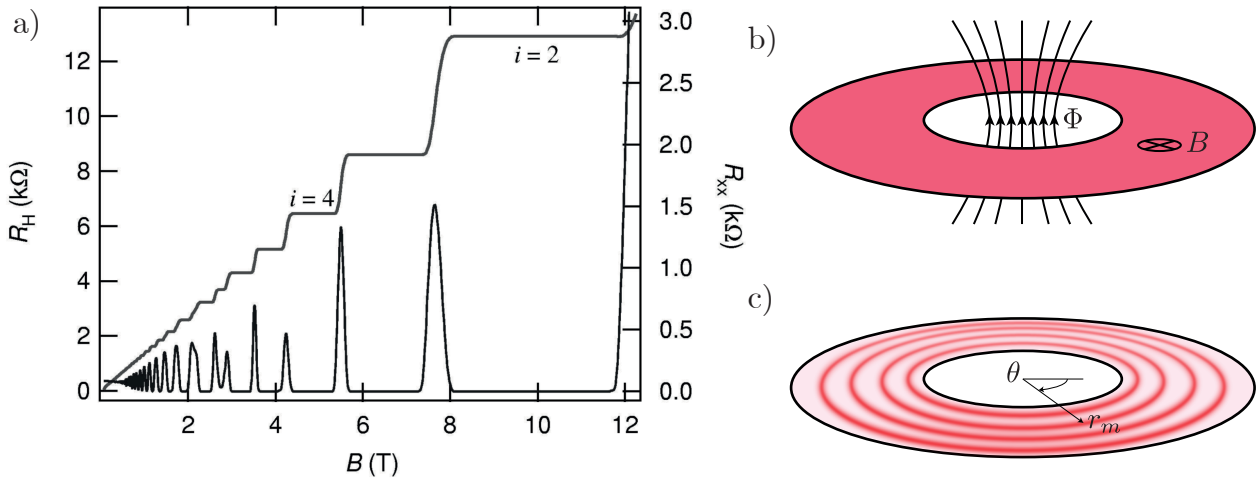


Figure 1.3: **(a)** The measured resistivity in a GaAs heterostructure at 0.1 K. *Figure reproduced from [13].* **(b)** The geometry proposed by Halperin [14]. Here a 2D electron gas is confined to the ring, pierced by a transverse magnetic field parametrised by B. A flux given by Φ is threaded through the centre of the ring, which adiabatically increased from $\Phi = 0 \to \Phi_0$. **(c)** Depiction of a set of wavefunctions that form part of the lowest Landau level. The m^{th} wavefunction is localised to a ring with radius r_m.

parameter space can be divided into a set of regions, where starting at any point in that region will always flow to the same fixed point, and have the same long-range effective description. Now let us consider making a microscopic change to the model. If this change does not alter the symmetries of the system, then it will only have the effect of perturbing the starting point in our RG flow. If this perturbation doesn't move us out of one region and into another, we have the guarantee that the long-range properties of the system are unaffected. On the other hand, if the perturbation does change the symmetry of the model we have no such guarantee, since it could introduce new terms to the free energy that could push us away from one fixed point to a completely different place in phase space. This universality is a fundamentally many-body effect, arising from the self-averaging that occurs in a sufficiently large system or interacting parts.

1.1.1 The Integer Quantum Hall Effect

In the early 1980s a very different single-particle form of universal physics was emerging at the National Laboratory for Intense Magnetic Fields in Grenoble. Here, Klaus von Klitzing was studying the transverse Hall conductivity in silicon-based MOSFETs (metal-oxide-semiconductor field-effect transistor) prepared by Gerhard Dorda and Michael Pepper. These transistors allowed von Klitzing to prepare a nearly ideal 2D electron gas at extremely low temperatures and under high magnetic fields. Here, rather than finding the linear relationship between transverse resistivity and applied field predicted by classical Drude theory [15], von Klitzing found that the transverse resistivity contained a set of plateaux at precisely quantised values given by

$$\rho_{xy} = \frac{2\pi\hbar}{e^2\nu}, \ \nu \in \mathbb{Z}, \tag{1.6}$$

as shown in Fig. 1.3a [16, 17]. This quantisation was extremely precise, accurate to one part in 10^6 and has since been adopted as the standard for defining the unit of resistance (Ω) [13]. The precision is particularly surprising given that the samples von Klitzing was using contained fairly

substantial disorder. In fact, as we shall see in the following discussion, the presence of some disorder was necessary for producing the sharp jumps in conductivity seen by von Klitzing.

One of the first steps towards understanding the precise quantisation of the Hall conductivity was proposed by Laughlin [18], and developed by Halperin [14] who considered a quantum Hall system constructed on a ring geometry as shown in Fig. 1.3b. The Hall conductivity could be tested by adiabatically threading some quantity of flux Φ through the centre of the ring. Including the perpendicular magnetic field and working in symmetric gauge, we may write the magnetic vector potential in the following form,

$$\mathbf{A} = \left(\frac{1}{2}Br - \frac{\Phi}{2\pi r}\right)\hat{\boldsymbol{\theta}}. \tag{1.7}$$

After solving the Schrödinger equation for this potential, one finds the electrons organised into Landau levels (LLs) with energy determined by the cyclotron frequency, $E = \hbar\omega_c(\nu + 1/2)$, with $\omega_c = \frac{eB}{m^* c}$. The lowest LL consists of a degenerate set of ring-like wavefunctions,

$$\psi_{LLL,m} \sim e^{im\theta} r^m e^{-r^2/4l_B^2}, \tag{1.8}$$

shown in Fig. 1.3c, where $l_B = \sqrt{\hbar/eB}$. The radial profile of the m^{th} state is peaked at r_m, which is determined by the flux enclosed, according to

$$B\pi r_m^2 = m\Phi_0 + \Phi, \tag{1.9}$$

where $\Phi_0 = 2\pi\hbar/e$ is a single flux quantum. Here the minimum and maximum values of m are determined by the inner and outer radii of the ring. By adiabatically threading a single flux quantum through the ring (by slowly tuning Φ from $0 \to \Phi_0$), we have the effect of transforming each $r_m \to r_{m+1}$. Each state in the Landau level moves outwards, taking the place of its neighbour, a process known as *spectral flow*. Once the process is complete, the spectrum must be identical to before – since a whole flux quantum can always be removed with a gauge transformation – however now there is a missing electron on the inner radius, and an extra electron that has been pushed to the outer radius. Thus, the ring behaves like a conveyor belt under flux insertion, transferring a single electron from the inside to the outside, as shown in Fig. 1.4c. To calculate the resistivity associated with this process, let us suppose the adiabatic process happened over some timescale T, and calculate the EMF,

$$\mathcal{E} = -\frac{\partial\Phi}{\partial t} = -\frac{\Phi_0}{T}, \tag{1.10}$$

and the current induced by the transfer of one electron,

$$I = -\frac{e}{T}, \tag{1.11}$$

giving an overall transverse resistivity of

$$\rho_{xy} = \frac{\mathcal{E}}{I} = \frac{\Phi_0}{e} = \frac{2\pi\hbar}{e^2}. \tag{1.12}$$

This calculation was performed for a single Landau level; however, the story is straightforwardly transferable to the case when several Landau levels sit below the Fermi energy, since each level independently transports an electron from the inside to the outside edge. Thus, for ν Landau

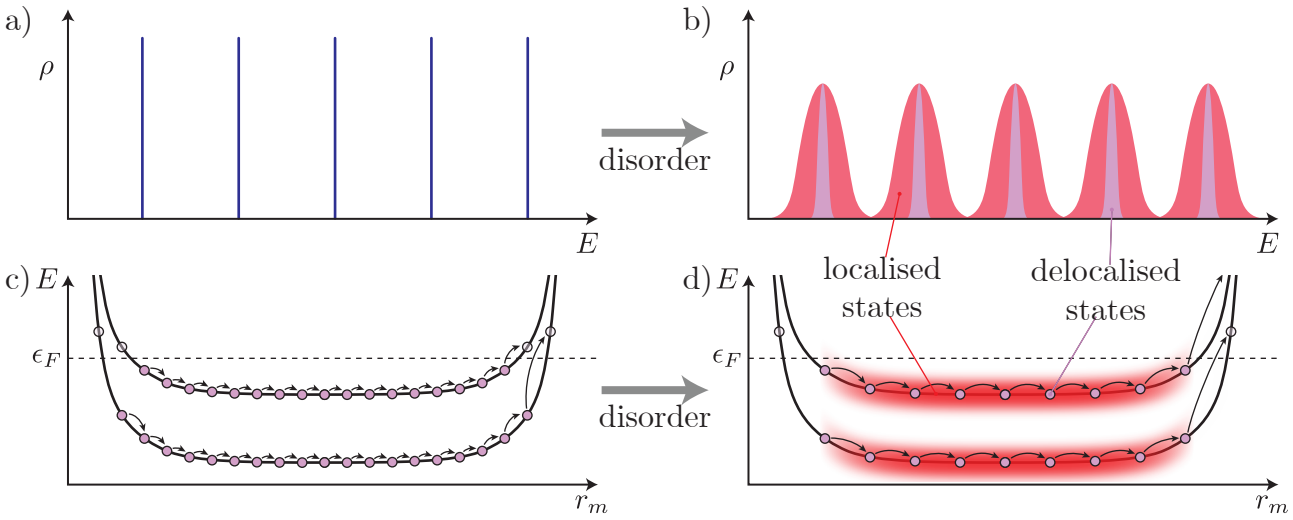


Figure 1.4: **(a)** Density of states for a set of five Landau levels in a clean system. Here all states in each LL are degenerate and delocalised around the ring. **(b)** In a disordered system, the Landau levels are broadened, and many states become localised. However, each LL still contains a central set of delocalised states. **(c)** Energy of a set of two Landau levels as a function of radius, showing the effect of a confining potential which raises the energy of Landau levels close to the boundaries. The effect of flux insertion for a clean material on a ring geometry. Here, each Landau level consists of a large number of delocalised states, denoted by the lilac circles. Under flux insertion, each of these states is transported over to the next state, such that by the end of the process each band has a hole on the inner edge, and an excited state on the outer edge. **(d)** In the disordered case the most of the states in each Landau level have become localised, however a minority of these states remain delocalised. These delocalised states transport an electron across the ring for the same reason as in the clean material.

levels below the Fermi energy, we find an overall conductivity given by Eqn. 1.6.

Let us now consider adding a disordered potential $V(\mathbf{r})$ to the system. To preserve the Hall effect, one must assume that this disorder is not strong enough to mix different Landau levels, $|V| \ll \hbar\omega_c$. Adding such a term will break the degeneracy within each Landau level, leading to a smearing out of the density of states into broad peaks. In addition, while the clean Landau levels are composed of delocalised states, in the disordered bands most of the states will become localised. However, in the centre of each band, there will remain a minority of delocalised states, as shown in Fig. 1.4b.[3]

The localised states are no longer able to change under flux insertion, since the effect of the threaded flux on a state that does not wrap the whole ring can always be removed with a gauge transformation. The remaining delocalised states will still be able to see the flux insertion, and so will still undergo spectral flow. As before, each delocalised state is adiabatically transformed onto the next delocalised state away from the centre of the ring, as shown in Fig. 1.4d. Thus, provided that some states remain delocalised, the net effect is still to transport a single electron from the inside to the outside of the ring. In fact, it was shown by Prange [22] that when a single state is localised, the nearby delocalised states will 'speed up' to compensate for the missing

[3]In fact, as long as the disorder is not strong enough to mix LLs, there must *always* remain a few delocalised states. Over the years, many arguments were provided to explain this phenomenon, often each concerning a different manifestation of disorder. The first was given by Halperin in [14], as well as early arguments in the case of short-ranged disorder [19, 20], and a very famous percolation picture in the case of slow-varying disorder [21].

current from the localised state. Thus, we see that as disorder is increased, the quantised Hall conductance remains, transported by a shrinking minority of delocalised states in each Landau level.

It is precisely the fact that a small minority of states are responsible for the Hall conductivity that stabilises the plateaux shown in Fig. 1.3a. Here, the tuning of the applied field B has the effect of shifting the energy and degeneracy of the Landau levels – effectively sweeping the Fermi level across the LL spectrum. The conductivity is determined only by the number of filled LLs, however only the extended states in the centre of each LL are able to transport charge. Thus, the conductivity is only allowed to change at the point where the Fermi energy sweeps through these states. The presence of disorder ensures that only a minority of states are delocalised, such that the transitions between plateaux become sharp and the plateaux themselves are precisely quantised.

1.1.2 The TKNN Invariant and the Chern Number

The Laughlin/Halperin picture was one of the first – and simplest – explanations for the quantised Hall conductivity and its remarkable insensitivity to disorder. However, in the following years a much deeper mathematical picture was uncovered, starting with the work of Thouless and his collaborators who provided a different argument for a quantised bulk conductivity [23]. Let us provide a brief description of their result.

For a periodic non-interacting electron gas, the eigenstates of the system may be expressed in terms of the Bloch states, $|\psi_{n\mathbf{k}}\rangle = e^{i\mathbf{k}\cdot\mathbf{x}}|u_{n\mathbf{k}}\rangle$, where $|u_{n\mathbf{k}}\rangle$ is a periodic eigenstate with energy E_n of the Bloch Hamiltonian $H(\mathbf{k}) = e^{-i\mathbf{k}\cdot\mathbf{x}}He^{i\mathbf{k}\cdot\mathbf{x}}$. In this context, the transverse conductivity can be expressed using a linear response formalism developed by Kubo [24], given by

$$\sigma_{xy} = i\hbar \sum_{\substack{n\in\text{occ}\\ m\in\text{unocc}}} \int_{BZ} \frac{d^2k}{4\pi^2} \frac{\langle u_{n\mathbf{k}}|J_x|u_{m\mathbf{k}}\rangle \langle u_{m\mathbf{k}}|J_y|u_{n\mathbf{k}}\rangle}{(E_n - E_m)^2} + h.c. \tag{1.13}$$

Here, eigenstates below the Fermi level are labelled by n and those above it by m. The operators J_α represent the current operator in the x and y directions, and the integral is over the whole Brillouin zone. By re-expressing the current operators in terms of the group velocity,

$$J_\alpha = -\frac{e}{\hbar}\frac{\partial H(\mathbf{k})}{\partial k_\alpha}, \tag{1.14}$$

the conductivity could be rewritten in the form,

$$\sigma_{xy} = \frac{ie^2}{\hbar} \sum_{\substack{n\in\text{occ}\\ m\in\text{unocc}}} \int_{BZ} \frac{d^2k}{4\pi^2} \frac{\langle u_{n\mathbf{k}}|\partial_x H|u_{m\mathbf{k}}\rangle \langle u_{m\mathbf{k}}|\partial_y H|u_{n\mathbf{k}}\rangle}{(E_n - E_m)^2} + h.c. \tag{1.15}$$

Here we use the shorthand $\partial_\alpha = \frac{\partial}{\partial k_\alpha}$. Next, using the orthogonality of the eigenstates, they rewrote the inner products using the following identity,

$$\langle u_{n\mathbf{k}}|\partial_\alpha H|u_{m\mathbf{k}}\rangle = (E_n - E_n)\langle \partial_\alpha u_{n\mathbf{k}}|u_{m\mathbf{k}}\rangle, \tag{1.16}$$

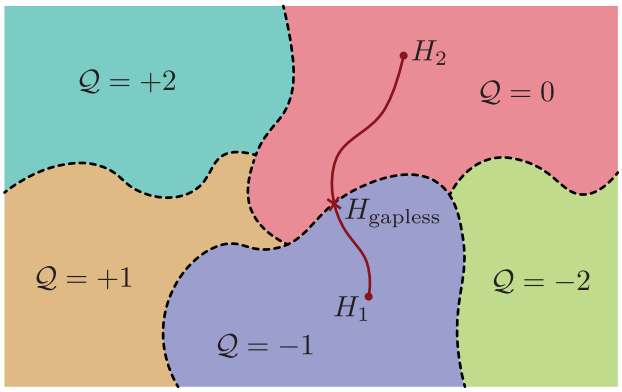


Figure 1.5: The space of all Hamiltonians can be divided into a set of Chern classes defined by the bands' Chern numbers (only one band's Chern number is shown in this illustration). Adiabatically transforming from one Hamiltonian H_1 to another H_2 in a different Chern class, one necessarily crosses a point where the Hamiltonian becomes gapless.

and simplified the expression to the form

$$\sigma_{xy} = \frac{ie^2}{4\pi^2\hbar} \sum_{n\in\text{occ}} \int_{BZ} d^2k \, \langle \partial_x u_{n\mathbf{k}} | \partial_y u_{n\mathbf{k}} \rangle - \langle \partial_y u_{n\mathbf{k}} | \partial_x u_{n\mathbf{k}} \rangle \,. \tag{1.17}$$

As we shall see in the next paragraph, this integral was necessarily quantised to $-2\pi i\nu$ for some integer ν, leading to an overall conductivity

$$\sigma_{xy} = \rho_{xy}^{-1} = \frac{e^2\nu}{2\pi\hbar}. \tag{1.18}$$

Independently, Michael Berry was considering the adiabatic theorem, [25] and showed that when a quantum system was transformed adiabatically around a closed loop in parameter space the final state would pick up some extra phase, now called Berry's phase, which could be interpreted as a surface integral. A detailed explanation of the Berry's phases is given in Chapter 2, we shall provide only a brief discussion here. Although it was not immediately obvious to Berry or Thouless,[4] Avron, Seiler and Simon showed that these ideas were profoundly linked, both deriving from the same concepts in differential geometry [27, 28]. Berry's phase was really the geometric angle accumulated by parallel transport around a closed path – the holonomy – which could be re-expressed as an integral of the curvature over the surface enclosed by the path. Similarly, the integral in the TKNN invariant was actually a quantised integer – the first Chern number,

$$\mathcal{Q} = -\frac{1}{2\pi} \int_{BZ} d^2k \, \langle \partial_x u_{n\mathbf{k}} | \partial_y u_{n\mathbf{k}} \rangle - \langle \partial_y u_{n\mathbf{k}} | \partial_x u_{n\mathbf{k}} \rangle \,, \tag{1.19}$$

which was a topological invariant of the mapping from the Brillouin zone to the Hilbert space, found by integrating Berry's curvature over the entire Brillouin zone [29].

Using these methods, it was now possible to associate a quantised Chern number to each energy level in the band structure of a material. As per the original motivation, the Chern number

[4] Reportedly Berry contacted David Thouless to ask if he thought these phases had anything to do with his TKNN invariant and Thouless responded that it was doubtful there was any connection [26].

determined the contribution of each band to the Hall conductivity. However, one could also view these invariants as a remarkably universal framework for classifying Hamiltonians, since their quantised nature meant that a band's Chern number could not change under any smooth deformation of the system that did not close the band gap (at which point the band, and thus Q, would become ill-defined). Thus, two Hamiltonians with different Chern numbers sit in two different Chern classes, where it is not possible to deform one into the other without a gap closing. Of course, these invariants strictly only applied to systems with a notion of band structure, i.e. for non-interacting systems with translational symmetry. Several proposals exist for extending these invariants to interacting or disordered materials, such as the construction of a real-space Chern number [30–33] which we shall discuss in Chapter 3. The simplest extension of the Chern classification can be defined by noting that the topological class of a Hamiltonian can only change with a closing of the band gap. Thus, as long as a general quantum system has a gapped ground state, and can (without closing this gap) be adiabatically connected to a Hamiltonian with well-defined Chern number, then the two systems are considered to have the same Chern numbers [34]. Thus, we see that, in analogy with the case of RG and universality discussed in the previous section, the Chern classification describes a set of physical properties that are deeply ambivalent to the microscopics of a model. Any changes to the system that do not close the band gap will have no effect on the Chern class or the Hall conductivity.

1.2 Magnetism, Frustration and Fractionalisation

Let us now turn our attention to the opposite case to that discussed in §1.1, to systems whose properties are highly sensitive to the microscopic arrangement of atoms in the material. One of the simplest examples can be found in the study of magnetism, by considering the Heisenberg model of interacting spins. We shall work with a toy model on an arbitrary lattice, consisting of a set of sites at positions $\mathbf{x}_j$ and a set of edges e_{jk} that connect nearest-neighbour vertices at $\mathbf{x}_j$ and $\mathbf{x}_k$. At each vertex we place a single spin-S degree of freedom, which interact with one another according to the Hamiltonian,

$$H = -J \sum_{\langle jk \rangle} \hat{\mathbf{s}}_j \cdot \hat{\mathbf{s}}_k, \tag{1.20}$$

where the sum is only taken over nearest-neighbour pairs of spins and J determines the strength and sign of the bonds' coupling. In contrast to §1.1, these are quantum spins, so the $\hat{s}_j^\alpha$ are operators defined by the spin algebra. Here we will discard the effect of thermal fluctuations and consider the ground state properties only. In the ferromagnetic (FM) regime ($J > 0$) this Hamiltonian favours the alignment of neighbouring spins and the ground-state can be straightforwardly constructed for any lattice by simply choosing a direction, say $\hat{\mathbf{z}}$ and aligning all spins in that direction. Each bond contributes a value $-JS^2$ to the ground state energy – the lowest contribution possible – so we consider all bonds fully satisfied. This phase is stable on any lattice, with any values of $J > 0$. Thus, the ferromagnetic case falls into the class of models described in the previous section – an emergent phase that is largely insensitive to the details of the system.

Now let us consider the antiferromagnetic (AFM) case ($J < 0$). Here neighbouring spins want to anti-align. On a bipartite lattice – where all sites can be divided into two sublattices, A and B, and a spin on an A-site is only adjacent to B-sites and vice-versa – a similar ground state can be constructed. Choosing a direction, we can set all spins on the A sublattice to point along

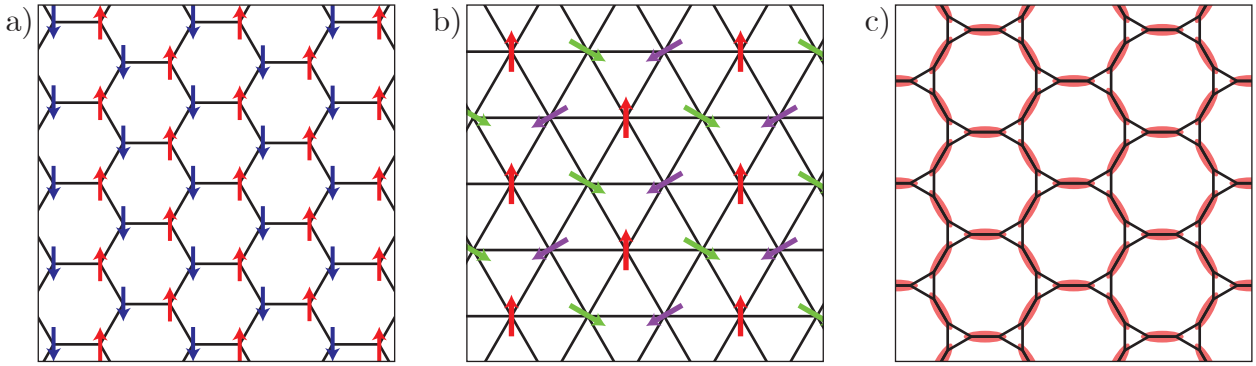


Figure 1.6: The ground state of the spin-$\frac{1}{2}$ antiferromagnetic Heisenberg model on three example lattices. **(a)** The honeycomb lattice is bipartite, so the ground state is Néel ordered. **(b)** On the triangular lattice the ground state is a three site 120° magnetically ordered phase. Here the spins are arranged such that the sum of the spins around each triangle always vanishes. **(c)** On the star lattice, the system forms a valence bond solid, with spin singlets on the inter-triangle bonds, indicated by the red ellipses.

this direction and all spins on the B sublattice to point in the opposite direction. In the classical case ($S \gg 1$), the quantum spin operators are well-approximated by a classical p-dimensional vector of fixed length S, where p (usually ≤ 3) defines the number of spin components. Here, this antiferromagnetic ordering gives us the ground state, and all bonds are maximally satisfied, contributing $-|J|S^2$ to the ground-state energy. In the quantum case ($S \sim 1$), this classical Néel state is typically a good approximation to the true AFM ground state, which is dressed with additional fluctuations. However, on any lattice with odd-length cycles – e.g. a lattice containing triangles, pentagons etc. – this picture is dramatically altered. Now it is no longer possible to construct a Néel-ordered state since the system lacks sublattice symmetry. Rather, the ground state of the system will depend strongly on the geometry of the lattice [35]. For example, after years of debate the consensus is that the triangular lattice forms a 120° ordered state [36–38], shown in Fig. 1.6b. On the star lattice, the ground state resists magnetic ordering altogether, forming a valence bond solid [39–44], shown in Fig. 1.6c, where spins are strongly anti-correlated on the inter-triangle bonds, close to a singlet state, $|s\rangle = (|\uparrow\downarrow\rangle - |\downarrow\uparrow\rangle)/\sqrt{2}$, and much more weakly correlated on the intra-triangle bonds.

As a rule of thumb, the magnetic properties of an antiferromagnetic material are most strongly influenced by two broad features of the lattice. The first is coordination number. In small-S systems, lattices with low coordination numbers favour strong quantum fluctuations, reducing the likelihood of forming a classically-ordered ground state [35]. The second property is frustration, which describes the extent to which the system is unable to simultaneously satisfy all bonds in the Hamiltonian, leading to a ground state energy that is higher than that in an equivalent unfrustrated system. In the example above, the triangle lattice is highly frustrated and has a high coordination number, so forms a classical frustrated order, whereas the star lattice is frustrated and has a low coordination number, leading to a non-classical ground state.

1.2.1 Classical Frustration

To better understand the role of frustration, let us consider the classical case, neglecting quantum fluctuations altogether. Our discussion will largely draw from the references [45–47]. In the large

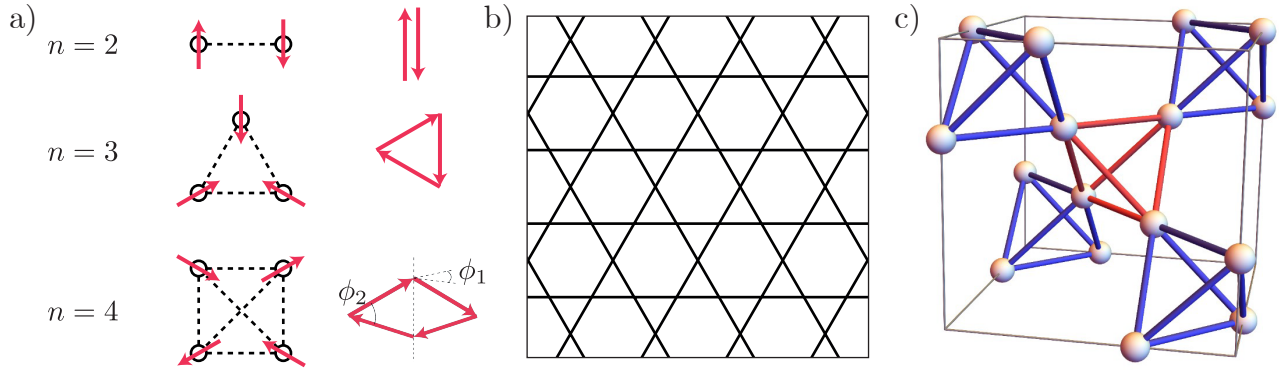


Figure 1.7: **(a)** Three clusters of $n \in \{2...4\}$ spins, showing a ground state configuration of spins. In the $n = 2$ and 3 case, there is a single unique configuration (up to global reflection and rotations), whereas for $n = 4$ there are two independent degrees of freedom, marked with ϕ_m leading to an extremely degenerate ground state. **(b)** A section of kagome lattice, formed by vertex-sharing triangles. **(b)** A section of pyrochlore lattice, formed by vertex-sharing tetrahedra. *Figure reproduced from Theory of Quantum Matter Unit, OIST*

spin limit ($S \gg 1$) as before, we approximate the spins as a classical p-dimensional vector. Let us set $J = -1$ and consider a cluster of n spins, with all-to-all interactions. The Hamiltonian of the cluster is given by

$$H_{Cl} = \frac{1}{2} \sum_{jk} \mathbf{s}_j \cdot \mathbf{s}_k. \tag{1.21}$$

Constructing the total spin operator $\mathbf{S} = \sum_j \mathbf{s}_j$, this Hamiltonian can be rewritten as

$$H_{Cl} = \frac{1}{2} \left(|\mathbf{S}|^2 - nS^2, \right) \tag{1.22}$$

where the constant terms come from the fact that $\mathbf{s}_j \cdot \mathbf{s}_j = S^2$. Thus, we see that the ground state corresponds to any arrangement with total spin $\mathbf{S} = 0$, and has energy

$$E_{\text{g.s.}} = -nS^2/2. \tag{1.23}$$

This is in contrast with the unfrustrated energy that the system would have if all bonds were satisfied, given by

$$E_{\text{u.f.}} = -\frac{1}{2} n(n-1)S^2/2, \tag{1.24}$$

where $n!/2$ is the number of bonds in a cluster of n fully connected spins. The difference between the true ground state energy $E_{\text{g.s.}}$ and the unfrustrated ground state energy $E_{\text{u.f.}}$ can give a rough measure of the degree of frustration in the lattice [48].

Not only does frustration cause the ground state energy to be higher than one might expect based on the coupling strength, but it can also lead to systems with *extensive ground state degeneracy*[5]. To see how this arises, let us count the number of ways to arrange the spins into an $\mathbf{S} = 0$ state. For $n = 2$ or 3, ignoring overall rotations and reflections, there is one unique

[5]Note that not all frustrated systems have degenerate ground states, for example the 120° order found on the triangular lattice does not have extensive degeneracy.

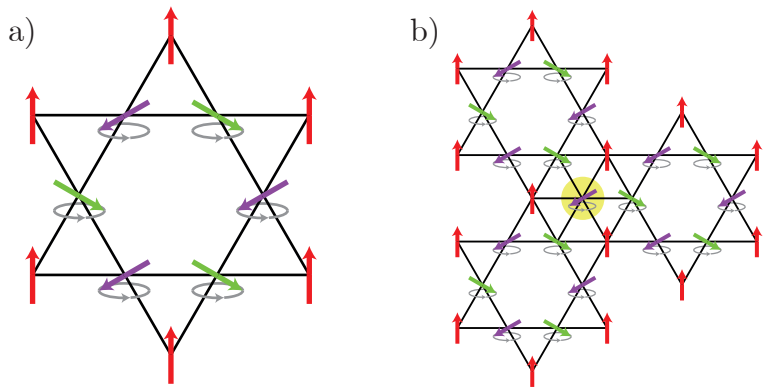


Figure 1.8: **(a)** On the Kagome lattice, the spin arrangement shown can undergo a simultaneous rotation of the purple and green spins without leaving the ground state. **(b)** Modifying the lattice, for example by adding the highlighted central spin, triples the size of the regions that must be rotated together, removing two degrees of freedom.

way. However, for $n = 4$ we have two continuous degrees of freedom, shown in Fig. 1.7a.

Now, let us consider a lattice composed of N_c corner-sharing clusters, for example the kagome lattice with $n = 3$ shown in Fig. 1.7b, or the pyrochlore lattice with $n = 4$, shown in Fig. 1.7c. The Hamiltonian can again be decomposed into a sum of the total spin for each interacting cluster, this time ignoring the constant terms,

$$H = \sum_{n_c}^{N_c} |\mathbf{S}_{n_c}| - \textit{constant}. \tag{1.25}$$

Again, the ground state is found by setting the total spin through each cluster to zero. The ground state degeneracy can be estimated by noting that of each spin contributes $d - 1$ degrees of freedom, each cluster contributes p constraints. Thus, one naively expects the ground state to have

$$D = \frac{N_c}{2}\left(n(p-1) - pd\right) \tag{1.26}$$

remaining degrees of freedom, where the factor of a half comes from the fact that each spin forms part of two clusters. According to this, the Kagome lattice ($n = 3$) has no remaining degrees of freedom, but the pyrochlore lattice has an extensive ground state degeneracy, with each tetrahedron contributing one parameter that can be freely adjusted while remaining in the ground state. In fact, this guess is usually an underestimate, since it does not take into account the fact that the constraints of adjacent plaquettes are not completely independent. For example, the kagome lattice ground state can, in certain ground states, be rotated locally around certain hexagons as shown in Fig. 1.8a, leading to a $D = N_c/9$ remaining unconstrained degrees of freedom [49, 50]. In general, the number of such remaining degrees of freedom is highly specific to the geometry of the lattice. For example, adding in an extra site to the kagome as shown in Fig. 1.8b has the effect of combining three regions, which must now be rotated together, effectively removing two degrees of freedom, despite the fact that the frustration as measured by comparing $E_{\text{g.s.}}$ and $E_{\text{u.f.}}$ has not changed.

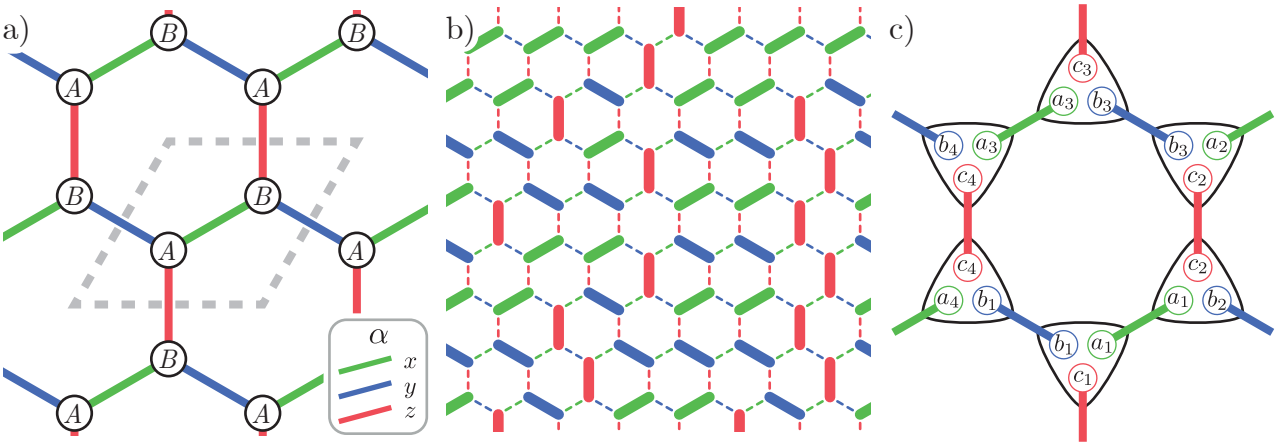


Figure 1.9: **(a)** The honeycomb lattice on which the Kitaev model is constructed. Bond labelling is indicated by colour, and the unit cell is shown by the dashed grey rhombus. **(b)** An example Cartesian state, where the adjacent spins on every highlighted bond are fully aligned in the direction corresponding to that bond's label, forming a dimerisation of the full lattice. **(c)** A parametrisation of the general classical Kitaev ground state, formed by setting the α-component of neighbouring spins on each side of an α-bond to be equal to one another.

1.2.2 The Classical Kitaev Honeycomb Model

Thus far, we have only discussed so-called *geometrical* frustration, where the inability of the system to satisfy all couplings is driven by the geometry of the lattice – usually the presence of odd cycles. However, frustration can also be introduced through the engineering of competing interactions on lattices that would otherwise not be considered frustrated, a type of frustration we shall refer to as *exchange* frustration. Here we shall present one such model, the Kitaev honeycomb model [30]. As the name suggests, the model is constructed on a honeycomb lattice, with a spin placed at each vertex. In the original formulation, Kitaev proposed (and solved) the quantum spin-$\frac{1}{2}$ model. In Chapter 4 we shall discuss in detail the method that he used for solving this model, as well as generalising it to arbitrary lattices. Thus, here let us start by considering the large-S, classical Kitaev model. This has been extensively studied [51–54]. Here we focus on the first part of the classical story, finding the ground state and discussing its degeneracy.

To construct the Hamiltonian, we must assign a label $\alpha \in \{x, y, z\}$ to each bond on the honeycomb, such that every vertex connects to one bond of each type, shown in Fig. 1.9. The Hamiltonian is given by,

$$H = -J^x \sum_{\langle jk \rangle_x} s_j^x s_k^x - J^y \sum_{\langle jk \rangle_y} s_j^y s_k^y - J^z \sum_{\langle jk \rangle_z} s_j^z s_k^z, \tag{1.27}$$

where $\langle jk \rangle_\alpha$ indicates a bond of type α. Let us work at the so-called isotropic point, found by setting all $J^\alpha = +1$, ensuring that each coupling is ferromagnetic.[6]

We wish to find the lowest energy under the condition of fixed-length spins $\mathbf{s}_j \cdot \mathbf{s}_j = S^2 \forall j$. Thus,

[6]We could equivalently use $J = -1$, since this Hamiltonian can be transformed back to the $J = +1$ case by reversing the orientation of every spin on the B sublattice.

let us enforce this total spin condition by adding a Lagrange multiplier to the Hamiltonian,

$$H_\lambda = -\sum_{\langle jk\rangle_\alpha} s_j^\alpha s_k^\alpha - \frac{1}{2}\sum_j \lambda_j(\mathbf{s}_j \cdot \mathbf{s}_j - S^2) \tag{1.28}$$

Taking a derivative with respect to the components of the two spins around an α-bond, s_j^α and s_k^α, we arrive at the following conditions

$$s_k^\alpha = \lambda_j s_j^\alpha, \tag{1.29}$$
$$s_j^\alpha = \lambda_k s_k^\alpha. \tag{1.30}$$

Thus, we may use the relation

$$s_j^\alpha s_k^\alpha = \lambda_j (s_j^\alpha)^2 = \lambda_k (s_k^\alpha)^2, \tag{1.31}$$

to re-express the Hamiltonian in two equivalent forms

$$H = -S^2 \sum_{j\in A} \lambda_j = -S^2 \sum_{j\in B} \lambda_j, \tag{1.32}$$

where we have used the condition $\mathbf{s}\cdot\mathbf{s} = S^2$, and each sum is on only the A or B sites, as shown in Fig. 1.9a. Now all that remains is to find the values of λ_j. For a given site, at least one of the three spin components at that site must be nonzero. Thus, for this pair we may substitute Eqns. 1.29 and 1.30 into one another to obtain the relation, $\lambda_j\lambda_k = 1$. Since the lattice is bipartite, extrapolating this relation implies that $\lambda_j = \lambda_A$ must be constant across all A sites, with the same relation holding for B sites. Furthermore, from Eqn. 1.32 we see that $\lambda_A = \lambda_B$. The lowest energy is found by setting all $\lambda = +1$,

$$E_{\text{g.s.}} = -\frac{1}{2}S^2 N_s, \tag{1.33}$$

with N_s being the number of sites in the system. Thus, the ground states may now be constructed, since we must simply choose a configuration that saturates the lower bound for the energy, as well as the conditions $s_j^\alpha = s_k^\alpha$ for each pair of sites that share an α-bond. The simplest ground states, which we refer to as the Cartesian states, are found by leaving only one of the three components of $\mathbf{s}_j$ nonzero on each site. To be a valid ground state, every site must be paired up with a neighbour, forming a dimerisation where the two spins around a dimer on an α-bond are completely aligned in the α direction. An example is shown in Fig. 1.9b. Thus, the degeneracy of the Cartesian states can be found by counting the number of dimerisations, which scales with $1.381^{N_s/2}$ [55, 56]. However, since each dimer has two directions it can align in, the degeneracy is

$$n_{\text{Cart.}} = 2.762^{N_s/2}. \tag{1.34}$$

The Cartesian states are not disconnected from one another, since it is possible to transform any Cartesian state into any other smoothly without leaving the ground state, since *any* state that satisfies $s_j^\alpha = s_k^\alpha$ on every bond is also in the ground state. Thus, a general ground state may be constructed by choosing one parameter for each bond, we shall use a on x-bonds, b on y-bonds and c on z-bonds, and assigning the components of $\mathbf{s}$ according to the three bond variables on each site, as shown in Fig. 1.9c. Provided that the bond parameters on any site

satisfy $a^2 + b^2 + c^2 = S^2$, a state of this form automatically saturates the lower bound for the energy. The ground state degeneracy can then be approximated by noticing that this ansatz has one degree of freedom for every bond, and one constraint – the total spin S – for every site. Since each site connects to 3 bonds, this leaves $D = N_s/2$ continuous remaining degrees of freedom, in comparison to the discrete set of Cartesian states. Although, it should be mentioned that, once the effect of fluctuations is taken into account, the Cartesian states are selected as the true ground states rather than the full manifold of classical ground states [53].

1.2.3 A Quantum Spin Liquid

So far we have defined a notion of magnetic frustration, and shown how it can arise both as a consequence of lattice geometry or, as in the Kitaev case, due to the presence of competing interactions. In a classical system, often the consequence of frustration is the creation of an extensive number of degenerate ground states. This allows classically frustrated systems to avoid magnetic long-range ordering at low temperatures, since even a small amount of thermal energy is sufficient for the system to freely explore these degenerate states. Indeed, one of the most robust signatures of frustration is that – in contrast to unfrustrated ferro- and antiferromagnets, which undergo a spin-ordering (or freezing) transition at a temperature determined by the microscopic coupling strength [4] – frustrated magnets tend to remain paramagnetic (or liquid) down to far lower temperatures than their coupling strength would suggest [47, 57]. In some systems, notably in the case of spin ice [58–60], the system does not undergo an ordering transition at any temperature. Such materials are collectively known as classical spin liquids, in reference to the unusually low temperatures to which these paramagnetic (liquid) phases persist.

However, thermodynamics is not the only mechanism by which fluctuations arise in nature. When the spin in a frustrated magnet is small (that is, close to $S = \frac{1}{2}$), quantum fluctuations can play a significant role, allowing the spins to resist ordering even at zero temperature. Furthermore, the consequences of quantum fluctuations can be drastically different from the classical case, since a quantum system is able to form coherent superpositions of these degenerate classical states. Thus, it is possible for the ground-state degeneracy of a classical spin liquid to be broken in the equivalent quantum system, which finds a lower-energy *quantum spin liquid* (QSL) ground state. Since a QSL state arises due to the frustration of classical order, the system is often forced to use entanglement as a resource to lower the ground state energy, resulting in a state with long-ranged quantum correlations. These states of matter provide a rich context for finding exotic phenomena with no classical analogue. Although no formally accepted definition exists, the consensus is that to qualify as a QSL, a phase of matter must exhibit some combination of two related emergent properties: fractionalised excitations and an emergent gauge field [61, 62].

In a fractionalised system, the quasiparticles carry a fraction of the quantum numbers of the constituent particles in the material. The most famous example of this phenomenon is the fractional quantum Hall effect [63], where the quasiparticles carry a fraction of the charge (and a fraction of the exchange statistics) of the electron. However, the last 30 years of research has revealed an astonishing number of ways that fractionalised particles can appear. For example, in classical spin ice, the natural dipolar spin-flip excitations split into pairs of magnetic monopoles, and as we shall see in the following discussion (and in detail in Chapter 4) excitations take the form of Majorana fermions in the Kitaev model. Of course, even in a fractionalised material, one must respect the conservation laws implied by the original, unfractionalised constituents. That is, quantities such as the total charge, or the total magnetic moment of the system are not

allowed to take fractionalised values. In a quantum Hall system where quasiparticles have $\frac{p}{q}$ charge, we must ensure that the system always contains a multiple of q such particles. Similarly, monopoles in spin ice must always be created and destroyed in pairs, else the system as a whole will have nonzero magnetic charge, which is forbidden in electromagnetism. This global constraint means that an effective description of the system must include an emergent gauge field, whose role is to enforce this symmetry, encoding the constraint locally in the configuration of the field.

Let us end this section by describing the exact solution to the spin-$\frac{1}{2}$, quantum Kitaev model and showing how it satisfies these two requirements. Note that this will largely be a qualitative discussion, and many important details will be missed – most notably the role of the ground-state projector. In Chapter 4 a lengthy discussion is provided, whereas here we keep only the minimum detail needed to give an intuitive picture of fractionalised excitations in the Kitaev model. For a system of spin-$\frac{1}{2}$ particles, we are no longer free to treat each spin as a classical vector, and instead must express the Hamiltonian (Eqn. 1.27) in terms of the Pauli matrices that define the spin algebra,

$$s_x \to \frac{1}{2}\sigma^x, \qquad s_y \to \frac{1}{2}\sigma^y, \qquad s_z \to \frac{1}{2}\sigma^z. \tag{1.35}$$

Discarding a global factor of $\frac{1}{2}$, the Kitaev Hamiltonian takes the following form,

$$H = -\sum_{\langle jk\rangle_\alpha} J^\alpha \sigma_j^\alpha \sigma_k^\alpha. \tag{1.36}$$

To diagonalise this Hamiltonian, Kitaev transformed to an artificially enlarged Hilbert space by replacing each spin-half degree of freedom with two fermionic states, which could then be expressed in terms of four Majorana fermionic operators, labelled as c, b^x, b^y and b^z according to the transformation $\sigma_j^\alpha \to i c_j b_j^\alpha$. These operators are self-adjoint, and obey the following relations,

$$c^\dagger = c, \tag{1.37}$$
$$\{c_j, c_k\} = \delta_{jk}. \tag{1.38}$$

After performing this transformation, Kitaev showed that the b-type Majoranas were essentially static. The two b^α operators on each α-bond could be paired up as a conserved operator $\hat{u}_{jk} = i b_j^\alpha b_k^\alpha$. Because each site connects to only one bond of each type, each $\hat{u}_{jk}$ operator also shows up only once, and so commute with each other as well as with the Hamiltonian. This means that they can be treated as a conserved quantity, and replaced in H with their eigenvalues, $\hat{u}_{jk} \to u_{jk} = \pm 1$, resulting in a Majorana Hamiltonian parametrised by these bond values,

$$H_u = \sum_{\langle jk\rangle_\alpha} J^\alpha u_{jk} i c_j c_k. \tag{1.39}$$

We started with a system of interacting spins, however this Hamiltonian constitutes a very different description of the model. Here, the spins have been transformed into two different coupled degrees of freedom: a fractionalised quasiparticle, given by the N_s remaining c-type Majorana fermions, and a classical $\mathbb{Z}_2$ gauge field given by the u_{jk} values. Let us discuss each in turn.

To see why the c_j operators represent a fractional quasiparticle, we note that the first step in

the solution involves representing each spin with a pair of fermionic operators f, which obey the standard fermionic anticommutation relations,

$$\{f_j, f_k\} = 0, \tag{1.40}$$
$$\{f_j, f_k^\dagger\} = \delta_{jk}. \tag{1.41}$$

Now, let us consider 'splitting' a complex fermionic operator into a real and imaginary part, represented by two Majorana operators,

$$f_j = \frac{1}{2}(c_j + ic_j'). \tag{1.42}$$

Plugging this substitution into the fermion anticommutation relations, we see that these operators must be Majorana fermions, obeying Eqns. 1.37 and 1.38. This transformation is essentially a basis change, where a system of N_f fermions can be represented by $2N_f$ Majorana fermions. These can only be constructed in pairs, such that the combination of two Majoranas maps back to the original fermionic operator's two-dimensional Hilbert space. Thus, each Majorana describes half the degree of freedom of a single fermion.

Of course, the existence of a Majorana representation does not imply the system has fractionalised excitations – any fermionic system can be trivially re-expressed in a Majorana basis. Furthermore, any excitation must have a representation in terms of the original fermionic operators, so must be expressible with an even number of Majorana operators. The fractionalised nature of the system is revealed when we ask whether two Majorana operators that describe an excitation can be separated from one another. In most systems the answer is no, these fractionalised modes are subject to a confining potential. Such a potential ensures that it costs an infinite amount of energy to infinitely separate the quasiparticles. However, in a fractionalised system the potential is not confining, and we only pay a finite energy cost for infinitely separating these two quasiparticles.

To understand how the Majorana fermions may become deconfined, let us turn our attention to the $\mathbb{Z}_2$ gauge field defined by $\{u_{jk} = ib_j^\alpha b_k^\alpha\}$. We take advantage of the fact that $u_{jk} = \pm 1$ to rewrite the factor iu_{jk} as an exponential, re-expressing the Hamiltonian in the form,

$$H_u = \sum_{\langle jk\rangle_\alpha} J^\alpha e^{\frac{i\pi}{2}u_{jk}} c_j c_k. \tag{1.43}$$

Thus, the u_{jk} values couple to this fermionic hopping Hamiltonian exactly as a Peierls phase would [64], and so we can interpret these as if they were a magnetic vector potential. However, unlike a true magnetic field, where the phase can take any value – a $U(1)$ field, here the phase can only take two values, $\pm\frac{\pi}{2}$, making it a $\mathbb{Z}_2$ field. In analogy with electromagnetism, we may define a gauge transformation, corresponding to changing the sign of u_{jk} on the three bonds that connect to a given site, as well as a gauge-invariant quantity analogous to the magnetic flux thorough a plaquette. In the $\mathbb{Z}_2$ field, a flux-like quantity can be defined by taking a product of the phase factors going clockwise around a given plaquette,

$$\phi_p = \prod_{jk\in p} e^{\frac{i\pi}{2}u_{jk}} \equiv \prod_{jk\in p} iu_{jk}. \tag{1.44}$$

These fluxes can also only take two values, $\phi_p = \pm 1$. Finding the energies and eigenstates of this Hamiltonian now has two parts: First we choose the flux, setting all values of ϕ_p, which defines

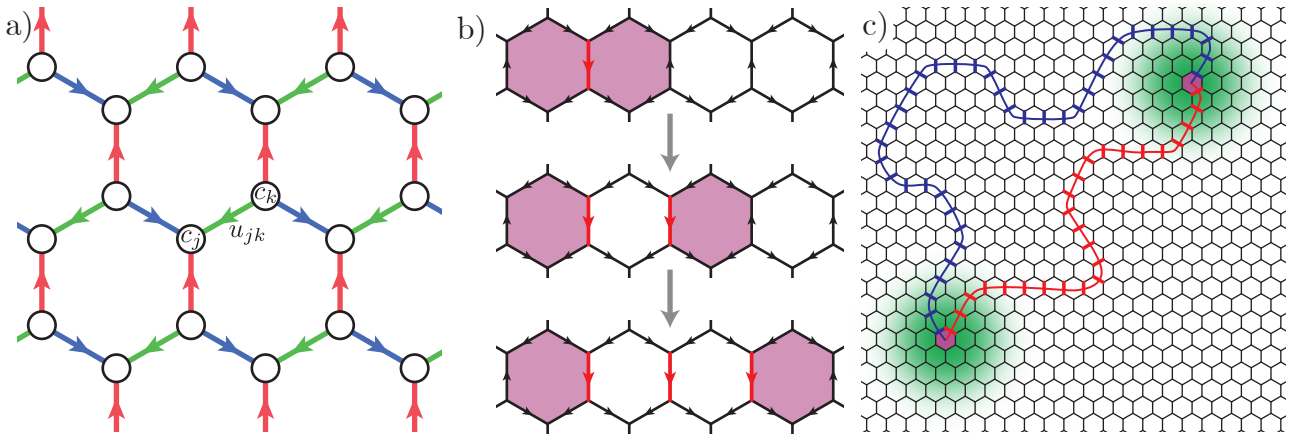


Figure 1.10: **(a)** A diagram of the Honeycomb model described in Eqn. 1.39. Here a single Majorana fermion lives at each site, indicated with the white circles, and each bond has a corresponding u_{jk}. Since the constituent b-operators anticommute, these bond variables satisfy $u_{jk} = -u_{kj}$. Thus, we may represent them with an arrow, where the direction of the arrow indicates the order of subscripts for which u_{jk} is positive. Bond labelling follows the same colouring convention as in Fig. 1.9. **(b)** An illustration of creating and transporting a pair of gauge fluxes. Starting with a background configuration where all plaquettes have flux $+1$, a single pair of fluxes (indicated with the purple plaquettes) is created by flipping the sign of the red bond. One of the plaquettes is then transported by flipping successive bonds. **(c)** Two fluxes are created, with a string of flipped bonds connecting them. Each flux has a Majorana mode localised to it, indicated by the green region.

a quadratic Majorana Hamiltonian. Then, this Hamiltonian is solved, giving the spectrum of the remaining fermionic degrees of freedom.

As is the case with a magnetic field, the flux through any complex path can always be written as a sum over the fluxes through every plaquette encircled by this path. However, there are two important exceptions to this for a system in periodic boundaries. Here it is possible to construct two different *non-contractible* loops, which wrap around the torus in the x and y directions. These enclose no area, so the flux through these loops cannot be written as a sum over hexagons. Additionally, the energetic cost of threading a flux through a loop decays exponentially in the loop length, so for a sufficiently large system these two non-contractible fluxes index a 2^2-fold degeneracy for all states in the system. If we construct a Kitaev model on a general closed manifold, the system must have $2g$ non-contractible loops, where g is the genus of the manifold. Following the same argument, once sees that the ground state (all states, in fact) has a 2^{2g}-fold degeneracy. Systems where the ground state degeneracy is determined by the topology of the manifold are said to have *topological order* [65, 66]. In fact, one can show that in a gapped system such a ground state degeneracy is a necessary prerequisite for the emergence of fractionalised excitations [67].

Thus, we see that excitations in this model can take two forms: flux excitations, which correspond to changing the value of ϕ_p through a given plaquette, and fermion excitations, which correspond to keeping the fluxes static and exciting a Majorana mode. Creating the latter excitation is straightforward, we simply choose an excited state of the Hamiltonian H_u, with $\{u_{jk}\}$ set to some arrangement of bond operators corresponding to the ground-state flux sector. Creating a flux excitation, however, is slightly more complex. This is because the fluxes are not a degree of freedom we have direct access to – they are derived from the gauge field u_{jk}, which places

constraints on which flux sectors can be created. Specifically, plaquette fluxes cannot be flipped in isolation. This can be seen by considering the effect of flipping the sign of one bond operator, which always changes the value of the flux through both adjacent plaquettes. The two flipped plaquettes can be moved arbitrarily far apart by a successive flipping of bond operators, as shown in Fig. 1.10b. These two fluxes are connected by a string of bonds that have been flipped with respect to the original configuration of u_{jk}, however this string is not measurable, since it can be arbitrarily moved around at no energy cost by a gauge transformation, shown in Fig. 1.10c. Thus, this string must be tensionless, distant fluxes will not pay an energy cost for separating further.

The final piece of this story comes from the realisation by Kitaev that one could engineer this system to have a gapped topological ground state – done by perturbing the model with a weak magnetic field. In this case, the fermionic spectrum of H_u had two clearly-separated non-interacting bands, for which one could calculate the Chern number. When this Chern number was odd, Kitaev showed that the fermionic excitations and the flux excitations would become tightly bound to one another.[7] Here, flipping a plaquette's flux with respect to the ground state would also have the effect of localising a single Majorana mode around that flux, as shown in Fig. 1.10c. Since fluxes would only be created in pairs, each excitation contains two Majorana fermions, corresponding to a single fermionic degree of freedom. However, provided that these fluxes were sufficiently well-separated that their respective Majorana modes could not interact with one another, the individual Majorana modes would have zero energy. Thus, the energy cost of creating the pair only depended on the cost of creating two fluxes, and once they were well-separated, they could be moved around freely – that is, the fermionic excitation split into two completely deconfined Majorana fermions. Thus, we see that the Kitaev honeycomb model has the sufficient qualities to be considered a quantum spin liquid, where the model could be transformed exactly into a set of fractionalised particles, interacting under a $\mathbb{Z}_2$ gauge field that enforced the constraints of even Majorana occupation, while still allowing them to exist as independent particles.

1.3 Thesis Outline

Thus far, we have introduced examples of two very different phenomena in condensed matter physics. In Section 1.1, we described the notion of universality, an inherently many-body property, that arises from the statistical averaging over enormous numbers of interacting particles. We also presented an introduction to the quantum Hall effect – a manifestly non-interacting, single particle phenomenon. Both of these theories provided an answer to the question: *How is it possible for many systems, with wildly different microscopic configurations, to realise the same types of collective properties?* Focussing on the quantum Hall effect, since it is most relevant to this thesis, the solution relied on the construction of a topological invariant, the Chern number, which could be calculated in any system with a notion of band structure. This provided us with a broad classification system, whereby vastly different Hamiltonians on a wide range of atomic lattices could be identified as sharing a 'universal' set of properties determined by this invariant. The power of this approach was that it proved deeply indifferent to the microscopics of a system. Provided that a notion of band structure could be defined – a relatively weak condition – the Chern number allows us to make statements about the materials properties, such as its Hall

[7] The proof of this statement may be found in Appendix C of Kitaev's original paper [30]

conductivity and the presence of edge modes, without having to account for the details of a specific model.

On the other hand, in Section 1.2 we told a very different story – that of frustration in magnetic materials. Here we found that superficially similar materials, i.e. those consisting of spins on a lattice, interacting according to a rather limited variety of couplings (Ferromagnetic, Antiferromagnetic, Ising, etc.), could give rise to an enormous variety of collective phases depending on the geometry of the material and the finer details of the spins' couplings. Often when frustration is present no single state can independently satisfy the requirement of every coupling, and the emergent phases are able to explore (and in the quantum case, entangle) a multitude of degenerate ground states. The character of these degenerate states, and the phases that emerge, are highly specific to the details of the system – there is no universal consequence of frustration. In a classical, zero temperature context, the emergent phases can be extremely fragile, where the presence of even weak perturbations, including disorder, can serve to lift the delicate ground-state degeneracy and either allow a system to select a single preferred state, or result in glassy physics – where system has many near-degenerate low-energy states which are well-separated in configuration space, and the order that forms depends unpredictably on quenched disorder [68, 69]. In the quantum context, the situation is less precarious, since in general a gapped QSL state is robust against weak disorder, and many gapless QSL systems can also be shown to be robust [62]. However, it remains the case that the formation of such materials generally depends on an intricate combination of lattice geometry and specific couplings. As we saw, depending on the lattice, the antiferromagnetic Heisenberg model can go from ordered (honeycomb/square) to VBS (star) to a potential QSL (kagome).

In this thesis, our line of inquiry will lie at the intersection of these two effects, where we investigate the veracity of both the assumptions presented above – that is that Chern physics is inherently indifferent to microscopics, and that frustrated magnetism and the formation of spin liquids is inherently sensitive to it. In particular, we shall focus on the structural properties of a material, where our approach will frequently be to start with a known system, defined on a particular lattice, and then ask which properties are altered and which survive when we allow the lattice to change. The structure of this thesis is as follows:

Chapter 2 is largely introductory material, where we present a detailed explanation of the Chern number, describing how it may be calculated given the band structure of an arbitrary non-interacting Hamiltonian with translational symmetry. We consider both the case of a discrete and a continuous Brillouin zone. We finish this chapter by introducing a simple model for a Chern insulator, the Qi-Wu-Zhang model, and provide a straightforward generalisation to amorphous systems.

In Chapter 3, we focus on understanding how robust the Chern number is against the breaking of translational symmetry. As we discussed in Section. 1.1.1, the underlying physical phenomena – the quantum Hall effect and topological insulators in general – are interesting specifically *because* they are robust against disorder. However, the Chern number is formulated as an integral over the Brillouin zone. Thus, in any physical system that lacks band structure, either through the presence of disorder or interactions, this quantity becomes ill-defined. Thus, there is a tension in our mathematical framework, where the tools we use to describe disorder-resistant phenomena are themselves fatally undermined by disorder. We introduce one of the methods that has been employed to circumvent this problem: the real-space Chern number. Several such proposals exist, of which we discuss three, namely the Chern marker [33], the Bott index [32] and Kitaev's local marker [30], showing the ways that they may be considered equivalent to one another. Each of these markers was originally constructed with no clear connection to experiment or a

simple physical interpretation of the quantity. We propose a physical observable – a localised reformulation of a Hall measurement, showing that the measured conductivity corresponds to a local Chern marker when evaluated in the bulk of a Chern insulator. Thus, our conclusion is that there exists a formulation or Chern number, with a well-defined physical interpretation, that shares the disorder-indifferent nature of the underlying physics.

In Chapter 4 we turn our attention back to frustrated magnetism, focussing on the Kitaev honeycomb model [30]. We study the spin-$\frac{1}{2}$, quantum version of this system, providing a review of Kitaev's exact solution via a transformation to a Majorana fermion representation. Here we consider whether the Kitaev QSL is as fragile as one would expect, given the general discussion of frustrated magnetism presented above. To do this, we consider the possibility of constructing and solving a Kitaev Hamiltonian on a general disordered lattice, the only constraint being that it must remain tri-coordinated to allow for x, y and z-bond labels to be assigned consistently. Remarkably, we find that an exact solution can be constructed on almost any tri-coordinated lattice. Furthermore, we verify that the presence of odd cycles on a general lattice leads to the formation of a ground state that spontaneously breaks time-reversal symmetry, transforming the originally gapless QSL phase into a gapped chiral amorphous QSL. In the construction of the exact solution, the strongly-interacting Kitaev model decomposes into a non-interacting system of Majorana fermions. As we shall see, the chiral gapped QSL phase depends explicitly on the Chern number of the Majorana Hamiltonian. Thus, we find that the robustness of this phase can be understood as a consequence of the robustness of the topological invariants presented in Chapter 3. In contrast to the general wisdom that 'frustrated magnets are inherently fragile phases of matter', the Kitaev QSL can be constructed and solved on a wide variety of lattices, and even with the addition of strong bond-dependent disorder.

Finally, in Chapter 5, we consider the effect of adding geometric frustration to the Kitaev model. As discussed above, the frustration in this model stems from competition between the three bond types and, as we see in Chapter 4, the pure Kitaev model is indifferent to the details of the lattice geometry. However, real candidate Kitaev materials – such as the iridates Na_2IrO_3 and α-Li_2IrO_3 [70–72], and α-$RuCl_3$ [73, 74] – do not realise a pure-Kitaev Hamiltonian. These materials are characterised by dominant Kitaev interactions, however they also contain other subdominant perturbations, such as Heisenberg couplings, which prevent the materials from realising Kitaev's QSL ground state. Previous studies of the Kitaev model that account for these extra terms have unearthed a rich phase diagram depending on the relative strength and sign of the perturbations. These generally contain QSL phases as well as a variety of ordered phases, for example Neél and various stripe-ordered phases. As we have discussed, antiferromagnetic systems are often highly susceptible to geometric frustration. Thus, we ask whether constructing a 'more realistic' Kitaev-Heisenberg (KH) model on a geometrically frustrated lattice can lead to the emergence of new magnetic order not seen on the conventional honeycomb model. The answer to this question is *yes*. We construct the KH model on the star lattice – the simplest example of a tri-coordinated lattice with odd cycles. Here, we find that, in the regions of the phase diagram where the Honeycomb model contains antiferromagnetic order, the star-lattice model forms two different valence bond (VBS) solid ground states. Thus, we find ourselves in the peculiar situation where of all the phases that emerge in our model, classically-ordered phases turn out to be the most susceptible to microscopic changes in the lattice, whereas the quantum spin liquid phases are among the most robust! Considering the effect of an applied magnetic field, we show that the VBS states hosts a rich phase diagram of topological triplon excitations and determine the Chern numbers of the bands.

1.4 Publications

The work in this thesis is based on the following publications:

- P. d'Ornellas, R. Barnett, and D. K. K. Lee, "Quantized bulk conductivity as a local Chern marker", Phys. Rev. B **106**, 155124 (2022)
  Covered in Chapter 3.
- G. Cassella, P. d'Ornellas, T. Hodson, W. M. H. Natori, and J. Knolle, "An exact chiral amorphous spin liquid", Nature Communications **14**, 6663 (2023)
  Covered in Chapter 4.
- P. d'Ornellas and J. Knolle, "Kitaev-heisenberg model on the star lattice: from chiral majorana fermions to chiral triplons", Phys. Rev. B **109**, 094421 (2024)
  Covered in Chapter 5.

Also published during this PhD:

- P. d'Ornellas, "Forces between kinks in ϕ^8 theory", Journal of Physics Communications **4**, 055014 (2020)

Chapter 2

Chern Number and Topological Insulators

To understand the role that topology plays in non-interacting insulators, we must first introduce several related concepts, the Berry phase, Berry curvature and Chern number. This chapter will only focus on the original formulation of these concepts, in a language first proposed by Berry, Simon and many others [25, 27, 28], however a number of excellent reviews also cover the topic, which has become a standard tool in condensed matter physics [79–82]. These concepts are initially presented as a property intrinsically tied to band structure, which can only be expressed for a translationally symmetric, non-interacting material. However, our intention is to extend these notions to also include disordered systems. Thus, in §2.2 we shall provide a useful toy model for a two-level Chern insulator, the Qi-Wu-Zhang model [83], along with a straightforward extension of this model to arbitrary lattices.

Throughout this chapter and the next we will focus on non-interacting electrons on a lattice, thus let us begin by defining our Hilbert space in a first-quantised framework. We will work with the most general definition of a non-interacting tight-binding Hamiltonian in two dimensions. The Hilbert space $\mathcal{H}$ is constructed from a set of N sites with η internal degrees of freedom, labelling site j at a position $\mathbf{r}_j$. For example, these sites could correspond to atoms, and the states at each site could represent individual orbitals around an atom. We will not assume that our sites are arranged in a regular lattice – we wish to also model amorphous structures – thus, a state in this system can be written as

$$|\psi\rangle = \sum_j c_{j,\alpha} |\mathbf{r}_j\rangle \otimes |\alpha\rangle \,, \tag{2.1}$$

where $c_{j,\alpha}$ are a set of complex coefficients and $\alpha \in \{1...\eta\}$ labels the internal degree of freedom. A general Hamiltonian in this context takes the form

$$H = \sum_{j,k,\alpha,\beta} H_{j,k,\alpha,\beta} |\mathbf{r}_j\rangle \langle \mathbf{r}_k| \otimes |\alpha\rangle \langle \beta| \,. \tag{2.2}$$

If the system has translational symmetry $\{\mathbf{r}_j\}$ will lie on a regular lattice with periodic boundaries and the Hamiltonian is invariant under translations.Here, we can diagonalise the Hamiltonian

in a basis of k-states,

$$|\mathbf{k}\rangle = \frac{1}{\sqrt{N}} \sum_{\mathbf{r}_j} e^{-i\mathbf{k}\cdot\mathbf{r}_j} |\mathbf{r}_j\rangle . \tag{2.3}$$

For a finite system the k-states are quantised to $k_a = 2\pi n/L_a$, where L_a is the length of the system in direction $\in \{x, y\}$, whereas in the case of an infinite system k can take any value in the interval $[0, 2\pi]$.

2.1 Abelian Berry Phase and the Chern Number

In this section we present a careful discussion of Berry's phase, Berry curvature and the Chern number [25, 27], showing how these quantities may be calculated form the band structure of a general non-interacting insulator. There are two cases to discuss: for a finite system the Brillouin zone constitutes a discrete lattice of states. Thus, in §2.1.1, we show that Berry phase can be understood as the relative phase between adjacent states, and that Berry flux is defined on the plaquettes of the lattice. In §2.1.2 we consider the case of an infinite system. There the Brillouin zone is a continuous manifold and the band structure defines a mapping from this manifold to the Hilbert space of periodic states. In this case, Berry's phase is a geometric property of this smooth mapping. In both cases, we derive the form of the Chern number and justify its quantisation. Finally, in §2.1.3 we provide an example – that of a two level system – where the Berry flux can be understood straightforwardly in terms of the flux emitted by a monopole, allowing us to present a simple visual argument for the quantisation of the Chern number. Our discussion will largely follow [82, 84].

2.1.1 A Discrete Brillouin Zone

In quantum mechanics a state is defined as an equivalence class of vectors, where two states that differ only by a complex phase are considered physically equivalent,

$$|\psi\rangle \sim e^{-i\alpha} |\psi\rangle . \tag{2.4}$$

Thus, we have a redundancy built into our description of physics. This means that one can define a gauge transformation – multiplying a state with a complex phase, a $U(1)$ gauge – that is guaranteed not to affect the state in any measurable way. Any derived quantity must be invariant under gauge transformations to qualify as a physical observable.

Now, let us consider an arbitrary set of states in the same Hilbert space, $\{|\psi_j\rangle\}$. Analogous to the 'global' gauge transformation presented above, we may define a 'local' gauge transformation here, where we apply a different phase to each individual state,

$$|\psi_j\rangle \to e^{-i\alpha_j} |\psi_j\rangle . \tag{2.5}$$

Again, the physical meaning of each state is unaffected, so all observable quantities must be invariant under this transformation. Thus, one might wonder whether any *phase-like* quantity calculated from these states can have a physical meaning. For example, the relative phase

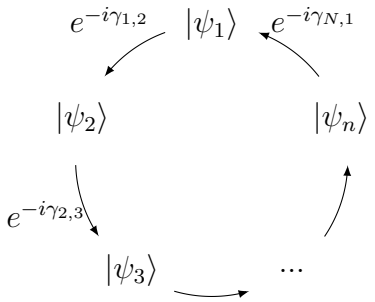
between state j and k, $\gamma_{j,k}$ can be defined as

$$e^{-i\gamma_{j,k}} = \frac{\langle\psi_j|\psi_k\rangle}{|\langle\psi_j|\psi_k\rangle|}. \tag{2.6}$$

Clearly this quantity is invariant under a global gauge transformation, however it is not invariant under a local transformation, changing according to

$$e^{-i\gamma_{j,k}} \to e^{-i(\gamma_{j,k}+\alpha_j-\alpha_k)}, \tag{2.7}$$

and so cannot be a physical observable. In order to construct a gauge-invariant object, let's pick a set of n (≥ 3) states $|\psi_j\rangle$ and arrange them in a loop.



We can now define a new quantity, the Berry phase, as

$$e^{-i\gamma_B} = \frac{\langle\psi_1|\psi_2\rangle\langle\psi_2|\psi_3\rangle ... \langle\psi_N|\psi_1\rangle}{|\langle\psi_1|\psi_2\rangle\langle\psi_2|\psi_3\rangle ... \langle\psi_N|\psi_1\rangle|} \tag{2.8}$$

Another way of writing this would be

$$\gamma_B = -\arg\mathrm{Tr}\left[\hat{\psi}_1\hat{\psi}_2 ... \hat{\psi}_N\right], \tag{2.9}$$

where the trace is over the whole system, and $\hat{\psi}$ is shorthand for the density operator

$$\hat{\psi}_i = |\psi_i\rangle\langle\psi_i|. \tag{2.10}$$

This quantity is clearly gauge-invariant, since any phase applied to a state $|\psi_m\rangle$ will show up twice, once from $\langle\psi_m|\psi_{m+1}\rangle$ and once from $\langle\psi_{m-1}|\psi_m\rangle$. The phase will have opposite sign in each of these expressions, so they cancel out. Furthermore, we can see that the Berry phase around a loop is simply the sum of all the relative phases around that loop modulo 2π.

$$\gamma_B = \sum_{n=1}^{N}\gamma_{n,n+1} \mod 2\pi \tag{2.11}$$

2.1.1.1 Berry Flux

Now suppose that we have a large number of states arranged in a 2D grid. These states $|\psi_{\mathbf{k}}\rangle$ are labelled with a pair of indices k_x and k_y. In general, this parameter $\mathbf{k}$ will refer to the crystal momentum, however the construction is equally valid for any other parameter that defines a 2D grid of quantum states, shown in Fig. 2.1.

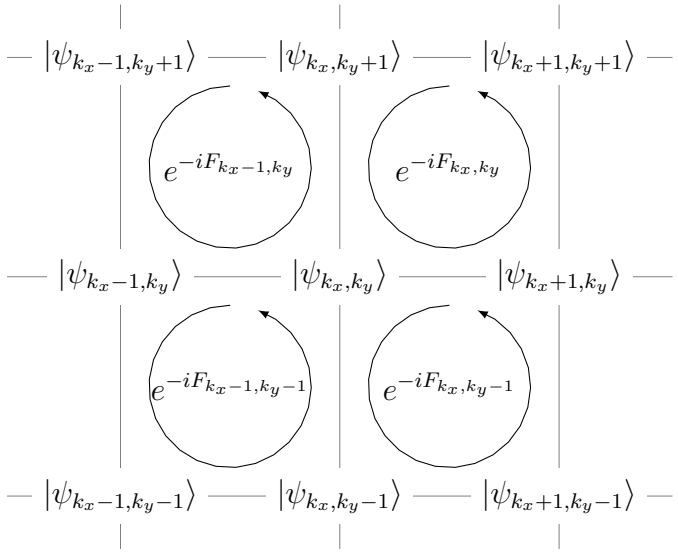


Figure 2.1: A grid of states parametrised by the discrete variables $\mathbf{k}$, given by $|\psi_{k_x,k_y}\rangle$. For each plaquette, the Berry phase is calculated by taking the inner products of the states going counterclockwise around the loop.

We introduce a new quantity called the Berry flux, defined as the Berry phase around a plaquette on the grid,

$$F_{\mathbf{k}} = -\arg \mathrm{Tr}\left[\hat{\psi}_{k_x,k_y}\hat{\psi}_{k_x+1,k_y}\hat{\psi}_{k_x+1,k_y+1}\hat{\psi}_{k_x,k_y+1}\right]. \tag{2.12}$$

$F_{\mathbf{k}}$ is just the sum (mod 2π) of the relative phases along each edge of the plaquette starting at point $\mathbf{k}$. Thus, the Berry phase around some arbitrary loop can be written as a sum of the Berry flux for all plaquettes encircled by the loop. In this sum, the phase along any internal edge appears with opposite sign in the values of $F_{\mathbf{k}}$ for the two adjacent plaquettes, leaving only the phase along the boundary,

$$\exp\left[-i\sum_{\substack{\text{inside}\\ \text{region}}} F\right] = \exp\left[-i\sum_{\text{boundary}} \gamma\right] \tag{2.13}$$

This resembles Stokes' law, however there is a subtlety worth mentioning. All we have required is that the complex exponential of each sum is the same. This does **not** mean that the sum of the Berry flux inside a region is equal to the sum of relative phases around the boundary, since they are allowed to differ by an arbitrary multiple of 2π.

2.1.1.2 Chern Number

Now let's assume that our grid of $\mathbf{k}$ points has periodic boundaries – as is the case for states on the Brillouin zone – with $1 \leq k_x \leq N_x$ and $1 \leq k_y \leq N_y$. The lattice is a discretisation of the torus – a closed manifold. Thus, let us ask what the total flux through the whole manifold is.

Following the argument of Eqn. 2.13, the total Berry flux must satisfy

$$\prod_{k_x=1}^{N_x}\prod_{k_y=1}^{N_y} e^{-iF_{k_x,k_y}} = 1, \tag{2.14}$$

because every edge in this sum is an internal edge, and thus they cancel out. As before, this does not mean that the sum of all Berry fluxes in the system vanishes, rather the sum must be a multiple of 2π. Thus let us define this multiple as the Chern number, $\mathcal{Q}$,

$$\mathcal{Q} = \frac{1}{2\pi}\sum_{k_x,k_y} F_{k_x,k_y}. \tag{2.15}$$

$\mathcal{Q}$ is necessarily restricted to integer values, since a non-integer value would contradict equation 2.14.

2.1.2 Topology of a General Hamiltonian

Now let us consider the case of a smooth parameter space. We start by defining some arbitrary Hamiltonian $H(\mathbf{R})$, which depends on some smooth parameter $\mathbf{R} \in \mathcal{R}$. For every value of $\mathbf{R}$, the Hamiltonian has eigenstates $|\psi_n(\mathbf{R})\rangle$ with corresponding energies ε_n. As before, these eigenstates are only well-defined up to a global phase. Thus, let consider a single state $|\psi(\mathbf{R})\rangle$ and define a local gauge transformation, applying an $\mathbf{R}$-dependent phase $\alpha(\mathbf{R})$ to all the states over this band.

$$|\psi(\mathbf{R})\rangle \to e^{-i\alpha(\mathbf{R})}\,|\psi(\mathbf{R})\rangle\,. \tag{2.16}$$

Before we continue, let us define a *smooth gauge* as a choice of gauge that ensures that the $\mathbf{R}$-derivative of a state, $\nabla_{\mathbf{R}}\,|\psi(\mathbf{R})\rangle$ is always well-defined – that is, $\alpha(\mathbf{R})$ does not change discontinuously. In general, it is not always possible to pick a gauge that is globally smooth over all of $\mathcal{R}$, however it *is* always possible to pick a locally smooth gauge around the neighbourhood of a given point in $\mathcal{R}$.

In analogy to the relative phase in the previous section, let us quantify phase between a state at $\mathbf{R}$ and a state that is infinitesimally displaced from it, at $\mathbf{R} + d\mathbf{R}$,

$$e^{-i\Delta\gamma} = \frac{\langle\psi(\mathbf{R})|\psi(\mathbf{R}+d\mathbf{R})\rangle}{|\,\langle\psi(\mathbf{R})|\psi(\mathbf{R}+d\mathbf{R})\rangle\,|}. \tag{2.17}$$

Taking the limit of small $d\mathbf{R}$ we can express $|\psi(\mathbf{R}+d\mathbf{R})\rangle$ to first order in $d\mathbf{R}$ as

$$|\psi(\mathbf{R}+d\mathbf{R})\rangle = |\psi(\mathbf{R})\rangle + d\mathbf{R}\cdot\nabla_{\mathbf{R}}\,|\psi(\mathbf{R})\rangle\,. \tag{2.18}$$

Which means that

$$\langle\psi(\mathbf{R})|\psi(\mathbf{R}+d\mathbf{R})\rangle = 1 + \langle\psi(\mathbf{R})|\nabla_{\mathbf{R}}|\psi(\mathbf{R})\rangle\cdot d\mathbf{R}. \tag{2.19}$$

Now, noticing that $\langle\psi(\mathbf{R})|\nabla_{\mathbf{R}}|\psi(\mathbf{R})\rangle$ is pure imaginary, we can show that

$$\Delta\gamma = \mathbf{A}\cdot d\mathbf{R}, \tag{2.20}$$

$$\mathbf{A}(\mathbf{R}) = i\,\langle\psi(\mathbf{R})|\nabla_{\mathbf{R}}|\psi(\mathbf{R})\rangle\,. \tag{2.21}$$

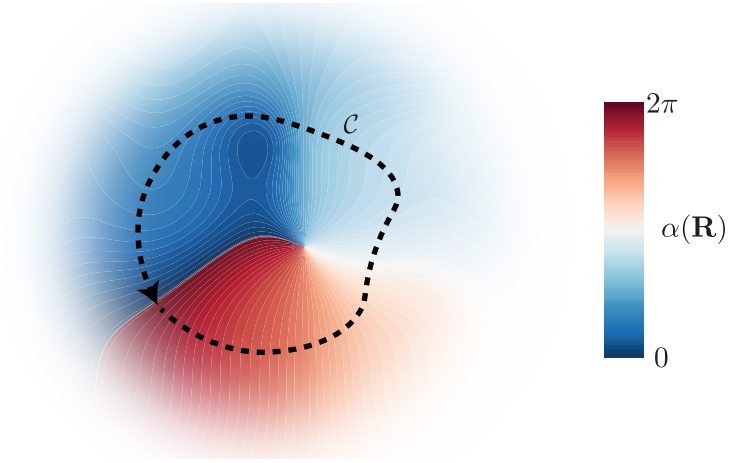


Figure 2.2: An example of a non-smooth gauge transformation designed to change the value of the Berry phase around the path $\mathcal{C}$ – marked with a dashed line – by an addition of 2π. Only a small region of $\mathbf{R}$-space is shown, with the local phase applied shown by the colourmap.

The quantity multiplying $d\mathbf{R}$ is the Berry connection $\mathbf{A}(\mathbf{R})$. Like the relative phase in the previous section, it is not a gauge-invariant quantity. Under a gauge transformation it changes according to

$$\mathbf{A}(\mathbf{R}) \to \mathbf{A}(\mathbf{R}) - \nabla_{\mathbf{R}}\alpha(\mathbf{R}) \tag{2.22}$$

Now let us suppose that we slowly transform our Hamiltonian around some closed path $\mathcal{C}$ in $\mathbf{R}$-space and keep track of the phase picked up by a given state.[1] In analogy with Eqn. 2.11, the Berry connection allows us to calculate the total phase accumulated over this route, according to

$$\gamma(\mathcal{C}) = \oint_{\mathcal{C}} \mathbf{A} \cdot d\mathbf{R}. \tag{2.23}$$

The exponential of the phase $e^{-i\gamma(\mathcal{C})}$ around the loop *is* gauge invariant, one can see this intuitively by realising that it is identical to the Berry phase from the discrete case, but in the limit where the discrete steps become arbitrarily close together. However, the Berry phase $\gamma(\mathcal{C})$ itself is not strictly gauge invariant, since one can introduce a gauge transformation that creates a branch cut around the path $\mathcal{C}$. After traversing the whole path, the state at the end of the loop would have picked up a total phase 2π, meaning that under a gauge transformation we can change the Berry phase according to

$$\gamma(\mathcal{C}) \to \gamma(\mathcal{C}) + 2\pi n \text{ for } n \in \mathbb{Z}. \tag{2.24}$$

An example of such a gauge transformation is shown in Fig. 2.2

[1] In [25], Berry originally proposed this transformation as an adiabatic process, where we modify the Hamiltonian extremely slowly, and many sources (e.g. [79]) propose the Berry phase in that framework. In that case, one has to do a little extra work to keep track of the energy-dependent phase that a state picks up $\sim e^{-i\varepsilon t}$ alongside the topological phase determined by $\mathbf{A}$. Here we shall neglect this, only considering the *instantaneous eigenstates* at different values of $\mathbf{R}$. For a thorough explanation, see [80].

2.1.2.1 Berry Curvature

Let us now define a quantity equivalent to the Berry flux from the previous discussion. Starting with Eqn. 2.23, we use Stokes' theorem to transform it into a surface integral over a surface $\mathcal{S}$ bounded by the curve $\mathcal{C}$. We will consider the case for a two and three-dimensional parameter space $\mathcal{R}$, but of course this argument generalises to arbitrary dimensions.

$$\text{In 2D: } \gamma(\mathcal{C}) = \int_{\mathcal{S}} d^2R \left(\partial_x A_y(\mathbf{R}) - \partial_y A_x(\mathbf{R})\right), \tag{2.25}$$

$$\text{In 3D: } \gamma(\mathcal{C}) = \int_{\mathcal{S}} d\mathbf{S} \cdot \left(\nabla_{\mathbf{R}} \times \mathbf{A}(\mathbf{R})\right), \tag{2.26}$$

where we use the shorthand $\partial_\alpha = \frac{\partial}{\partial R_\alpha}$. Thus, we may define the Berry curvatures,

$$\Omega(\mathbf{R}) = \partial_x A_y(\mathbf{k}) - \partial_y A_x(\mathbf{R}) \tag{2.27}$$

$$\mathbf{\Omega}(\mathbf{R}) = \nabla_{\mathbf{R}} \times \mathbf{A}(\mathbf{R}). \tag{2.28}$$

Two Useful Ways to Re-express the Berry Curvature — Now let us focus only on the 2D case and reformulate this expression in two different ways.

1. The first way finds the curvature in terms of the rate of change of the Hamiltonian only. Writing this quantity out explicitly in terms of the states $|\psi(\mathbf{R})\rangle$, we arrive at

$$\Omega(\mathbf{R}) = i \langle \partial_x \psi(\mathbf{R}) | \partial_y \psi(\mathbf{R}) \rangle + h.c. \tag{2.29}$$

   We can insert a resolution of the identity $\mathbb{1} = \sum_n |\psi_n\rangle\langle\psi_n|$ to obtain

$$\Omega(\mathbf{R}) = i \sum_{\psi_n \neq \psi} \langle \partial_x \psi | \psi_n \rangle \langle \psi_n | \partial_y \psi \rangle + h.c. \tag{2.30}$$

   Using the identity,

$$\langle \psi_n | \partial_\alpha \psi \rangle = \frac{\langle \psi_n | \partial_\alpha H | \psi \rangle}{\epsilon - \epsilon_n}, \text{ for } \psi \neq \psi_n, \tag{2.31}$$

   we can re-express the Berry curvature in the form

$$\Omega(\mathbf{R}) = i \sum_{\psi_n \neq \psi} \frac{\langle \psi | \partial_x H | \psi_n \rangle \langle \psi_n | \partial_y H | \psi \rangle}{(\epsilon - \epsilon_n)^2} + h.c. \tag{2.32}$$

2. Note that the definition provided for the Berry curvature (Eqn. 2.29) is only well-defined across $\mathcal{R}$ when the state remains fully gapped. That is, no other states ever have the same energy as $|\psi(\mathbf{R})\rangle$. When another state's energy crosses that of $|\psi\rangle$, the individual states become ill-defined and so it becomes challenging to write down a natural derivative for the states. With this in mind, let us consider re-expressing the Berry curvature in terms of the single state projector $\hat{\psi} = |\psi\rangle\langle\psi|$,

$$i \langle \partial_x \psi | \partial_y \psi \rangle + h.c. = i \text{Tr} \left[\hat{\psi} \partial_x \hat{\psi} \, \partial_y \hat{\psi} \right] + h.c. \tag{2.33}$$

For a single state, this is identical to the regular Berry curvature, however the utility of this expression becomes evident when we construct it for a projector onto a set of states $P = \sum_{i\in\text{band}} |\psi_i\rangle\langle\psi_i|$. Since ∂P is still well-defined when the states in P are degenerate, we can write an expression for the combined Berry curvature of a set of states that can handle degeneracy (provided no states outside P become degenerate with P).

$$\Omega_P = i\text{Tr}\left[P\partial_x P\partial_y P\right] + h.c. \tag{2.34}$$

This calculation has one important caveat. It is only possible to apply Stokes' theorem when $\mathbf{A}$ is smooth over the region $\mathcal{R}$. This means that we need to have already picked a smooth gauge in the region we are integrating over to have a guarantee that Eqns. 2.25 and 2.26 hold. If we transform to a non-smooth gauge then it is possible that the Berry phase will change by a multiple of 2π, however the Berry curvature is truly gauge invariant. This can be seen from Eqn. 2.32, where the Berry curvature is defined without the differentiation of states, so is invariant under even a non-smooth gauge transformation. Thus in general we only have the guarantee that

$$e^{-i\gamma(\mathcal{C})} = e^{\int_S d^2R\,\Omega(\mathbf{R})}. \tag{2.35}$$

2.1.2.2 Chern Number

As in §2.1.1.2, we make the assertion that the manifold parametrised $\mathbf{R}$ is closed, generally one is working on the torus. The Chern number can then be defined as the integral of the Berry curvature across the whole manifold,

$$\mathcal{Q} = \frac{1}{2\pi}\int d^2R\,\Omega. \tag{2.36}$$

As in the discrete case, the Chern number is restricted to only take integer values. The argument follows the same lines as previously, where we can use our modified form of Stokes' theorem (Eqn. 2.35). Since the manifold is close, it has no boundary, so the flux integral equivalent to the Berry phase around a loop enclosing no area, implying that

$$e^{\int d^Rk\,\Omega(\mathbf{R})} = 1, \implies \mathcal{Q}\in\mathbb{Z} \tag{2.37}$$

2.1.3 An Example – The Two-Level System

Let us illustrate these concepts with the example of a two-state system. Our first step is to parametrise the possible Hamiltonians in such a system using a vector $\mathbf{d}$. We will then solve this Hamiltonian for the positive and negative energy eigenstates. This allows us to look at how the eigenstates change as we smoothly deform the Hamiltonian, exploring the parameter space. By examining how the eigenstates of $\hat{H}$ depend on $\mathbf{d}$, we can calculate the Berry curvature of the positive and negative energy states. We then connect this with our understanding of the Bloch states in a periodic quantum system. We discuss how the bulk Hamiltonian of a periodic system

corresponds to the embedding of a closed surface in **d**-space and describe how to calculate the Chern number of the bands in such a system.

The Hilbert space of a two-level system is given by rays in $\mathbb{C}^2$. Any Hamiltonian acting on this space must be a 2×2 Hermitian matrix, which we parametrise in terms of a Pauli vector $\mathbf{d}$,

$$H = \mathbf{d} \cdot \hat{\sigma} = d_i \sigma^i, \tag{2.38}$$

where the σ^i are the Pauli matrices. This gives us a complete basis for 2×2 traceless Hermitian matrices. Of course, we could include a multiple of the identity to span the full space of Hermitian matrices, however this would have no effect on the topology, and shall be omitted.

The set of traceless Hamiltonians is thus a manifold in itself, $\{H\} \cong \mathbb{R}^3$, since $\mathbf{d} \in \mathbb{R}^3$. Here we shall restrict to gapped Hamiltonians, so $\mathbf{d} = 0$ is forbidden, leaving $\{H\} \cong \mathbb{R}^3 \backslash 0$. The first thing we will do is to express the vector $\mathbf{d}$ in spherical polar coordinates,

$$H = |\mathbf{d}| \begin{pmatrix} \cos(\theta) & e^{-i\phi} \sin\theta \\ e^{i\phi} \sin\theta & -\cos(\theta) \end{pmatrix} \tag{2.39}$$

This matrix has $H^2 = |\mathbf{d}|^2 \mathbb{1}$, so its eigenvalues are $\pm|\mathbf{d}|$, with eigenvectors

$$|+_{\mathbf{d}}\rangle = \begin{pmatrix} e^{-i\phi/2} \cos(\theta/2) \\ e^{i\phi/2} \sin(\theta/2) \end{pmatrix}, \; |-_{\mathbf{d}}\rangle = \begin{pmatrix} -e^{-i\phi/2} \sin(\theta/2) \\ e^{i\phi/2} \cos(\theta/2) \end{pmatrix}. \tag{2.40}$$

We have thus arrived at a set of states, $|\pm_{\mathbf{d}}\rangle$ that depend on the parameter $\mathbf{d}$, meaning we can apply the techniques of the last section. From Eqns. 2.21 and 2.26 we know that the Berry connection and Berry curvature of the $|\pm\rangle$ states are given by

$$\mathbf{A}^{\pm}(\mathbf{d}) = i \langle \pm_{\mathbf{d}} | \nabla_{\mathbf{d}} | \pm_{\mathbf{d}} \rangle \tag{2.41}$$

$$\mathbf{\Omega}^{\pm}(\mathbf{d}) = \nabla_{\mathbf{d}} \wedge \mathbf{A}^{\pm}(\mathbf{d}). \tag{2.42}$$

Using this equation it is possible to directly calculate the Berry curvature, arriving at the following expression:

$$\mathbf{\Omega}^{\pm} = \pm \frac{\hat{n}_{\mathbf{d}}}{2\mathbf{d}^2} \tag{2.43}$$

where $\hat{n}_{\mathbf{d}}$ is a unit vector pointing parallel to $\mathbf{d}$.

This Berry curvature is equivalent to a monopole field radiating out from the origin in **d**-space, in analogy with electrostatics. Thus, the Berry phase of the $|+_{\mathbf{d}}\rangle$ state around some path in **d**-space is given by

$$\gamma^{+}(C) = \oint_{\mathcal{C}} \mathbf{A}^{+}(\mathbf{d}) \cdot d\mathbf{d}. \tag{2.44}$$

Re-expressing this in terms of the Berry curvature gives us

$$\gamma^{+}(C) = \int_{\mathcal{R}} \mathbf{\Omega}^{+}(\mathbf{d}) \cdot d\mathbf{S}, \tag{2.45}$$

where the integral is over a region $\mathcal{R}$ that has the curve $\mathcal{C}$ as its boundary. Since the Berry curvature is just a monopole field with charge $\frac{1}{2}$, this integral ends up evaluating half the solid

angle subtended by the curve $\mathcal{C}$.

2.1.3.1 Chern Number

Now we can connect this with our understanding of Bloch states. For a two-dimensional translationally symmetric system, the Hamiltonian can be diagonalised according to

$$H = \sum_{\mathbf{k}} |\mathbf{k}\rangle \langle \mathbf{k}| \otimes H(\mathbf{k}). \tag{2.46}$$

If the unit cell contains two sites, then $H(\mathbf{k})$ is a 2×2 matrix that depends on $\mathbf{k}$. We can write it in terms of a $\mathbf{d}$ vector that depends on $\mathbf{k}$.

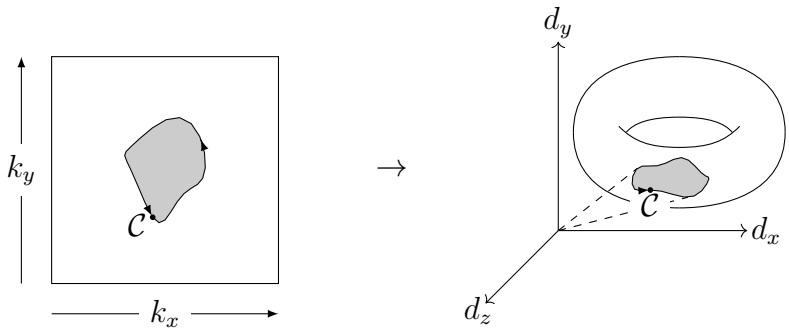
$$H(\mathbf{k}) = \mathbf{d}(\mathbf{k}) \cdot \sigma. \tag{2.47}$$

Here, $\mathbf{k}$ lives on the surface of a torus, since k_x and k_y are periodic. Furthermore, $\mathbf{d}$ (and by extension H) live in the space $\mathbb{R}^3 \backslash 0$. Thus, $\mathbf{d}(\mathbf{k})$ is a map of the form

$$\mathbf{d} : S^1 \times S^1 \to \mathbb{R}^3 \backslash 0. \tag{2.48}$$

The map is an embedding of a two-dimensional surface (the torus) into three-dimensional flat space ($\mathbb{R}^3$). The only constraint placed on this map is that it must remain smooth, however the embedded torus can take any shape.

To calculate the Berry phase around a loop in k-space, all we have to do is look at the corresponding loop in d-space. Then we integrate the Berry connection over some surface that has this loop as its boundary. Since the Berry curvature has the form of a monopole flux, we can simplify further – one must simply find the solid angle subtended by the curve around the origin and divide it by two.



What about the Chern number? This is found by the integrating the Berry curvature across the whole surface of the torus in d-space. If the embedding of the torus does not contain the origin, then the value of this integral is necessarily zero. Now suppose the torus is embedded such that it contains the origin, then we will have a surface that catches all the Berry flux on its inside and the solid angle subtended is 4π. Thus, the Chern number is $+1$. Similarly, for an embedding that wraps the torus twice around the origin, the subtended flux will correspond to twice the charge of the monopole, leading to a Chern number of $+2$. Thus, we see that the Chern number in this context must be quantised, and can often be read directly from the form of $\mathbf{d}(\mathbf{k})$ by asking how many times this embedding of the torus wraps the origin.

2.1.4 Final Notes

We close this section with an explanation of the consequences of Chern number in topological insulators.

2.1.4.1 Smoothly Deforming the Hamiltonian

Consider a pair of quantum systems in the same Hilbert space, described by Hamiltonians $\hat{H}_1$ and $\hat{H}_2$ which are both gapped at the Fermi level. We might ask: *Is it possible to smoothly deform $\hat{H}_1$ into $\hat{H}_2$ without crossing a point where the gap at the Fermi level closes?*

The answer is that it is only possible if the sum of the Chern numbers of the occupied bands of $\hat{H}_1$ and $\hat{H}_2$ are the same. This is because the total Chern number of the occupied bands is restricted to only take integer values – it cannot smoothly change as we deform the Hamiltonian. For the total Chern number to change, we must somewhere cross a point where it is impossible to define a Chern number at all, allowing it to jump discontinuously when we leave that point. This is precisely what happens when the gap at the Fermi level closes. At this point, the occupied bands can no longer be defined as a smooth object in momentum space, since there must be a discontinuity at the band touching point.

We can illustrate this with the example in §2.1.3. Smoothly deforming the Hamiltonian amounts to changing the shape of the torus embedded in $\mathbf{d}$-space. If any point on the surface of the torus touches the origin, a pair of zero-energy states must appear – the gap has closed, and the system is conductive. If the band has a Chern number of $+1$, this means that the torus contains the origin. In order to smoothly deform this into a system with zero Chern number, we would need to move the torus such that the origin was now outside. At some point in this deformation the torus surface will have to pass through the origin, creating a conducting Hamiltonian at that point.

Thus, we can classify all Hamiltonians according to the Chern number of their bands. It is always impossible to smoothly deform a Hamiltonian into one with a different Chern number while remaining insulating. Similarly, it is always possible to smoothly deform two Hamiltonians into one another without closing a gap, provided that their bands have identical Chern numbers[2] [27].

2.1.4.2 The Bulk-Boundary Correspondence

The argument presented above allows us to make a rough justification for why conducting edge states must appear wherever we have a material with nonzero Chern number. Suppose we have a large system where the Hamiltonian is allowed to vary slowly over space, defined by $\hat{H}(\mathbf{r})$. In one region this Hamiltonian locally has non-zero Chern number, $\hat{H}_{\text{topological}}$, but in a different distant region it locally has zero Chern number, $\hat{H}_{\text{trivial}}$. We expect that between these regions the Hamiltonian must be gradually transforming between $\hat{H}_{\text{topological}}$ and $\hat{H}_{\text{trivial}}$. As we have seen, it is impossible for our Hamiltonian to make this transformation without passing through a conducting region somewhere along the way – edge states must appear! Exploiting

[2] A simple justification for this comes from band flattening. Any Hamiltonian can be smoothly band flattened, where all the states in each band are set to the same energy. Furthermore, for a given set of Chern numbers, all band flattened Hamiltonians (with the same dimensionality) are equivalent. Thus, any two Hamiltonians with identical Chern numbers can be transformed into one another by using the common band flattened Hamiltonian as an intermediate step.

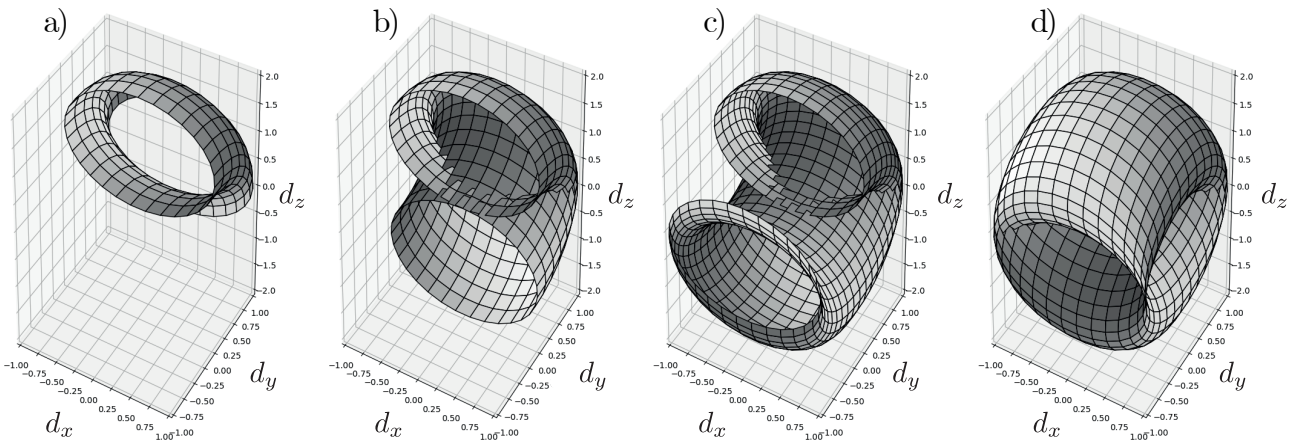


Figure 2.3: The embedding of the Brillouin zone in **d**-space for the QWZ model. This is shown in four progressive cutaways to ensure the internal structure can be seen. In all four images k_x spans the interval $[0, 2\pi)$, however in **(a)** k_y spans $\left[0, \frac{\pi}{2}\right)$, in **(b)** k_y spans $[0, \pi)$, in **(c)** k_y spans $\left[0, \frac{3\pi}{2}\right)$, and in **(d)** k_y spans $[0, 2\pi)$.

this intuition, one might view the vacuum as having zero Chern number. Thus, we would expect that if a material with non-zero Chern number transforms over space into the vacuum – that is, it has a boundary – then conductive states must appear at the boundary. This property of Chern insulators is called the bulk-boundary correspondence [85–87].

2.1.4.3 Chern Number and Globally Smooth Gauges

Carefully considering the gauge used in Eqn. 2.40, one might notice that there is a discontinuity at $\phi = \pi$ where $e^{i\phi}$ suddenly jumps as you cross over to $\phi = -\pi$. This is no oversight, it is completely impossible to define a globally smooth set of states $|\psi(\mathbf{d})\rangle$ for any band that has nonzero Chern number. This is because if $|\psi(\mathbf{d})\rangle$ were continuous everywhere, then the Berry connection would also have to be continuous everywhere. Thus, we could invoke Stokes' theorem in Eqn. 2.36, showing that the Chern number must vanish since the integral is over the whole (closed) manifold. A nonzero Chern number thus relies on there being points where Stokes' theorem cannot be used. In this sense, the Chern number can be regarded as a measure of the amount of discontinuity that *must* be present regardless of the gauge you choose for the space.

2.2 The Qi-Wu-Zhang Model

Let us introduce the Qi-Wu-Zhang (QWZ) model as a paradigmatic example of a two-dimensional topological insulator with nearest-neighbour interactions [83]. We work on a square lattice of unit cells indexed by a two-dimensional lattice vector $\mathbf{m}$, where each cell contains two sites. The QWZ model is defined by three terms, a hopping between unit cells in the x-direction, a hopping in the y-direction, and a staggered on-site potential whose strength is determined by a parameter u.

$$\begin{aligned}\hat{H} = &\sum_{\mathbf{m}} |\mathbf{m} + 1_x\rangle \langle \mathbf{m}| \otimes \frac{\sigma_z + i\sigma_x}{2} + h.c. \\ &+ \sum_{\mathbf{m}} |\mathbf{m} + 1_y\rangle \langle \mathbf{m}| \otimes \frac{\sigma_z + i\sigma_y}{2} + h.c. \\ &+ \sum_{\mathbf{m}} |\mathbf{m}\rangle \langle \mathbf{m}| \otimes u\, \sigma_z, \end{aligned} \tag{2.49}$$

where 1_x and 1_y represent the unit displacement in their respective directions,

$$1_x = \begin{pmatrix} 1 \\ 0 \end{pmatrix}, \; 1_y = \begin{pmatrix} 0 \\ 1 \end{pmatrix}. \tag{2.50}$$

Using Bloch's theorem, we can find the bulk Hamiltonian,

$$\hat{H}(\mathbf{k}) = \begin{pmatrix} \sin k_x \\ \sin k_y \\ u + \cos k_x + \cos k_y \end{pmatrix} \cdot \boldsymbol{\sigma}. \tag{2.51}$$

Here, k_x and k_y determine our position in the Brillouin zone. As explained in §2.1.3, this represents the embedding of a torus in **d**-space, shown in Fig. 2.3.

The u-parameter has the effect of translating the torus by a fixed amount in the z-direction. From this we can see that the QWZ model only has non-zero Chern number for values of u between -2 and 2. Translating the torus by any more will move the origin completely outside. Thus, the Chern number is

$$Q = \begin{cases} -1 & : \quad -2 < u < 0, \\ 1 & : \quad 0 < u < 2, \\ 0 & : \quad \textit{otherwise}, \end{cases} \tag{2.52}$$

not including the points at $u = -2$, 0 and 2, at which the Chern number is undefined because the band gap closes, and the material becomes conducting. Some example band structures for varying values of u are shown in Fig. 2.4.

2.2.1 Strip Geometry and Edge Modes

According to the bulk-boundary correspondence, whenever the Chern number $\mathcal{C}$ is nonzero, the QWZ model must have gapless edge modes appearing. To provide an example, here we construct the model on strip geometry and provide an analytical expression for the edge modes.

We shall require that the system is periodic and uniform in the y-direction, but is allowed to be non-uniform and have open boundaries in the x-direction. To allow u to vary in the x-direction, we add a subscript to indicate position-dependence, $u \to u_{m_x}$. We can apply Bloch's theorem in the y-direction only, and the eigenstates take the following form,

$$|\psi\rangle = |k_y\rangle \otimes |v_{k_y}\rangle, \tag{2.53}$$

where $|k_y\rangle$ is a plane wave in the y direction and $|v_{k_y}\rangle$ is a $2 \times L_x$ element vector. The v-states

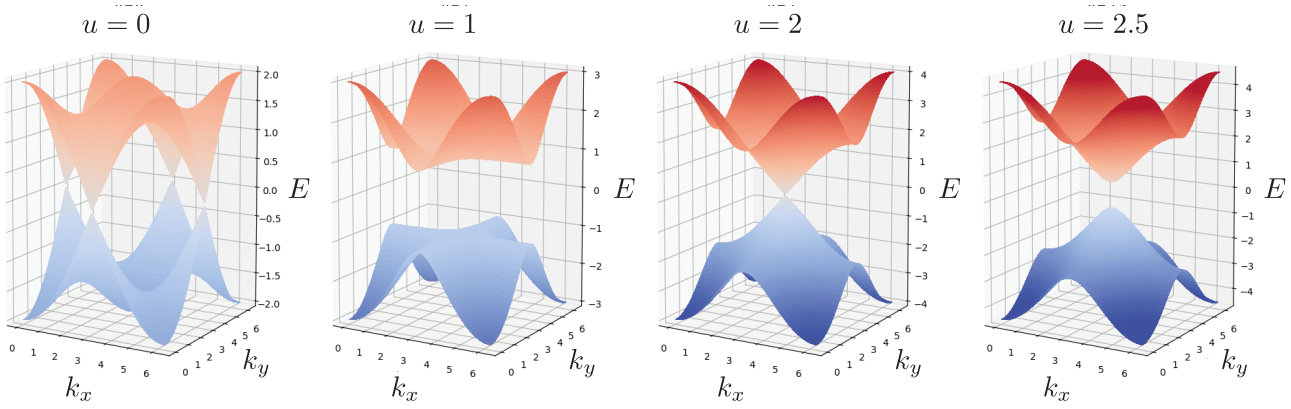


Figure 2.4: Four examples of the band structure of the QWZ model are shown, for varying u values between 0 and 2.5. At $u = 0$ and 2, the bands touch and Chern number is undefined. At $u = 1$, $\mathcal{C} = +1$, and at $u = 2.5$, $\mathcal{C} = 0$.

are solutions of the semi-bulk Hamiltonian

$$\begin{aligned}\hat{H}(k_y) = &\sum_{m_x} |m_x + 1\rangle \langle m_x| \otimes \frac{\sigma_z + i\sigma_x}{2} + h.c. \\ &+ \sum_{m_x} |m_x\rangle \langle m_x| \otimes \left[(u_{m_x} + \cos k_y)\, \sigma_z + \sin k_y\, \sigma_y\right].\end{aligned} \tag{2.54}$$

We have effectively reduced our system from a lattice of sites in x and y, to a set of chain models in x, that are each labelled by a value of k_y. The band structure for this system in both periodic boundaries and strip geometry is shown in Fig. 2.5. Note that edge states are only present for certain values of k_y, which can be seen in figure 2.5, where the edge states peel away from the bulk in a region around $k_y = \pi$.

The strip Hamiltonian can be solved by proposing modes that decay exponentially away from the boundary. Thus, a left-edge state has the form

$$|\psi_{k_y}^{\text{left}}\rangle = \sqrt{1 - \xi_l^2} \sum_{m=1}^{L_x} \xi_l^{m-1} |m\rangle \otimes \begin{pmatrix} 1 \\ -i \end{pmatrix} \tag{2.55}$$

where

$$\xi_l = -u - \cos k_y. \tag{2.56}$$

This state has energy

$$E_l = -\sin k_y. \tag{2.57}$$

Similarly, the right edge state is determined by

$$|\psi_{k_y}^{\text{right}}\rangle = \sqrt{1 - \xi_r^2} \sum_{m=1}^{L_x} \xi_r^{L_x - m} |m\rangle \otimes \begin{pmatrix} 1 \\ i \end{pmatrix} \tag{2.58}$$

$$\xi_r = -u - \cos k \tag{2.59}$$

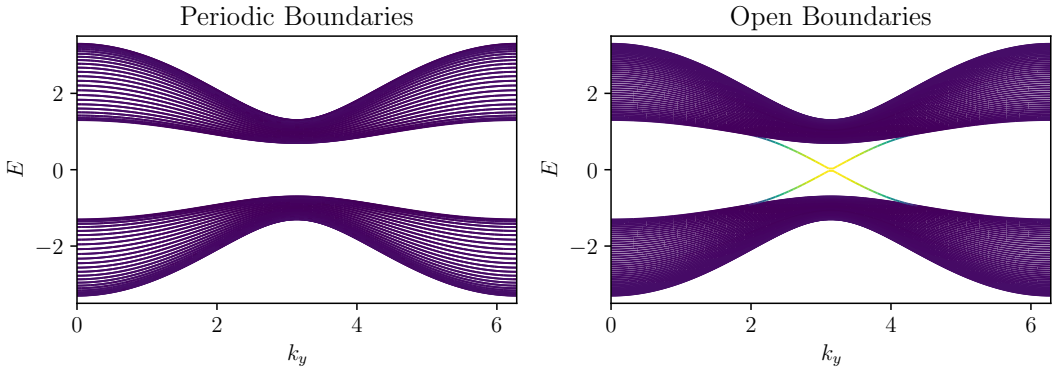


Figure 2.5: An example band structure for a QWZ model with $u = 1.3$ and $L_x = 30$. States are coloured according to their inverse participation ratio, indicating their relative degree of localisation. **(Left)** The example for periodic boundary conditions, showing two well-separated bands. **(Right)** The case for open boundary conditions. Two edge states are shown leaving the bulk and crossing the gap, with the descending state being a left edge state, and the ascending state being a right edge state.

$$E_r = \sin k. \tag{2.60}$$

These edge states are only valid solutions for k_y in the region

$$-1 < u + \cos k_y < 1. \tag{2.61}$$

These limits can be seen in Fig. 2.5, where the edge states peel away from the bands to cross the energy gap. These expressions are only strictly valid in the limit of a large system. Since we have made the assumption the edge states can be calculated by taking into consideration only one edge and ignoring the effect of the other. The edge states decay exponentially through the system, so we are relying on the assumption that the edge state has effectively decayed to nothing before reaching the other side. When this condition is relaxed the edge states are able to couple to one another. This has two effects, the first being that at the crossing of edge states, our energy eigenstates become positive and negative superposition states of both edge states. The other is that the left state coupling to the right state shifts their energy levels producing an avoided crossing such that no states cross $E = 0$.

2.2.2 The Amorphous QWZ Model

We now look at extending the QWZ model beyond a grid to arbitrary amorphous lattices. This is done by defining a smooth continuation of the QWZ model to allow for edges that can point in an arbitrary direction. Given an arbitrary lattice, we first require that every vertex hosts two states, and the on-site energy term containing $u\sigma_z$ is identical as in Eqn. 2.49. To construct an amorphous equivalent of the hopping terms, let us first look at the hopping in the QWZ model more carefully. We have two hopping matrices, one that hops a state in the x-direction, h_x, and one that hops in the y-direction, h_y.

$$h_x = \frac{\sigma_z + i\sigma_x}{2} = \frac{1}{2}\begin{pmatrix} 1 & i \\ i & 1 \end{pmatrix} \tag{2.62}$$

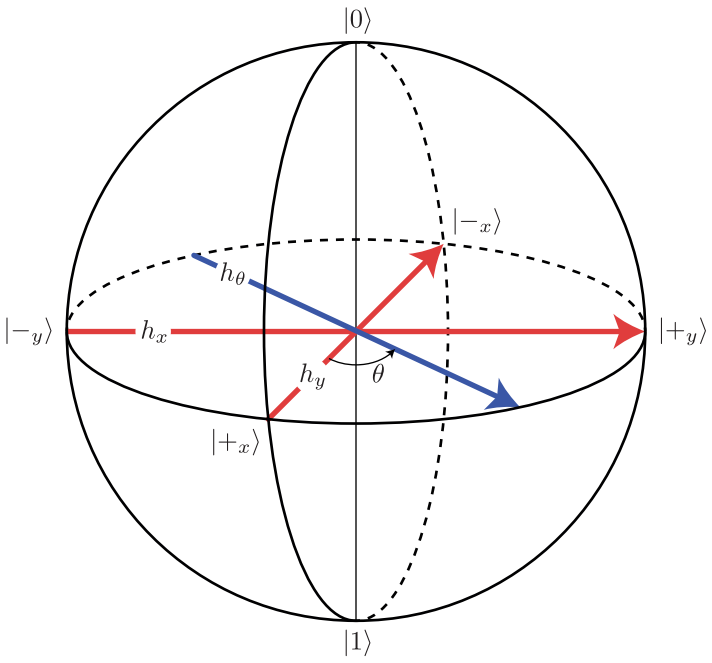


Figure 2.6: The Bloch sphere, showing the positions of the eigenstates of the three Pauli matrices. The action of the hopping matrices is shown in red, where the h_x and h_y operators act as creation operators on the y and x bases respectively. The action of our arbitrary angle hopping operator is shown in blue, acting as a creation operator between a pair of orthogonal states that lie on the x-y plane.

$$h_y = \frac{\sigma_z + i\sigma_y}{2} = \frac{1}{2}\begin{pmatrix} 1 & 1 \\ -1 & 1 \end{pmatrix}. \tag{2.63}$$

These operators can be viewed as creation operators on different bases, h_x acts on the basis of σ_y, and h_y acts on the basis of σ_x. Viewed in the Bloch sphere, these operators hop the state across the sphere in the x or y direction.

In our amorphous lattice, hopping operators can act across an edge connecting two sites that points in an arbitrary direction. Thus, rather than trying to assign edges with h_x or h_y operators, let us define an arbitrary-angle hopping matrix h_θ, that hops in a direction θ over the x-y plane of the Bloch sphere,

$$h_\theta = |+_\theta\rangle \langle -_\theta| \tag{2.64}$$

$$= \frac{1}{2}\begin{pmatrix} 1 & -e^{-i\theta} \\ e^{i\theta} & -1 \end{pmatrix}. \tag{2.65}$$

Thus, the Hamiltonian we use for the amorphous system is given by

$$\begin{aligned} \hat{H} = &\sum_{i,j} |\mathbf{r}_i\rangle \langle \mathbf{r}_j| \otimes h_{\theta_{i,j}} + h.c. \\ &+ \sum_i |\mathbf{r}_i\rangle \langle \mathbf{r}_i| \otimes u_i \sigma^z, \end{aligned} \tag{2.66}$$

where $\theta_{i,j}$ is the angle between the edge connecting $\mathbf{r}_i$ and $\mathbf{r}_j$ and the x axis.

As before, the parameter u controls whether the system is in a topological or trivial state. The exact dependence of the system on u depends strongly on the lattice geometry, however there is generally a region around which the system has nonzero topological character. In the absence of a momentum-space description, the system's topological character can be seen indirectly by comparing the spectrum in open and periodic boundary conditions. Generally one expects the presence of a gap in periodic boundaries that becomes populated with edge modes in open boundaries. Two examples are shown in Fig. 2.7.

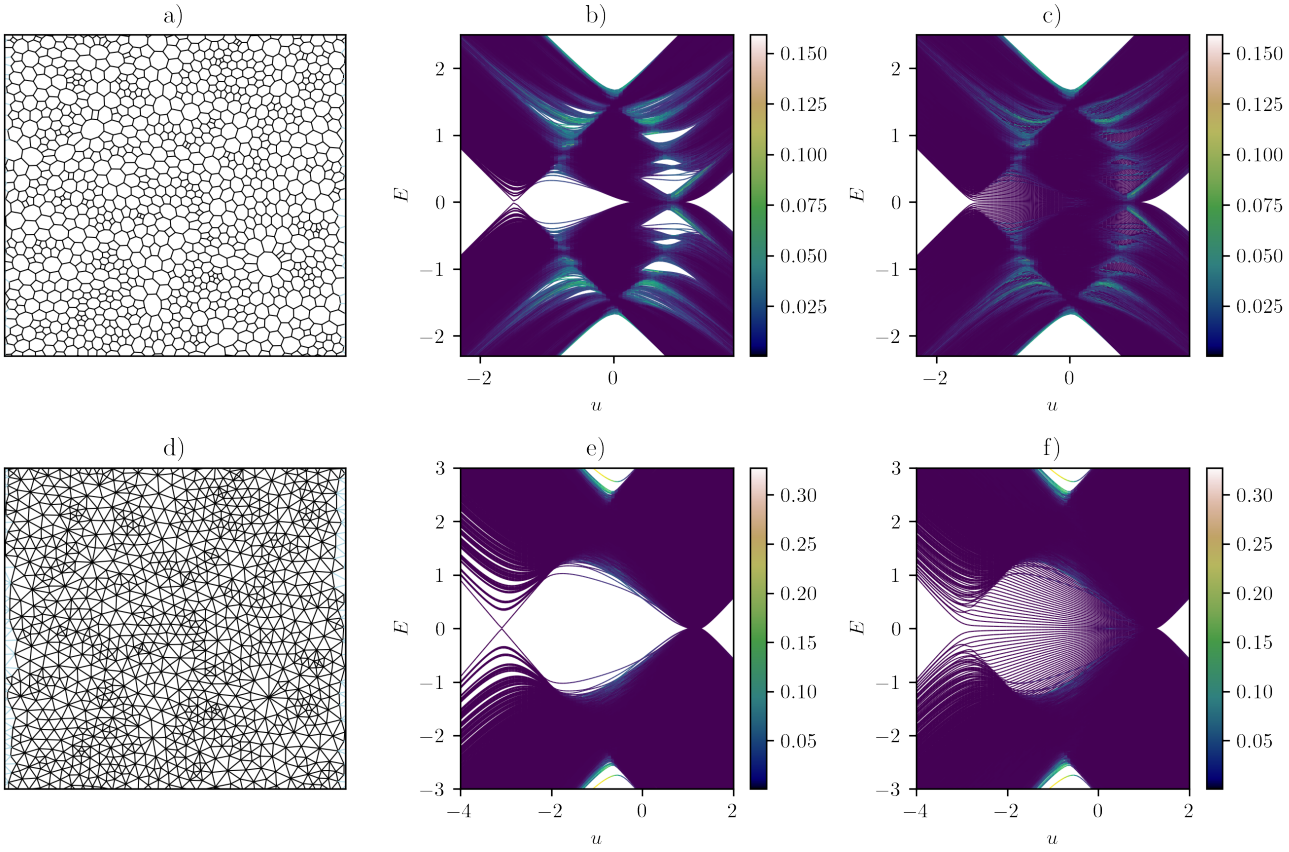


Figure 2.7: Plots showing the spectra of the amorphous QWZ model for two different example lattices. States are coloured according to their inverse participation ratio. **(a)** A trivalent lattice generated from a Voronoi decomposition of a set of random points, followed by five iterations of LLoyd's algorithm (detailed in Appendix A) to regularise bond lengths. **(b)** The spectrum of the QWZ model on the voronised lattice as a function of u. Several gaps are present at different values of u and E. **(c)** The spectrum of the same model as (b), but in open boundary conditions. Here we can see that all gaps for $u \in [-1.5, 1]$ are now filled with edge modes, indicating that the system is in a topological phase. **(d)** An example of a lattice forming a Delaunay triangulation, constructed as the dual of the lattice in (a). **(e)** The spectrum of the QWZ model on the Delaunay lattice as a function of u showing one single large gapped region. **(f)** The spectrum of the same model as (e), but in open boundary conditions. Here we can see that the gaps is now filled with edge modes, again indicating that here the system is in a topological phase. The colouring of each plot is determined by the IPR of the states, given by $\text{IPR} = \sum_x |\langle x|\psi\rangle|^4$.

Chapter 3

Local Chern Markers

The concepts outlined in Chapter 2 – Berry phase, curvature and Chern number – were first proposed in the 1980s to explain the newly discovered quantum Hall effect [16, 18], where they provided the mathematical underpinning for the TKNN invariant that defines the Hall conductance [23, 25]. In the decades since, the Chern number has been one of the central tools for classifying condensed matter systems beyond the Landau symmetry-breaking framework [86–89]. They have found use in describing ocean waves [90] coupled mechanical systems [91–93], as well as providing the foundations for the modern theory of polarisation [80, 94, 95].

One of the defining characteristics of quantum Hall physics is the robustness of the edge states and Hall conductance to impurities in the sample, where – as discussed in the introduction – a certain amount of disorder is even required to stabilise the quantised conductivity [21, 96]. Despite this, our definition of the Chern number cannot be calculated in a disordered material. In order to calculate the Berry curvature – and thus the Chern number – we must work in momentum space. If a material lacks translational symmetry, it is not possible to apply Bloch's theorem, crystal momentum is not a good quantum number, and we simply have no concept of momentum space. Disorder-resistant methods exist [97, 98], however they compute a global Chern number, and cannot capture the local properties of materials with compound structure. This tension, that our tools for describing disorder-resistant physics are themselves undermined by disorder, suggests that our mathematical framework is incomplete.

One potential solution to this problem is the development of real space methods for calculating the Chern number. These attempt to translate the Chern number into a mathematical language that is resolved in real space, ensuring it is well-defined when the system has no translational symmetry. There are a litany of proposals, such as the Bott Index [99–102], the Chern marker [33, 103], Kitaev's Chern marker [30, 93, 104], the localizer index [32] and most recently structural spillage [105]. In all of these cases, the aim is to re-express the definition of Chern number in terms of a set of real-space local operators, and thus does not rely on the notion of momentum space to make sense. Such a quantity should be equivalent to the Chern number when calculated in a translationally symmetric context; however would still be well-defined in cases where these conditions have been relaxed, and the notion of k-space is gone. These quantities afford the researcher tools with which to comment on the topological characteristics of materials that had previously been out of reach, such as amorphous crystals [106], quasi-periodic lattices [107], systems out of equilibrium [100, 108–110] and even strongly interacting systems [31].

In this chapter we present three such markers, and discuss the use and merits of each, as well as showing how they are related to one another. We start in §3.1 with an explanation of the Bott

index. This is the most intuitive of the markers, since it can be understood as a restatement of the Chern number as defined in Eqn. 2.15, using real-space operators to effect momentum translations. Following this, we show how the Bott index in a large system can be approximated by the Chern marker. We show several examples of these markers calculated for an amorphous QWZ model and discuss the limitations in interpreting their local value as a truly topological quantity.

In §3.2 we introduce Kitaev's proposal for a local Chern number, which predates both the Bott and Chern markers. We show how the marker evaluates the Chern number in a translationally symmetric, infinite system and show how the Chern marker can be understood as an averaged Kitaev marker. Finally, in §3.3 we present a physical interpretation of Kitaev's marker, showing how the marker may be constructed as a physical observable. Using a Kubo-like formalism [24], we show that the marker can be interpreted as a localised version of the Hall conductivity.

3.1 The Bott and Chern Markers

Let us start with the Bott index, initially proposed by Hastings and Loring [101, 111]. This marker is most naturally suited to systems in periodic boundary conditions. This section is as follows: We derive the exact form of the Bott index, showing that it is exactly equal to Chern number in a periodic, translationally symmetric system. In §3.1.1 we show how the Chern marker [33] (also given by Kitaev in Eqn. 3.64) can be understood as the Bott index in the large-system limit.

We will work with a lattice model, where unit cells are indexed by a vector of the form (m_x, m_y). The lattice has size (L_x, L_y), and we have set periodic boundary conditions. Sites are indexed by

$$|\mathbf{m}\alpha\rangle = |\mathbf{m}\rangle \otimes |\alpha\rangle \,, \tag{3.1}$$

where $\mathbf{m}$ is a vector labelling the unit cell and α selects a site within the unit cell. We shall use a Hamiltonian that has translational symmetry, so we may apply Bloch's theorem to obtain the form of the energy eigenstates,

$$H = \sum_{\mathbf{k}} |\mathbf{k}\rangle \langle \mathbf{k}| \otimes H(\mathbf{k}) \tag{3.2}$$

$$|\psi_{\mathbf{k},n}\rangle = |\mathbf{k}\rangle \otimes |u_{\mathbf{k},n}\rangle \,, \tag{3.3}$$

where $|u_{\mathbf{k},n}\rangle$ are the eigenstates of $H(\mathbf{k})$ and the momentum states are defined as in Eqn. 2.3. We assume that the system has a total of η bands, so $n \in \{1, ..., \eta\}$. Henceforth, we will assume that only the n^{th} band is occupied, so we can construct a projector onto the occupied subspace, P, and its complement, Q.

$$P = \sum_{\mathbf{k}} |\psi_{\mathbf{k},n}\rangle \langle \psi_{\mathbf{k},n}| \tag{3.4}$$

$$Q = \sum_{\mathbf{k},\, m\neq n} |\psi_{\mathbf{k},m}\rangle \langle \psi_{\mathbf{k},m}| \,. \tag{3.5}$$

We also introduce a pair of operators $e^{i\delta_x x}$ and $e^{i\delta_y y}$, with

$$\delta_x = \frac{2\pi}{L_x},\ \delta_y = \frac{2\pi}{L_y}. \tag{3.6}$$

In order to understand the effect of these operators, we consider their effect on the plane wave states

$$e^{i\delta_x x}\left|\mathbf{k}\right\rangle = \frac{1}{\sqrt{L_x L_y}}\sum_{\mathbf{m}} e^{i\delta_x x} e^{i\mathbf{m}\cdot\mathbf{k}}\left|\mathbf{m}\right\rangle \tag{3.7}$$

$$= \frac{1}{\sqrt{L_x L_y}}\sum_{\mathbf{m}} e^{i\mathbf{m}\cdot(\mathbf{k}+\boldsymbol{\delta}_x)}\left|\mathbf{m}\right\rangle \tag{3.8}$$

$$= \left|\mathbf{k}+\boldsymbol{\delta}_x\right\rangle, \tag{3.9}$$

with a similar expression for $e^{i\delta_y y}$. Here the symbols $\boldsymbol{\delta}_x$ and $\boldsymbol{\delta}_y$ represents a vector translation in $\mathbf{k}$-space,

$$\boldsymbol{\delta}_x = \begin{pmatrix}\delta_x\\0\end{pmatrix},\ \boldsymbol{\delta}_y = \begin{pmatrix}0\\\delta_y\end{pmatrix}. \tag{3.10}$$

Thus, these operators effect a translation in $\mathbf{k}$ space by the minimum step in the reciprocal lattice. Now let's look at the effect of these operators on the projector P,

$$e^{i\delta_x x} P e^{-i\delta_x x} = \sum_{\mathbf{k}} e^{i\delta_x x}\left|\mathbf{k}\right\rangle\left\langle\mathbf{k}\right| e^{-i\delta_x x} \otimes \left|u_{\mathbf{k},n}\right\rangle\left\langle u_{\mathbf{k},n}\right| \tag{3.11}$$

$$= \sum_{\mathbf{k}} \left|\mathbf{k}+\boldsymbol{\delta}_x\right\rangle\left\langle\mathbf{k}+\boldsymbol{\delta}_x\right| \otimes \left|u_{\mathbf{k},n}\right\rangle\left\langle u_{\mathbf{k},n}\right| \tag{3.12}$$

$$= \sum_{\mathbf{k}} \left|\mathbf{k}\right\rangle\left\langle\mathbf{k}\right| \otimes \left|u_{\mathbf{k}-\boldsymbol{\delta}_x,n}\right\rangle\left\langle u_{\mathbf{k}-\boldsymbol{\delta}_x,n}\right|, \tag{3.13}$$

where the last line follows from a redefinition of $\mathbf{k}$. For the sake of clarity later on, we will re-express the density operator $\left|u_{\mathbf{k},n}\right\rangle\left\langle u_{\mathbf{k},n}\right|$ in the following form

$$\left|u_{\mathbf{k},n}\right\rangle\left\langle u_{\mathbf{k},n}\right| = u_{\mathbf{k},n}, \tag{3.14}$$

so we get

$$e^{i\delta_x x} P e^{-i\delta_x x} = \sum_{\mathbf{k}} \left|\mathbf{k}\right\rangle\left\langle\mathbf{k}\right| \otimes u_{\mathbf{k}-\boldsymbol{\delta}_x,n}. \tag{3.15}$$

Now we have enough tools to introduce the definition of the Bott index!

$$B(\mathbf{r}) = -\frac{N}{2\pi}\Im\mathrm{Tr}_{\mathbf{r}} \log\left[UVU^\dagger V^\dagger + Q\right]. \tag{3.16}$$

Here N denotes the total number of unit cells in the system, $\mathrm{Tr}_{\mathbf{r}}$ is a local trace over the unit cell at position $\mathbf{r}$, and the log is the matrix logarithm. The operators U and V are given by

$$U = Pe^{i\delta_x x}P, \tag{3.17}$$

$$V = Pe^{i\delta_y y}P. \tag{3.18}$$

To make sense of this expression, let us focus on the $UVU^\dagger V^\dagger$ part only, writing this out explicitly gives us

$$UVU^\dagger V^\dagger = Pe^{i\delta_x x}Pe^{i\delta_y y}Pe^{-i\delta_x x}Pe^{-i\delta_y y}P. \tag{3.19}$$

We now add in identities of the form $e^{i\delta_x x}e^{-i\delta_x x}$ and regroup the equation, taking advantage of the fact that x and y commute,

$$UVU^\dagger V^\dagger = P\left[e^{i\delta_x x}Pe^{-i\delta_x x}\right]\left[e^{i\delta_y y}e^{i\delta_x x}Pe^{-i\delta_y y}e^{-i\delta_x x}\right]\left[e^{i\delta_y y}Pe^{-i\delta_y y}\right]P. \tag{3.20}$$

Using Eqn. 3.15 we can now rewrite this in terms of Bloch states to get

$$UVU^\dagger V^\dagger = \sum_{\mathbf{k}} |\mathbf{k}\rangle\langle\mathbf{k}| \otimes u_{\mathbf{k},n}u_{\mathbf{k}-\boldsymbol{\delta}_x,n}u_{\mathbf{k}-\boldsymbol{\delta}_x-\boldsymbol{\delta}_y,n}u_{\mathbf{k}-\boldsymbol{\delta}_y,n}u_{\mathbf{k},n}. \tag{3.21}$$

Since the first and last u density operator in this expression are identical, we can rewrite this in terms of a trace to get

$$UVU^\dagger V^\dagger = \sum_{\mathbf{k}} |\mathbf{k}\rangle\langle\mathbf{k}| \otimes |u_{\mathbf{k},n}\rangle\langle u_{\mathbf{k},n}| \cdot \mathrm{Tr}\left[u_{\mathbf{k},n}u_{\mathbf{k}-\boldsymbol{\delta}_x,n}u_{\mathbf{k}-\boldsymbol{\delta}_x-\boldsymbol{\delta}_y,n}u_{\mathbf{k}-\boldsymbol{\delta}_y,n}\right]. \tag{3.22}$$

If we compare this to the definition of Berry flux (Eqn. 2.12), we see that we have exactly constructed an inner product of a loop of adjacent states on the Brillouin zone, and this reduces to

$$UVU^\dagger V^\dagger = \sum_{\mathbf{k}} |\mathbf{k}\rangle\langle\mathbf{k}| \otimes |u_{\mathbf{k},n}\rangle\langle u_{\mathbf{k},n}| \cdot r_{\mathbf{k}}e^{-iF_{\mathbf{k}-\boldsymbol{\delta}_x-\boldsymbol{\delta}_y}}, \tag{3.23}$$

where $r_{\mathbf{k}}$ is just some real number that we don't care about, arising from adjacent u states not having a perfect overlap. Since we are aiming to get a sum of $F_{\mathbf{k}}$ over the whole Brillouin zone, let us take the logarithm of this matrix

$$\log\left[UVU^\dagger V^\dagger + Q\right] = \sum_{\mathbf{k}} |\mathbf{k}\rangle\langle\mathbf{k}| \otimes |u_{\mathbf{k},n}\rangle\langle u_{\mathbf{k},n}| \left(\log(r_{\mathbf{k}}) - iF_{\mathbf{k}-\boldsymbol{\delta}_x-\boldsymbol{\delta}_y}\right), \tag{3.24}$$

where we have added the projector onto the unoccupied subspace to ensure it does not diverge. Finally, let us select some arbitrary unit cell in our system at position $\mathbf{r}$ and take a local trace,

$$\mathrm{Tr}_{\mathbf{r}}\log\left[UVU^\dagger V^\dagger + Q\right] = \sum_{\mathbf{k}} |\langle\mathbf{r}|\mathbf{k}\rangle|^2 \langle u_{\mathbf{k},n}|u_{\mathbf{k},n}\rangle \left(\log(r_{\mathbf{k}}) - iF_{\mathbf{k}-\boldsymbol{\delta}_x-\boldsymbol{\delta}_y}\right). \tag{3.25}$$

We can show that $|\langle\mathbf{r}|\mathbf{k}\rangle|^2 = \frac{1}{N}$ and $\langle u_{\mathbf{k},n}|u_{\mathbf{k},n}\rangle = 1$. All that is left to do is take the imaginary part,

$$\Im\mathrm{Tr}_{\mathbf{r}}\log\left[UVU^\dagger V^\dagger + Q\right] = \frac{1}{N}\sum_{\mathbf{k}} -F_{\mathbf{k}-\boldsymbol{\delta}_x-\boldsymbol{\delta}_y}. \tag{3.26}$$

Now, redefining $\mathbf{k}$ and adding back in the factor of $-\frac{N}{2\pi}$ gives us

$$-\frac{N}{2\pi}\Im\mathrm{Tr}_{\mathbf{r}}\log\left[UVU^\dagger V^\dagger + Q\right]. = \frac{1}{2\pi}\sum_{\mathbf{k}} F_{\mathbf{k}}. \tag{3.27}$$

By comparing with Eqn. 2.15, we can see that we have arrived at an expression for the Chern number!

$$\mathcal{Q} = -\frac{N}{2\pi}\Im\mathrm{Tr}_{\mathbf{r}} \log\left[UVU^\dagger V^\dagger + Q\right]. \tag{3.28}$$

Thus, we have shown that in the case of a translationally symmetric system with periodic boundaries, the Bott index evaluated at any point in our material always exactly calculates the Chern number.

3.1.1 The Chern Marker

Most sources cite [33] for the invention of the Chern marker, however as we shall see in §3.2, the Chern marker is a relatively trivial restatement of Kitaev's marker. Here we will derive the Chern marker by showing that it can be obtained from the Bott index in the limit of large system size.

Our starting point is the expression for Bott index, Eqn. 3.16, which we rewrite using the following shorthand

$$P_x = e^{i\delta_x x} P e^{-i\delta_x x}, \tag{3.29}$$
$$P_y = e^{i\delta_y y} P e^{-i\delta_y y}, \tag{3.30}$$
$$P_{xy} = e^{i\delta_x x + i\delta_y y} P e^{-i\delta_x x - i\delta_y y}. \tag{3.31}$$

Thus, the Bott index can be written as

$$B(\mathbf{r}) = -\frac{N}{2\pi}\mathrm{Im}\mathrm{Tr}_{\mathbf{r}} \log\left[PP_xP_{xy}P_yP + Q\right]. \tag{3.32}$$

Now let us expand the translated projectors in δ,

$$P_x = P + i\delta_x[x, P] \tag{3.33}$$
$$P_y = P + i\delta_x[y, P] \tag{3.34}$$
$$P_{xy} = P + i\delta_x[x, P] + i\delta_y[y, P]. \tag{3.35}$$

Thus, the term in the trace can be expanded up to second order as

$$PP_xP_{xy}P_yP + Q = \mathbb{1} - 2\delta_x\delta_y P[x, P][y, P]P + ... + \mathcal{O}(\delta^3), \tag{3.36}$$

where we have used the identity $P[P, O]P = 0$ for any O, and '...' represents two Hermitian terms of order δ_x^2 and δ_y^2, which vanish when the imaginary part of the trace is taken. Now let us use the identity $\log(\mathbb{1} + x) \approx x$ to express the expanded Bott index as

$$B(\mathbf{r}) = -\frac{N\delta_x\delta_y}{2\pi}\mathrm{Tr}_{\mathbf{r}}\left(P[x, P][y, P]P\right) - h.c. + \mathcal{O}(\delta^3). \tag{3.37}$$

Now, writing explicitly the form of δ_α and expanding out the commutators one arrives at

$$B(\mathbf{r}) \to C(\mathbf{r}) = -2\pi i\mathrm{Tr}\left[PxP, PyP\right], \tag{3.38}$$

which is precisely the expression for the Chern marker [33].

A Quick Note on Periodic Boundaries — As we shall see in the following examples, the Chern marker is ill-suited to periodic boundaries. This is because the position operators x and y have discontinuities at the system boundaries. However, Eqn. 3.37 hints at the correct way to modify the Chern marker to be well-behaved in PBC. This can be done by noticing that the commutators $[x, P]$ and $[y, P]$ effectively calculate a displacement. Expressing P in the position basis, $P = \sum_{jk} P_{jk} |x_j\rangle\langle x_k|$ these commutators may be written as,

$$[x, P] = \sum_{jk} P_{jk}(x_j - x_k) |x_j\rangle\langle x_k| , \tag{3.39}$$

with a similar expression for $[y, P]$. If x_j and x_k are on opposite sides of the 'stitch' in the boundary conditions, where x is discontinuous then this displacement will be incorrect. Thus, we may fix this by ensuring that the displacements are always calculated using the shortest distances *in period boundary conditions.*

$$[x, P]_{PB} = \sum_{jk} P_{jk}\Delta_{x,jk} |x_j\rangle\langle x_k| , \tag{3.40}$$

where $\Delta_{x,jk}$ is the shortest displacement from point j to point k in PBC. Of course this will only work when P is short-ranged compared to the system size, since this argument only makes sense when we are finding the displacement between two points that are relatively close to one another, ensuring that the shortest path from i to j is obvious. In general, this is true in any region where the system is locally gapped, which we discuss further in §3.2 [112].

Thus, a version of the Chern marker that is well-behaved in PBC is given by

$$C_{PB}(\mathbf{r}) = -2\pi \mathrm{Tr}_{\mathbf{r}} \left(P[x, P]_{PB}[y, P]_{PB}P\right) - h.c. \tag{3.41}$$

3.1.2 Some Examples

Let us finish this section by illustrating a few examples of Bott and Chern markers for an amorphous QWZ model, shown in Fig. 3.1. In each case we calculate the marker for the same Hamiltonian – corresponding to the model with internal parameter $u = -0.5$ – around the centre of the topological gap seen in Fig. 2.7b. Both the Bott index and the Chern markers have average bulk values of $+1$, verifying that this model does indeed have a nonzero topological invariant.

In all the examples shown, the Bott index, Chern marker and periodic Chern marker have an average bulk value that corresponds to the Chern number, although there are substantial deviations around this average, which we discuss in the next subsection. Additionally, both markers display unexpected behaviour around the boundaries of the system. In the case of the Bott index, the local value around the edges of the material must be ignored, where the presence of edge modes leads to sharp positive and negative peaks. Considering the Chern marker, edge effects appear in both periodic and open boundaries, where in both cases the global sum of the Chern marker, being the trace of a commutator in a finite system, must vanish. In periodic boundaries the origin of this discontinuity of obvious, the x and y operators are not periodic,

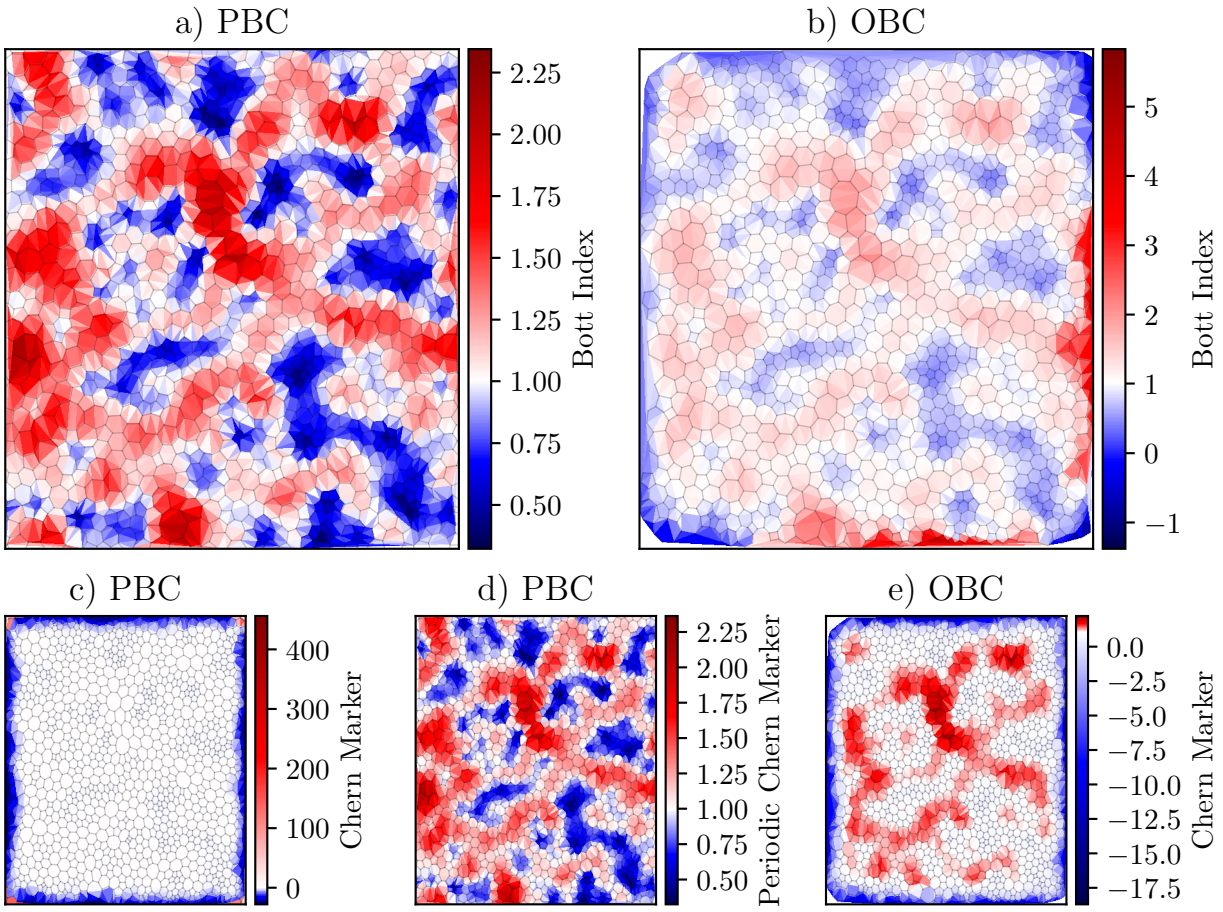


Figure 3.1: Bott index and Chern markers calculated for an example amorphous QWZ model with $u = -0.5$. **(a)** The Bott index calculated in periodic boundary conditions (PBC). **(b)** The Bott index calculated in open boundary conditions (OBC). Here we see sharp drops on some edges and a large spike localised on two edges, and in the bulk an identical profile as in subplot (a). **(c)** The Chern marker calculated according to Eqn. 3.38 in PBC. The bulk variation in the marker is barely visible due to the large discontinuities at the boundaries of the material, where the x and y operators are discontinuous. **(d)** The modified periodic Chern marker calculated according to Eqn. 3.41 in PBC. Here the boundary discontinuities vanish, and the marker is almost identical to the Bott index in subplot (a). **(e)** The Chern marker calculated according to Eqn. 3.38 in OBC. Here the marker must sum to zero, which leads to the presence of sharp drops at the boundaries, counteracting the positive bulk value.

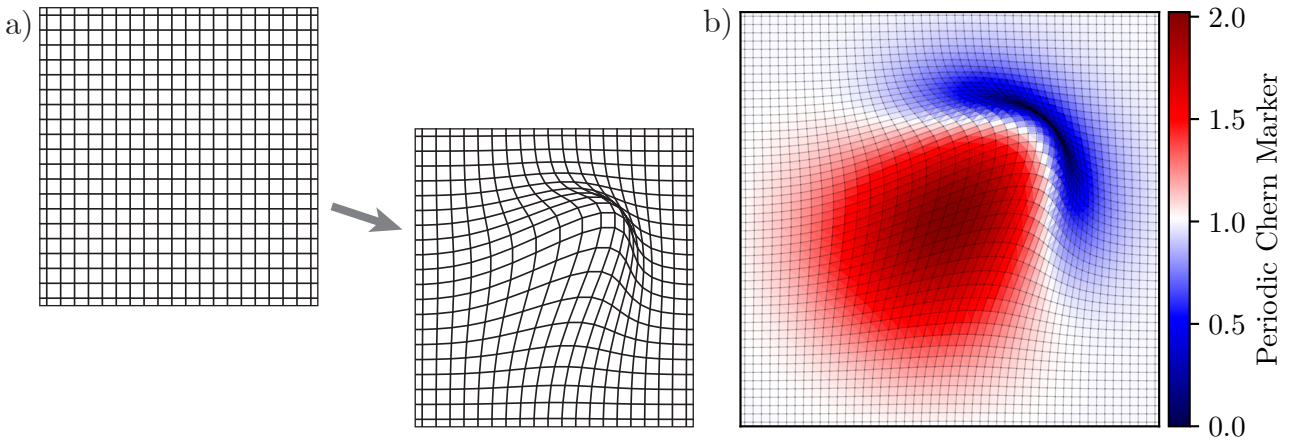


Figure 3.2: The effect of a lattice-only distortion on the Chern marker of a translationally uniform QWZ model in PBC with $u = 0.5$ – a system with Chern number $\mathcal{Q} = +1$. **(a)** A lattice distortion is applied to the system, where individual sites are translated according to a Gaussian function of their position. **(b)** The Chern number is calculated using an identical Hamiltonian and projector to the undistorted, with spatial positions shifted by the lattice distortion. Where the inter-site distances have been stretched, the Chern marker is larger than the exactly known Chern number, appearing to indicate a region of Chern number $\mathcal{Q} = +2$. Equally, where the lattice is compressed the Chern marker is reduced, appearing to show $\mathcal{Q} = 0$.

and have large discontinuities at the boundaries, so the marker could not be expected to be smooth at these points. Although we note that, using the 'periodic Chern marker' described in Eqn. 3.41, these discontinuities can be removed, providing a marker that is almost identical to the Bott index, but with the added advantage of being much less computationally expensive, since the Chern marker avoids the need for a matrix logarithm. Finally, we see that in open boundaries the Chern marker has sharp drops at the boundaries of the system which ensure that the sum over the whole system vanishes.

3.1.2.1 Are These Markers Purely Topological?

Careful inspection of the examples shown in Fig. 3.1 will reveal a peculiar structure to the deviations of the Bott and Chern markers around their bulk average (the Chern number, +1). In some regions the marker appears to indicate a Chern number of +2 and in other regions it seems to show $\mathcal{Q} = 0$. Thus, one might conclude that the material has a deeply complex topological structure, where pockets of different Chern numbers appear scattered throughout. This would be a mistake however, which can be seen by considering the geometry of the amorphous lattice. Areas where the marker is larger tend to correspond to regions where the plaquettes are larger and the sites are spaced further apart. Equally, dips in the value correspond to regions where the vertices are closer together. Thus, uneven spacing between vertices has the effect of overestimating the Chern number when vertices are further apart (so Δx appears larger between sites) and underestimating it when vertices are closer together (so Δx appears smaller between sites).

In order to illustrate this, let us consider a translationally symmetric QWZ model constructed on a square lattice with uniform $u = 0.5$. Here we expect that the Bott index or periodic Chern marker will be precisely +1 throughout the system. Let us consider distorting the lattice as

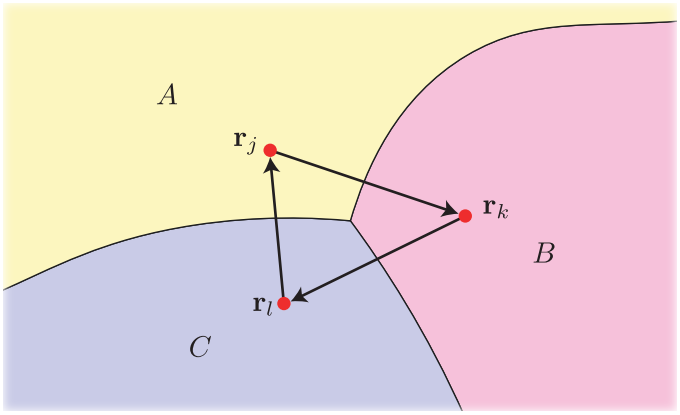


Figure 3.3: Diagram showing the partition of the plane into three regions labelled with A, B and C. An example of h_{jkl} is depicted with red dots, where arrows indicate the positive direction.

shown in Fig. 3.2a while keeping the Hamiltonian (and thus the projector P) invariant. Since the properties of the state itself have not changed under such a transformation, one expects the topological properties of the system to remain invariant. However, calculating the local Chern marker, as shown in Fig. 3.2b, we find the value substantially inflated at points where the lattice has expanded, and vice versa at points of contraction. Thus, we see that these local markers do not solely capture the topological properties of the occupied band, but also depend on the details of the lattice embedding on the plane. Of course, averaging over a sufficiently large area one can always recover a close to quantised value. However, if we accept that such markers can only be interpreted by considering an average over a large region of the bulk then how can they be considered local? In the next section we shall present an alternative, where the Chern number is calculated around a single point in the bulk of the material, and the locality of the marker can be explicitly seen from the spatial distribution of the marker value around that point.

3.2 Kitaev's Local Marker

The majority of accounts of local markers tend to focus on the development of the Bott index and the Chern marker. However, the first construction of a real-space Chern number can (along with the rest of modern physics) be found in the appendices of a seminal work by Kitaev [30]. Thus, we shall start our discussion with an explanation of Kitaev's local marker, the discussion will largely follow the source material, however we provide some additional detail at various points.

As always, our starting point is a Hamiltonian defined on an arbitrary lattice with sites at positions $\mathbf{r}_j$, however in this case we shall work with an infinite system. Here, let us define the projector onto a band $P = \sum_{\text{band}} |\psi\rangle\langle\psi|$, along with a shorthand for off-diagonal correlations given by

$$P_{jk} = \langle \mathbf{r}_j | P | \mathbf{r}_k \rangle \,. \tag{3.42}$$

In general, if this is onto a gapped set of states, then the projector will satisfy the following

condition [112],

$$|P_{jk}| \leq c|\mathbf{r}_j - \mathbf{r}_k|^{-\alpha}, \tag{3.43}$$

for any α greater than the dimensionality of the system. Following Kitaev, let us define a 2-current,

$$h_{jkl} = 12\pi i(P_{jk}P_{kl}P_{lj} - P_{jl}P_{lk}P_{kj}). \tag{3.44}$$

We divide our system into three regions in real space, A, B and C, and define the real-space Chern number,

$$\mathcal{Q}_{\text{Kit}}(P) = \sum_{j\in A}\sum_{k\in B}\sum_{l\in C} h_{jkl}, \tag{3.45}$$

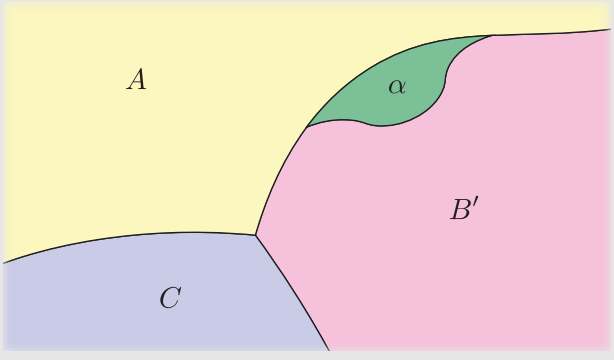
which we can re-express in terms of a set of projectors onto the three regions $A = \sum_{j\in A}|\mathbf{r}_j\rangle\langle\mathbf{r}_j|$, with a similar definition for B and C,

$$\mathcal{Q}_{\text{Kit}}(P) = 12\pi i\text{Tr}(PAPBPC - PCPBPA). \tag{3.46}$$

This quantity remains invariant when we relabel any finite area from one region to another. Additionally, due to the localised nature of P, the only nonzero contributions to it come from around the point where the three regions A, B and C meet.

The Invariance of $\mathcal{Q}_{\text{Kit}}$ to changes in A, B and C — In order to see why this is the case, let us consider picking up some finite chunk of the region B, which we label with α and moving it over into region A. Thus, let us make the redefinition

$$A' = A + \alpha \tag{3.47}$$
$$B' = B - \alpha \tag{3.48}$$



Thus, the matrix term in the Kitaev Chern number becomes

$$PAPBPC - h.c. = PA'PB'PC + PAP\alpha PC - P\alpha PB'PC - h.c. \tag{3.49}$$

Now let us use the identity $B' = \mathbb{1} - \alpha - A - C$ to re-express this in the form

$$\begin{aligned} PAPBPC - h.c. =& PA'PB'PC + PAP\alpha PC + P\alpha PAPC \\ &- P\alpha PC + P\alpha P\alpha PC + P\alpha PCPC - h.c. \end{aligned} \tag{3.50}$$

Here we have used the identity $P^2 = P$ to obtain this line. All the extra terms on the RHS vanish when the trace is taken. Note that generally one cannot use the cyclic property of the trace here, since our operators are infinite matrices, so there is no guarantee that the rearranged infinite sum converges to the same value. However, since α represents a finite region, the sum vanishes far from α, and so we are free to cycle any trace containing α. Thus, we are left with

$$\mathrm{Tr}(PAPBPC - h.c.) = \mathrm{Tr}(PA'PB'PC - h.c.). \tag{3.51}$$

In fact, the extra finite region α need not be a projector, since the above proof holds regardless of the properties of α provided that it has finite support. Thus, we can go even further and see that the value of $\mathcal{Q}_{\mathrm{Kit}}$ is invariant under the addition of any finite matrix to one of out three regions, provided we subtract it from another region as well.

Let us re-express $\mathcal{Q}_{\mathrm{Kit}}$ to a form that will be useful in the following discussion. Since the expression is invariant under cycling of the order of our three regions, we may write it as

$$\mathcal{Q}_{\mathrm{Kit}} = 4\pi i \mathrm{Tr}(PAPBPC + PBPCPA + PCPAPB \tag{3.52}$$
$$- PAPCPB - PCPBPA - PBPAPC), \tag{3.53}$$

note that we are not allowed to cycle the terms in the trace here. Inserting the identity

$$C = \mathbb{1} - A - B, \tag{3.54}$$

we arrive at the following expression,

$$\mathcal{Q}_{\mathrm{Kit}}(P) = 4\pi i \mathrm{Tr}[PAP, PBP] \tag{3.55}$$

This is a trace of a commutator, which will always vanish if one of the operators in the commutator has finite support. This supports our assertion that $\mathcal{Q}_{\mathrm{Kit}}$ is invariant under addition of any finite matrix to $A \to A + \alpha$, since $\mathrm{Tr}[P\alpha P, PBP]$ vanishes. Of course, we must also transform either $B \to B - \alpha$ or $C \to C - \alpha$ for the identity 3.54 to hold.

This invariance to the form of A, B and C affords us with an astounding amount of freedom in how we choose to define this Chern number. Not only can we select any three regions with any shape (provided the overall topology of the three regions far from the triple contact point remains the same), but we can even blur the boundaries between the projectors or allow them to overlap and nothing will change.

3.2.1 Relation to the Chern Number

So far we have constructed a quantity, $\mathcal{Q}_{\mathrm{Kit}}$ and shown that there is a remarkable amount of freedom in how we can modify it without changing its value. In order to connect this to band topology, we will need to show that when evaluated in a translationally symmetric context, $\mathcal{Q}_{\mathrm{Kit}}$ corresponds exactly to the Chern number. Let us start by re-expressing $\mathcal{Q}_{\mathrm{Kit}}$ again in a new

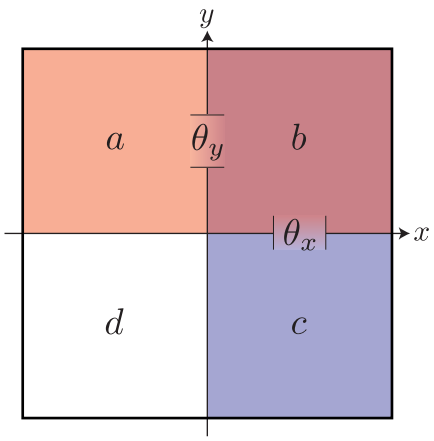


Figure 3.4: The decomposition of the two-step functions proposed in Eqn. 3.58 into a set of four projectors on the quarters of the plane. The x-step function is composed of regions b and c, and the y-step function is composed of regions a and b.

form. We define a set of step function projectors ϑ_x, ϑ_y that satisfy

$$\vartheta_\alpha |\mathbf{r}\rangle = \begin{cases} |\mathbf{r}\rangle & \text{for } r_\alpha \geq 0, \\ 0 & \text{for } r_\alpha < 0. \end{cases} \tag{3.56}$$

Let us now consider the operator

$$2\pi i \mathrm{Tr}[P\vartheta_x P, P\vartheta_y P]. \tag{3.57}$$

By decomposing the step function into projectors onto the four quarters of the plane, we arrive at

$$\begin{aligned} 2\pi i \mathrm{Tr}[P\vartheta_x P, P\vartheta_y P] = 2\pi i \mathrm{Tr}\big([PaP, PbP] + [PbP, PbP] \\ + [PaP, PcP] + [PbP, PcP]\big), \end{aligned} \tag{3.58}$$

where the labelling of the regions a-d is shown in Fig. 3.4. Clearly the second term on the RHS vanishes. The third term also vanishes, which can be seen by its invariance under a mirror symmetry across the line $y + x = 0$ (a mirror reflection will always flip the sign of h_{jkl}). Finally, we see that the first and last terms are both equal to $\mathcal{Q}_{\mathrm{Kit}}/2$, thus

$$\mathcal{Q}_{\mathrm{Kit}} = 2\pi i \mathrm{Tr}[P\vartheta_x P, P\vartheta_y P]. \tag{3.59}$$

In order to make contact with momentum space, we shall work in an infinite translationally invariant system. Clearly, in this context the position of the step functions will have no effect on the value of $\mathcal{Q}_{\mathrm{Kit}}$. Thus, let us define a set of translated step functions

$$\vartheta_{R_\alpha} |\mathbf{r}\rangle = \begin{cases} |\mathbf{r}\rangle & \text{for } r_\alpha \geq R_\alpha, \\ 0 & \text{for } r_\alpha < R_\alpha. \end{cases} \tag{3.60}$$

Obviously, the value of $\mathcal{Q}_{\mathrm{Kit}}(\mathbf{R}) = 2\pi i \mathrm{Tr}[P\vartheta_{R_x} P, P\vartheta_{R_y} P]$ is the same as $\mathcal{Q}_{\mathrm{Kit}}$. Thus, let us choose some (arbitrarily large) square region of area L^2 the plane and take the average of

$\mathcal{Q}_{\text{Kit}}(\mathbf{R})$ over this region,

$$\mathcal{Q}_{\text{Kit}} = \frac{1}{L^2}\int_{-L/2}^{L/2} dR_x\, dR_y\, \mathcal{Q}_{\text{Kit}}(\mathbf{R}) \tag{3.61}$$

$$= \frac{2\pi i}{L^2}\text{Tr}[PxP, PyP] \tag{3.62}$$

$$= \frac{2\pi i}{L^2}\text{Tr}P\big[[x,P],[y,P]\big] \tag{3.63}$$

In the limit of large L, we expect that the contribution to the trace is uniform in space, and so can replace the global trace with a local trace around some arbitrary point in the system $\mathbf{r}$, $\frac{1}{L^2}\text{Tr} \to \text{tr}_{\mathbf{r}}$. Thus, we arrive at

$$\mathcal{Q}_{\text{Kit}} = 2\pi i \text{tr}_{\mathbf{r}}\big[P[x,P],[y,P]\big]. \tag{3.64}$$

Now let us construct the exact form of the projector onto a band for a translationally symmetric Hamiltonian. From Bloch's theorem, we know the projector will have the following form

$$P = \frac{1}{4\pi^2}\int d^2\mathbf{k}\, |k\rangle\langle k| \otimes \psi(\mathbf{k}) \tag{3.65}$$

This means that we can use the identity $[x,P] \to -i\partial_x\psi(\mathbf{k})$, where ∂_x represents a derivative with respect to k_x, to show that

$$\mathcal{Q}_{\text{Kit}} = \frac{-i}{2\pi}\int d^2\mathbf{k}\, \text{tr}_{\mathbf{r}}\big(\, |\mathbf{k}\rangle\langle\mathbf{k}| \otimes \psi(\mathbf{k})[\partial_x\psi(\mathbf{k}), \partial_y\psi(\mathbf{k})]\big) \tag{3.66}$$

Now, using the fact that $\langle \mathbf{r}\,|\mathbf{k}\rangle\langle\mathbf{k}|\,\mathbf{r}\rangle = 1$, this reduces to a trace over the unit cell degree of freedom only,

$$\mathcal{Q}_{\text{Kit}} = \frac{-i}{2\pi}\int d^2\mathbf{k}\, \text{Tr}\big(\psi(\mathbf{k})[\partial_x\psi(\mathbf{k}), \partial_y\psi(\mathbf{k})]\big). \tag{3.67}$$

Comparing to Eqn. 2.33, we see that this quantity exactly evaluates an integral of the Berry curvature over the Brillouin zone. Thus, we have shown that – at least in the context of an infinite, translationally symmetric system – $\mathcal{Q}_{\text{Kit}}$ evaluates the Chern number.

A Useful Identity for Operators in Momentum Space — Let us start by considering an arbitrary operator in a translationally symmetric system with the following form,

$$A = \int_{BZ}\frac{dk}{2\pi}\, |k\rangle\langle k| \otimes A(k), \tag{3.68}$$

where $A(k)$ acts on the degrees of freedom inside the unit cell. Here we use a 1D Brillouin zone, but this can be straightforwardly extended to higher dimensions. Let us consider the following expression,

$$[x,A] = \frac{1}{2\pi}\int_{BZ} dk\big[x, |k\rangle\langle k|\,\big] \otimes A(k). \tag{3.69}$$

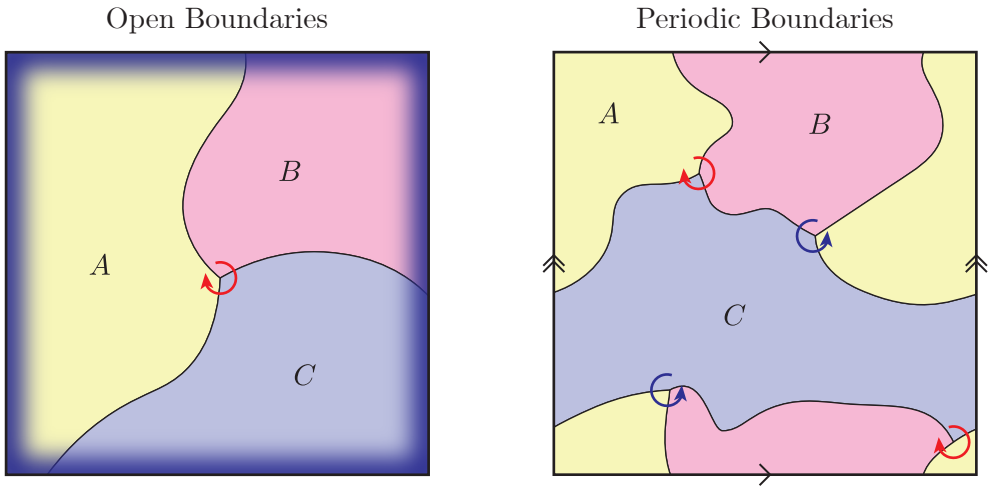


Figure 3.5: Two examples depicting how $\mathcal{Q}_{\text{Kit}}$ vanishes in finite systems. **(Left)** A topological system in open boundary conditions with necessarily have gapless edge modes present (depicted here with a blue border), which contribute a term to $\mathcal{Q}_{\text{Kit}}$ that exactly cancels out the topological value around the triple contact point. **(Right)** An example partition of the torus (shown with opposite edges identified) into three regions. In this case, four triple contact points are present. Around each two have the regions arranged clockwise around them and two counter-clockwise, so overall $\mathcal{Q}_{\text{Kit}}$ vanishes.

Using the identity $x\,|k\rangle = i\partial_k\,|k\rangle$, we can rewrite this in the form

$$[x, A] = \frac{1}{2\pi}\int_{BZ} dk\, i\partial_k\big(\,|k\rangle\langle k|\,\big) \otimes A(k) \tag{3.70}$$

$$= \frac{1}{2\pi}\int_{BZ} dk\ |k\rangle\langle k| \otimes (-i\partial_k A(k)), \tag{3.71}$$

where we used the fact that an integral of total derivative of the RHS vanishes, as the integral is over the whole Brillouin zone. Thus, we can make the general substitution

$$[x, A] \to -i\partial_k A(k) \tag{3.72}$$

3.2.2 Kitaev's Marker in a Finite System

So far, we have defined Kitaev's Chern number for a system with infinite boundary conditions. This version of the Chern number is useful in analytical arguments – for example, a similar quantity was used to prove the quantisation of Hall conductivity in the presence of disorder [98]. However, to be of broad practical use, $\mathcal{Q}_{\text{Kit}}$ must still work in a finite system with open or periodic boundary conditions. Our current definition is unsuitable, which can be seen from Eqn. 3.55. Since the trace of a commutator vanishes in a finite system, this quantity is only nonzero in infinite boundary conditions.

Before we modify $\mathcal{Q}_{\text{Kit}}$, let us first consider the details of how it misbehaves in finite systems. The stability of $\mathcal{Q}_{\text{Kit}}$ depends on two assumptions – that the projector P is exponentially localised,

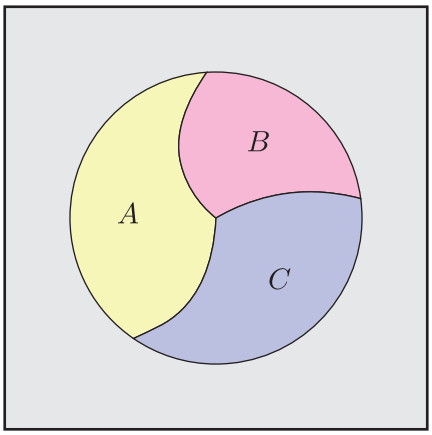


Figure 3.6: Three restricted regions for which $\mathcal{Q}_{\text{Kit}}$ can be calculated. Now there is only one point where the three regions meet. Provided that P remains short ranged in the circular region and the distance from the triple contact point to the boundary of the circle is larger than the correlation length of P, this will calculate a quantised Chern number.

and that the three regions A, B, C all touch at a single point only. In a finite system, at least one of these two assumptions will always fail. In the case of the localisation of the projector, as long as the band remains gapped, we can expect that this condition will hold. However, in a system with nonzero Chern number and open boundaries, the bulk boundary correspondence forces the existence of gapless edge modes. This means that the topological bulk is surrounded by a gapless region where the projector no longer has short-ranged correlations, allowing for a contribution to Eqn. 3.46 that cancels out the central contribution from the triple contact point. In periodic boundaries we have no edge modes, however it is impossible to partition the torus into three regions with only a single point where the three meet. Instead, triple contact points are always created in pairs. Furthermore, of these pairs, one contact point always has the regions ordered clockwise and the other counter-clockwise around the point. This means that the contributions to $\mathcal{Q}_{\text{Kit}}$ from the two points will always cancel out perfectly. An example of each of these effects is shown in Fig. 3.5.

In order to remedy this, let us restrict the three regions over which the Chern number is calculated, such that the boundaries and other triple contact points are avoided, as shown in Fig. 3.6. In this case, there is only a single point where A, B and C meet. Let us define a projector onto the circular region as O. In this case, the finite version of $\mathcal{Q}_{\text{Kit}}$ is defined the same as Eqn. 3.46, however with the following redefinition of the projectors

$$A \to \tilde{A} = OA. \tag{3.73}$$

The restricted Chern number can be written as

$$\mathcal{Q}^{O}_{\text{Kit}} = 12\pi i \text{Tr}(P\tilde{A}P\tilde{B}P\tilde{C} - P\tilde{C}P\tilde{B}P\tilde{A}). \tag{3.74}$$

Using the identity

$$\tilde{C} = O - \tilde{A} - \tilde{B}, \tag{3.75}$$

we can re-express this similarly to Eqn. 3.55,

$$\mathcal{Q}^{O}_{\mathrm{Kit}} = 4\pi i \mathrm{Tr}_{O}[P\tilde{A}P, P\tilde{B}P], \tag{3.76}$$

where the trace is taken only over the region O. Finally, assuming that the boundary of O is sufficiently far from the triple contact point (or any region where P is long-ranged), we can expect that there is no contribution near the boundary of O, we can drop the tilde on A and B to get,

$$\mathcal{Q}^{O}_{\mathrm{Kit}} = 4\pi i \mathrm{Tr}_{O}[PAP, PBP]. \tag{3.77}$$

The value of the marker is not dependent to the exact shape of O, provided its boundary avoids any other triple contact points, or gap closings.

3.2.3 Numerical Examples

Let us now provide a slide show of numerical examples of Kitaev's Chern number calculated in the amorphous QWZ model, verifying the arguments presented above. In each case, we calculate the step-function form of the Chern number given in Eqn. 3.59. Rather than immediately summing over a bulk region, we shall consider the real-space contribution to the trace by finding the local trace of the marker, $\mathrm{Tr}_{\mathbf{r}}(...) = \mathrm{Tr}\,\langle\mathbf{r}|...|\mathbf{r}\rangle$. Thus, we evaluate the local contribution given by

$$\mathcal{Q}_{\mathrm{Kit}}(\mathbf{r}) = 4\pi i \mathrm{Tr}_{\mathbf{r}}[P\vartheta_x P, P\vartheta_y P]. \tag{3.78}$$

By plotting $\mathcal{Q}_{\mathrm{Kit}}(\mathbf{r})$ over the system, it is easy to see where the central contribution to $\mathcal{Q}_{\mathrm{Kit}}$ ends, and thus deduce what area to trace over to find a quantised Chern number.

In each case, we also calculate the trace of the marker over a circular region, O, around the central peak, varying the radius of the circular region. We expect that as the region is increased, the trace should quickly converge to a near-quantised number. Once the circle becomes large enough to approach the edges of the system, the sum approaches zero as the trace becomes a trace over the whole system.

We show three sets of examples. In Fig. 3.7 we compare the marker value in periodic boundary conditions and open boundary conditions, giving a direct example of the picture presented in §3.2.2, where we discuss the two ways that finite size effects can cause the full trace to vanish. In Fig. 3.8 we plot the marker while tuning the QWZ model from a topological phase to a trivial phase. This is done by tuning the on-site splitting parameter u (see Eqn. 2.66) over the phase transition at $u = -1.5$. Finally, in Fig. 3.9, we add disorder by locally varying the value of u with a perturbation drawn from a normal distribution. By increasing the standard deviation, we see how the marker changes as disorder gradually destroys the topological phase.

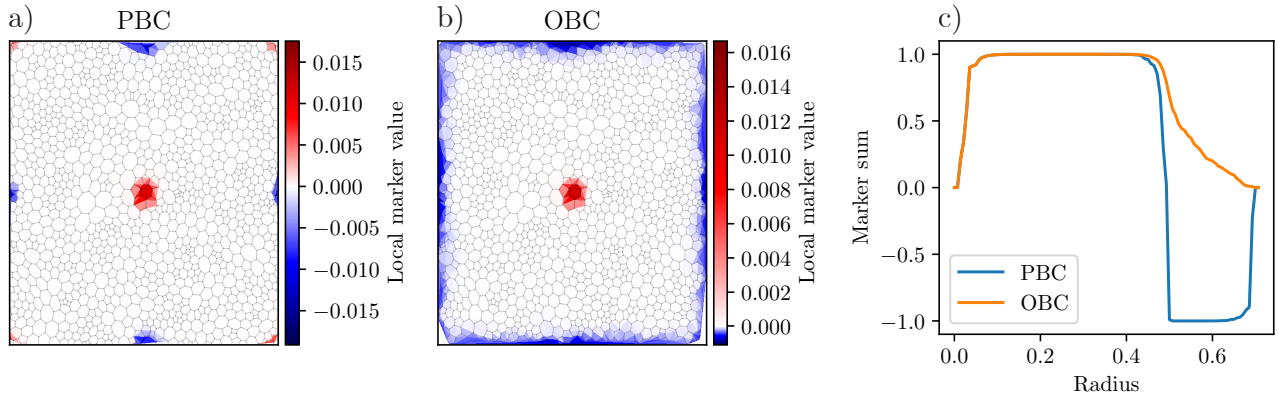


Figure 3.7: $\mathcal{Q}_{\text{Kit}}$ for the same amorphous QWZ model in periodic and open boundary conditions. In both cases u is tuned to -0.5, close to the centre of the topological region shown in Fig. 2.4. **(a)** In periodic boundaries, there are four points where both step functions meet. One in the centre and three on the boundary. At each of these points, the marker has a contribution determined by the Chern number, however at two of these points the step functions are such that the ordering of the regions is counter-clockwise, so the contribution is negative. Thus, the total trace vanishes. **(b)** In open boundaries the bulk Chern insulator is surrounded by a ring of gapless edge modes. Thus, on the boundary the projector is long-ranged and contributes a non-vanishing term to $\mathcal{Q}_{\text{Kit}}$ that exactly cancels out the bulk term. **(c)** A plot showing the trace of $\mathcal{Q}_{\text{Kit}}$ over a circular region O around the central peak, showing the sum against circle radius. The maximum values reached in the PBS and OBC cases both quantised to one part in 10^6, this extremely precise quantisation can be improved by increasing system size, further separating the bulk and edge effects. Once the circle becomes large enough to include boundary effects, both markers vanish.

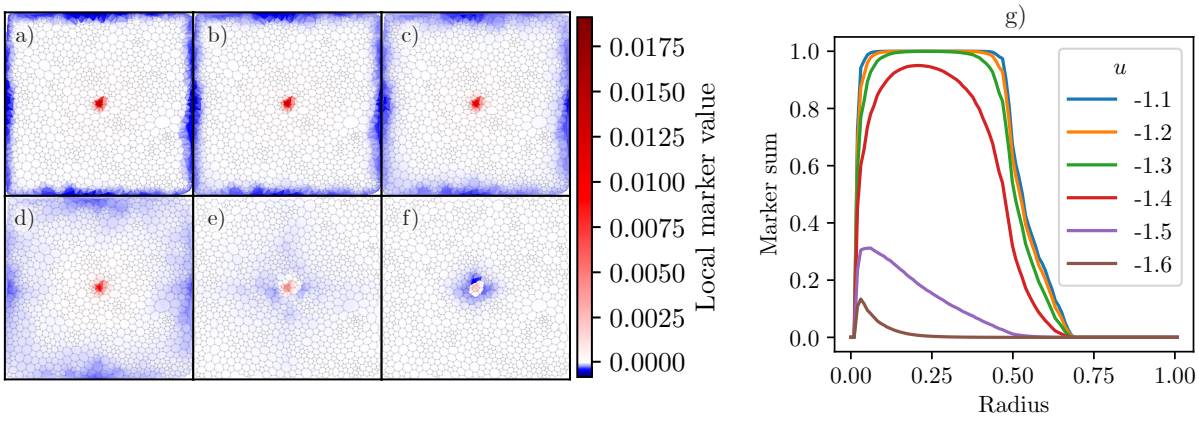


Figure 3.8: $\mathcal{Q}_{\text{Kit}}$ for an amorphous QWZ system in OBC for a range of u values across a transition from a topological to a trivial phase. **(a-f)** Local distribution of *qkit* for a set of u values that range from $u = -1.1$ to $u = -1.6$, where the phase boundary is at $u = -1.5$. Nearing the phase boundary, the edge modes permeate deeper into the bulk – and so the edge contributions get closer to the central peak in $\mathcal{Q}_{\text{Kit}}$. At the exact phase transition the entire system is conducting, and the bulk and edge parts of $\mathcal{Q}_{\text{Kit}}$ are not separable. Past the boundary, the marker vanishes. **(g)** Trace of $\mathcal{Q}_{\text{Kit}}$ over a circular region O around the central peak. Before the phase transition, the line tends towards $+1$ until it starts to include the edge effects, after the phase transition it tends to 0.

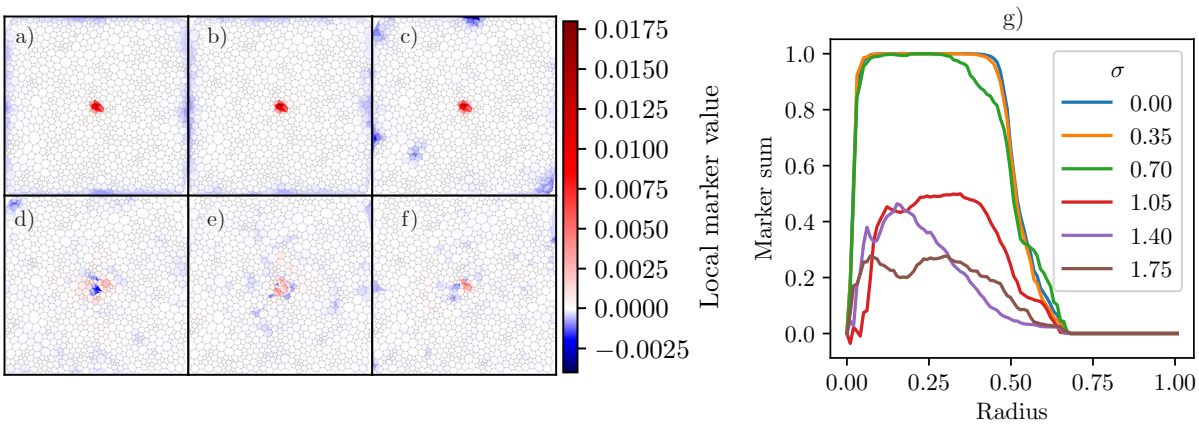


Figure 3.9: $\mathcal{Q}_{\text{Kit}}$ for an amorphous QWZ system in OBC with increasing on-site disorder, added by locally varying the value of u – sampling from a Gaussian distribution centred on $u = -0.5$. **(a-f)** Local distribution of *qkit* for a set of u values sampled with a standard deviation ranging from $\sigma = 0$ to $\sigma = 1.75$ in steps of 0.35. Once σ is sufficiently large, the disorder is strong enough to create topologically trivial regions in the material that destroy the quantisation of $\mathcal{Q}_{\text{Kit}}$, and the material is topologically trivial. **(g)** Trace of $\mathcal{Q}_{\text{Kit}}$ over a circular region O around the central peak. At sufficiently weak disorder, the marker remains close to quantised. However past a threshold around $\sigma \sim 1$, the marker no longer approaches a quantised value.

3.3 A Physical Interpretation

So far, we have presented three real-space formulations of the Chern number – the Bott index, Chern marker and Kitaev's Chern number. Each of these quantities at least approximately solve the problem of defining a Chern number without relying on momentum space. However, these markers still all suffer from one substantial drawback. That is, they were defined as a purely mathematical exercise, by restating the Chern number in a real-space mathematical language. Thus, it is not clear at all whether they correspond to a real, observable physical quantity. In other words, on handing these markers to an experimentalist we could expect a variety of responses along the lines of:

- 'What the hell am I supposed to do with this'
- 'Christ, I hate talking to theorists'
- *Presses button under desk*, 'Security, get this person out of here'
- 'This is completely pointless, we already know how to do this using the Streda formula' [113, 114]

Although several attempts have been made [93, 103, 115], there is currently no straightforward consensus for how one might construct a physical observable that corresponds to a local marker of the Chern number. In this section, we present a derivation for a local marker that starts from physical grounds, defined as a localised version of the Kubo Hall conductivity [24]. Local current is measured around the position $\mathbf{R}$ of a crosshair placed in the bulk of the material, motivating the name 'crosshair marker'. The derived quantity is precisely the finite-system Kitaev Chern number given in Eqn. 3.59.

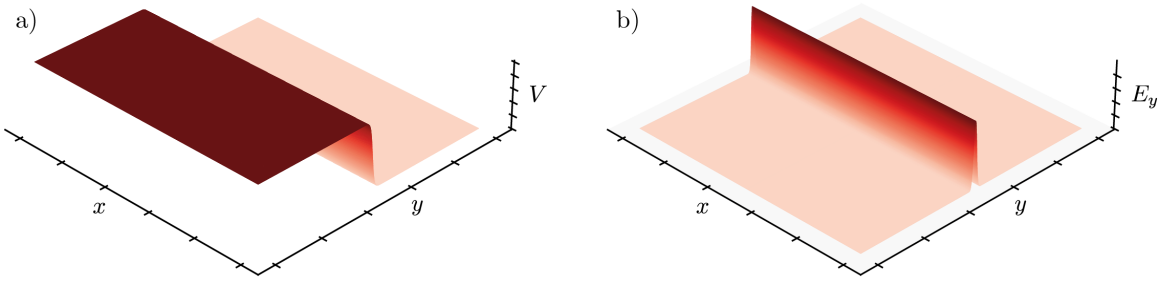


Figure 3.10: **(a)** The electric potential used to generate our electric field. **(b)** The electric field, with only the nonzero y-component is shown.

This section is structured as follows: We start by deriving the necessary prerequisites to understand the marker. These are threefold, in §3.3.1 we describe the formalism for modelling the effect of electric fields on our system, in §3.3.2 we define a set of pseudo-local current operators on a lattice, and in §3.3.3 we describe Kato's formalism for adiabatic quantum evolution [116, 117]. In §3.3.4 we use these concepts to re-derive Eqn. 3.77 as a physical quantity.

As usual, let us work with a general non-interacting Hamiltonian on a two-dimensional tight-binding lattice. The system consists of set of N sites, with positions $\mathbf{r}_i$ arranged on either a regular or amorphous lattice. Each site has an internal degree of freedom hosting η states. Thus, the Hamiltonian can be written in the form

$$H = \sum_{i,j} |\mathbf{r}_i\rangle \langle \mathbf{r}_j| \otimes H_{i,j}, \tag{3.79}$$

where $H_{i,j} = H_{j,i}^\dagger$ acts on the internal degrees of freedom. We will focus only on systems with open boundary conditions.

3.3.1 Electric Fields

Since we plan to calculate the response of the system under an applied electric field, let us start by precisely defining the potential we wish to apply to our system, and describing the effect on the Hamiltonian.

We wish to model the effect of raising the potential of one half of the system with respect to the other, resulting in an electric field across the boundary separating the two regions. Without loss of generality, let us consider raising the potential of the region below a dividing line at position $y = R_y$ with respect to the region above the line. In the continuum, this corresponds to an electric potential of the form $V(\mathbf{r}) = -V_0\theta(y - R_y)$, where θ is a Heaviside step function. The electric field acts over the line at $y = R_y$, as shown in figure 3.10,

$$\mathbf{E}(\mathbf{r}) = V_0\delta(y - R_y)\mathbf{e}_y, \tag{3.80}$$

where $\mathbf{e}_y$ is a unit vector in the y direction. We transform to a gauge with zero scalar potential, representing the electric field with a magnetic vector potential,

$$\mathbf{A}(\mathbf{r}, t) = -V_0 t\delta(y - R_y)\mathbf{e}_y. \tag{3.81}$$

Making the assumption that V_0 is small, we shall use Peierls substitution to describe the effect of a slow-varying magnetic vector potential on our lattice system [64]. The translation operators

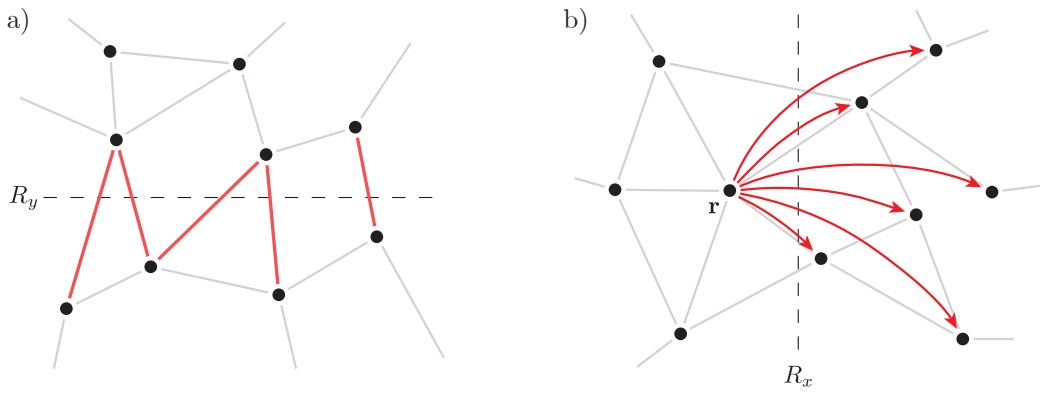


Figure 3.11: **(a)** A section of amorphous lattice is shown. All hopping terms in the Hamiltonian that cross the line $y = R_y$ acquire a Peierls phase given by Eqn. 3.83, these are depicted in red. Unaffected hopping terms are shown in grey. Note that the phase is ill-defined when a site $\mathbf{r}_i$ lies on the line, however this can be remedied by infinitesimally shifting R_y. **(b)** A depiction of the 'local' current operator $J_{R_x}(\mathbf{r})$ that calculates the total hopping to or from the site at $\mathbf{r}$ that crosses the boundary at R_x. Background lattice is shown in grey.

are modified by a Peierls phase $|\mathbf{r}_j\rangle\langle\mathbf{r}_i| \to |\mathbf{r}_j\rangle\langle\mathbf{r}_i| e^{i\alpha(\mathbf{r}_i,\mathbf{r}_j)}$, given by

$$\alpha(\mathbf{r}_i, \mathbf{r}_j) = \int_{\mathbf{r}_j}^{\mathbf{r}_i} \mathbf{A}(\mathbf{r}) \cdot d\mathbf{r}. \tag{3.82}$$

Note that we work in natural units, setting the electronic charge $q = \hbar = 1$. Given the form of the magnetic vector potential, we can see that translation operators only pick up a phase if they cross the line $y = R_y$. This is illustrated in Fig. 3.11a. The Peierls phase can be expressed as

$$\alpha(\mathbf{r}_i, \mathbf{r}_j) = A(t)\left[\theta(y_i - R_y) - \theta(y_j - R_y)\right], \tag{3.83}$$

with $A(t) = V_0 t$. Thus, the Hamiltonian is modified according to

$$H(A) = e^{iA(t)\vartheta_{R_y}} H e^{-iA(t)\vartheta_{R_y}}, \tag{3.84}$$

In the limit of small A, this can be expanded to first order,

$$H(A) = H - iA(t)\left[H, \vartheta_{R_y}\right]. \tag{3.85}$$

As we shall see in the next section, the change in the Hamiltonian is expressed in terms of a current operator for flow across the line $y = R_y$.

Note that for a static $A(t)$ in open boundaries, the A-dependence can be completely removed by a gauge transformation, so there will be no physical effect on our system. This is reflected by the fact that $\mathbf{E}$ depends on $\partial_t A$, so static A corresponds to zero electric field.

3.3.2 Current Operators

We construct an operator representing the flow of particles across a line bisecting the system. Again, without loss of generality, we will look at the flow of particles in the x-direction, across the

vertical boundary at $x = R_x$. The number operator for particles to the right of this line is given by ϑ_{R_x}. The time-evolution for the number of particles in this region is $\partial_t \langle \vartheta_{R_x} \rangle = i\langle [H, \vartheta_{R_x}] \rangle$. Thus, we can identify the operator representing flow of particles across the boundary as

$$J_{R_x} = i[H, \vartheta_{R_x}]. \tag{3.86}$$

This allows us to re-express Eqn. 3.85 in the familiar form $H(A) = H - AJ_{R_y}$, where A is defined in equations 3.83.

The operator J_{R_x} evaluates the overall flow across the whole system, however in the following discussion we wish to separate the bulk and edge contributions. Thus let us decompose this operator into a sum of terms local to some point at $\mathbf{r}$, according to

$$J_{R_x}(\mathbf{r}) = \frac{1}{2} \left(\delta_{\mathbf{r}} J_{R_x} + J_{R_x} \delta_{\mathbf{r}} \right), \tag{3.87}$$

with $\delta_{\mathbf{r}} = |\mathbf{r}\rangle \langle \mathbf{r}|$. The two terms evaluate the contributions to J_{R_x} from hopping into site $\mathbf{r}$, and from hopping out of site $\mathbf{r}$ respectively, a diagram is shown in Fig. 3.11b. The factor of $1/2$ is included to ensure that $\sum_{\mathbf{r}} J_{R_x}(\mathbf{r}) = J_{R_x}$, since every pair of sites is counted twice. This decomposition is not unique – there are many ways one could express J_{R_x} as a sum over local terms. However, the final result will be insensitive to particular method since we shall sum over all the bulk contributions, which will be well-separated from edge contributions.

3.3.3 Kato Dynamics

We will work in the adiabatic limit, with a Hamiltonian that changes over a long timescale T, where the local density of states in the bulk has an energy gap Δ. We define the projector onto the occupied states at $t = 0$ as $P_0 = \sum_{\text{occ}} |\psi_i(0)\rangle \langle \psi_i(0)|$, where $|\psi_i(0)\rangle$ is an eigenstate of H at $t = 0$. In general, time-evolution will result in a final state $P(t)$ that is related to the initial state by the Schrödinger equation. However. if the evolution is sufficiently slow (for $T \gg \Delta^{-1}$), we expect that P_0 will adiabatically evolve to the instantaneous projector, $P_I(t) = \sum_{\text{band}} |\psi_i(t)\rangle \langle \psi_i(t)|$, where $|\psi_i(t)\rangle$ are eigenstates of H at time t [118]. To ensure that our time-evolution is exactly adiabatic, we use a formalism based on that introduced in [116], although a modern description can be found in [117–119]. We sketch out the basics here. However for a detailed discussion, see Appendix B.1.

Rather than using H to generate time evolution, we define an adiabatic Hamiltonian, K, which satisfies the instantaneous Von-Neumann equation

$$\partial_t P_I(t) = -i[K, P_I], \tag{3.88}$$

where the change in P_I follows the instantaneous eigenstates of H. Using the identity $P\dot{P}P = 0$ (where dot denotes a time-derivative), we can verify that the equation is satisfied by K of the form

$$K(t) = i[\dot{P}_I, P_I]. \tag{3.89}$$

The full time evolution of the projector follows the instantaneous eigenstates in the limit of large $T \gg \Delta$. Thus, in the following discussion, where we are working in the adiabatic regime, we may use Eqn. 3.88 to describe the change in P, and drop the subscript on P_I, since all our

time evolution is adiabatic. Having defined the adiabatic Hamiltonian, let us examine the exact form of K for our applied electric field, as well as deriving an adiabatic equivalent of the current operator in Eqn. 3.87.

3.3.3.1 Adiabatic EM Fields

The time-dependence of our Hamiltonian is given by Eqn. 3.84. We work in open boundaries, so the operator $e^{iA(t)\vartheta_{R_y}}$ behaves as a straightforward unitary rotation on the eigenstates. Note that in periodic boundaries, this operator would enforce twisted boundary conditions, shifting both the eigenstates and eigenenergies of H. Thus, the time-dependence of the projector is

$$P(t) = e^{iA(t)\vartheta_{R_y}} P_0 e^{-iA(t)\vartheta_{R_y}}, \tag{3.90}$$

and the time-derivative is $\dot{P} = i\dot{A}\left[\vartheta_{R_y}, P\right]$. This can be inserted into definition 3.89 to arrive at the form of the adiabatic Hamiltonian,

$$K = \dot{A}\left(P\vartheta_{R_y}Q + Q\vartheta_{R_y}P\right), \tag{3.91}$$

where $Q = \mathbb{1} - P$ is the complement of the projector.

3.3.3.2 Adiabatic Current

The adiabatic current operator is derived following an analogous argument to that in §3.3.2. We find the change in particle number for the region $x > R_x$, given by ϑ_{R_x}. In this case, however, we use the adiabatic Von-Neumann equation 3.88 to express the expectation value, $\partial_t\langle\vartheta_{R_x}\rangle = i\langle[K, \vartheta_{R_x}]\rangle$. Thus, we can identify an adiabatic current operator

$$J^A_{R_x} = i[K, \vartheta_{R_x}]. \tag{3.92}$$

As before, we can localise this operator to extract only the current hopping to and from a position $\mathbf{r}$ according to

$$J^A_{R_x}(\mathbf{r}) = \frac{1}{2}\{\delta_{\mathbf{r}}, J^A_{R_x}\}. \tag{3.93}$$

In Appendix B.2 we discuss carefully how the non-adiabatic expression for current relates to the adiabatic form as we approach the adiabatic limit.

3.3.4 Marker Derivation

Before we give the formal derivation, let us describe the physical intuition behind our topological marker, which can be understood as a localised version of the Hall conductivity. The standard Hall conductivity is measured by applying a uniform electric field to a 2D material and measuring the current induced perpendicular to the field. This current is quantised and corresponds to the Chern number of the Hamiltonian [18]. A disadvantage of this calculation is that it is necessarily global, with the electric field uniform over the system and the current measured across the whole sample. In a material with disorder or compound structure, the calculation gives no spatially-resolved information about its topological properties.

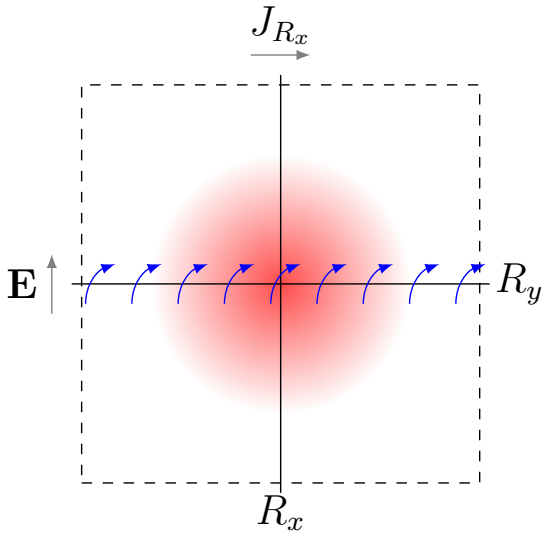


Figure 3.12: A schematic for local Hall measurement. The bottom half of the system has its potential raised with respect to the top half, generating an electric field acting over the horizontal line. Current is measured between the left and right halves, across the vertical line. The flow of charge is represented in blue, showing the curved path due to the presence of a magnetic field. The red shading shows the region around the crosshair where a nonzero contribution to the marker is measured.

Our objective is to find an analogous quantity that can be spatially resolved, giving information about which parts of a complex material are responsible for topological behaviour. It is not obvious how one should localise the Hall conductivity: neither the electric field, nor the current operator can be easily localised to a point. Maxwell's laws prohibit one from creating an electric field at a single point only. Equally, on the lattice, it is difficult to write down a consistent expression for current at a point.

Despite that fact that neither electric field nor current can individually be made local to a point, it is possible to localise the overall Hall conductance. This is because both field and current can be localised to a line. By partitioning the system, and raising the electric potential of one part, we induce an electric field acting across the dividing line. Similarly, given a partition, by measuring the transfer of electrons from one part to the other, we are able to determine the current across the dividing line.

The route to a local Hall current is to partition the system along two perpendicular dividing lines, as shown in Fig. 3.12. An electric field is induced between the top and bottom parts of the system by uniformly raising the voltage of the lower part. This will induce a vertical current acting across the dividing line. When the material has nonzero Chern number, a Hall current will also be induced from left to right. If the system is insulating (i.e. gapped) we expect that all current should be localised to the region around the horizontal line. Measurement of the current is then taken over the vertical line, catching only induced current in the horizontal direction - effectively only the Hall current. We expect all nonzero contributions to come from the region around the point where the lines cross - motivating the name 'crosshair marker'.

As we shall see in the following examples, this argument fails when the system becomes conducting and the gap closes. In a conducting system, current is no longer locally constrained - an electron can easily tunnel across the entire system. Thus we expect that the marker will be

nonzero even very far from the crosshair. Consequently, as well as the central peak, we expect to see an additional term wherever conducting edge states are present, at any distance from the crosshair.

We measure the local contribution to current across the line $x = R_x$ in the adiabatic regime. The current will be expressed in the form of a conductivity $J = \sigma E$, where σ is to be determined. Our starting point is the expectation value of the current operator defined in §3.3.3.2 for the case of a filled band of states,

$$\left\langle J^A_{R_x}(\mathbf{r})\right\rangle = \frac{1}{2}\mathrm{Tr}\left[P\{\delta_{\mathbf{r}}, J^A_{R_x}\}\right], \tag{3.94}$$

where P projects onto a fully occupied band of states. By cycling terms in the trace and using the identity $\mathbb{1} = P + Q$, we can split this expression into two terms

$$\begin{aligned}\left\langle J^A_{R_x}(\mathbf{r})\right\rangle &= \mathrm{Tr}_{\mathbf{r}}\left(PJ^A_{R_x}P\right)\\ &\quad + \frac{1}{2}\mathrm{Tr}_{\mathbf{r}}\left(PJ^A_{R_x}Q + QJ^A_{R_x}P\right),\end{aligned} \tag{3.95}$$

where $\mathrm{Tr}_{\mathbf{r}} := \mathrm{Tr}(\delta_{\mathbf{r}}\ ...)$ denotes a local trace over the internal degrees of freedom at site $\mathbf{r}$. We treat these two terms separately. The first term is a local marker of Chern number whereas the second term vanishes. Considering only the second term, let us insert the exact form of $J^A_{R_x} = -[[\dot{P}, P], \vartheta_{R_x}]$ and use the Jacobi identity,

$$\begin{aligned}\mathrm{Tr}_{\mathbf{r}}\left(PJ^A_{R_x}Q\right) + h.c. &= \mathrm{Tr}_{\mathbf{r}}\left(P\left[[P,\vartheta_{R_x}],\dot{P}\right]Q\right)\\ &\quad + \mathrm{Tr}_{\mathbf{r}}\left(P\left[[\vartheta_{R_x},\dot{P}],P\right]Q\right) + h.c.\end{aligned} \tag{3.96}$$

Using the identities $P[P,\vartheta_{R_x}] = [P,\vartheta_{R_x}]Q$ and $P\dot{P} = \dot{P}Q$, we see that the first term here vanishes. We are left with the second term which can be written as

$$\mathrm{Tr}_{\mathbf{r}}\left(PJ_{R_x}Q\right) + h.c. = -\mathrm{Tr}_{\mathbf{r}}\left(P[\vartheta_{R_x},\dot{P}]Q\right) + h.c. \tag{3.97}$$

Using $Q = \mathbb{1} - P$, we may re-express this in the form,

$$\mathrm{Tr}_{\mathbf{r}}\left(PJ_{R_x}Q\right) + h.c. = -\mathrm{Tr}_{\mathbf{r}}\left(P[\vartheta_{R_x},\dot{P}]\right) + h.c. \tag{3.98}$$

Now, let us insert the exact form for $\dot{P}$ for a system undergoing adiabatic application of the step-function electric field defined in §3.3.3.1: $\dot{P} = i\dot{A}[\vartheta_{R_y}, P]$. We get a final expression

$$\begin{aligned}&\mathrm{Tr}_{\mathbf{r}}\left(PJ_{R_x}Q\right) + h.c.\\ &\qquad = -i\dot{A}\mathrm{Tr}_{\mathbf{r}}\left(P\left[\vartheta_{R_x},[\vartheta_{R_y},P]\right]\right) + h.c.\end{aligned} \tag{3.99}$$

Writing out the terms in the trace explicitly, we get

$$\begin{aligned}i\mathrm{Tr}_{\mathbf{r}}\left(P\left[\vartheta_{R_x},[\vartheta_{R_y},P]\right]\right) &= i\mathrm{Tr}_{\mathbf{r}}(P\vartheta_{R_x}\vartheta_{R_y}P)\\ &\quad - i\mathrm{Tr}_{\mathbf{r}}(P\vartheta_{R_x}P\vartheta_{R_y})\\ &\quad - i\mathrm{Tr}_{\mathbf{r}}(\vartheta_{R_x}P\vartheta_{R_y}P)\\ &\quad + i\mathrm{Tr}_{\mathbf{r}}(P\vartheta_{R_x}\vartheta_{R_y}).\end{aligned} \tag{3.100}$$

The step functions commute with one another, and with $\delta_{\mathbf{r}}$. This means that every constituent term in Eqn. 3.99 is anti-Hermitian due to the factor of i. Thus the whole expression vanishes when the Hermitian conjugate is added,

$$\mathrm{Tr}_{\mathbf{r}}\left(PJ_{R_x}Q\right) + h.c. = 0. \tag{3.101}$$

Now, let us return to Eqn. 3.95. We have shown that the second term vanishes, so we are left with

$$\begin{aligned}\langle J_{R_x}(\mathbf{r})\rangle &= \mathrm{Tr}_{\mathbf{r}}\left(PJ_{R_x}P\right) &(3.102)\\ &= i\mathrm{Tr}_{\mathbf{r}}\left(P[K,\vartheta_{R_x}]P\right). &(3.103)\end{aligned}$$

We use expression 3.91 to insert the exact form of K

$$\langle J_{R_x}(\mathbf{r})\rangle = i\dot{A}\mathrm{Tr}_{\mathbf{r}}\left(P\vartheta_{R_x}Q\vartheta_{R_y}P\right) + h.c. \tag{3.104}$$

Using the fact that $\dot{A} = -E$, we see that this expectation value has taken the form of a conductance, $\langle J\rangle = \sigma E$. We also use $Q = \mathbb{1} - P$ to get the conductance in the form

$$\sigma(\mathbf{r};\mathbf{R}) = 2\Im\mathrm{Tr}_{\mathbf{r}}\left(P\vartheta_{R_x}P\vartheta_{R_y}P\right). \tag{3.105}$$

Finally we insert a factor of 2π to get the final expression for the marker

$$C(\mathbf{r};\mathbf{R}) = 4\pi\Im\mathrm{Tr}_{\mathbf{r}}\left(P\vartheta_{R_x}P\vartheta_{R_y}P\right). \tag{3.106}$$

This quantity is analogous to the Chern marker presented in appendix C of [30], although where Kitaev used a global trace, here we have a local trace. Kitaev's marker was shown to exactly equal the Chern number in an infinite system. For finite system size, however, his marker vanishes due to edge-state contributions. By replacing the global trace with a local trace, we are here able to separate the bulk contribution from the edge contribution, allowing for the marker to be calculated in a finite system. We can extract the quantised Chern number by only summing over the bulk contributions – found at $\mathbf{r}$ close to $\mathbf{R}$ – and ignoring the edge-state terms at $\mathbf{r}$ far from $\mathbf{R}$. We note two important caveats. Firstly the marker is only strictly well-defined as the sum of the bulk contributions around $\mathbf{R}$, rather than as a function of $\mathbf{r}$. This is because there is a degree of arbitrariness to how the current was made local to a point in definition 3.87, since the purpose is to separate the bulk and edge contributions before summing only the bulk terms. Physically, the summed marker corresponds to the total current measured in the bulk over the line at $x = R_x$. The second caveat is that the adiabatic current defined in Eqn. 3.93 only captures the current generated by the change in P over time. However, it is also possible for a system to have persistent currents, i.e. flow between occupied states that does not change the projector itself. Since this type of circulating current cannot change the number density at any site, it does not contribute to the net flow of electrons into a given region. Despite this, it can still contribute terms to the current defined in Eqn. 3.87. Thus we must also require that the system has no persistent currents at any point in the adiabatic time evolution. This effect is explained in detail in Appendix B.2.

Finally it is worth mentioning that – following the argument presented for Eqn. 3.64 – the

crosshair marker can be used to calculate the Chern marker, $\mathfrak{C}$, given in [33] according to

$$\mathfrak{C}(\mathbf{r}) = \int d^2\mathbf{R}\; C(\mathbf{r};\mathbf{R}), \tag{3.107}$$

where the integral is over the whole system.

Chapter 4

The Amorphous Kitaev Model

After the development of the real-space Chern markers detailed in the previous chapter, it was suddenly possible to precisely characterise the topological properties of a band in a wide variety of disordered – and thus previously somewhat inaccessible – contexts. This led to a number of works analysing bulk invariants and protected edge modes in amorphous insulators [93, 120–124]. However, investigation into amorphous topological physics has been predominantly focused on non-interacting electrons with a few exceptions, for example, to account for the observation of superconductivity in amorphous materials [125–129] or very recently to understand the effect of strong electron repulsion in TIs [130]. Thus, it is worth asking if there are more exotic physical systems where one might be able to similarly characterise the topological properties of a quantum system without crystalline structure. One particularly rich context for finding topological physics is in quantum magnetism, where the properties of amorphous systems have been investigated since the 1960s [131–136]. Generally research has focussed on classical Heisenberg and Ising models, which are able to realise ferromagnetic and disordered antiferromagnetic, as well as spin glass behaviour [68, 69, 137].

However, little work has been done to understand whether it is possible to realise a quantum spin liquid (QSL) phase in an amorphous material. There is good intuitive reason why one might avoid this topic. Amorphous magnets often have glassy physics and the problem of finding even the classical ground state is famously difficult. Such systems have an exponentially large number of local minima, and finding the correct one is usually an NP-hard problem [138] with new numerical techniques still being developed today [139–141]. Thus, one might reasonably expect that the inclusion of quantum fluctuations would do little to ease the intractability of this problem. If one is searching for QSL phases, looking at amorphous systems would seem to be an even more ill-considered idea. Structural disorder is generally expected to undermine the delicate classical degeneracy necessary for spin liquids to form, instead selecting some arbitrary complex classical state as the ground state and destroying the prospect of forming a long-range entangled ground state.

In the case of a geometrically frustrated candidate QSL, such as the kagome antiferromagnet, the classical frustration is a consequence of lattice structure. Thus, there is little reason to expect that the same model constructed on an arbitrary lattice would inherit any interesting properties of the original frustrated-lattice model. In order to find an amorphous QSL, we turn our attention to exchange frustration. Given an arbitrary lattice, we can ask whether it is possible to construct a set of frustrated couplings such that the system has a QSL ground state. One of the paradigmatic examples of an exchange-frustrated QSL is the Kitaev honeycomb model [30]. Here, adjacent spins are coupled with three bond-anisotropic Ising interactions

in the x, y and z directions, which each try to align the spin on the three incommensurate axes. Thus, it is clear that the system has extensive frustration even before considering the geometry of the lattice, making it a promising candidate for realising an amorphous QSL. As we shall review in the following section, Kitaev showed that the model could be exactly solved by transforming to a system of Majorana fermions. In the following years, several instances of Kitaev candidate materials were synthesized [142–145] following the suggestion that heavy-ion Mott insulators formed by edge-sharing octahedra may realise dominant Kitaev interactions [146]. Recently, it has been shown that the Kitaev material Li_2IrO_3 can be created with an amorphous structure [147]. In fact, with sufficiently fast cooling, any crystalline material can be made amorphous [148, 149], opening the possibility for exploring a wide variety of non-crystalline Kitaev materials, although it must be noted that in such materials the strength of the Kitaev-type interaction and suppression of competing couplings generally depends on the geometric details of the lattice around each ion. Thus, distortions in lattice structure will allow perturbing interactions to be introduced into the Hamiltonian that threaten the stability of the Kitaev QSL phase [144, 150, 151].

By now it is well known that the Kitaev model on any three-coordinated ($z = 3$) lattice retains many of the properties that allowed for an exact solution to be constructed in the Honeycomb case. The system retains the conserved plaquette operators and local symmetries that facilitate a mapping onto an effective free Majorana fermion problem in a background of static $\mathbb{Z}_2$ fluxes [152–157]. However, this neither means that any $z = 3$ lattice Kitaev model can be straightforwardly constructed, nor that the QSL properties are obvious. Several obstacles remain. First, the labelling of bonds necessary to create a soluble Hamiltonian can be an NP-complete problem. Second, once the Majorana system has been constructed, determining the ground state out of the exponentially large number of $\mathbb{Z}_2$ flux sectors is generically hard, since Lieb's theorem [158] – which defines the ground state flux configuration for the translationally invariant honeycomb – is not applicable for most lattices. Previous studies have relied on translation and reflection symmetries to reduce the number of sectors that must be checked [156, 159, 160], which cannot be done in an amorphous system. Third, once the ground state flux sector is found, it needs to be determined whether lattice disorder induces a gapless phase [161–163] or whether the fermionic spectrum is gapped, possibly with non-trivial topology [156].

In this chapter we introduce the amorphous Kitaev model and establish it as an example of a topologically ordered amorphous QSL. We start in §4.1 with a review of the Kitaev model on the Honeycomb lattice. We present in detail the transformation from spins to Majoranas, the role of the $\mathbb{Z}_2$ gauge field, the role of time reversal symmetry, the ground-state phase diagram and finally the properties of the Majorana excitations. In §4.2 we turn our attention to the amorphous case. Concentrating on random lattices generated via Voronoi tessellation [93, 121] with $z = 3$, we show how to colour the bonds consistently. We find that the presence of plaquettes with an odd-number of sites lead to a chiral QSL with spontaneously broken time-reversal symmetry (TRS) [156, 164–169] and establish via extensive numerics that the ground state $\mathbb{Z}_2$ flux sector follows a remarkably simple counting rule consistent with Lieb's theorem. We map out the phase diagram of the model and show that the chiral phase around the symmetric point is gapped and characterized by a quantized local Chern number with protected chiral Majorana edge modes. Finally, we discuss the effect of additional bond disorder, showing that the QSL phase is remarkably resistant to local bond-length dependent disorder.

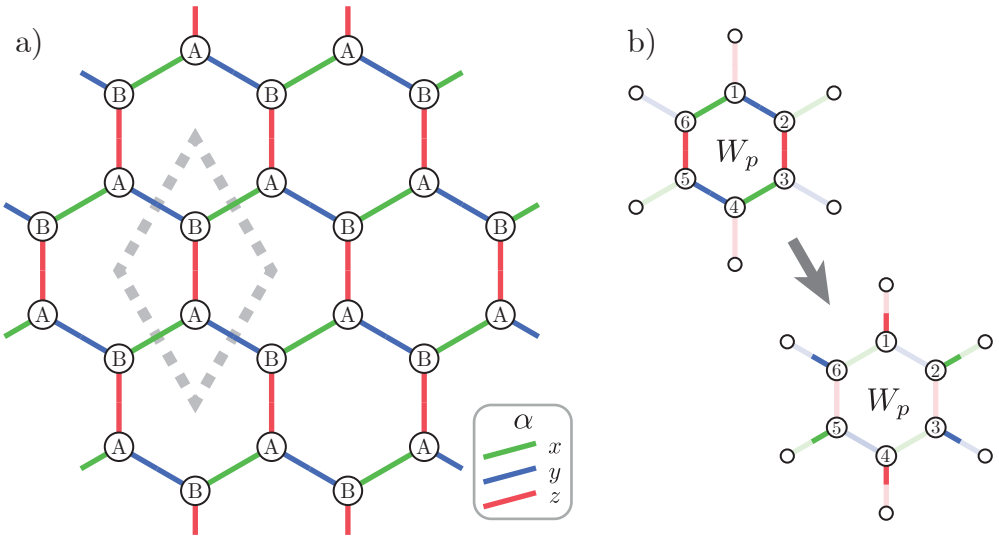


Figure 4.1: **(a)** A section of honeycomb lattice with the bond labels shown according to colour. Sites are labelled according to sublattice. Our choice for the unit cell is marked by the dashed grey rhombus. **(b)** A single W_p operator, where the full-colour lines indicate the bond operators that take part in W_p. After multiplying out the Pauli operators, the remaining terms are shown, corresponding to spin operators that connect outwards from the plaquette. States are numbered to correspond to the ordering in Eqn. 4.3.

4.1 Kitaev's Honeycomb Model

Let us begin by providing a review of the model as it was originally proposed by Kitaev in [30]. We shall present the spin Hamiltonian, as well as the Majorana transformation used to diagonalise it. Following this, we shall discuss the ground-state phase diagram and properties of excitations. In §4.2, we will describe the extension of this model to arbitrary and amorphous lattice geometry. Thus, here we will focus primarily on the aspects of the Honeycomb model that are relevant for the amorphous case.

The Kitaev honeycomb model is defined for a set of spin-half degrees of freedom on the vertices of a honeycomb lattice, as shown in Fig. 4.1a. Note that this lattice is bipartite, so the sites can be organised into two sublattices A and B, where bonds are always between two sites in different sublattices. The bonds in this lattice are labelled with an index $\alpha \in \{x, y, z\}$, such that each site connects to one bond of each type. On each bond, neighbouring spins interact with a bond-directional Ising-type coupling. The Hamiltonian is given by

$$H = -J^x \sum_{x\text{-bonds}} \sigma_j^x \sigma_k^x - J^y \sum_{y\text{-bonds}} \sigma_j^y \sigma_k^y - J^z \sum_{z\text{-bonds}} \sigma_j^z \sigma_k^z, \tag{4.1}$$

where the parameters J^α determine the strength of the x, y and z bonds, and σ_j^α represents a Pauli operator acting on the spin at site j. The exact solution of this model – as with all integrable systems – depends on the presence of an extensive set of conserved quantities, given by the product of the bond operators around a given hexagonal plaquette, p,

$$W_p = \prod_{\langle jk \rangle \in p} \sigma_j^\alpha \sigma_k^\alpha, \tag{4.2}$$

where the order of the σ_j operators is arranged such that they run clockwise around the hexagonal plaquette. Using that standard Pauli multiplication rules, we can show that the product can be simplified into a product of the six Pauli operators that connect outwards from each site on the hexagon. For example, the plaquette shown in Fig. 4.1b has W_p given by

$$W_p = \sigma_1^z \sigma_2^x \sigma_3^y \sigma_4^z \sigma_5^x \sigma_6^y. \tag{4.3}$$

All W_p operators commute with each other and H. Furthermore, we have $W_p^2 = 1$, which means that W_p have eigenvalues ± 1. The Hilbert space has dimension 2^N, where N is the number of spins. Since we have $N/2$ plaquettes in the system, these conserved quantities allow us to split the Hilbert space into $2^{N/2}$ sectors according to the eigenvalues of $\{W_p\}$.

4.1.1 Spins to Fermions to Majoranas

Although the Kitaev model can be solved with a Jordan-Wigner transformation [170–173], here we will follow the original construction in terms of Majorana fermions. The first step is an old trick, often referred to as the parton construction [66, 174, 175]. We introduce a pair of fermion operators for each site, $f_\uparrow^\dagger$ and $f_\downarrow^\dagger$, which create a spin up and spin down state respectively. Spin operators are straightforwardly modified to

$$\sigma^\alpha \to f_\mu^\dagger \sigma_{\mu\nu}^\alpha f_\nu. \tag{4.4}$$

In performing this transformation we have artificially enlarged our Hilbert space, since each site can now host four states. Two of these states are the original spin up and down states, constituting the physical part of the enlarged Hilbert space, $\mathcal{H}_{\text{phys}}$. The other two correspond to no spin at all, or both a spin up and spin down on a single site. These states contribute an unphysical auxiliary Hilbert space $\mathcal{H}_{\text{aux}}$.

$$\begin{aligned} & & f_\uparrow^\dagger |0\rangle = |\uparrow\rangle \quad & \Big\} \mathcal{H}_{\text{phys}} \\ |\downarrow\rangle & & f_\downarrow^\dagger |0\rangle = |\downarrow\rangle \quad & \Big\} \\ & \Rightarrow & & \\ |\uparrow\rangle & & f_\uparrow^\dagger f_\downarrow^\dagger |0\rangle = |\uparrow\downarrow\rangle \quad & \Big\} \mathcal{H}_{\text{aux}} \\ & & |0\rangle = |\varnothing\rangle \quad & \Big\} \end{aligned}$$

We construct a parity operator that determines whether a state is in the physical or auxiliary Hilbert space using a product over fermionic number operators on a single site, $n_{j\mu} = f_{j\mu}^\dagger f_{j\nu}$,

$$D_j = -(1 - 2n_{j\uparrow})(1 - 2n_{j\downarrow}). \tag{4.5}$$

This operator has the property that $D_j |\psi\rangle = +(-) |\psi\rangle$ for states in the physical (auxiliary) Hilbert space. Next let us decompose each fermion into a pair of Majorana fermions according to the following substitution,

$$f_\downarrow = \frac{1}{2}(c + ib^z), \tag{4.6}$$

$$f_\uparrow = \frac{1}{2}(b^y + ib^x), \tag{4.7}$$

where the Majorana operators have standard Majorana commutation relations,

$$c^\dagger = c, \qquad \{c_j, c_k\} = 2\delta_{jk}, \tag{4.8}$$

with the same relations for b-type Majoranas. In this new formalism, a fermionic parity operator becomes

$$icb^z = 2f_\downarrow^\dagger f_\downarrow - 1, \tag{4.9}$$

with the corresponding identity for $f_\uparrow$ using b^y and b^x. Thus, the parity operator D becomes

$$D = b^x b^y b^z c. \tag{4.10}$$

In the Majorana representation, the spin operators take the following form,

$$\sigma^x \to \frac{i}{2}(cb^x - b^z b^y), \tag{4.11}$$

$$\sigma^y \to \frac{i}{2}(cb^y + b^z b^x), \tag{4.12}$$

$$\sigma^z \to \frac{i}{2}(cb^z - b^y b^x). \tag{4.13}$$

This expression can be simplified by requiring that we act only on states in the physical subspace – which satisfy $D\,|\psi\rangle = |\psi\rangle$. First we note that the spin operators preserve the physical subspace since D commutes with any product of two Majoranas on the same site, e.g. $[cb^x, D] = 0$. Any state in the physical Hilbert space satisfies $cb^z b^y b^x\,|\psi\rangle = |\psi\rangle$, which can rearranged into the following identity,

$$cb^z\,|\psi\rangle = -b^y b^x\,|\psi\rangle\,, \tag{4.14}$$

with an equivalent identity for any other pairing of the Majoranas. Thus, we see that when acted *only on the physical subspace* the spin operators may be written as

$$\sigma^x = icb^x, \qquad \sigma^y = icb^y, \qquad \sigma^z = icb^z. \tag{4.15}$$

We are now in a position to transform the Hamiltonian into the Majorana basis. Applying the identities derived above and reordering the Majorana operators, we arrive at the following,

$$H = -\sum_{jk} J_{jk}^\alpha \sigma_j^\alpha \sigma_k^\alpha \to \sum_{jk} J_{jk}^\alpha (ib_k^\alpha b_j^\alpha)(ic_j c_k). \tag{4.16}$$

Note that the Majoranas forming $\hat{u}_{jk} = ib_k^\alpha b_j^\alpha$ appear only once in this Hamiltonian. This means that all $\hat{u}$ operators satisfy $[\hat{u}_{jk}, \hat{u}_{mn}] = 0$ and $[\hat{u}_{jk}, H] = 0$. Furthermore, they satisfy $\hat{u}_{jk}^2 = \mathbb{1}$, ensuring that their eigenvalues are ± 1. Thus, these represent an extensive set of conserved quantities, where we may partition the Majorana Hilbert space according to the eigenvalues of these operators, $u_{jk} = \pm 1$. For a given choice of bond variables, Eqn. 4.16 reduces to a quadratic Majorana Hamiltonian

$$H_u = \frac{i}{4}\sum_{j,k} A_{jk} c_j c_k, \tag{4.17}$$

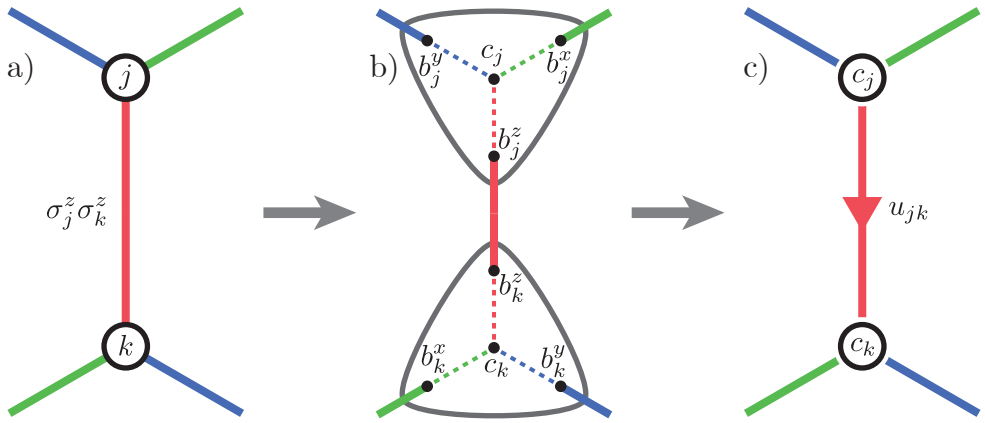


Figure 4.2: A depiction of the three steps in transforming the spin Hamiltonian into a quadratic Majorana Hamiltonian. **(a)** A single z-bond with two spins located at the endpoints, labelled with j and k. **(b)** After the transformation to the Majorana basis each spin becomes a set of four Majorana fermions. On each site, the b^x, b^y and b^z Majorana takes part only in the x, y and z bond respectively. The c-Majorana takes part in all three couplings. **(c)** Once the eigenvalues of the u_{jk} operators have been assigned, we are left with a quadratic Hamiltonian on the c_j degrees of freedom only, with hopping determined by the u_{jk} values, where the arrow indicates the direction in which $u_{jk} = +1$.

where

$$A_{jk} = 2J^\alpha u_{jk}. \tag{4.18}$$

Note that the bond variables satisfy $u_{jk} = -u_{kj}$. Thus, the matrix A is real and antisymmetric. We may graphically represent the bond variables by replacing every edge in the lattice with an arrow, where the arrow depicts the direction in which u_{jk} is positive.

Once a set of $\{u_{jk}\}$ have been chosen, the Hamiltonian H_u can be solved to find the ground state $|\psi_u\rangle$. In general one might expect each distinct set of $\{u_{jk}\}$ to correspond to a unique system and thus a unique ground state, however as we shall see in the next section, the u terms may be understood as a $\mathbb{Z}_2$ gauge field, where the only physical degrees of freedom are the $\mathbb{Z}_2$ fluxes through each plaquette.

4.1.2 Gauge Transformations and Fluxes

Let us consider the effect of the parity operators D_j on our system. Before a set of u_{jk} values are chosen, the Hamiltonian in Eqn. 4.16 satisfies $[D_j, H] = 0$ for $\forall j$. However, once u_{jk} are no longer operators, D_j has the effect of flipping the sign of u on the three bonds that connect to site j, since

$$D_j u_{jk} c_j c_k D_j = -u_{jk} c_j c_k. \tag{4.19}$$

Thus, the effect applying a set of D_j on some subset of sites ($j \in \mathcal{S}$) is to transform to a new set of bond operators $\{u\} \to \{u'\}$, where every bond that touches one flipped site has $u'_{jk} = -u_{jk}$. We can represent this pictorially by drawing a loop the sites on which D_j are applied and flipping the value of u on every bond that intersects the loop. This is shown by the pink loops

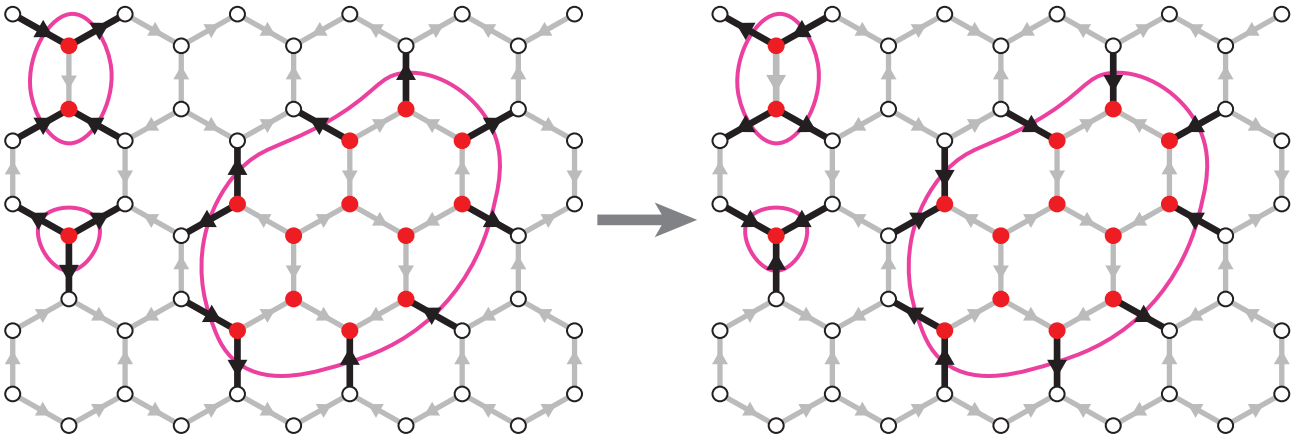


Figure 4.3: A depiction of a gauge transformation. We start with the configuration of $\{u_{jk}\}$ shown on the left. Now we apply a gauge transformation to the system by applying D_j operators to all sites in some subset $\mathcal{S}$, here coloured red. All bonds that connect to one red site have the sign of u flipped. Bonds between two red sites are flipped twice, and so remain invariant. The flipped bonds are highlighted. This is pictorially represented by the pink loops that encircle all the red sites. Any bond that crosses a pink loop has u_{jk} flipped.

in Fig. 4.3. The transformation effected by D_j has no effect on the spectrum of H_u, thus we may interpret D_j as a gauge transformation, transporting us to a different set of $\{u_{jk}\}$ that represents the same physical system.

Proof that D_j leaves the spectrum invariant — This can be seen by examining how the A matrix is changed in Eqn. 4.16. A single D_j operator's effect on A can be represented as

$$A \to RAR, \tag{4.20}$$

where R is a diagonal matrix given by

$$R_{ii} = \begin{cases} +1 \text{ for } i \neq j, \\ -1 \text{ for } i = j. \end{cases} \tag{4.21}$$

Clearly, R is a unitary matrix, so the spectrum of A is unaffected. Thus, the spectrum of H_u is the same as the spectrum of $H_{u'}$

Since H_u is not invariant under the action of D_j, the ground state $|\psi_u\rangle$ does not live in the physical Hilbert space. To construct a physical state we must apply a projector onto $\mathcal{H}_{\text{phys}}$, given by

$$P = \prod_j \frac{1 + D_j}{2}. \tag{4.22}$$

From the form of P, we see that the physical state $|\psi_{\text{phys}}\rangle = P\,|\psi_u\rangle$ is found by taking an equal superposition of every possible gauge-equivalent arrangement of $\{u_{jk}\}$.

The above argument does not imply that *all* sets of u_{jk} are equivalent. To see why, let us

construct a gauge-invariant quantity – the $\mathbb{Z}_2$ flux through each plaquette p,

$$\phi_p = \prod_{(j,k)\in p} -iu_{jk}, \tag{4.23}$$

where the product is taken over the u_{jk} values going clockwise around each plaquette. The gauge invariance of this can be seen clearly from Fig. 4.3. An individual D_j operator flips three adjacent bonds, so will always flip the values of two bonds on a given plaquette, leading to an overall factor of $(-1)^2$ – the flux therefore remains invariant. For a more general gauge transformation including multiple sites, we flip the bonds that intersect a closed loop, (shown in pink in Fig. 4.4). These closed loops must both enter and exit a given plaquette, so again will contribute a factor of $(-1)^2$ to any flux.

In fact, the plaquette flux defined here is identical to the conserved quantity defined in Eqn. 4.2 which can be seen by applying the substitution in Eqn. 4.15 to the definition of W_p. Thus, gauge inequivalent sectors of the Hilbert space may be labelled by the values of $\phi_p = \pm 1$ through each plaquette. In order to change the flux through a given plaquette, we perform a line of flips that terminates at the plaquette, as shown in Fig. 4.4a. Such a change to the bond operators can never be achieved with a gauge transformation. Thus, in periodic boundary conditions, it is only possible to flip ϕ_p in pairs, however in an open or infinite system we may flip a single flux with a line that starts at that plaquette and extends to the boundary of the system, or to infinity. In this case, the other Majorana zero mode is created at the boundary, or at infinity for an unbounded system.

Finally, we note that in periodic boundaries every flux sector is fourfold degenerate. This is because one may flip a line of u_{jk} that wraps the system in either the x or y-direction, producing a new flux sector that has identical values of ϕ_p, but is not gauge equivalent to the starting state. To measure this, we may construct a pair of global fluxes Φ_x and Φ_y, by taking a product of bond operators around a loop L_x or L_y that wraps the system in the x or y direction

$$\Phi_\alpha = \prod_{(j,k)\in L_\alpha} -iu_{jk}, \tag{4.24}$$

as shown in Fig. 4.4b.

4.1.3 Time Reversal Symmetry

Here, we add a brief comment about the effect of time reversal symmetry (TRS) in our system. In the original spin-formulation, time reversal is performed by applying the following anti-unitary operator to each spin,

$$\hat{T} = \mathcal{K}(-i\sigma^y), \tag{4.25}$$

where $\mathcal{K}$ denotes complex conjugation. This operator satisfies

$$\hat{T}\sigma_j^\alpha \hat{T}^{-1} = -\sigma_j^\alpha. \tag{4.26}$$

Thus, the Hamiltonian (Eqn. 4.1) is manifestly TRS invariant, since every term contains two spin operators. In the Majorana basis, time reversal is defined as

$$\hat{T} = \mathcal{K}, \tag{4.27}$$

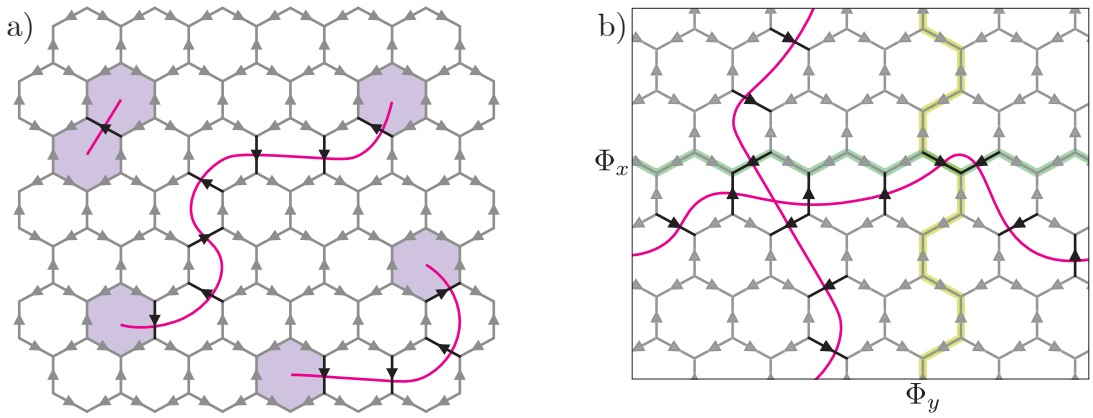


Figure 4.4: **(a)** An example of a bond operator flip that corresponds to the creation of six fluxes. We start with a constant background (shown by the grey edges) where every plaquette has flux $+1$. On this background we flip three sets of bonds (in black). Each of these sets forms a line, where the flux of the coloured plaquettes at each end has been flipped to -1. **(b)** An example of flipping bonds along two non-contractible loops in periodic boundary conditions. Each of these flips transports the system to a gauge inequivalent set of bond operators, resulting in a four-fold degeneracy for each flux sector.

and does not change any of the Majorana operators,

$$\hat{T}c_j\hat{T}^{-1} = c_j, \qquad \hat{T}b_j\hat{T}^{-1} = b_j. \tag{4.28}$$

This means that the Majorana Hamiltonian is not obviously TRS invariant, since the time reversal operator has the property

$$\hat{T}iu_{jk}c_jc_k\hat{T}^{-1} = -iu_{jk}c_jc_k, \tag{4.29}$$

so has the effect of flipping all bond operators in the system, $u_{jk} \to -u_{jk}$. On a bipartite system such as the Honeycomb this has no measurable effect, since we can flip all bonds back by applying a gauge transformation D_j to every spin on the A sublattice. The time reversed Hamiltonian is gauge equivalent to the original Hamiltonian. In general, provided the Majorana Hamiltonian has no coupling between two sites on the same sublattice, it is guaranteed to respect TRS. The only way to break TRS is thus to introduce a next-nearest neighbour coupling that acts between pairs of sites on the same sublattice. This is just a restatement of the fact that chiral symmetry (or sublattice symmetry) satisfies $\mathcal{C} = \mathcal{PT}$. Since the system already has particle-hole symmetry (iA is pure imaginary), chiral symmetry necessarily implies time-reversal symmetry.

4.1.4 Solving the Hamiltonian

Once a flux sector has been chosen, we are left with a Majorana Hamiltonian, H_u, as defined in Eqn. 4.17. The full methodology for diagonalising such a Hamiltonian is detailed in Appendix D.1 – we present only the broad strokes here. We diagonalise the Hamiltonian by rotating to a new Majorana basis consisting of pairs of operators $\tilde{c}$.

$$\tilde{c}_j = O_{jk}c_k, \tag{4.30}$$

where O is a real orthogonal matrix. Since the iA_{jk} matrix is pure imaginary, energies come in pairs, meaning that we can pair up the diagonalising Majoranas as $\tilde{c}'_j, \tilde{c}''_j$, In this basis the Hamiltonian takes the form

$$H = \sum_j \varepsilon_j \, i\tilde{c}'_j \tilde{c}''_j. \tag{4.31}$$

Each of these paired sets of Majorana operators may now be transformed back to a new fermionic basis according to the identity $i\tilde{c}'_j\tilde{c}''_j = 2f_i^\dagger f_i - 1$. Thus, the Hamiltonian becomes

$$H = \sum_j \varepsilon_j \, (2f_i^\dagger f_i - 1). \tag{4.32}$$

The ground state energy can now be read directly from the Hamiltonian, since it corresponds to leaving every fermionic state unoccupied.

$$E_{\text{g.s.}} = -\sum_j \varepsilon_j. \tag{4.33}$$

For each eigen-energy, there exists a fermionic excitation, created by applying the corresponding $f_j^\dagger$ to the ground state, with energy cost $2\varepsilon_j$.

In practice, it is often unnecessary to find the real orthogonal matrix O, and corresponding Majorana modes. If one is solely concerned with the fermionic spectrum – that is, the values of ε_j – one can simply diagonalise the Hermitian matrix iA. This matrix has particle hole symmetry, so the eigenvalues come in pairs $\pm\varepsilon_j$ where ε_j correspond exactly to the energies of the fermionic modes given above.

In a system with n_p plaquettes, we have 2^{n_p} possible flux sectors (2^{n_p-1} in periodic boundaries), and in general it is a non-trivial task to determine which flux sector corresponds to the lowest ground state energy. However, on the honeycomb lattice the ground state was shown by Lieb to be found by setting $\phi_p = +1$ for all plaquettes [158]. Thus, the ground state can always be found by bipartitioning the sites into an A and B sublattice, and setting the bond operators such that u_{jk} always points from each A site towards its three neighbouring B sites (this was the 'background' flux sector depicted in Fig. 4.4). In the following, we shall refer to this flux configuration as the *canonical flux sector.*

Thus, we see that our interacting spin system has been divided into two separate degrees of freedom: a 'classical' $\mathbb{Z}_2$ flux degree of freedom corresponding to the bond operators and plaquette fluxes, and a fermionic degree determined by the Majorana spectrum in a given flux sector. In what follows we will distinguish between these two aspects as the 'flux' and 'fermionic' properties of the system. For example, the flux gap is defined as the difference in energy between the ground state in the canonical sector and the ground state energy in any other flux sector. The fermionic gap, however, is determined by the lowest fermionic energy ε_j in the canonical flux sector.

4.1.5 The Ground-State Phase Diagram

We finish this review with a brief discussion of the ground-state phase diagram, which we shall explore by varying the three J^α parameters. Changing the sign of each individual J^α has no effect on the system, since a change in sign can always be countered by flipping the value of all

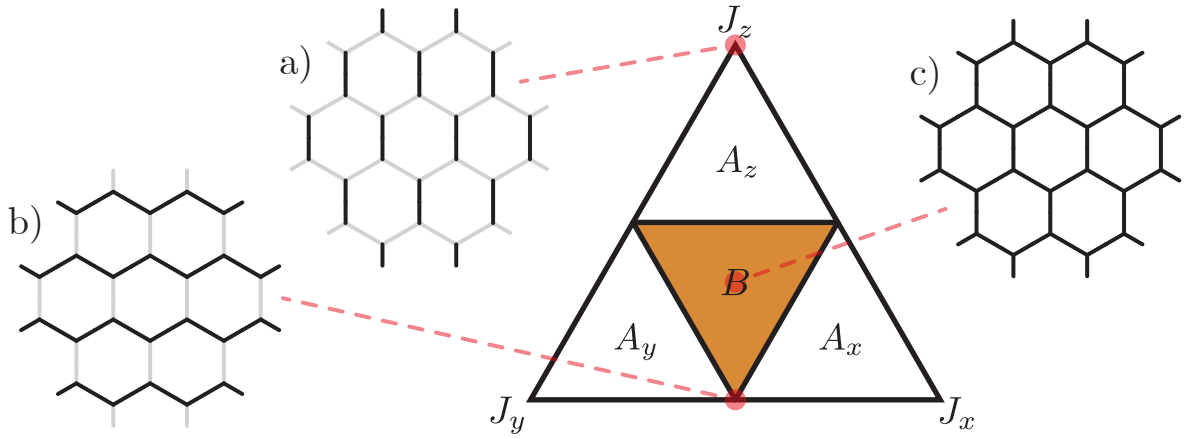


Figure 4.5: The Honeycomb model phase diagram, shown as a function of the three J^α parameters. Three limiting cases are depicted. **(a)** Close to the corners of the triangle, one set of bonds is much stronger than the other two. Thus, the system effectively dimerises on the strong bonds, with the remaining two couplings acting on the dimerised sites as a weak perturbation. **(b)** In the centre of one of the sides of the triangle, two sets of bonds are much stronger than the third. In this case, the system decomposes into a set of disconnected chain models, which individually have gapless dispersion. The remaining coupling serves to weakly couple adjacent chains. **(c)** At the centre of the triangle all bonds are equally strong, and the system is in some sense maximally frustrated. Around this point we have a gapless phase. If a magnetic field is used to open a gap, the system forms a quantum spin liquid phase, which supports anyon excitation with non-Abelian braiding statistics.

u values on the corresponding bonds. A completely general two-dimensional phase diagram can be constructed by considering only values of J^α on the triangle defined by $\sum_\alpha J^\alpha = 1$, $J^\alpha \geq 0$.

In the canonical flux sector, the Hamiltonian (Eqn. 4.17) has translational symmetry. Thus, the fermionic spectrum can be calculated by transforming to momentum space, obtaining a Bloch Hamiltonian of the form

$$iA(\mathbf{q}) = \mathbf{d}(\mathbf{q}) \cdot \boldsymbol{\sigma}, \tag{4.34}$$

defined by the Pauli vector,

$$\mathbf{d}(\mathbf{q}) = -\begin{pmatrix} J^x \sin q_x + J^y \sin q_y \\ J^x \cos q_x + J^y \cos q_y + J^z \\ 0 \end{pmatrix} \tag{4.35}$$

The phase diagram of this Hamiltonian has two distinct sectors determined by whether the Pauli vector defined above sweeps over the origin or not, shown in Fig. 4.5. Around each corner of the triangle, in the regime where one of the J parameters is larger than the sum of the other two, $iA(\mathbf{q})$ defines a gapped system, which we label as the A_α phase. When the J-parameters satisfy $J^\alpha \leq J^\beta + J^\gamma$ for all permutations of indices, the dispersion has two Dirac cones, and the system is in a gapless phase, which we label the B phase.

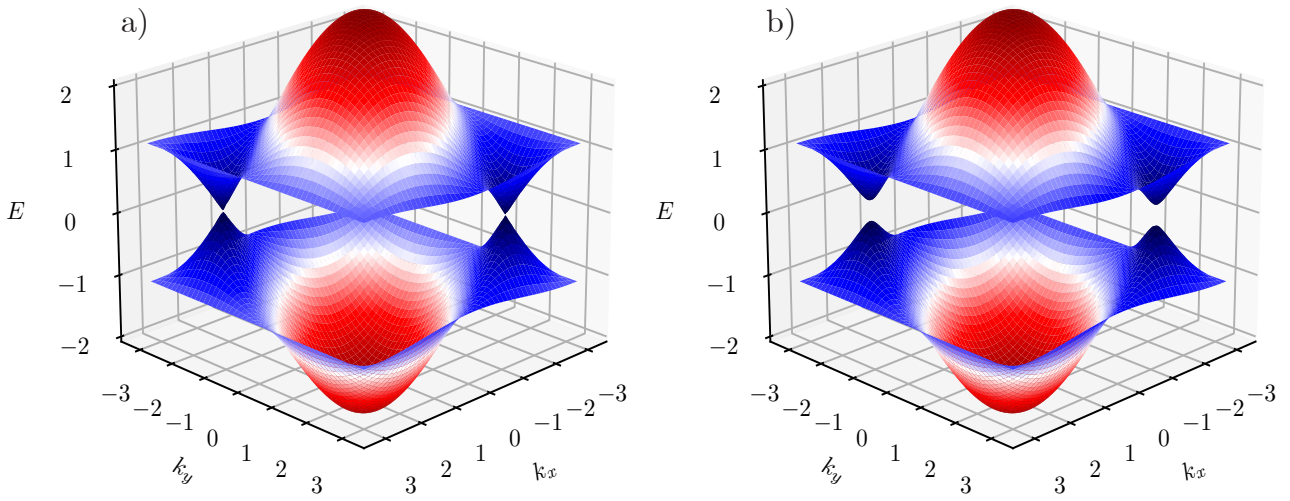


Figure 4.6: The effect of a magnetic field on the band structure of the Majorana Hamiltonian in the B phase, with $\mathbf{J} = (1, 1, 1)$. **(a)** Band structure of the gapless B phase, where the two dirac cones can be seen. **(b)** Band structure of the model with a magnetic field added with $\kappa = 0.2$, leading to the formation of a band gap.

4.1.5.1 The Gapped *A* Phases

The three gapped phases are best understood by considering the model very close to the corners of the triangle. Here, one of the couplings is orders of magnitude stronger than the other two. For example, in Fig. 4.5a, we depict the limit $J^z \gg J^y, J^x$. Let us consider without loss of generality this limit. Here, the Hamiltonian may be treated using perturbation theory, where the x and y-bonds are treated as a perturbation of a ground state calculated only from the z-part of the Hamiltonian.

Since the $\sigma^z\sigma^z$ couplings dominate, we expect the two spins on each bond to arrange into a $|\uparrow\uparrow\rangle$ or $|\downarrow\downarrow\rangle$ configuration, thus effectively combining, forming a single spin on each z-bond. Each of these effective spins is then coupled to four neighbours with $\sigma^x\sigma^x$ and $\sigma^y\sigma^y$ interactions – forming a square lattice. Here we will omit a full discussion of the perturbation theory, however it was shown that this model can be exactly mapped onto the toric code Hamiltonian at lowest order in perturbation theory [30, 176–179]. Thus, this phase inherits the properties of the toric code, including the presence of Abelian anyonic excitation.

4.1.5.2 From the Gapless to the gapped *B* Phase

Around the centre of the phase diagram all J^α are comparably strong, so the system can be considered maximally frustrated, and thus the best candidate for a strongly entangled ground state. In this phase the fermionic Hamiltonian is gapless, and so excitations have long-ranged spatial extent, so cannot be sufficiently separated to have well-defined exchange statistics. Thus, let us introduce a small perturbation capable of gapping out the Dirac cones in the dispersion relation of Eqn. 4.34.

Any perturbation that respects time reversal symmetry is unsuitable for this task. This is because, as we discussed in §4.1.3, a time-reversal symmetric perturbation can only introduce couplings

between an A site and a B site. For a Bloch Hamiltonian of the form $iA(\mathbf{q}) = f_x(\mathbf{q})\sigma^x + f_y(\mathbf{q})\sigma^y$, such a perturbation will only serve to modify the form of f_x and f_y, shifting the position of the Dirac cones in phase space. However, the Pauli vector will remain confined to the x-y plane, so a small perturbation will not be sufficient to prevent it from crossing the origin as it sweeps out the full Brillouin zone. Rather, we must introduce a perturbation that breaks TRS, and couples pairs of A or B sites. This introduces a σ^z-type term to the Bloch Hamiltonian. One example of such a perturbation corresponds to applying a weak magnetic field to our system. A straightforward magnetic field term of the form $V = h_\alpha \sigma^\alpha$ destroys the integrability of the system, however using perturbation theory one can construct an effective magnetic field term that respects it. The lowest term in perturbation theory that breaks TRS is found at third order [30], given by a term of the form

$$V_{\text{eff}} = -\kappa\, \sigma_j^x \sigma_k^y \sigma_l^z, \tag{4.36}$$

with $\kappa = \frac{h_x h_y h_z}{J^2}$, acting over adjacent triples of sites. We shall omit the details of this calculation since it shall not be relevant to the amorphous case. Rather we just state the result, which is that the perturbation has the effect of introducing a complex next-nearest neighbour coupling to the Majorana Hamiltonian, such that the Pauli vector is modified to

$$\mathbf{d}(\mathbf{q}) = -\begin{pmatrix} J^x \sin q_x + J^y \sin q_y \\ J^x \cos q_x + J^y \cos q_y + J^z \\ 4\kappa[\sin q_x - \sin q_y + \sin(q_x - q_y)]. \end{pmatrix} \tag{4.37}$$

As can be seen in Fig. 4.6, this perturbation is enough to gap the two Dirac cones.

4.1.6 The Chern Number

We finish the review of the Honeycomb model by discussing the topological properties of the model in the A and B phases. This has two parts. First we will consider the Chern number of the Majorana Hamiltonian in each case, before discussing the effect of the Chern number on the fractionalised excitations of the model in the B phase.

In this model, the Chern number is calculated as a property of the fermionic Hamiltonian, defined by the matrix iA. Of course, we could explicitly calculate the Chern number using the machinery presented in §2.1. However, we can instead infer the Chern number directly from the form of the $\mathbf{d}(\mathbf{q})$ vector that defines the Bloch Hamiltonian, given by Eqn. 4.35. This is because – as discussed in §2.1.3 – in a two-level system we can find the Chern number by just counting the number of times the surface swept out by $\mathbf{d}$ encloses the origin. In the A phases, this surface is confined to the x-y plane. Furthermore, since the system is gapped, $\mathbf{d}$ does not ever cross the origin. This means that the surface cannot enclose the origin and thus the A phase has $\mathcal{Q} = 0$. In the B phase, $\mathbf{d}(\mathbf{q})$ is also confined to the x-y plane, and crosses the origin at two points in phase space, which we label with $\mathbf{q}_*$ and $-\mathbf{q}_*$, since they are related by reflection over the origin. Once the magnetic perturbation is added, we find that $\mathbf{d}$ is shifted away from the origin in the z-direction at these two points. Furthermore, the z-position, given in Eqn. 4.37 is an odd function of $\mathbf{q}$. This ensures that one of the Dirac cones is gapped with $\mathbf{d}$ avoiding the origin with positive d_z, whereas the other Dirac cone is gapped with $\mathbf{d}$ avoiding the origin with negative d_z. Thus, the surface swept out by $\mathbf{d}$ encloses the origin once, and the Chern number in this phase is given by $\mathcal{Q} = \pm 1$, where the sign is determined by the sign of κ.

When the Chern number is odd, i.e. when it is ± 1, the presence of a flipped plaquette binds a

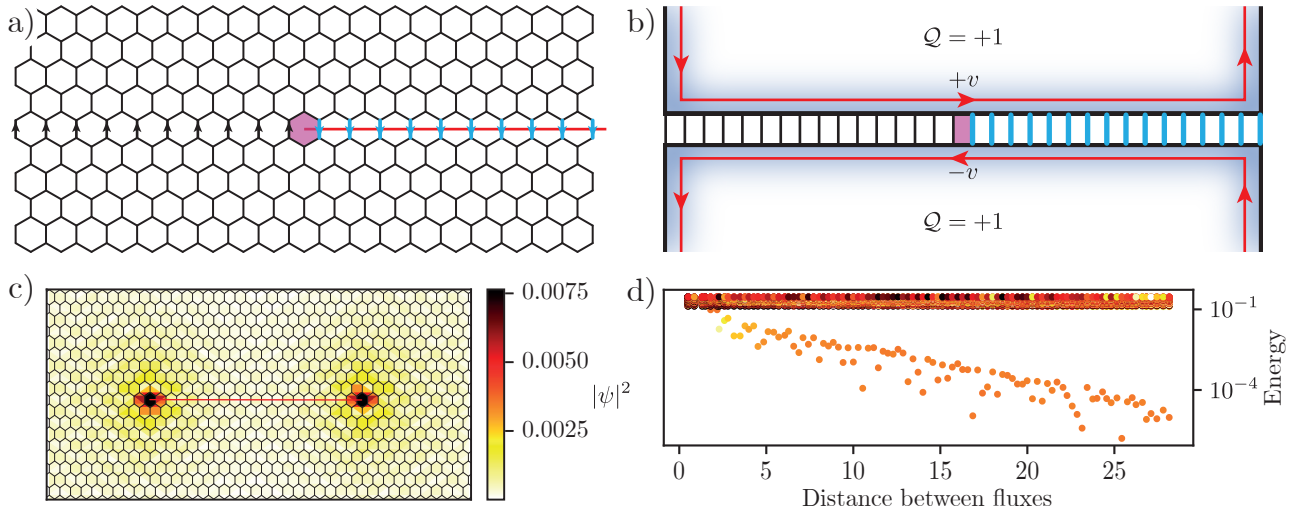


Figure 4.7: **(a)** A single flux (shown in purple) is created in an infinite honeycomb model by flipping a line of bond operators starting at the flux and extending horizontally to infinity. **(b)** The system in subplot (a) can be rewritten as a pair of Chern insulators which are then coupled together using the remaining horizontal line of bonds. Each of the two systems contributes an edge mode travelling with velocity $\pm v$ at the boundary, shown in red. **(c)** A pair of fluxes is flipped with respect to the ground state in a Kitaev model at the isotropic point with $\kappa = 0.0025$. The local number density of the Majorana bound state is shown by the colourmap. **(d)** Plot showing the energies of the states in the Kitaev model with the same parameters as in (c). Each set of points corresponds to the system with a pair of flipped fluxes at some given separation shown in units of the spacing between a pair of plaquette centres, showing how the energy of the Majorana modes decays exponentially with the distance between fluxes.

Majorana zero mode around that plaquette. A rigorous proof of this statement is provided by Kitaev in Appendix C of [30], which we shall not restate. Rather, let us provide an intuitive argument for why this must be the case. The first step is to turn our Majorana Hamiltonian into an equivalent fermionic system. This is done by overlaying two copies of the system, labelled with c'_j and c''_j respectively, without coupling them to one another. Thus, the Hamiltonian (Eqn. 4.17) becomes

$$H = \frac{i}{4} \sum_{jk} A_{jk} (c'_j c'_k + c''_j c''_k). \tag{4.38}$$

By constructing a fermion operator as $a_j = \frac{1}{2}(c'_j + i c''_j)$, we can then rewrite this as

$$H = \sum_{jk} i A_{jk} a^\dagger_j a_k. \tag{4.39}$$

Thus, the system has become a straightforward fermionic hopping hamiltonian. Note that because the hopping matrix iA_{jk} is pure imaginary, the Hamiltonian anti-commutes with the complex conjugation operator, so has particle-hole symmetry. Since the hopping Hamiltonian is changed only by a factor of four, the Chern number we calculated for the Majorana case is the same for the doubled fermion system – this Hamiltonian is just a standard Chern insulator!

Now, let us consider the spectrum of the system with a single flipped plaquette in the centre, as

shown in Fig. 4.7a, which has been created by flipping a horizontal line of spins that starts at the plaquette and extends to infinity. To see how a bound state arises, let us consider creating this system by sandwiching together two Chern insulators. We divide the system such that the line of flipped bond operators lies along the seam between the two halves, meaning that each Chern insulator is individually clean and uniform. Thus, the flipped plaquette is found in between the two halved systems. Now, in order to couple the two systems together, let us introduce hoppings between the two systems such that the coupling parameter changes sign as it crosses the flipped plaquette, as shown in Fig. 4.7b.

Before the coupling is introduced, each Chern insulator must have a single edge mode propagating along the boundary. Furthermore, as we showed in §2.2.1, we can expect that this edge mode will have linear dispersion as it crosses the Fermi energy. Thus, in the long-wavelength limit, we may approximate the Hamiltonian for the edge mode as $H \approx -iv\partial_x$, where v is a parameter that determines the group velocity of the edge mode. On the upper Chern insulator, the velocity will be positive, and on the lower insulator the velocity will be negative. Thus, the effective Hamiltonian describing the two uncoupled edge modes is given by

$$H = -iv\sigma^z\partial_x. \tag{4.40}$$

Now let us introduce the coupling between the two half-systems. Since we must respect the overall particle-hole symmetry of the system, the only allowed coupling must be proportional to σ^y – the Hamiltonian must remain pure imaginary and antisymmetric. Thus, the overall Hamiltonian is equivalent to the Jackiw-Rebbi model [180],

$$H = -iv\sigma^z\partial_x + \mu(x)\sigma^y, \tag{4.41}$$

where $\mu(x)$ is a parameter that changes sign exactly at the point where the flux is placed, let us assume that μ is $+1$ on the left and -1 on the right. The existence of a zero mode can be determined by finding a solution to $H|\psi\rangle = 0$, which is straightforwardly given by a state of the form $|\psi\rangle = \mathcal{N}e^{\pm\frac{x}{v}}|-\rangle$, where the sign in the exponential changes depending on whether x is to the left or right of the flux. Thus, we have an exponentially localised zero mode appearing. In general, such a mode will always appear anywhere that the sign of μ changes.

As we have seen, the fermionic Chern insulator binds a single fermionic zero mode, exponentially localised around the plaquette with a flux threaded through. All that remains is to remember that the fermionic system was really composed of two uncoupled Majorana systems. This means that the fermionic operator representing the zero mode can now be split back into two Majorana modes, $a_0 = \frac{1}{2}(c_0' + ic_0'')$. Each of these Majoranas must reside on one of the two overlaid systems, so we see that in the original Kitaev model, a $\mathbb{Z}_2$ flux excitation will always bind a Majorana zero mode, provided that the system has an odd Chern number. In Fig. 4.7c, we show an example of two fluxes, with the local density of the Majorana mode around each flux, and in Fig. 4.7d we show how the energy of the flux-bound Majoranas decreases exponentially as the distance between fluxes is increased.

4.2 The Amorphous Kitaev Model

Let us now consider the extension of the Kitaev honeycomb model to arbitrary lattice geometry. Remarkably, many of the techniques discussed in §4.1 carry over straightforwardly to the amorphous case – including the conserved plaquette operators and their associated local

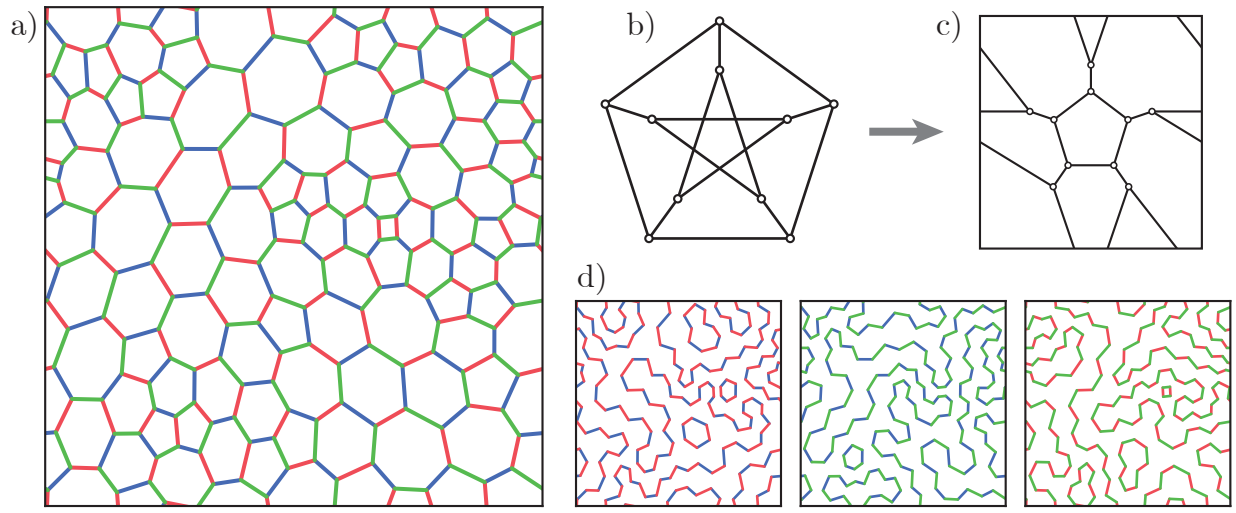


Figure 4.8: **(a)** An example of a Voronoi lattice with a valid three edge colouring. **(b)** The Peterson snark, the first example of a non-edge-colourable cubic graph. **(c)** In periodic boundaries, the Peterson snark can be rearranged into a planar graph. **(d)** Three examples of the coloured lattice from subfigure (a), each with one of the three sets of edges removed, revealing the loop structure of each pair of edge labels.

symmetries (the W_p/ϕ_p quantities) [152, 153], as well as the general process for mapping onto an effective free Majorana system. Two complications arise that we shall discuss in detail. First, the labelling of bonds necessary to create a soluble Hamiltonian is an NP-complete problem. Second, finding the ground state flux sector out of the exponentially large number of $\mathbb{Z}_2$ flux sectors is generically hard since Lieb's theorem no longer applies [158].

In this section we will present the full procedure for constructing and solving the Kitaev model on an amorphous lattice, and demonstrate that the model forms a robust quantum spin liquid phase over a wide variety of lattice geometries. We show how the Hamiltonian may be defined on any lattice with coordination number $z \leq 3$,[1] including how assign a σ^α labelling to the bond operators to ensure that it remains integrable. We consider the structure of the $\mathbb{Z}_2$ gauge field, finding that the presence of plaquettes with an odd-number of sites lead to a chiral QSL with spontaneously broken time-reversal symmetry (TRS) [156, 164–169]. Next, we provide a careful analysis of how the fermionic ground state energy depends on the $\mathbb{Z}_2$ flux sector, showing how the energy may be understood in terms of an expansion over closed loops in the system, where the lowest order terms hint at a solution of the general Lieb's theorem. We provide numerical evidence that the ground state flux sector follows a remarkably simple counting rule consistent with Lieb's theorem [158]. Finally, we map out the phase diagram of the model and see that the chiral phase is generally gapped and characterized by a quantized Chern number as well as protected chiral Majorana edge modes.

4.2.1 Setting up the Model – Bond Colouring

Let us begin, as we did in §4.1, by defining the Hamiltonian. We work with a system of spin $\frac{1}{2}$ on the vertices of an arbitrary lattice where each bond has been labelled with an index $\alpha \in \{x, y, z\}$ – henceforth we will refer this these labels as a bond colouring. The Hamiltonian is written

[1] Although exceptions exist, some lattices exist that cannot be coloured, see Fig. 4.8b and Fig. 4.8c.

identically as in the honeycomb case,

$$H = -\sum_{\langle jk \rangle_\alpha} J^\alpha \sigma_j^\alpha \sigma_k^\alpha \tag{4.42}$$

As before, plaquettef operators can be defined by taking the product of bond operators around a given plaquette p. In order for all plaquette operators to commute with one another and the Hamiltonian, the colouring must be chosen such that no vertex connects to more than one bond of each type. Thus, we restrict our investigation to lattices in which every vertex has coordination number $z \leq 3$. Here we generate such lattices using Voronoi tessellation, as described in §A, an example of a coloured Voronoi lattice is shown in Fig. 4.8a.

The problem of finding such a colouring on a three-coordinated lattice was first studied in the late 19th century by Scottish physicist Peter Tait in an unsuccessful attempt at solving the famous four-colour theorem. Tait proved that the problem of finding a 3-edge colouring was equivalent to finding a four-colouring of the faces [181], detailed in Appendix C. The four-colour theorem was proved 100 years later [182], so we have the guarantee that in open boundaries every planar cubic graph is 3-edge colourable. On the torus, both Tait's proof and the four-colour theorem fail, a face colouring can take up to seven colours [183]. In the graph theory literature, a cubic graph that cannot be 3-edge coloured is called a snark, the most famous of which being the Peterson snark. As a consequence of the four-colour theorem, all snarks must be non-planar, however the Peterson snark can be made planar on the torus, shown in Fig. 4.8. Thankfully, in practice we shall find that snarks on the torus are extraordinarily rare – when working on this project we never encountered an un-colourable Voronoi lattice.

Of course, it is not sufficient to simply state that a colouring exists – a process is necessary for colouring an arbitrary lattice. The 3-edge colouring problem is one of the canonical examples of an NP-complete problem [184], so no polynomial-time algorithm can be used to find a valid colouring. In order to solve this, we map the colouring problem onto a boolean-satisfiability problem, which is then solved using the open-source solver `MiniSAT` [185].

Although one might expect such an NP-complete problem to be computationally demanding to solve, we found that this process generally required little computing power. This is due to the fact that, on the lattices considered, there are many valid colourings to choose from. To illustrate this, note that given a colouring it is always possible to generate a new colouring. This can be done, as shown in Fig. 4.8d, by considering two colours only. If bonds with the third colour are removed, we see that the lattice separates into a series of loops of even length, which are alternatingly coloured. For each individual loop, we may swap the two colours leaving the rest invariant. Doing this will generate a new colouring as well as changing the loop structure for the other two pairings. Thus, this process can be repeated for different pairs of colours and loops, each time generating completely inequivalent colourings. In fact, by considering a set of randomly generated lattices, some rough numerics indicate that the number of valid colourings grows with the exponential of system size according to $n_{\text{colourings}} \sim 3^{0.13 n_{\text{sites}}}$, compared to the total number of colourings which scales as $3^{2n_{\text{sites}}}$.

4.2.2 Fluxes on an Amorphous Lattice

Once the lattice has been constructed and colouring has been found, the amorphous Hamiltonian can be diagonalised using the same procedure as that for the honeycomb model, described in §4.1.1. We transform each spin into four Majorana degrees of freedom, resulting in a Hamiltonian

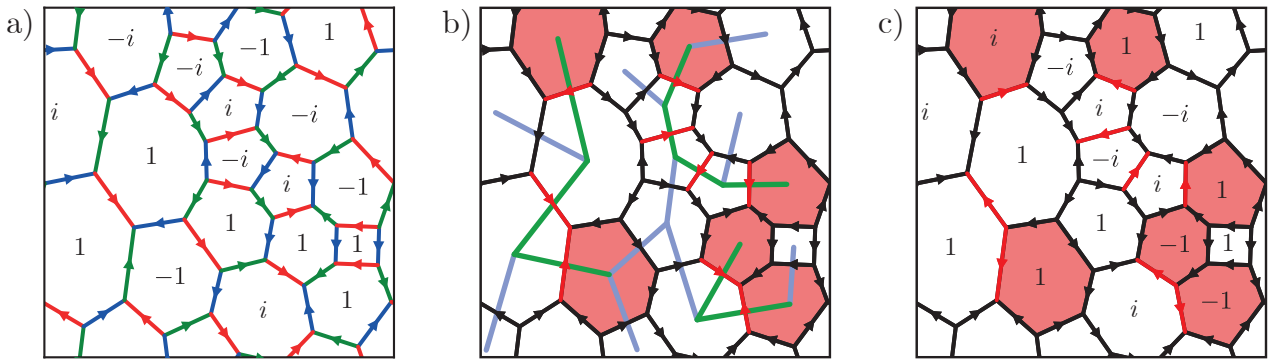


Figure 4.9: An example of the procedure for flipping a set of fluxes. **(a)** The initial system, with the flux through each plaquette labelled, and u_{jk} values indicated with bond arrows. **(b)** A set of plaquettes (highlighted in pink) are chosen to be flipped. The plaquette spanning tree is constructed (shown in blue and green). Blue parts of the tree have an even number of plaquettes to flip on both sides, so their corresponding edge is not flipped. Green parts of the tree have an odd number of plaquettes to flip on both sides, so their corresponding edge is flipped. **(c)** The lattice after the flip has been performed, with the flipped edges highlighted in red.

analogous to that in Eqn. 4.16. Again, we find a set of n_{edge} bond operators, labelled as u_{jk}, which commute with one another and H so can be treated as a Z_2 gauge field $u_{jk} = \pm 1$. Gauge transformations are also identical to those in the honeycomb case, where the D_j operator's effect is to flip the value of u_{jk} for all bonds connected to site j. When represented in the Majorana Hilbert space, the flux operators $W_p = \prod_{\partial p} \sigma_j^\alpha \sigma_k^\alpha$ again become a set of conserved gauge fluxes $\phi_p = \prod_{\partial p} -iu_{jk}$, with one flux per plaquette in the system.

The spin Hamiltonian is real, so it has time reversal symmetry. However, unlike the honeycomb case, the gauge flux through any plaquette with an odd number of sites is imaginary. A gauge sector is specified by a set of $\phi_p = \pm 1$ for every even plaquette and a set of $\phi_p = \pm i$ for every odd plaquette, see the example in Fig. 4.9a. Thus, we find that the presence of odd plaquettes leads to a spontaneous breaking of time reversal symmetry, since the effect of time reversal will be to flip the sign of every bond operator on the lattice. Any odd-plaquette flux ϕ_p will thus also have its sign flipped. On the honeycomb, the flipping of every bond operator in the system could be done via a gauge transformation applied to all the sites on one of the two sublattices. On a lattice with odd cycles we no longer have A and B sublattices, so this is no longer possible – a time reversed system is not gauge equivalent to the original. Thus, any state with a fixed flux sector spontaneously breaks time reversal symmetry, which in the context of crystalline Kitaev models was first described by Yao and Kivelson[2] [156]. All flux sectors come in degenerate pairs, where time reversal is equivalent to inverting the flux through every odd plaquette.

On our model, we have seen that only the gauge fluxes though each plaquette have physical significance, however the degrees of freedom we actually have access to are the bond operators. Thus, let us detail an efficient process for choosing the bond operators such that a particular flux sector can be reproduced. The space of bond operator configurations is massively degenerate – that is, many different configurations are gauge equivalent. However, we can deal with this by restricting to only changing u_{jk} on a subset of bonds. In particular, we construct a spanning tree on the dual lattice, which passes through every plaquette in the system, but contains no

[2]Actually, Kitaev alluded to it in the original paper on the honeycomb model but said little about the result. Perhaps he did not think this was interesting enough to devote much time to studying, or perhaps he wanted to leave a few exercises for the interested reader.

loops, as shown in Fig. 4.9b. The tree contains $n_p - 1$ edges, shown in red, whose configuration space has a $1:1$ mapping onto the 2^{n_p-1} distinct flux sectors. Starting with some arbitrary flux sector, every other flux sector can be created in precisely one way if we only flip edges on the tree (provided all other bond variables not on the tree remain fixed).

To construct the correct set of bond operators, we start with some arbitrary flux sector generated at random. We then count which plaquettes have the incorrect flux compared to the configuration we are targeting. We then construct our dual spanning tree and consider only the bonds that lie on this tree. To decide whether a bond should be flipped, we remove the bond from our spanning tree, cutting the tree into two. Now we count the number of incorrect plaquettes on one of the two trees. If the number is odd then the bond must be flipped, if the number is even then the bond is left as it is. An example of this process is depicted in Fig. 4.9.

4.2.3 The Ground State Flux Sector

We now have all the tools necessary for constructing the amorphous Kitaev model. We can choose a flux sector, solve the system, and determine all the fermionic properties. However, we are missing one final piece of the puzzle: the flux sector of the ground state. On the honeycomb, Lieb's theorem [158] applies, and the ground state is found by setting $\phi_p = +1$ for every hexagon. Here we are not so lucky since an extension of Lieb's theorem to more general lattices has not been proved. In this section we will provide numerical evidence to support the conjecture that, for an arbitrary lattice, the ground state may be found by setting the flux through each plaquette to

$$\phi_p^{\text{g.s.}} = -(\pm i)^{n_{\text{sides}}}, \tag{4.43}$$

where n_{sides} is the number of edges that form the plaquette and the $\pm$ represents a global sign choice which gives us the two TRS-degenerate ground state flux sectors. We collect this evidence by generating a large number of lattices and exhaustively checking every possible flux sector to find the configuration with the lowest energy.

The argument has one complication: for a graph with n_p plaquettes, there are 2^{n_p-1} flux sectors which must be searched over. Thus, one is necessarily restricted to looking at small system sizes – we were able to check all flux sectors for systems with $n_p \leq 16$ in a reasonable amount of time. At such small system size we find that finite size effects are substantial and extra care must be taken to account for such effects.

The argument has three parts. First we present a formulation of the ground state energy in terms of quantities defined on cycles on the lattice. Next, we shall use this formulation to discuss the effect of finite system size, and propose a method for dealing with these finite size effects. Finally, we shall present the numerical results – that all lattices we checked had a ground state consistent with our conjecture, and argue that the result may be straightforwardly extrapolated to larger system sizes.

4.2.3.1 Cycles and the Ground State Energy

As discussed previously, the ground state energy can be found by taking the sum of the negative eigenvalues of the antisymmetric Hermitian matrix iA, defined in Eqn. 4.18. This Hamiltonian

has particle-hole symmetry, since it is pure imaginary, so has $\mathcal{K}H\mathcal{K} = -H$, forcing all the eigenvalues to pair up with opposite signs,

$$iA = \sum_{i}^{N/2} \left(\varepsilon_i \left|\psi_i\right\rangle \left\langle\psi_i\right| - \varepsilon_i \left|\psi_i^*\right\rangle \left\langle\psi_i^*\right|\right), \tag{4.44}$$

where ε_i are always positive and N is the dimensionality of the Majorana Hilbert space. To find the ground state energy, let us square this matrix and then take the square root - forcing all the eigenstates to be positive,

$$\sqrt{(iA)^2} = \sum_{i}^{N/2} \varepsilon_i \left(\left|\psi_i\right\rangle \left\langle\psi_i\right| + \left|\psi_i^*\right\rangle \left\langle\psi_i^*\right|\right). \tag{4.45}$$

Thus, the trace of this quantity is exactly double the magnitude of the ground state energy (which is negative),

$$\mathrm{Tr}\sqrt{(iA)^2} = 2\sum_i \varepsilon_i = 2|E_{\text{g.s.}}|. \tag{4.46}$$

We want to re-express this square root as a power series in iA. Our starting point is the binomial expansion for the square root

$$(1+x)^{\frac{1}{2}} = \sum_{n=0}^{\infty} \frac{\left(\frac{1}{2}\right)_n}{n!} x^n. \tag{4.47}$$

The symbol $(\cdot)_n$ represents a falling factorial,

$$(\alpha)_n = \alpha(\alpha-1)(\alpha-2)...(\alpha-n+1). \tag{4.48}$$

To apply this to our problem, we wish to replace $(iA)^2 = 1 + x$, however there is a complication. The series only converges for $|x| \leq 1$, so we must first rescale $(iA)^2$ such that none of its eigenvalues are > 2, let us therefore introduce a rescaling factor s,

$$\sqrt{(iA)^2} = \sqrt{s}\sum_{n=0}^{\infty} \frac{\left(\frac{1}{2}\right)_n}{n!} \left[\frac{(iA)^2}{s} - \mathbb{1}\right]^n. \tag{4.49}$$

Rearranging slightly to make the sign structure more explicit, we have the following power series expression for the energy of the ground state,

$$2|E_{\text{g.s.}}| = \sqrt{s}n_v - \sqrt{s}\sum_{n=1}^{\infty} \left|\frac{\left(\frac{1}{2}\right)_n}{n!s^n}\right| \mathrm{Tr}\left[s - (iA)^2\right]^n, \tag{4.50}$$

where n_v is the number of vertices on the lattice.

The Spectral Radius of iA — Let us briefly comment on the value of s, which is defined by the largest eigenvalue of $(iA)^2$. Thankfully, there has already been some work put into understanding the properties of matrices like iA by the graph theorists [186, 187]. At the isotropic point $J^\alpha = 1$, (iA) is a *skew-adjacency matrix* (although they don't include the

factor of i), the energy we are after is called the *skew-energy*. Their emphasis is rather different, spectral graph theorists use quantities like this as a signature to differentiate between different graphs. In [187] they prove that the spectral radius of the skew adjacency graph is always less than the spectral radius of the regular adjacency matrix,

$$\rho(iA) \leq \rho(|iA|), \tag{4.51}$$

where $|\cdot|$ denotes an element-wise modulus. This is incredibly handy because it is well known that the spectral radius of the adjacency matrix is always equal or less than the largest vertex coordination number Δ,

$$\rho(|iA|) \leq \Delta, \tag{4.52}$$

with equality if the lattice is Δ-regular (i.e. all vertices have coordination number Δ). Our lattices are guaranteed to always have coordination number 3 (or lower if we have open boundaries for example). Thus, we have a guarantee that the spectral radius of iA has

$$\rho(iA) \leq 3. \tag{4.53}$$

This means that provided $s \geq 4.5$, our series is guaranteed to converge. As we move away from the isotropic point in J^α, provided we still satisfy $J^\alpha \leq 1$, the above inequality still holds.

Now let us show that the trace of the k^{th} power of a matrix is determined solely by the products of matrix elements around loops in the lattice. Consider a diagonal element of M^k,

$$(M^k)_{jj} = \sum_{\alpha,\beta,\ldots,\chi,\omega} (M_{j\alpha})(M_{\alpha\beta})\ldots(M_{\chi\omega})(M_{\omega j}). \tag{4.54}$$

The summand in this expression can be visualised as taking a k-edge walk that starts at p_j, then traverses over all the intermediate points $(p_\alpha, p_\beta \ldots)$ before coming back to finish at p_j. Thus, the matrix element above calculates the sum of all walks that start and end at point p_j. The whole trace can thus be seen as a sum over all closed k-walks on our lattice.

Now let's consider traces of iA at the isotropic point ($J^\alpha = 1$). In this case, up to an overall factor, we have $iA_{jk} = iu_{jk}$. This means that a trace of $(iA)^k$ sums the flux ϕ_{w_k} through every walk w_k of length k,

$$\text{Tr}\left[(iA)^k\right] = \sum_{w_k} \phi_{w_k} \tag{4.55}$$

Note that this flux differs from our previous definition in that it is calculated for an arbitrary walk around the lattice, rather than specifically for individual plaquettes. Let us state two properties of these fluxes:

1. The flux around a walk that encircles zero area is always +1. For a path to encircle no area, it needs to leave and return to point p_1 along the same path. This means that every constituent u_{jk} in the flux product must appear twice in the overall expression,

$$\phi_w = (iu_{12})(iu_{23})\ldots(iu_{n-1\ n})(iu_{n\ n-1})\ldots(iu_{32})(iu_{21}). \tag{4.56}$$

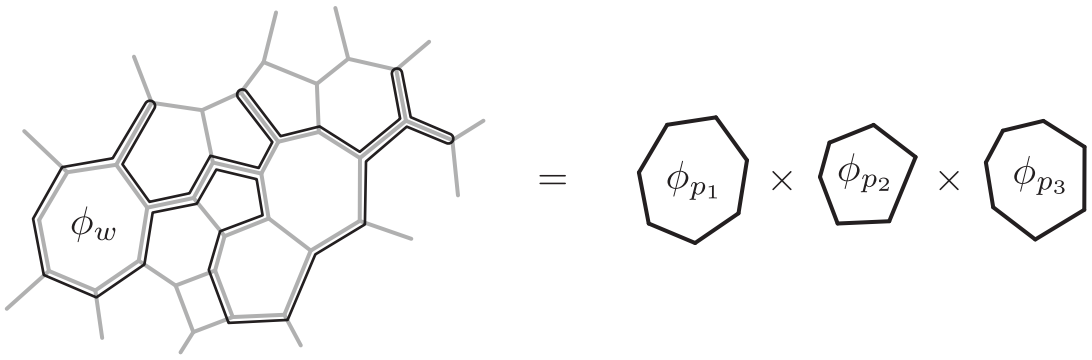


Figure 4.10: The flux through a large and complex walk, ϕ_w can be decomposed as the product of the flux through its constituent plaquettes, neglecting the parts of the walk that enclose no area.

From the antisymmetry of u_{jk} we can immediately see that each pair of u values gives an overall $+1$ factor, so the overall flux is $+1$.

2. The flux of a closed walk is the product of the flux through the plaquettes it encircles.

$$\phi_w = \prod_{p \in w} \phi_p \tag{4.57}$$

This can be proved by noticing that a combined path has all the same constituent edges as the plaquettes minus some shared edges. Since the shared edges show up with opposite direction in each plaquette, the iu_{ij} factors cancel out when their fluxes are multiplied.

As a consequence of these two properties, we see that the flux through any complex closed walk around the lattice can be decomposed into the product of its constituent plaquettes, as shown in Fig. 4.10. Thus, every term in Eqn. 4.50 is a trace of a power iA, which then can be decomposed into products of fluxes through individual plaquettes,

$$|E_{\text{g.s.}}| \sim \sum_{p_j} c_j \phi_{p_j} + \sum_{p_j, p_k} c_{jk} \phi_{p_j} \phi_{p_k} + ... \tag{4.58}$$

Determining the exact values of c_j in this expansion is, of course, complex and dependent on the specific geometry of the individual lattice.

In periodic boundaries, not every walk can be expressed as a product over plaquette operators, since any walk that wraps the torus encircles no plaquettes. Torus wrapping walks have a minimum length that scales with system size L, so first show up in the series at order L. Thus, we expect these to vanish for arbitrarily large systems, and consider their influence to be a finite size effect, which we discuss in the next section.

A Clue for the Ground State Flux Sector — Let us consider the sign structure of the sum in Eqn. 4.50. Since the sum is in powers of $-(iA)^2$, we see that, ignoring the magnitude of each term, the sum looks like

$$|E_{\text{g.s.}}| \sim a_0 + |a_1|(iA)^2 - |a_2|(iA)^4 + |a_3|(iA)^6 - |a_4|(iA)^8 - ... \tag{4.59}$$

For a given plaquette p with n_s sides, we expect it to contribute at lowest order in Eqn. 4.50 in a term of the form

$$(-1)^{\frac{n_s}{2}}(iA)^{n_s} \sim \text{terms} + (-1)^{\frac{n_s}{2}}\phi_p \tag{4.60}$$

The lowest ground state energy is found by extremising this sum. Thus, if we set the flux through every plaquette of length $4m$ to -1 and the flux through every plaquette of length $4m+2$ to $+1$, we can be sure that their lowest order contribution to the sum will be positive. Thus, we expect that this should give us the best chance of maximising $|E_{\text{g.s.}}|$.

The flux through odd plaquettes does not show up in this expression. However, if we consider the ways that odd plaquettes can combine to form even plaquettes, we may extend this argument to include them as well. For two odd plaquettes with n_{s1} and n_{s2} sides which share an edge, the combined even plaquette will have $n_{s1}+n_{s2}-2$ sides, and the flux through the combined plaquette will be $\phi_1\phi_2$. Thus, if we set the flux through all plaquettes with $4m+1$ sides to $+i$ and the flux through all $4m+3$ sided plaquettes to -1, we have a guarantee that they will always combine with a neighbour to form an even plaquette whose flux agrees with the rule stated above. Note that this also works if we swap the $+i$ and $-i$ in this argument. Thus, we might be tempted to suggest that the ground state flux sector corresponds to setting all plaquettes to

$$\phi_p^{\text{g.s.}} = -(\pm i)^{n_{\text{sides}}}. \tag{4.61}$$

Unfortunately, the above argument only works at the lowest order at which each plaquette appears. If you include higher order terms, the counting is not so straightforward, since individual plaquettes can reappear at arbitrarily high order in arbitrarily long walks that show up with both positive and negative coefficients. Quod <u>not</u> erat demonstrandum.

4.2.3.2 Finite Size Effects

In our numerical investigation, the objective was to test as many example lattices as possible. We aim for the largest lattice size that could be efficiently solved, requiring a balance between lattice size and cases tested. Each added plaquette doubles the number of flux sectors that must be checked. 25,000 lattices containing 16 plaquettes were used. However, in his study of the honeycomb model, Kitaev demonstrated that finite size effects persist up to much larger lattice sizes than we were able to access.

In order to circumvent this problem, we treat the 16-plaquette amorphous lattice as a unit cell in an arbitrarily large periodic system. The bonds that originally connected across the periodic boundaries now connect adjacent unit cells. This infinite periodic Hamiltonian can then be solved using Bloch's theorem, since the larger system is diagonalised by a plane wave ansatz. For a given crystal momentum $\mathbf{q} \in [0, 2\pi)^2$, we are left with a Bloch Hamiltonian, which is identical to the original Hamiltonian aside from an extra phase on edges that cross the periodic boundaries in the x and y directions,

$$iA_{jk}(\mathbf{q}) = \frac{i}{2}J^{\alpha}u_{jk}e^{iq_{jk}}, \tag{4.62}$$

where $q_{jk} = q_x$ for a bond that crosses the x-periodic boundary in the positive direction, with

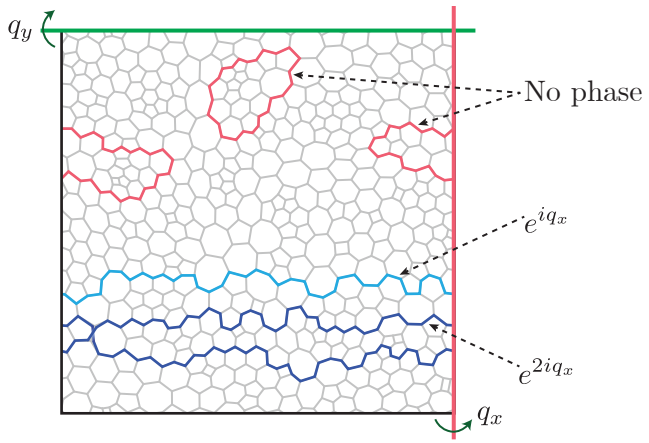


Figure 4.11: A lattice in twisted boundaries, with a phase q_α obtained on crossing the boundary in the α-direction. Several loops are shown. The red loops pick up no phase since they either do not cross the boundaries or cross it once in each direction. The light blue path crosses the x-boundary once, so picks up a phase e^{iq_x}. The dark blue path crosses the x-boundary twice, so picks up a phase e^{2iq_x}.

the analogous definition for y-crossing bonds. We also have $q_{jk} = -q_{kj}$. Finally, $q_{jk} = 0$ if the edge does not cross any boundaries at all – in essence we are imposing twisted boundary conditions on our system. The total energy of the tiled system can be calculated by averaging over the energy for every value of $\mathbf{q}$.

Let us recontextualise the effect of such a twist-averaging procedure to the loop-sum picture presented in the previous section. Let us consider a walk w on our lattice. If the walk does not wrap the torus in either the x or y directions, then ϕ_w is invariant to $\mathbf{q}$. Even if the walk does cross the boundaries, a non-wrapping walk will cross once forward (picking up e^{iq}) and then again backward (picking up e^{-iq}), leaving the overall flux invariant.

However, consider a general walk that wraps the system n_x times in the x-direction and n_y times in the y-direction. When a twist $\mathbf{q}$ is applied, the flux through this walk will pick up an extra phase

$$\phi_w \to \phi_w e^{in_x q_x + in_y q_y}. \tag{4.63}$$

Thus, each successive set of $\mathbf{q}$ included in our averaging procedure has the effect of cancelling out the contribution to $|E_{\text{g.s.}}|$ from walks with larger values of n_α. To illustrate this, consider first averaging over $\mathbf{q} = (0, 0)$ and $\mathbf{q} = (\pi, 0)$. Any walk with odd n_x will appear with opposite sign in the two respective sums for each twist, cancelling out. Adding in $\mathbf{q} = (\frac{\pi}{2}, 0)$ and $\mathbf{q} = (\frac{3\pi}{2}, 0)$, then cancels out all walks with $n_x = 2, 6, 10...$ Thus, we see that averaging over sufficiently many phase twists has the effect of cancelling out all torus-wrapping walks, while leaving all non-wrapping walks invariant.

4.2.3.3 Numerics

We now detail the numerical evidence collected to support our claim for the flux configuration of the ground state. We generated a large number ($\sim$ 25,000) of lattices and exhaustively checked every possible flux sector to find the configuration with the lowest energy. This was done both at the isotropic point ($J^\alpha = 1$), and in the toric code phase ($J^{x,y} = 0.25, J^z = 1$).

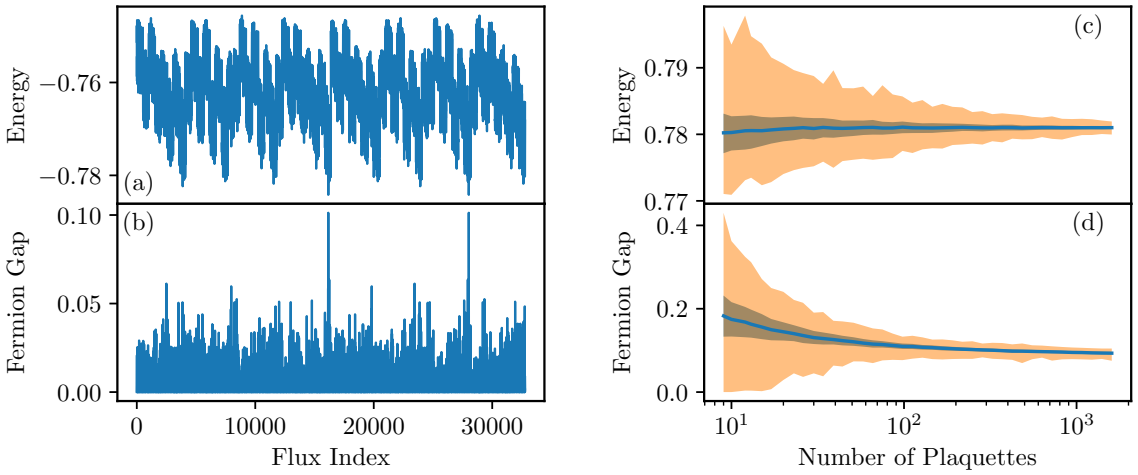


Figure 4.12: **(a)** The energy of every flux sector explored for a system of 16 plaquettes, the order is arbitrary. The two ground state flux sectors can be identified as the points with the lowest energy. **(b)** The fermion gap for each of the flux sectors explored. Note that the largest fermion gap coincides with the ground state flux sector. This occurred in $\sim 85\%$ of cases tested. (c) Average energy of the systems tested over a range of system sizes from $n_p = 9$ to $n_p = 1600$. The region between the upper and lower quartiles is shown in red, and the full range of energies obtained is shown in orange. (d) Average fermion gap as a function of system size. Again, the region between the upper and lower quartiles is shown in red, and the full range is shown in orange. As can be seen, no gapless systems were found for $n_p > 20$.

Since a lattice with n_p plaquettes has 2^{n_p-1} distinct flux sectors to search over, one is necessarily restricted to looking at small system sizes – we were able to check all flux sectors for systems with $n_p \leq 16$ in a reasonable amount of time. Practically, this is done by iterating over all possible configurations of $\{u_{jk}\}$ a plaquette-spanning tree, as described in §4.2.2. At such small system size, the substantial finite size effects are thus accounted for by averaging over 50×50 sets of twisted boundary conditions.

For each lattice, $2^{15} = 32{,}768$ flux sectors are generated. In each case we find the energy (averaged over all twist values) and the size of the fermion gap, which is defined as the lowest energy excitation for any value of $\mathbf{q}$. We then check if the lowest energy flux sector aligns with our ansatz ($\phi_p^{\text{g.s.}} = -(\pm i)^{n_{\text{sides}}}$) and whether this flux sector is gapped. At the isotropic point ($J^\alpha = 1$), all 25,000 examples conformed to our guess for the ground state flux sector. A tiny minority (~ 10) of the systems were found to be gapless. As we shall see shortly, the proportion of gapless systems vanishes as we increase the size of the amorphous lattice. An example of the energies and gaps for one of the systems tested is shown in Fig. 4.12a. For the anisotropic phase (we used $J^{x,y} = 0.25$, $J^z = 1$) the overwhelming majority of cases adhered to our ansatz, however a small minority ($\sim 0.5\%$) did not. In these cases, however, the energy difference between our ansatz and the ground state was at most of order 10^{-6}. Further investigation would need to be undertaken to determine whether these anomalous systems are a finite size effect due to the small amorphous system sizes used or a genuine feature of the toric code phase on such lattices. Especially since the flux gap (i.e. the second-lowest ground state energy of any flux sector) of the honeycomb toric code phase scales with $J^{x2}J^{y2}/J^{z3}$, so is expected to be very small in this regime.

We turn our attention to checking that the ground state flux sector is gapped. Here, there is no longer any need to exhaustively search over flux space for the ground state, so it is possible to

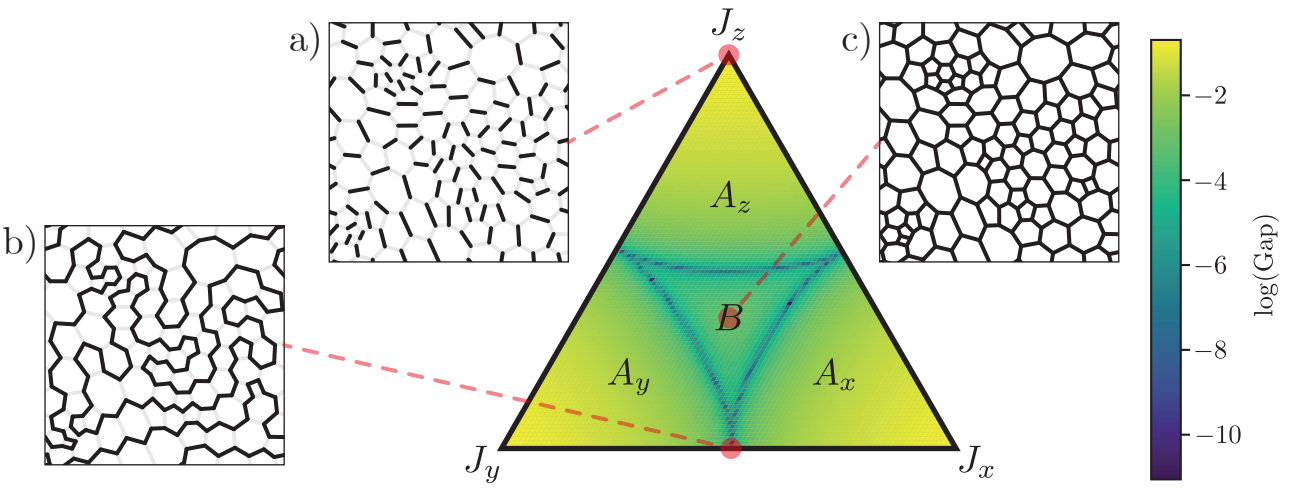


Figure 4.13: Ground-state phase diagram calculated for an example amorphous lattice with 800 sites. The phase diagram is coloured with the logarithm of the gap size, showing clearly the lines where the gap closes, separating a gapped B phase from the three A_α toric code phases. Three example lattices (for a much smaller lattice) are shown in order to illustrate the state of the system at three points in the phase space. **(a)** Around the corners the system is dimerised, with the remaining couplings acting as a weak perturbation on the dimerised system. **(b)** In the centre of a side of the triangle, the system is decoupled into a set of chain models. **(c)** At the centre of the phase diagram there is a gapped chiral quantum spin liquid phase.

go to much larger system size. We generate 40 sets of systems with plaquette numbers ranging from 9 to 1600. For each system size, 1000 distinct lattices are generated and the energy and gap size are calculated without phase twisting, since the effect is negligible for such large system sizes. As can be seen in Fig. 4.12c-d, for very small system size a small minority of gapless systems appear, however beyond around 20 plaquettes all systems had a stable fermion gap in the ground state. Finally, we note that the energy and gap difference between the phase twisted and non-phase twisted results vanished exponentially in the system size, supporting the claim that the results can be straightforwardly extrapolated to large systems.

4.2.4 The Ground-State Phase Diagram

The ground-state phase diagram can now be determined by varying the strength of each bond type, J^α, while remaining in the ground state flux sector. In Fig. 4.13, we show the phase diagram for an example system on a lattice with 800 sites. The diagram contains two distinct phases: close to the corners of the triangle the gapped A_α phases appear. The phase has a fermionic gap and supports Abelian excitations. Around the isotropic point $J^x = J^y = J^z$, the B phase is also gapped, in contrast to the honeycomb case. This is because the presence of odd plaquettes leads to a spontaneous breaking of time reversal symmetry. Note that the phase diagram for this specific 800-site lattice is general - for a sufficiently large amorphous system, the phase diagram depends weakly on the detailed geometry of an individual lattice – many different lattices give an almost identical phase diagram.

As the values of J^α are varied, the fermionic gap closes at the boundary between the two phases. On the amorphous lattice these boundaries exhibit an inward curvature relative to the Honeycomb case. This curvature is similar to that seen on the honeycomb Kitaev models with flux [188] or bond [189] disorder. At the centre of the sides of the triangle, the system has

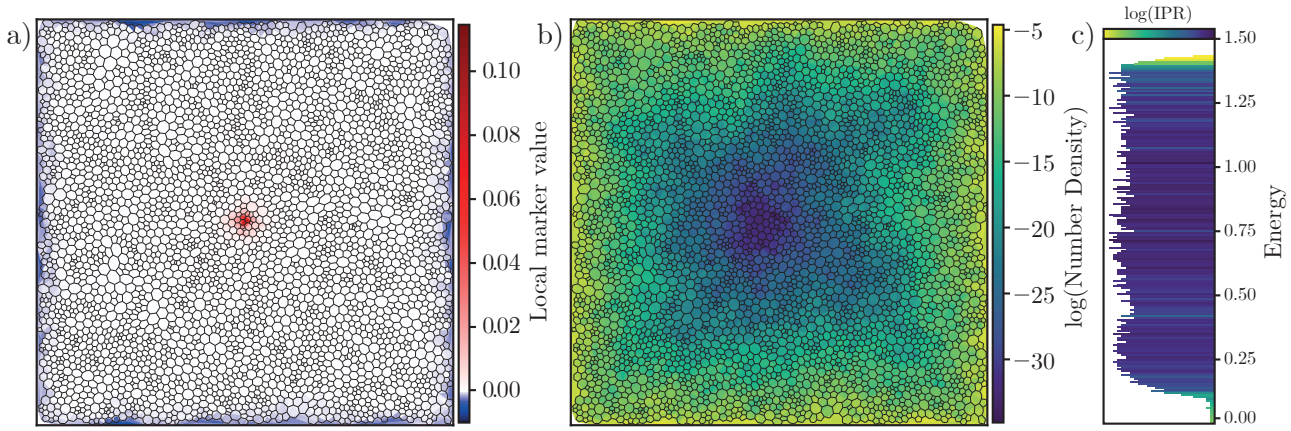


Figure 4.14: An example system in the B phase, on a lattice with ~ 8000 vertices. **(a)** The local Kitaev marker $\mathcal{Q}_{\text{Kit}}$ for a crosshair placed in the centre of the material. The sum of the central positive contribution is quantised to $\mathcal{Q} = +1$ by one part in 10^{-5}. **(b)** A plot of the logarithm of number density for a gap crossing edge mode with energy $\varepsilon = 0.003$. The log of the density decays linearly from the edge to the bulk, indicated that the that is exponentially localised to the boundary. **(c)** The density of states of the Majorana Hamiltonian, coloured according to the average IPR of states at a given energy.

completely decoupled into a set of chains, as shown in Fig. 4.13b. Provided the chains are long enough – i.e. the system is sufficiently large – they are guaranteed to have a gapless spectrum, ensuring that the three A_α phases are separated by gap crossings.

A fundamental tool for understanding the distinction between the two phases is the Chern number. The original definition relies on momentum space, and so cannot be used here, where the system lacks any translational symmetry. However, we may use the real-space Chern number discussed in Chapter 3. Using this local Chern marker, we determine that the A_α phases have Chern numbers $\mathcal{Q} = 0$, whereas the two TRS-degenerate ground state flux sectors in the B phase have Chern number $\mathcal{Q} = \pm 1$ respectively. In open boundaries, this leads to the appearance of gap-crossing protected edge modes, in accordance with the bulk-boundary correspondence [85], an example is shown in 4.14. The edge modes are exponentially localised to the boundary of the system, and can be qualitatively distinguished from bulk states by their large inverse participation ratio. Of course, the closing of the fermionic gap on the boundary between the two phases is necessary in order to transition between two ground states with different Chern numbers.

4.2.5 Accounting for Bond Disorder

The effect of bond disorder in the Kitaev honeycomb lattice model is well studied [161, 189–192]. When bond disorder is introduced the fermionic gap closes as a function of disorder strength, leading generically to a thermal metal phase [161, 189]. The changes to the fermionic spectrum of the flux-free sector are much more dramatic than those observed in our amorphous model. *A priori* one might expect that a similar gap closing should be introduced by the lattice disorder present in the amorphous model. As we have shown, this is not the case. We believe the essential difference between these kinds of disorder is the disruption of the local motif: in the amorphous model, the global translational symmetry of the system is disrupted, but the coupling strengths remain locally homogeneous on each site.

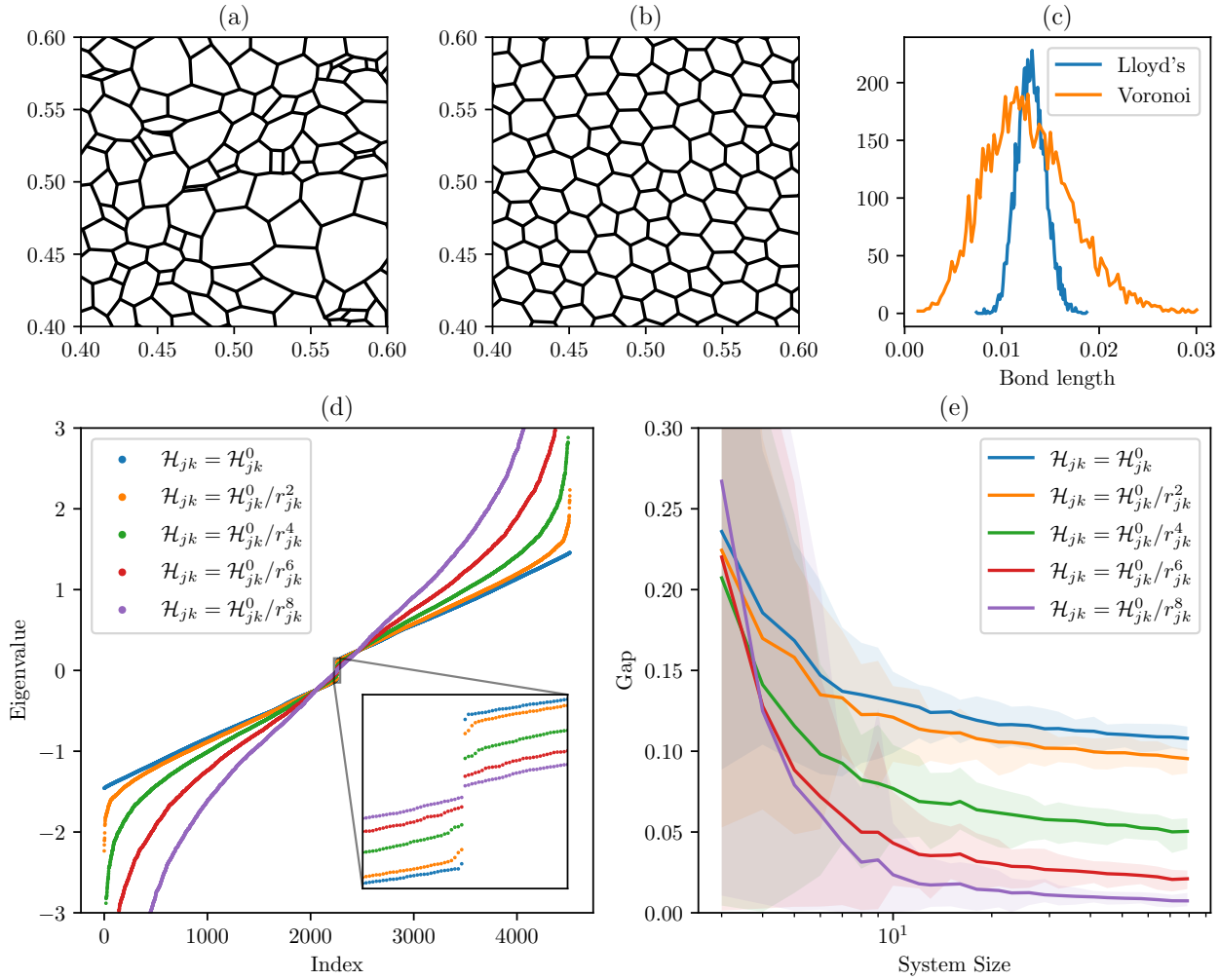


Figure 4.15: **(a)** Close up of a section of amorphous lattice generated using a single Voronoi partition on a set of uniformly sampled seed points. **(b)** A section of amorphous lattice generated using the regularised method detailed in Appendix 4.2.5, by creating a Voronoi partition using seed points sampled from a blue noise distribution. This is then followed by four iterations of Lloyd's algorithm to further regularise the bond lengths. **(c)** A histogram of bond lengths for the example graphs in sub figures a and b. Note that the distribution is much more tightly peaked around the mean bond length in the regularised lattice, with no extremely short bonds present. **(d)** The Majorana spectrum for a single example of an amorphous lattice for five different values of $\alpha \in [0, 8]$. **(e)** Finite-size scaling analysis of the fermion gap in the flux-free sector. Solid lines indicate the gap averaged over 50 random lattice samples for each system size, and the shaded regions indicate the full range of the sampled gaps.

We study the effect of bond disorder on the amorphous lattice by introducing a bond-length dependent factor to the hopping terms in the Hamiltonian, such that $J_{jk} = J^0_{jk}/r^\alpha_{jk}$, where r_{jk} is the bond length from site j to site k, which has been normalised such that $\langle r^\alpha_{jk}\rangle = 1$ to prevent this term from substantially rescaling the energies of the system. The parameter α controls the strength of the disorder, where setting $\alpha = 0$ reproduces the original Hamiltonian. As α is varied, we calculate the fermionic spectrum, observing how the band gap is affected by this disorder.

Clearly, this Hamiltonian will produce unphysical results on any lattice where some bonds are extremely short-ranged, leading to extremely strong hopping terms. Thus, in order to get physical results, one must first regularise the bond lengths of the lattice. This is done in two steps. First, the initial points are sampled from a blue noise distribution, rather than a uniform distribution, using Mitchell's best-candidate algorithm [193, 194]. This produces seed points that are regularly spaced, yet still amorphous. The second step is to regularise the lattice using Lloyd's algorithm [195] – where vertices are repeatedly moved to the centre of mass of the plaquettes adjacent and the Voronoi diagram is regenerated. In practice, we used four iterations of this method. An example of such a lattice is shown in Fig. 4.15b.

The fermionic spectrum is calculated for a range of α between 0 and 8, at a variety of lattice sizes parametrised by the length L, where the number of vertices N scales with $N \sim L^2$. As disorder is increased, the gap shrinks however no truly gapless systems are generated for systems sizes larger than $L \sim 10$, providing evidence of the Kitaev phase's stability in the presence of even relatively strong bond disorder. We note that these calculations were carried out in periodic boundary conditions, hence the absence of in-gap edge states.

Chapter 5

The Kitaev-Heisenberg Model on the Star Lattice

As we saw in the previous chapter, the Kitaev model has turned out to be remarkably insensitive to changes in lattice geometry. Besides the TRS breaking effected by the presence of odd-sided plaquettes, we have shown that one can expect to find largely the same physics from a Kitaev model constructed on almost any trivalent lattice. If one were in the business of looking for new phases of matter, this result might be something of a disappointment! Such stability leaves very little space for qualitatively new physics to be found simply by changing the board that the game is played on. Thankfully, nature is rarely so straightforward. The Kitaev model was originally proposed as a purely theoretical exercise [30] – with little expectation that any extant material could realise the bond-dependent spin couplings necessary for such a phase. However, following the initial proposal, it was suggested that one could engineer such couplings in certain transition metal compounds with strong spin-orbit coupling [144, 146, 196]. In the subsequent years, several material candidates were synthesised, such as the iridates Na_2IrO_3 and α-Li_2IrO_3 [70–72], and later α-$RuCl_3$ [73, 74]. In such 'Kitaev materials', the Hamiltonian was shown to realise a dominant Kitaev-type bond-directional coupling, as well as other symmetry-allowed perturbations such as Heisenberg and Γ couplings [197]. These perturbing interactions generally destroy the QSL phase, instead giving rise to a rich phase diagram with various long-range ordered magnetic phases [198–200].

Remarkably, topological excitations persist even in these magnetically ordered phases. In the presence of a large magnetic field, the bulk magnon bands in these ordered phases can have nonzero topological invariants. Thus, they realise a magnonic equivalent of the quantum Hall effect, with surface states appearing with uni-directional propagation – a so-called topological magnon insulator [201–205]. Hence, excitations of the (extended) Kitaev honeycomb model can be tuned from the chiral Majorana excitations (described in §4.1.6) to stable chiral magnons as a function of increasing magnetic field. This is not only interesting theoretically but of direct experimental relevance – both chiral magnetic excitations and chiral Majorana excitations give rise to a thermal Hall response [202, 206]. The latter has been measured in the Kitaev magnet α-$RuCl_3$ [207, 208], but whether its origin is related to QSL or TMI behaviour is still under debate [209, 210].

Unlike the QSL phase, the magnetically ordered phases that form in real Kitaev materials – phases such as Néel, zigzag and stripy order – are extremely sensitive to changes in the lattice geometry. For example, antiferromagnetic order depends on sublattice symmetry. By breaking this symmetry, one would expect to geometrically frustrate the formation of such phases, leaving

space for more exotic ground states to form. In this chapter we will consider the star lattice, as a particularly simple example of a lattice that breaks sublattice symmetry. This lattice, shown in Fig. 5.1a, can be formed from the Honeycomb by decorating each vertex with a triangle. The Kitaev model on this lattice constituted the first rigorous example of a chiral QSL with *spontaneously* broken TRS, due to the presence of odd plaquettes [156] – exactly the mechanism detailed in §4.2.2. Despite much research on the stability of the Kitaev QSL on the honeycomb lattice [142–144] the effect of perturbing interactions on the chiral Kitaev QSL has not been investigated on the star lattice. This is even more surprising given that the pure antiferromagnetic Heisenberg model on the star lattice is one of the rare established examples hosting a singlet VBS ground state phase with triplon excitations [39–44]. Additional motivation comes from the recent synthesis of the first $S = 1/2$ materials realisation of the star lattice [211, 212] (previous star lattice realisations contained $S = 5/2$ spin clusters [213]).

In this chapter we will investigate the rich ground-state phase diagram and distinct types of chiral excitations of the Kitaev-Heisenberg model on the star lattice. Here, the presence of odd plaquettes (and thus the frustration of Néel order) leads to the formation of a valence bond solid (VBS). In its most common form, a VBS is created by neighbouring pairs of spins anti-aligning into singlets, forming a dimer covering of the entire lattice – however, we also find a more exotic 'triplet VBS', where neighbouring bonds couple into bond anisotropic triplet states. On a singlet VBS background, excitations involve breaking a singlet and creating a spin-1 triplet – a so-called triplon mode that can be represented as a bosonic particle [214]. Since such excitations are electrically neutral, and interact weakly with one another, triplon systems have been suggested as a context where one could realise a bosonic bulk boundary correspondence with edge modes that do not suffer strongly from dissipation. This has been proposed both in 1D topological chain systems [215], and 2D bosonic analogues of the quantum Hall effect [216–220]. In general, such effects have relied on the presence of Dzyaloshinskii-Moriya (DM) interactions to generate complex hoppings in the triplon Hamiltonian, allowing for non-zero Chern and winding numbers to appear. Here, we will show that the Kitaev interaction provides an alternative route for a triplon Hall state forming in the absence of DM interactions and unearth an extremely rich phase diagram with a wide range of Chern numbers. Thus, we establish that – in analogy to the honeycomb Kitaev model, which can be tuned with a magnetic field from hosting chiral Majorana to chiral magnon excitations – the Kitaev-Heisenberg model on the star lattice tunes from chiral Majoranas to chiral triplons.

The structure of this chapter is as follows. First we introduce the model, describing the parameters used to tune the system and discussing previous studies that have looked at both the star and the honeycomb lattices. Following this, our investigation is composed of three parts. In §5.1 we start by numerically characterising the ground-state phase diagram using infinite density matrix renormalisation group (iDMRG) methods. In particular, we find two phases in the star lattice that do not have an analogue on the Honeycomb lattice, where geometric frustration leads to the formation of a VBS ground state. We will also present a *four-unit-cell spin rotation* that reveals a hidden isometry of the ground-state phase diagram. We show that the four non-spin liquid phases may be categorised into two sets, which are equivalent under this transformation. In §5.2 we construct a parton Majorana mean field description that corroborates the ground-state phase diagram, and allows us to determine the topological properties of the bands and the presence of chiral Majorana excitations in the extended KSL regime. Finally, in §5.3 we construct a bosonic mean field theory describing the triplon excitations of the VBS phase. The topological properties of the triplon phases are derived and we confirm the existence of topologically protected triplon edge modes.

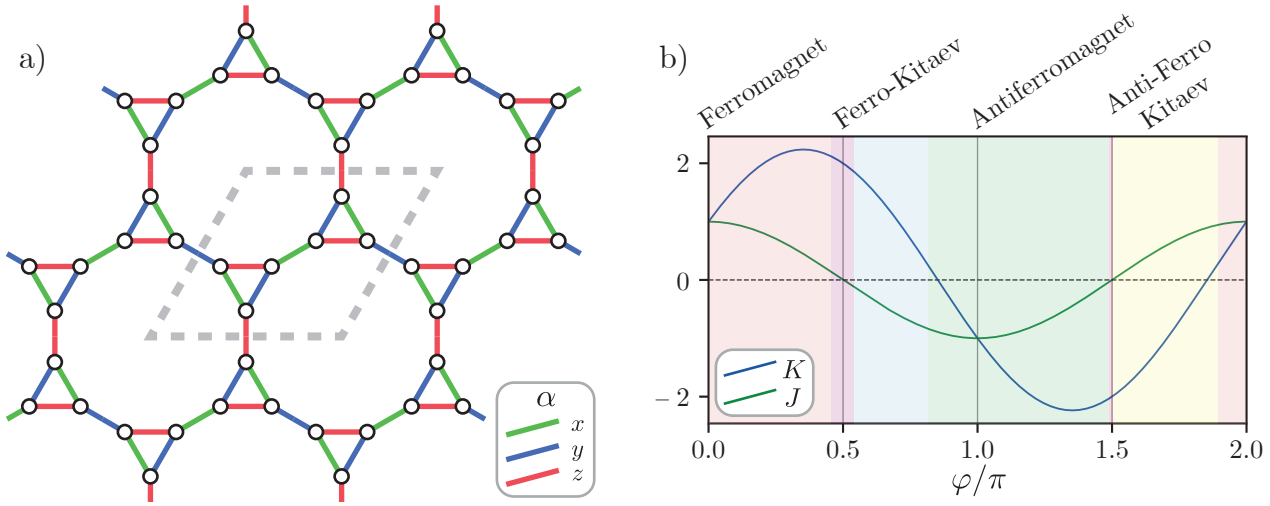


Figure 5.1: **(a)** A fragment of the star lattice is shown. Bond labelling is indicated by the colouring, and the six-site unit cell is depicted with a grey dashed rhombus. **(b)** The dependence of the J and K values on the parameter φ is shown. The two pure Heisenberg and two pure Kitaev points are labelled. The background colouring corresponds to the phase boundaries obtained using DMRG in §5.1.

Let us start by defining the model, which we shall construct on the star lattice shown in Fig. 5.1a. As in the previous chapter, each site hosts a single spin-1/2, and bonds are coloured with a label $\alpha \in \{x, y, z\}$ such that no vertex touches two bonds of the same colour. We choose the Hamiltonian to interpolate between two well-studied limits: the spin isotropic Heisenberg and the anisotropic Kitaev limit. In the Heisenberg limit, adjacent spins are coupled with an isotropic $\sigma_j \cdot \sigma_k$ coupling. In the Kitaev limit each bond of type α is coupled by a $\sigma_j^\alpha \sigma_k^\alpha$, thus only in the direction that matches the colouring.

$$H = -\sum_{\langle jk \rangle_\alpha} \left(K \sigma_j^\alpha \sigma_k^\alpha + J \sum_{\bar{\alpha} \neq \alpha} \sigma_j^{\bar{\alpha}} \sigma_k^{\bar{\alpha}} \right). \tag{5.1}$$

Here $\langle jk \rangle_\alpha$ indicates a bond of type α that connects adjacent sites j and k. The parameter K determines the strength of the "on-colouring" coupling, where the coupling direction matches α, and J determines the strength of the two remaining "off-colouring" couplings. In analogy with previous studies [198, 200], let us introduce a single parameter $\varphi \in [0, 2\pi]$ that smoothly maps onto the possibilities for K and J according to

$$\begin{aligned} K &= 2 \sin \varphi + \cos \varphi, \\ J &= \cos \varphi, \end{aligned} \tag{5.2}$$

shown in Fig. 5.1b.

5.1 The Ground-State Phase Diagram

Let us briefly recap the phase diagram of the standard Kitaev model on the honeycomb lattice [198, 200], which will be useful for elucidating the novel features of the star lattice. The full phase diagram, shown in Fig. 5.2 in φ contains two Kitaev spin liquid phases, equivalent

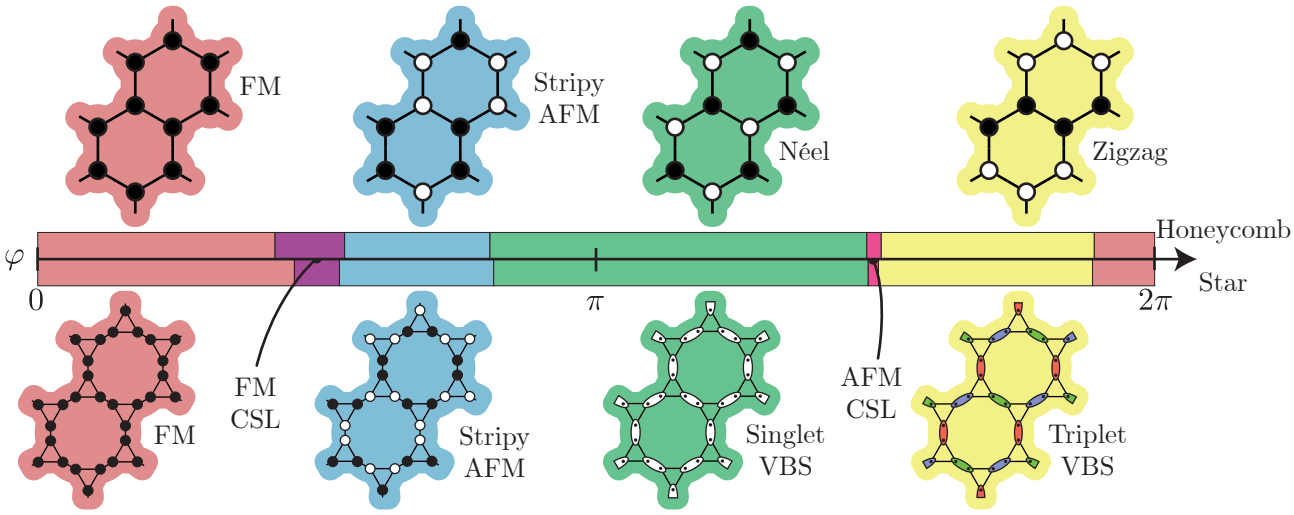


Figure 5.2: The full Kitaev-Heisenberg phase diagram, shown for both the honeycomb model and the star lattice model. Honeycomb phase boundaries are reproduced from [200].

to the phase discussed in the previous chapter, and four distinct magnetically ordered phases. These come in two pairs, where the two phases in each pair can be mapped exactly onto one another by rotating the coordinate system of certain spins in the lattice according to a four unit cell pattern [196, 221, 222]. Around $\varphi = 0$ ($K, J > 0$) the system orders into a ferromagnetic (FM) phase, with completely aligned spins. Around $\varphi = 0.6\pi$ ($K > 0, J < 0$) the system forms a stripy ordered phase, which can be mapped onto the ferromagnetic phase by the four unit cell spin rotation. Around $\varphi = \pi$ ($K, J < 0$) the system forms an antiferromagnetic (AFM) Néel ordered phase, which is again isomorphic to a zigzag phase that appears around $\varphi = 1.6\pi$ ($K < 0, J > 0$). The mapping implies that the dynamics in each pair of isomorphic phases is identical.

Next, let us turn our attention to the star lattice. We numerically determine the ground state across the full range of φ using the density matrix renormalisation group (DMRG) method. DMRG is a variational optimisation algorithm used to find the ground state of many-body Hamiltonians. Although it is predominantly used for characterising 1D physics, recent work has shown that it can provide an effective description of several 2D frustrated systems [200, 223]. Here, we construct the Hamiltonian on a system with infinite cylindrical geometry, using a 2×2 unit cell fragment of the star lattice, with 12 sites wrapping the system in the finite direction and 24 sites in total. The ground state is represented with a matrix product state ansatz with bond dimension $\chi = 1600$, and is calculated using the TeNPy library [224] for 1000 values of φ across the full range $[0, 2\pi]$. Each time, we start with a magnetically aligned initial state and converge to the correct ground state. Two initial states were used, a ferromagnetically aligned state and an anti-aligned state corresponding to the stripy AFM ground state. In each case we determine the expectation value of the magnetisation in the z-direction,

$$m_j^z = \langle \sigma_j^z \rangle \tag{5.3}$$

as well as the expectation value of the x, y and z-spin-spin correlations for each bond,

$$s_{jk}^{\alpha} = \langle \sigma_j^{\alpha} \sigma_k^{\alpha} \rangle \,. \tag{5.4}$$

The results are shown in Fig. 5.3. The phases that comprise the ground state can be identified

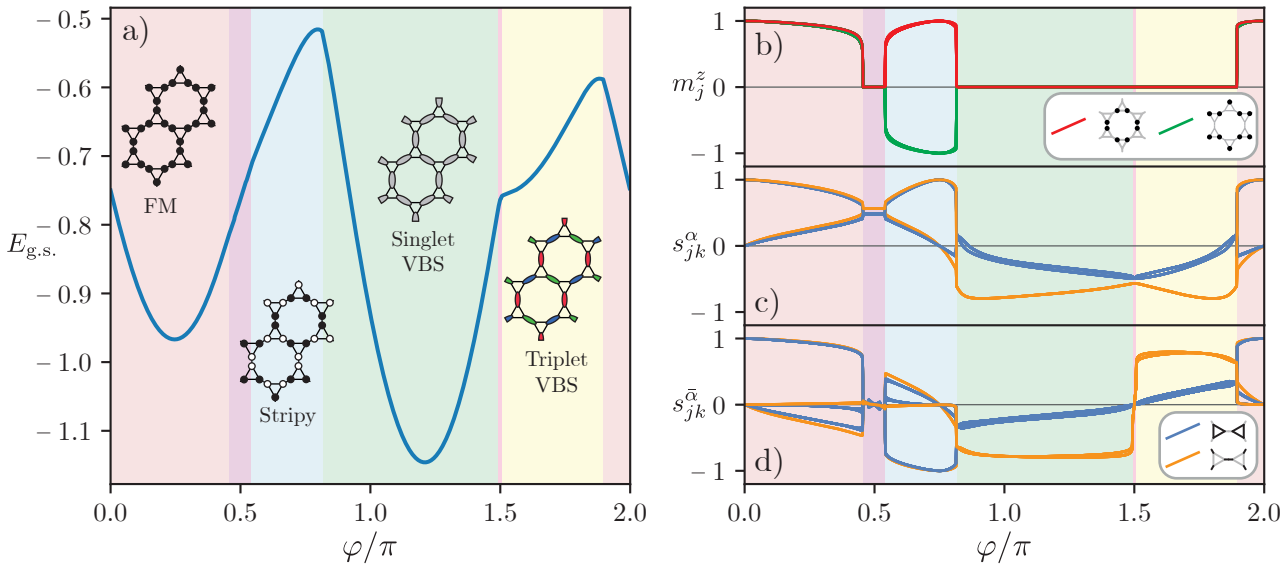


Figure 5.3: The iDMRG results for the star lattice KH model as a function of the parameter φ, defined in Eqn. 5.2. Phase boundaries are indicated with background colour. **(a)** Ground state energy per site as a function of φ. The four non-KSL phases are shown with a diagram of the corresponding phase. KSL phases appear at $\varphi = 0.5\pi, 1.5\pi$. **(b)** Expectation value of the z-component of magnetisation for each site on the lattice $m_z = \langle \sigma_j^z \rangle$. **(c)** Spin-spin correlations for each bond in the *on-colouring* direction, $\langle \sigma_j^{\alpha} \sigma_k^{\alpha} \rangle$. **(d)** Spin-spin correlations for each bond in the two remaining *off-colouring* directions, $\langle \sigma_j^{\alpha} \sigma_k^{\alpha} \rangle$. In (c) and (d), correlations for in-triangle bonds are coloured in blue, whereas inter-triangle bonds are shown in orange.

by considering these observables. We find that the phase diagram contains six distinct phases, shown in Fig. 5.2.

In the regime where $K > 0$ ($\varphi \sim [-0.2\pi, 0.8\pi]$) – which we will refer to as the broadly FM regime – we find two magnetically ordered phases. Around $\varphi \sim 0$, we encounter the standard FM phase with $m_j^z \sim 1$, indicating that all spins are aligned. Of course, this phase includes the FM Heisenberg point at $\varphi = 0$. Around $\varphi = 0.6$ we find a stripy phase with an equal proportion of spin up and spin down sites. This phase may be understood in direct analogy with the stripy ordered phase found in the honeycomb model, where each triangle in the star lattice can be treated as an effective spin-half site, since they form either a $|\uparrow_{\text{eff}}\rangle = |\uparrow\uparrow\downarrow\rangle$ or a $|\downarrow_{\text{eff}}\rangle = |\uparrow\downarrow\downarrow\rangle$ state. These effective spin-half triangles then order identically to the stripe order found on the honeycomb. Remarkably, we also find that the FM and stripy ground states can be mapped onto one under an extended four unit cell rotation described in §5.1.1. In both of these phases, the values of s_{jk}^{α} can then be inferred directly from the m^{α} magnetisations, indicating that the system is in a magnetically ordered phase.

In the regime where $K < 0$ ($\varphi \sim [0.8\pi, 1.8\pi]$) – referred to as the broadly AFM regime – the system forms two distinct VBS phases. Here, the system has zero net magnetisation on all axes, so all m^{α} vanish. In both the VBS phases, the spin correlations (s_{jk}^{α}) on inter-triangle bonds are much stronger than those on in-triangle bonds, suggesting that the VBS is dimerising on the inter-triangle bonds. Around $\varphi \sim \pi$ we have a singlet VBS. Here, both the on and off-colouring correlations are negative on inter-triangle bonds, indicating that the spins are anti-aligned in all

three axes, forming a spin singlet,

$$|s\rangle = \frac{1}{\sqrt{2}}\left(|\uparrow\downarrow\rangle - |\downarrow\uparrow\rangle\right). \tag{5.5}$$

At the point $\varphi \sim \pi$ the system is exactly an antiferromagnetic Heisenberg model, where previous studies support our conclusions [39, 41, 43]. This VBS phase has no analogue on the honeycomb lattice, which forms a Néel ordered ground state. This is due to geometric frustration, where the presence of odd cycles on the star lattice disallows the formation of the Néel AFM phase.

Around $\varphi \sim 1.7\pi$, the system forms an exotic spin triplet VBS. Here, the spins on each bond anti-align in the on-colouring direction and align in the two off-colouring directions. This corresponds to the formation one of three triplet states depending on the bond type. Bonds of type x, y or z form a $|t_x\rangle$, $|t_y\rangle$ or $|t_z\rangle$ state respectively, defined as

$$|t_x\rangle = \frac{i}{\sqrt{2}}\left(|\uparrow\uparrow\rangle - |\downarrow\downarrow\rangle\right), \tag{5.6}$$

$$|t_y\rangle = \frac{1}{\sqrt{2}}\left(|\uparrow\uparrow\rangle + |\downarrow\downarrow\rangle\right), \tag{5.7}$$

$$|t_z\rangle = \frac{-i}{\sqrt{2}}\left(|\uparrow\downarrow\rangle + |\downarrow\uparrow\rangle\right). \tag{5.8}$$

We will show in §5.1.1 that the singlet and triplet VBS phases are also isomorphic under a generalized four unit cell spin rotation.

Around $\varphi \sim 0.5\pi$ and $\varphi \sim 1.5\pi$ the system forms two extended chiral spin liquid phases. We note that the AFM Kitaev phase is stable over a much smaller region of phase space than the FM QSL. This can be explained by noticing that the two competing phases (both the VBS phases) have lower energy than their ferromagnetic counterparts, whereas the energy scale of both Kitaev phases are identical. Thus, as we tune across the phase diagram, the VBS phases very quickly become energetically favourable over the QSL. As in the honeycomb case, all phase transitions corresponded to cusps in the ground state energy, indicating that the transitions are first order. However, it remains an open and numerically challenging question whether they remain first order in the thermodynamic limit.

Finally, we confirm that the pure Kitaev points ($\varphi = 0.5\pi$ or 1.5π) exactly recover the chiral QSL studied Yao and Kivelson [156]. Here, the model is exactly solvable and can be decoupled into non-interacting Majorana fermions in the presence of a static $\mathbb{Z}_2$ gauge field [30]. However, as soon as we tune away from these points (and some Heisenberg interactions are present) the $\mathbb{Z}_2$ gauge field is no longer conserved, and the system ceases to be exactly solvable.

5.1.1 Isometries of the Phase Diagram

One of the remarkable aspects of the Heisenberg-Kitaev model on the honeycomb lattice is a hidden symmetry between different phases of the model [198]. In fact, such a transformation can be performed on a variety of lattices [222]. In this section we discuss a transformation that holds on the star lattice, which will help us to understand the phase diagram and clarify the connection between the distinct types of VBS phases.

Let us introduce a spin transformation by dividing the spins in the system into four sets, each labelled with 0, x, y or z, arranged in a four-unit-cell pattern as shown in Fig. 5.4a. Spins

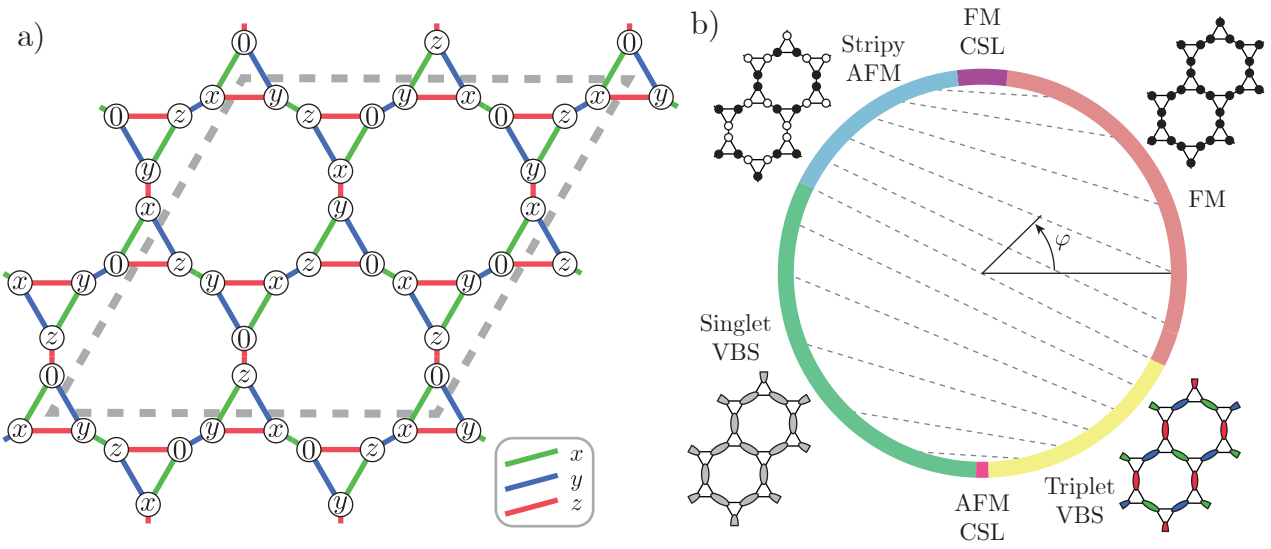


Figure 5.4: **(a)** Plot of the four unit cell transformation that encodes the isometry of the KH phase diagram. Each 0-marked site is untouched, however the sites labelled with x, y or z each experience a π-rotation around the labelled axis in spin space. Bond-types are indicated by colour. Enlarged unit cell is depicted with the dashed rhombus. **(b)** The KH phase diagram as parametrised by φ defined in Eqn. 5.2. Dashed lines indicate points that are isomorphic under the spin rotation.

marked with 0 will be left untouched, however on the other spins we apply a π-rotation in spin space, where the axis of rotation is determined by the site labels. Under such a rotation, the sign of the two spin operators that do not line up with the rotational axis will be flipped, for example if the site j is labelled with x we have

$$\begin{aligned} \sigma_j^x &\to \sigma_j^x \\ \sigma_j^y &\to -\sigma_j^y \\ \sigma_j^z &\to -\sigma_j^z, \end{aligned} \tag{5.9}$$

with a similar relation for y and z-labelled sites.

Under this transformation, we note that every x-bond is always bordered by either a $0-x$ pair of sites or a $y-z$ pair. Thus, every x-type bond operator in H transforms according to

$$\begin{aligned} \sigma_j^x\sigma_k^x &\to \sigma_j^x\sigma_k^x \\ \sigma_j^y\sigma_k^y &\to -\sigma_j^y\sigma_k^y \\ \sigma_j^z\sigma_k^y &\to -\sigma_j^z\sigma_k^y. \end{aligned} \tag{5.10}$$

Similarly, y-bonds are bordered by $0-y$ or $x-z$, and z-bonds are bordered by $0-z$ or $x-y$. These both transform analogously under the spin rotation, where the on-colouring direction remains unchanged and the off-colouring directions have their sign flipped. Thus, our spin rotation is equivalent to transforming the parameters of the Hamiltonian according to

$$K \to K, \;\; J \to -J. \tag{5.11}$$

In terms of the single parameter φ, this is equivalent to transforming to a new $\tilde{\varphi}$ that satisfies

$$\tan\tilde{\varphi} = -\tan\varphi - 1 \tag{5.12}$$

with the correspondence indicated with dashed lines in Fig. 5.4b.

Thus, we see that there is a correspondence between the ferromagnetic Hamiltonian and the stripy ordered Hamiltonian, as well as a correspondence between the singlet VBS and the stripy VBS Hamiltonians. We can similarly verify that the transformation gives the correct relation between the phases: First, The FM case is easy – starting with FM alignment in the z-direction, we can see that any site labelled with x or y has its spin flipped, which leads precisely to the stripy magnetically ordered phase. Second, we look at the more subtle VBS correspondence. A spin singlet on an x-labelled bond will be adjacent to either a $0-x$ pair of sites, in which case the resulting state will be transformed as

$$|s\rangle \sim |\uparrow\downarrow\rangle - |\downarrow\uparrow\rangle \to |\uparrow\uparrow\rangle - |\downarrow\downarrow\rangle \sim |t_x\rangle\,, \tag{5.13}$$

or the bond will border two sites of type $y-z$, in which case the transformation is

$$|s\rangle \sim |\uparrow\downarrow\rangle - |\downarrow\uparrow\rangle \to i\,|\downarrow\downarrow\rangle - i\,|\uparrow\uparrow\rangle \sim |t_x\rangle\,. \tag{5.14}$$

In both cases we see that (up to a phase) the singlet is mapped onto a triplet $|t_x\rangle$ state. Similar arguments apply for y and z-bonds. Thus, from the mapping we observe that the resulting stripy VBS consists of a condensate of triplet states, where each x-bond has a $|t_x\rangle$ triplet, each y-bond has a $|t_y\rangle$ triplet and so on. This is perfectly consistent with our DMRG results.

5.2 A Majorana Parton Mean Field Study

Let us now study the entire phase diagram using a Majorana MFT [221, 225]. The uses of this method are twofold: first we shall corroborate the ground-state phase diagram determined in §5.1 – providing evidence that the results are robust for large system sizes. Secondly, the MFT will allow us to obtain the excitation spectrum of the chiral QSLs away from the soluble points, obtaining the Majorana band structure and Chern numbers as well as the ground state phases. Thus, we shall see that across the extended KSL phases, nonzero Chern numbers of the bulk bands give rise to chiral edge modes whose dispersions are weakly renormalized by the presence of Heisenberg interactions.

We construct the parton description by using the Majorana fermion decomposition originally proposed by Kitaev [30], and presented in Chapter 4. Each spin is represented with four Majorana operators $(c\,b^x\,b^y\,b^z)$, such that $\sigma_j^\alpha \to ic_jb_j^\alpha$. Under this transformation, the Hamiltonian takes the form

$$H = -\sum_{\langle jk\rangle_\alpha}\left[K(ib_j^\alpha c_j)ib_k^\alpha c_k + J\sum_{\bar{\alpha}\neq\alpha}(ib_j^{\bar{\alpha}}c_j)ib_k^{\bar{\alpha}}c_k\right]. \tag{5.15}$$

In order to apply a mean field treatment, the Majorana operators must be paired up into fermionic bilinears, which can then be replaced with their ground state expectation value – resulting in a quadratic Majorana Hamiltonian. Of course, there are several ways that the operators can be paired up, each giving a different MFT channel. We shall consider two

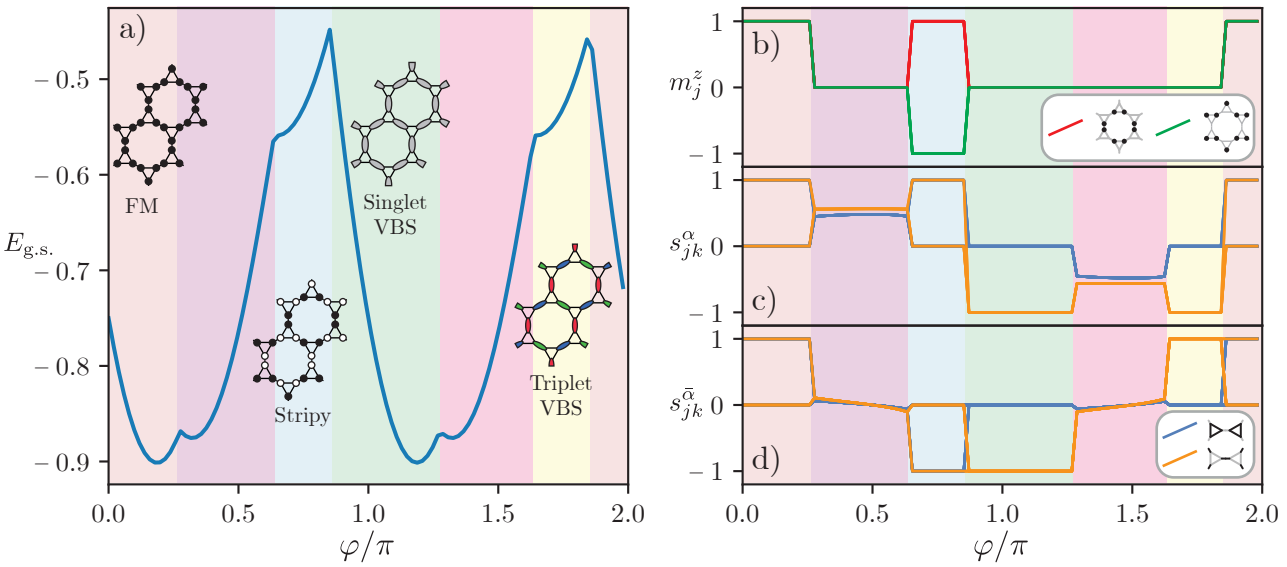


Figure 5.5: The Majorana MFT results for the star lattice KH model as a function of the parameter φ, defined in Eqn. 5.2. Phase boundaries are indicated with background colour. **(a)** Ground state energy per site as a function of φ. The four non-KSL phases are shown with a diagram of the corresponding phase. KSL phases appear at $\varphi = 0.5\pi, 1.5\pi$. **(b)** Expectation values of the z-component of magnetisation for each site on the lattice $m_z = \langle \sigma_j^z \rangle$, found using the magnetically ordered mean field channel. Line colour indicates the site position with respect to arrangement of spins in the stripy phase. **(c)** Spin-spin correlations for each bond in the *on-colouring* direction, $s_{jk}^{\alpha} = \langle \sigma_j^{\alpha} \sigma_k^{\alpha} \rangle$, where we sum over the correlations calculated with both mean field channels. **(d)** Spin-spin correlations for each bond in the two remaining *off-colouring* directions, $\langle \sigma_j^{\alpha} \sigma_k^{\alpha} \rangle$, calculated as in part c. In (c) and (d), correlations for in-triangle bonds are coloured in blue, whereas inter-triangle bonds are shown in orange.

physically-motivated channels for decoupling the Hamiltonian, a spin liquid channel and a magnetically ordered channel.

The Spin Liquid Channel — In the Kitaev limit ($\varphi = 0.5\pi$ or 1.5π) J vanishes completely, leaving only the 'on-colouring' K-part of the Hamiltonian. Here, the Hamiltonian is identical to that presented and solved in Chapter 4. Thus, the set of fermionic operators $\hat{u}_{jk}^{\alpha} = ib_j^{\alpha} b_k^{\alpha}$ are guaranteed to be completely static, commuting with one another and the Hamiltonian. Once we stray from the exact Kitaev limit, off-colouring bond operators are introduced that break the exactly commuting structure of the $\hat{u}_{jk}^{\alpha}$ operators, meaning that no exact solution exists. However, at least in the limit of $J \ll K$ we expect that the spin liquid phase will persist, and propose a mean field decoupling that can capture this state [221, 225]. We start by rearranging the Hamiltonian to the form

$$H = \sum_{\langle jk \rangle_{\alpha}} \left[K(ib_j^{\alpha} b_k^{\alpha}) ic_j c_k + J \sum_{\bar{\alpha} \neq \alpha} (ib_j^{\bar{\alpha}} b_k^{\bar{\alpha}}) ic_j c_k \right], \tag{5.16}$$

and introducing the following two sets of mean field parameters.

$$\langle ic_j c_k \rangle = \chi_{jk} \tag{5.17}$$

$$\langle ib_j^{\alpha} b_k^{\alpha} \rangle = u_{jk}^{\alpha}. \tag{5.18}$$

Using the standard approximation $\hat{U}\hat{V} \approx \langle U\rangle\hat{V} + \hat{U}\langle V\rangle - \langle U\rangle\langle V\rangle$, we transform the Hamiltonian to the form

$$\begin{aligned} H_{SL} = \sum_{\langle jk\rangle_\alpha} \big[\left(K u^\alpha_{jk} + J u^{\bar{\alpha}}_{jk}\right) i c_j c_k \\ + \chi_{jk}(K i b^\alpha_j b^\alpha_k + J i b^{\bar{\alpha}}_j b^{\bar{\alpha}}_k)\big] \\ - \sum_{\langle jk\rangle_\alpha} (K u^\alpha_{jk} + J u^{\bar{\alpha}}_{jk})\chi_{jk}. \end{aligned} \tag{5.19}$$

Note that here and in the following discussion, we will assume summation over the two off-colouring spin operators labelled by $\bar{\alpha}$.

The Magnetically Ordered Channel — In the ferromagnetic case ($\varphi = 0$), we expect the ground state to magnetically align, with some non-zero expectation value for $\langle\sigma^\alpha_j\rangle = \langle i c_j b^\alpha_j\rangle$. Clearly this is not captured by the above mean field theory, so we introduce a second channel using the parameters

$$\langle i b^\alpha_j c_j\rangle = m^\alpha_j. \tag{5.20}$$

Under this parametrisation, the Hamiltonian is decomposed into the following form,

$$\begin{aligned} H_M = -\sum_{\langle jk\rangle} \big[K \left(i m^\alpha_j b^\alpha_k c_k + i b^\alpha_j c_j m^\alpha_k \right) \\ + J \left(i m^{\bar{\alpha}}_j b^{\bar{\alpha}}_k c_k + i b^{\bar{\alpha}}_j c_j m^{\bar{\alpha}}_k \right) \big] \\ + \sum_{\langle jk\rangle} \left[K m^\alpha_j m^\alpha_k + J m^{\bar{\alpha}}_j m^{\bar{\alpha}}_k \right]. \end{aligned} \tag{5.21}$$

Overall, our final mean field Hamiltonian is given by the sum of these two decouplings as $H_{MF} = H_{SL} + H_M$.

The resulting quadratic Hamiltonian is parametrised by the three sets of mean fields, and can be written in terms of the Majorana vector $\Psi = (\boldsymbol{c}, \boldsymbol{b}^x, \boldsymbol{b}^y, \boldsymbol{b}^z)^T$. Here $\boldsymbol{c} = (c_0, c_1 ... c_N)$, with an equivalent description for $\boldsymbol{b}^\alpha$. Thus, the overall Hamiltonian may be expressed as

$$H_{MF}(\chi, u, m) = \Psi^T i A(\chi, u, m)\Psi, \tag{5.22}$$

where A is a real skew-symmetric matrix determined by the mean fields. The ground state expectation value of the mean fields can be determined by diagonalising the matrix iA, finding the matrix projector onto the negative eigenstates P, and then using the identity

$$\langle i\hat{\psi}_j \hat{\psi}_k\rangle = -2iP_{jk}, \tag{5.23}$$

where $\hat{\psi}_j$ is the corresponding Majorana operator at position j in the Majorana vector Ψ.

Thus, a self-consistent MFT can be determined for a given Hamiltonian by starting with an ansatz for the three mean fields. The quadratic Hamiltonian $H_{MF}(\chi, u, m)$ is then created, and the ground state is calculated. Next, updated values for the mean fields are calculated according to Eqns. 5.17, 5.18 and 5.20. Given a new set of mean fields, one can define a new Hamiltonian, and the process can be repeated. This is iterated until a self-consistent set of mean fields is found, where their values no longer change under such an update. This was performed for 100 φ values across the range $[0, 2\pi]$, each time starting from a set of initial ansätze and selecting the

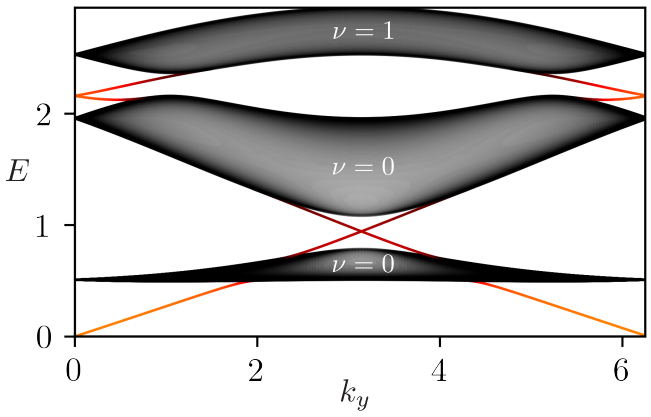


Figure 5.6: The Majorana fermion band structure calculated for the chiral QSL phase within a parton MFT for a strip-geometry, with periodic boundaries in the x-direction and open boundaries in the y direction. We have tuned the model to the antiferromagnetic Kitaev regime ($\alpha = 1.45\pi$) in the vicinity of the soluble point. Energies are plotted as a function of momentum in the y-direction, for a sample with $L_x = L_y = 200$. The Chern number ν of the three bands is labelled. States are coloured according to their inverse participation ratio, where red indicates a localised edge mode and grey a delocalised bulk mode.

final converged state with the lowest energy. In each case, we tested two magnetically ordered ground state ansätze – ferromagnetic and stripy – and two spin liquid ansätze – ferromagnetic and antiferromagnetic Kitaev states. However, in general we note that results often depended on the choice of initial guess – starting with an unphysical initial state, one often converges to an unphysical final state – some physical intuition must be used to ensure the right initial states are chosen.

Results are shown in Fig. 5.5, where we plot the ground state energy, the on-site z-magnetisation, m_j^z, and the spin-spin correlations, which are summed over both mean field channels,

$$s_{jk}^{\alpha} := \langle \sigma_j^{\alpha} \sigma_k^{\alpha} \rangle = m_j^{\alpha} m_k^{\alpha} - \chi_{jk} u_{jk}^{\alpha}. \tag{5.24}$$

Note that in practice the system always converged to a ground state where one of the two decoupling channels vanishes.

Six phases are found, with the phase boundaries shown in Fig. 5.5. Four of these phases – the ferromagnetic and stripe order, as well as the two chiral spin liquid phases – have analogues in the honeycomb KH model. For $\varphi \in [0.83\pi, 1.26\pi]$ a singlet valence bond solid appears. Here, the mean fields on all triangle bonds vanish completely and on inter-triangle bonds we have $\langle \sigma_j^{\alpha} \sigma_k^{\alpha} \rangle = -\chi_{jk} u_{jk}^{\alpha} = -1$ for all α, with $m = 0$, indicating that the spins are fully anti-aligned into a singlet. For $\varphi \in [1.63\pi, 1.83\pi]$, a similar VBS appears with non-zero fields only on the inter-triangle bonds. However, in this case we have $\langle \sigma_j^{\alpha} \sigma_k^{\alpha} \rangle = -1$ for α matching the bond colouring, and $\langle \sigma_j^{\bar{\alpha}} \sigma_k^{\bar{\alpha}} \rangle = +1$ for the two off-colouring directions, $\bar{\alpha}$. This is consistent with a triplet valence bond solid, where on each bond a triplet state forms whose direction depends on the bond colouring.

Now we turn our attention to the topological nature of the Kitaev phases around $\varphi = \pi/2$ and $3\pi/2$. Here, the m-fields vanish, as well as the off-colouring u-fields. This means that the mean field Hamiltonian is block-diagonal, with the c_j Majoranas and three sets of b_j^{α} Majoranas completely decoupled from one another. Thus, we have four decoupled sets of three energy levels. The ground state Chern number is encoded in the c-type Majorana spectrum.

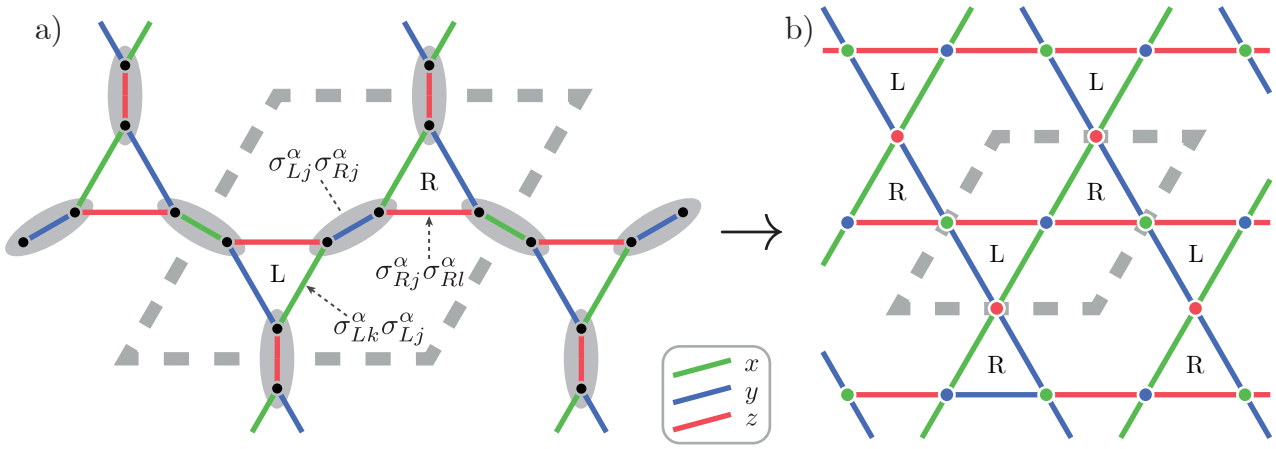


Figure 5.7: **(a)** Diagram of the lattice with positions of spin singlets highlighted in grey. Spins are labelled as $\sigma_{R/L}$ depending on which triangle they form a part of in the unit cell. **(b)** The derived Kagome lattice once all the singlets are collapsed to a single site. Here, both edges and sites have a Kitaev labelling $\alpha \in x, y, z$, denoted by colour.

In both Kitaev phases, the system has two degenerate ground states related by a sign flip of all u fields. This is a generic feature of the Kitaev model on any lattice with odd cycles [156]. The Chern number of the ground state can be calculated from the projector P onto the negative energy eigenstates of the matrix iA. Here, the two degenerate states have Chern numbers ± 1. In open boundaries, this means that chiral edge modes form at the boundaries. An example is shown in Fig. 5.6.

5.3 Triplon Excitations in the VBS

Having found an exact mapping between the VBS phases we now focus on the singlet VBS around $\varphi = \pi$. Our objective is to find an effective description of this phase and analyse its excitation spectrum. The numerics indicate that spin singlets form on the inter-triangle bonds, thus we shall start by pairing the spins on these bonds and transform to the bond operator representation introduced by Sachdev and Bhatt [214, 226]. Spins on a given bond are labelled with σ_L and σ_R, and treated as a single site, collapsing the star lattice into a Kagome lattice, as shown in Fig. 5.7. We can then rewrite the Hamiltonian in a two-spin basis for each dimerised bond, given by Eqns. 5.5-5.8.

In order to apply mean field theory, let us re-express these states in terms of bosonic creation operators. Starting with a vacuum $|0\rangle$ which contains no particles whatsoever, we define four bosonic creation operators that create singlet and triplet states, $s^\dagger |0\rangle = |s\rangle$, $t^\dagger_\alpha |0\rangle = |t_\alpha\rangle$, which satisfy the relevant commutation relations, $[s, s^\dagger] = 1$, $[t_\alpha, t^\dagger_\beta] = \delta_{\alpha\beta}$, $[s, t^\dagger_\alpha] = 0$. In this basis, the spin operators take the following form

$$\sigma^\alpha_L = -i(s^\dagger t_\alpha - t^\dagger_\alpha s) - i\varepsilon_{\alpha\beta\gamma} t^\dagger_\beta t_\gamma, \tag{5.25}$$

$$\sigma^\alpha_R = i(s^\dagger t_\alpha - t^\dagger_\alpha s) - i\varepsilon_{\alpha\beta\gamma} t^\dagger_\beta t_\gamma. \tag{5.26}$$

Of course, in doing so we have artificially enlarged our Hilbert space. For a state to be legitimate, all sites must be populated by a single boson – any state with empty or multiply occupied sites will be in the 'unphysical' part of the extended Hilbert space. Thus, we introduce a chemical

potential term to H that enforces single occupancy per site on average,

$$H_\mu = -\sum_{j\in\mathcal{D}} \mu \left(s_j^\dagger s_j + t_{\alpha j}^\dagger t_{\alpha j} - 1 \right). \tag{5.27}$$

Additionally, we shall model the effect of an applied magnetic field on our triplon bands. For an arbitrary field $\mathbf{h} = (h_x, h_y, h_z)$, the magnetic term in H is $H_h = -\sum_j h_\alpha(\sigma_{jL}^\alpha + \sigma_{jR}^\alpha)$, which, when expressed in terms of our triplon operators, becomes

$$H_h = \sum_j h_\alpha 2i\varepsilon_{\alpha\beta\gamma} t_\beta^\dagger t_\gamma. \tag{5.28}$$

Since we expect the system to form a singlet VBS, let us introduce a real singlet condensate density order parameter $\bar{s} = \langle s_j \rangle$. The three dimers in the unit cell (shown in Fig. 5.7a) are equivalent by C_3 rotation, so we may describe all singlets with the same $\bar{s}$. Finally, the total Hamiltonian can be rewritten as

$$H = H_0 + H_2 + H_4, \tag{5.29}$$

with

$$H_0 = N\left[\bar{s}^2(K + 2J - \mu) + \mu\right], \tag{5.30}$$

$$\begin{aligned} H_2 = &\sum_{j\in\mathcal{D}} (K - 2J - \mu) t_{\alpha j}^\dagger t_{\alpha j} - (K + \mu) t_{\bar{\alpha} j}^\dagger t_{\bar{\alpha} j} + h_\alpha 2i\varepsilon_{\alpha\beta\gamma} t_\beta^\dagger t_\gamma \\ &- \sum_{jk\in\mathcal{D},\alpha} J_{jk}^\alpha \bar{s}^2 \left(t_{\alpha k}^\dagger t_{\alpha j} - t_{\alpha j} t_{\alpha k} + h.c. \right), \end{aligned} \tag{5.31}$$

$$H_4 = -\sum_{jk\in\mathcal{D},\alpha} J_{jk}^\alpha \left(t_{bj}^\dagger t_{bk} t_{ck}^\dagger t_{cj} - t_{bj}^\dagger t_{bk}^\dagger t_{cj} t_{ck} + h.c. \right), \tag{5.32}$$

where the parameter J_{jk}^α represents either K or J, depending on whether α matches the bond colouring or not. In H_4, the indices b and c describe the two directions that do not match α. Note that we have discarded terms with three t_α[1].

Finally, the quartic terms can be decoupled by introducing the following standard mean-fields

$$P_{jk}^\alpha = \langle t_{j\alpha}^\dagger t_{k\alpha} \rangle \tag{5.33}$$

$$Q_{jk}^\alpha = \langle t_{j\alpha} t_{k\alpha} \rangle \tag{5.34}$$

Thus, we are left with a quadratic Hamiltonian $H_{MF}(\mu, \bar{s}, P_{jk}^\alpha, Q_{jk}^\alpha)$ for the triplons and the four parameters are determined self-consistently. A valid ground state is given by choosing μ and $\bar{s}$ such that the Hamiltonian satisfies the saddle point equations

$$\left\langle \frac{\partial H_{MF}}{\partial \mu} \right\rangle = \left\langle \frac{\partial H_{MF}}{\partial \bar{s}} \right\rangle = 0, \tag{5.35}$$

where the expectation value is calculated in the ground state. Furthermore, P and Q must satisfy the self-consistency relations (Eqns. 5.33 and 5.34). Self-consistent values for $\mu, \bar{s}, P$ and

[1]The Kagome lattice admits a reflection that swaps L and R triangles, which reverses the sign of the triple t terms. Since the original spin system is invariant to this transformation we expect that these terms should vanish.

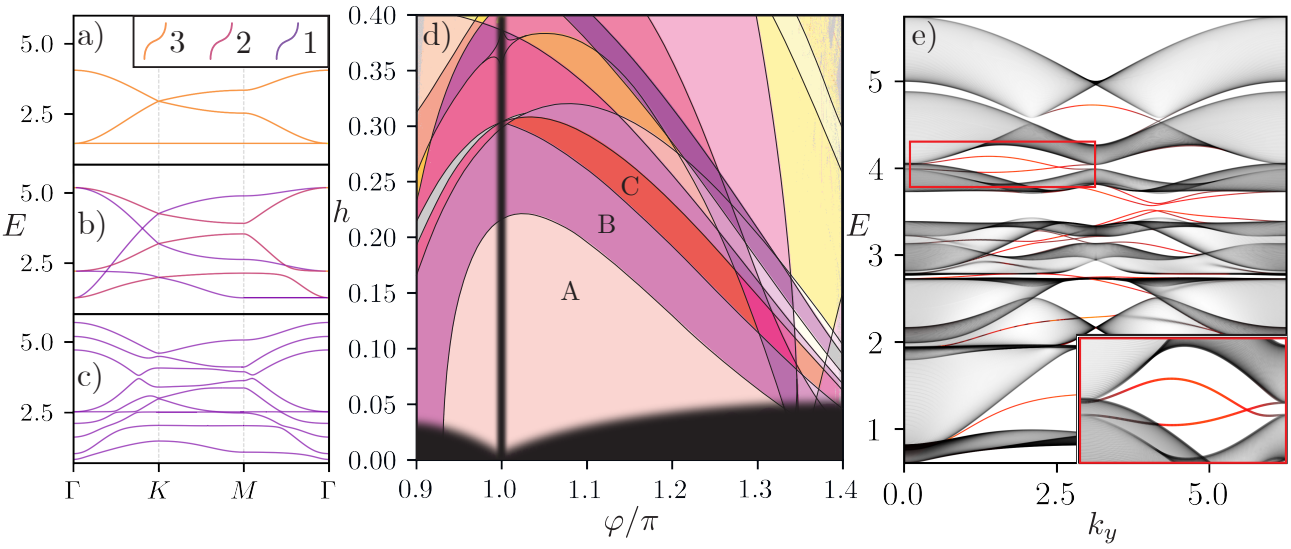


Figure 5.8: **(a-c)** Triplon excitation band structure, with the degeneracy of each energy indicated by line colour – a legend is provided at the top of panel a. **(a)** Band structure for the pure Heisenberg case ($\varphi = \pi$) with no applied field. The triple degenerate energy levels correspond to states t_α with $\alpha = x, y, z$. **(b)** The band structure for a system with some Kitaev anisotropy ($\alpha = 1.25\pi \implies K \sim -2.1, J \sim -0.71$) and zero magnetic field. Here the triple degenerate bands are split into one double degenerate band and one non-degenerate band, however all bands remain gapless. **(c)** The band structure in the above case ($\varphi = 1.25\pi$), with an applied magnetic field ($h = 0.15$). Here we see that all bands are non-degenerate and gapped. **(d)**A plot showing the rich phase diagram of possible Chern numbers for the nine triplon bands as a function of the two parameters: Kitaev anisotropy (α) and applied magnetic field (h). Regions where the bands are gapless are indicated in black and regions where the numerical process failed to converge to a stable solution are shown in grey. Each area with a distinct colouring represents a different set of the Chern numbers of the nine bands. For example the region labelled A has Chern numbers $(-1, 3, -5, 6, -6, 6, -5, 3, -1)$, the B region has $(-1, 3, -5, 6, -6, 3, -2, 3, -1)$, and the C region has $(-1, 3, 1, 0, -6, 3, -2, 3, -1)$. **(e)** Band structure for a strip system with periodic boundaries in the y-direction and open boundaries in the x-direction. We have set $\varphi = 1.25\pi$, $h = 0.15$ - thus are in region B. Bands are plotted as a function of k_y for a strip containing 130 unit cells in the x-direction. States are coloured by their inverse participation ratio, $\text{IPR} = \sum_x |\psi(x)|^4$, where red indicates a localised edge mode, and grey indicates a delocalised bulk mode. Inset shows an enlarged section of the band structure, where a pair of edge modes can be seen connecting two otherwise gapped bands.

Q are determined by using a root finding algorithm (`scipy.optimize.root`) to converge to a set of mean fields that satisfy these conditions. At each step of the iteration, the Hamiltonian is solved using the bosonic Bogoliubov-de-Gennes method [227], and the mean fields are determined from the bosonic ground state. Details for the method are given in Appendix D.2.

We now investigate the triplon excitation spectrum obtained from the self-consistently determined Hamiltonian. Since the unit cell contains 3 sites, each hosting three triplon states, the excitation spectrum will contain 9 energy levels. Provided these are gapped, the Chern number of each band can be calculated. A detailed description of the Bogoliubov-de-Gennes method and how the topological invariants are obtained is provided in Appendix D.

Triplon spectra were determined using two parameters to tune the Hamiltonian. The Kitaev anisotropy (i.e. the relative strength of K/J) was controlled by sweeping over a range of $\varphi \in [0.9\pi, 1.4\pi]$, approximately the range over which the system forms a stable VBS. Additionally, we applied a magnetic field in the $(1,1,1)$ direction, sweeping over a range of field strengths $h_\alpha = h \in [0, 0.35]$. The results for these calculations are shown in Fig. 5.8.

In the pure Heisenberg limit, we have three exactly degenerate triplon bands, each corresponding to a t_x, t_y or t_z-type excitation, with a Dirac-like band touching at the Γ point. In order to allow for topological excitations to form, two ingredients are needed: gaps need to be opened between the bands, and TRS must be broken to allow for non-zero Chern number. Applying a magnetic field to the Heisenberg system is not sufficient for topological bands, as a field simply splits the three degenerate triplons with an energy shift, producing a $|\uparrow\uparrow\rangle$ state aligned with the field with slightly lower energy, a $|\downarrow\downarrow\rangle$ state with slightly higher energy, and a $|\uparrow\downarrow\rangle + |\downarrow\uparrow\rangle$ band that is unaffected. Similarly, introducing only a Kitaev anisotropy $\varphi \neq \pi$ is also insufficient as the bosonic Hamiltonian retains TRS. Spectra for these cases are shown in Fig. 5.8a and b.

However, in the presence of both a magnetic field and the Kitaev anisotropy, the system generally has nine distinct gapped triplon bands, shown in Fig. 5.8c. Most interestingly, the bands have a rich phase diagram of possible Chern numbers depending on these two parameters. A full phase diagram is shown in Fig. 5.8d. With open boundaries, the bands then have chiral triplon edge modes by the bulk-edge correspondence, an example is shown in Fig. 5.8e.

Chapter 6

Conclusion and Outlook

Let us finish by summarising the three projects discussed in this thesis, and commenting on future prospects, presenting in each case a few open questions that could provide a fruitful avenue for further research.

6.1 Local Markers

In Chapter 3, we considered the role of band topology in insulators where the presence of disorder makes the notion of band structure ill-defined. In particular, we asked whether it was possible to construct a topological invariant analogous to the Chern number, that could be robustly formulated without a notion of k-space. We provided a review of three approaches to this problem, each proposing a different way to build a local 'marker' of Chern number [30, 32, 33], and discussed the ways that these quantities are related to one another. In each of these proposals, the local Chern number was constructed without a clear understanding of whether these may be measured as a real, physical observable. This approach has two drawbacks. Firstly, the markers are of little use to an experimentalist, since there is no obvious physical observable to which they correspond. Secondly, although the markers are useful theoretical tools, they do not provide a satisfying intuitive answer to the question of what it meant for a material to have a physical notion of local topology. In §3.3 we proposed a solution to this problem by constructing a physical observable – a localised Hall conductivity – that corresponds exactly to Kitaev's local Chern marker [30] when evaluated in the adiabatic limit. We provided a careful discussion of the exact operators that must be measured to give a quantised topological result, in particular showing that an extremely weak notion of local conductivity is required, where we must be able to differentiate between conductivity that is localised around a point deep within the bulk of the system and the conductivity that is transported along the edge modes, with no current in the in-between area. Nevertheless, many open questions remain.

Firstly, the arguments used to derive this local observable are essentially a prescription for measuring the quantity in the lab: a step-function potential is used to excite current across the system in the vertical direction. The cross-conductance is then determined by measuring the horizontal transport of electrons across a line dividing the system. Thus, an obvious next step will be to look at experimentally verifying the proposed method. In particular, note that the observable we present benefits from many of the remarkably invariant properties of Kitaev's marker, which we discussed in §3.2. The step function potential can be smoothed into a localised

slope, and the two lines – one for an electric field and one for a measurement – need not be exactly perpendicular.

From a theory perspective, this proposal also suggests a number of avenues for further study. One particularly interesting example comes when considering how these markers may be extended to strongly interacting matter, especially since the Chern number was shown by Niu, Thouless and Wu to have a straightforward many-body construction as an integral over twisted boundary conditions [97]. In general, local markers have been constructed in a purely non-interacting context, as a property of the projector onto a band of single-particle states. However, in any interacting system, the ground state corresponds to a single highly complex state, and it is usually impossible to separate this into single-particle states. Thus, one cannot use the existing constructions of these local markers, although some progress has been made using Green's functions [31]. Although the marker itself does not work in a many-body context, the intuitive picture we have presented – that of currents and fields – is still applicable. An interesting avenue of further study is to test whether it is possible to exploit this physical picture in order to construct a local Chern marker that is robust in a many-body framework. In particular, the Kitaev honeycomb model (and Kitaev materials in general) presents an interesting challenge, since the signature of the non-Abelian phase in the Kitaev model is a quantised *thermal* Hall effect. It remains an open question whether a similar reasoning can be used to define a localised measure of thermal conductivity [228] that was robust even away from the exactly solvable Kitaev point.

Finally, this thesis has focussed exclusively on two-dimensional phases with no special symmetries – those characterised by the Chern number. However, this is a small window into a much larger classification, that of symmetry-protected topological (SPT) phases [229]. Depending on dimensionality and symmetry, a broader range of topological phases can be constructed with qualitatively different invariants, for example winding numbers in the Su-Schrieffer-Heeger model [230], $\mathbb{Z}_2$-type invariants found on the Kitaev Chain [231], or the Bernevig-Hughes-Zhang model [232]. In general, local markers have been constructed for many of these phases [107, 233–235], however few have been constructed using Kitaev's original formalism, and even fewer with a robust physical interpretation. Thus, a valuable extension would be to look at extending the arguments presented here to across the full classification of SPT phases.

6.2 The Amorphous Kitaev Model

In Chapter 4 we turned our attention to the Kitaev honeycomb model [30]. We started by providing a review of the model, and explaining the Majorana fermion construction used to find an exact solution, showing how the Hamiltonian may be re-expressed in terms of a $\mathbb{Z}_2$ gauge field, and discussed the role of time reversal symmetry. We presented the full ground-state phase diagram containing the three 'toric code' A_α phases, as well as the gapless B phase and discussed how the addition of a magnetic field can serve to open a gap, allowing the phase to host non-Abelian anyonic excitations. In §4.2 we presented a general method for constructing and solving the Kitaev Hamiltonian, using the Majorana method, on an arbitrary three-coordinated lattice. This included the method for assigning a valid edge-colouring, as well as showing how the $\mathbb{Z}_2$ fluxes can be calculated on an arbitrary lattice and providing numerical evidence for the conjecture that the ground state flux sector could be found in any lattice according to a simple counting rule. We presented the full ground-state phase diagram and showed that an analogous phase to Kitaev's original non-Abelian B phase exists. We calculated the Chern number using

the local markers discussed in the previous chapter, and demonstrated the presence of edge modes in this phase. Finally, we discussed the role of disordering the coupling strengths, showing that the gapped phases were robust against such disorder. Finally, we concluded that the Kitaev spin liquid ground state is robust on a general lattice, providing the first example of an amorphous quantum spin liquid.

Of course, the most obvious next step is to look for a physical material that might be able to realise a Hamiltonian with dominant Kitaev-type interactions on an amorphous lattice. There are a number of promising candidates, for example it has recently been shown that the Kitaev material Li_2IrO_3 can be created with amorphous structure [147]. In fact, by using the standard method of repeated liquifying and fast cooling any crystalline material can be made amorphous [132, 136, 148, 149], opening the possibility for exploring a wide variety of non-crystalline Kitaev materials. We expect that an experimental signature of a chiral amorphous QSL would be a half-quantized thermal Hall effect similar to the magnetic field induced behaviour of honeycomb Kitaev materials [207, 208, 236, 237].

Every result presented in §4.2 depends on our ansatz for the ground-state flux sector, which is an extension of the theorem proved by Lieb in 1994 [158]. However, this theorem remains unproven, and we were only able to collect compelling numerical evidence to support the conjecture. In §4.2.3.1 we provided some analytical progress, suggesting that – at least at the lowest order that each plaquette appears in the energy – Lieb's ansatz seems correct. Thus, a very interesting next step would be to find a route towards proving this theorem.

In our analysis, we largely focussed on the non-Abelian B phase, however there is good reason to suspect that new physics could be found also by considering the 'toric code' phases found by setting only one bond type to be much stronger than the other two. This would effectively form a dimerisation of the lattice, with the dimers weakly interacting through the remaining two bond types. Kitaev showed in the original work that these weak interactions could be treated using perturbation theory, arriving at an effective Hamiltonian where the couplings formed loop operators around each (square – since two bonds in each hexagon formed a dimer) plaquette. This provided a mapping onto the toric code model [176]. The Kitaev model has been studied extensively in this limit, on the honeycomb as well as star lattice [177–179], however no work has been done to understand the amorphous case. This is particularly exciting since the order in perturbation that a loop operator appears depends on the number of sides in the constituent plaquette, meaning that the amorphous lattice has the potential to realise a much richer and more complex effective system than the honeycomb case.

Finally, we also note that the classical Kitaev model warrants investigation in an amorphous context. Firstly, the degenerate manifold of classical states presented in §1.2.2 can be straightforwardly extended to the amorphous model. In the honeycomb case, even the $S \gg 1$ model has been shown to form a quantum spin liquid state – remarkably also equivalent to the toric code [51, 53]. The construction of this QSL phase relied extensively on the symmetries of the lattice: the system preferentially orders in a small subset of the Cartesian states due to the effect of fluctuations, forming a honeycomb super-lattice of frozen spin dimers. Each of these pseudospins then act as an effective spin-$\frac{1}{2}$ interacting according to a toric code Hamiltonian. Due to the strong dependence of this argument on the symmetries of the honeycomb lattice, it would be worth investigating whether Cartesian states are still selected by fluctuations on an amorphous lattice, and whether these models are also able to realise an effective toric code phase.

6.3 Triplons and the Kitaev-Heisenberg Model

In Chapter 5, we considered an extension of the Kitaev honeycomb model to include the more 'physical' influence of Heisenberg couplings. This was motivated by research that had shown that a number of candidate materials exist, such as the iridates Na_2IrO_3 and α-Li_2IrO_3 [70–72], as well as α-$RuCl_3$ [73, 74] which have been conjectured to realise a dominant Kitaev interaction, as well as other subdominant terms such as Heisenberg coupling, motivating an effective description in terms of the Kitaev-Heisenberg (KH) model. On the honeycomb, this model was shown to have a ground-state phase diagram containing the expected QSL phases, as well as a variety of classically magnetically ordered phases such as ferro-, antiferromagnetic and stripy ordering [198–200].

In light of the previous chapter, where we showed that the QSL phase was remarkably insensitive to changes in the lattice geometry, we considered how the phase diagram as a whole would depend on lattice geometry. To probe this question, we focussed on the breaking of sublattice symmetry, constructing the KH model on the star lattice – one of the simplest examples of a lattice with odd cycles. Three methods were used to explore the model. First, we used state-of-the-art DMRG [224] to numerically determine the ground state across the entire parameter range of the KH model. Next, we tested the robustness of the phase diagram using a Majorana mean field calculation, verifying that – at least in a mean field context – the phases were robust in the thermodynamic limit. Additionally, we constructed a local transformation, showing that the ground state phase diagram had a hidden symmetry, where different phases could be exactly mapped onto one another by a local spin rotation. We found some familiar phases, the ferromagnetic and QSL phases could be constructed similarly as in honeycomb case. However, the investigation also revealed a pair of valence bond solid (VBS) phases – a singlet phase and a triplet phase – which had no honeycomb analogue. These phases formed due to the geometric frustration of Néel order. Next, we characterised the singlet VBS phase by constructing a bosonic mean field theory following Sachdev and Bhatt's bond operator formalism [214]. This allowed us to characterise the triplon excitations that form in such a VBS. Finally, by considering the effect of an applied $[1, 1, 1]$ magnetic field, we showed that the triplon bands realised a rich variety of topological bands and confirmed the existence of topologically protected triplon edge modes.

The work opens a number of possible avenues of further study. Firstly, we emphasise that the star lattice was chosen because it provided the simplest example of a tri-coordinated lattice breaking bipartite symmetry, and because several studies existed for the star-lattice Heisenberg model, allowing us to benchmark our results [39–44]. However, the ultimate goal is to understand the properties of the Kitaev-Heisenberg phase diagram on general amorphous lattices. In particular, one motivation for this study was the possibility that, by geometrically frustrating many of the competing phases, it might be possible to tune the lattice geometry such that the QSL phase was stable over a larger region of phase space. This is especially relevant since many candidate Kitaev materials are expected to sit reasonably close to the transition to a QSL phase, but none have been shown conclusively to realise it yet. This question remains open. Certainly in the case of the star lattice the answer is negative (see Fig. 5.2), however this does not necessarily apply to all lattices that break sublattice symmetry. Thus, it will be worth repeating this study on a larger range of lattices, and investigating the resulting phase boundaries to see if the robustness of the QSL phase can be improved just through lattice geometry.

There is also a rich variety of further modifications that one could make to the Hamiltonian to further assess the robustness of these phases and their chiral excitations. This is particularly timely in light of recent experimental work which demonstrated the successful synthesis of a

spin 1/2 star lattice structure with antiferromagnetic couplings [211]. The material is expected to have intra-triangle couplings much stronger than the inter-triangle couplings. Thus, it would be worth considering how the phase diagram is affected when the relative strength of these two symmetry-inequivalent couplings is adjusted. In addition, it would be interesting to derive microscopic Hamiltonians based on the microscopic orbital configuration and ab-initio calculations, e.g. considering the effect of including symmetric off-diagonal exchanges [197, 225], as well as Dzyaloshinskii-Moriya interactions [238, 239].

The new triplet VBS phase we discover around $\varphi \approx 1.7\pi$ in Fig. 5.2 shows intriguing topological triplet and singlet excitations but many open questions remain. For example, in the absence of an external magnetic field, the dynamics are expected to be identical to the singlet VBS phase due to the four-unit-cell rotation discussed in §5.1.1. However, an applied magnetic field breaks this symmetry, and the possibility remains that this phase could have qualitatively very different properties than the singlet VBS. In addition, it will be important to understand the stability of these topological triplons as well as their experimental signatures.

Bibliography

[1] F. Bloch, "Über die Quantenmechanik der Elektronen in Kristallgittern", Zeitschrift für Physik **52**, 555–600 (1929).

[2] J. C. Slater and G. F. Koster, "Simplified LCAO method for the periodic potential problem", Phys. Rev. **94**, 1498–1524 (1954).

[3] W. A. Harrison, "Tight-binding methods", Surface Science **299-300**, 298–310 (1994).

[4] S. H. Simon, *The Oxford solid state basics*, 1st ed (Oxford University Press, Oxford, 2013).

[5] A. Nussbaum, "Crystal symmetry, group theory, and band structure calculations", in , Vol. 18, edited by F. Seitz and D. Turnbull, Solid State Physics (Academic Press, 1966), pp. 165–272.

[6] N. F. Mott, "The basis of the electron theory of metals, with special reference to the transition metals", Proceedings of the Physical Society. Section A **62**, 416 (1949).

[7] S. B. Roy, *Mott insulators*, 2053-2563 (IOP Publishing, 2019).

[8] V. L. Ginzburg and L. D. Landau, "On the Theory of superconductivity", Zh. Eksp. Teor. Fiz. **20**, edited by D. ter Haar, 1064–1082 (1950).

[9] K. G. Wilson, "The renormalization group: critical phenomena and the kondo problem", Rev. Mod. Phys. **47**, 773–840 (1975).

[10] L. Onsager, "Crystal statistics. i. a two-dimensional model with an order-disorder transition", Phys. Rev. **65**, 117–149 (1944).

[11] J. Cardy, *Scaling and renormalization in statistical physics*, Cambridge Lecture Notes in Physics (Cambridge University Press, 1996).

[12] P. M. Chaikin and T. C. Lubensky, *Principles of condensed matter physics* (Cambridge University Press, 1995).

[13] B. Jeckelmann and B. Jeanneret, "The quantum Hall effect as an electrical resistance standard", Measurement Science and Technology **14**, 1229–1236 (2003).

[14] B. I. Halperin, "Quantized hall conductance, current-carrying edge states, and the existence of extended states in a two-dimensional disordered potential", Phys. Rev. B **25**, 2185–2190 (1982).

[15] P. Drude, "Zur elektronentheorie der metalle", Annalen der Physik **306**, 566–613 (1900).

[16] K. V. Klitzing, G. Dorda, and M. Pepper, "New Method for High-Accuracy Determination of the Fine-Structure Constant Based on Quantized Hall Resistance", en, Phys. Rev. Lett. **45**, 494–497 (1980).

[17] K. von Klitzing, "The quantized hall effect", Rev. Mod. Phys. **58**, 519–531 (1986).

[18] R. B. Laughlin, "Quantized Hall conductivity in two dimensions", en, Phys. Rev. B **23**, 5632–5633 (1981).

[19] H. Aoki and T. Ando, "Critical localization in two-dimensional landau quantization", Phys. Rev. Lett. **54**, 831–834 (1985).

[20] S. Hikami, "Localization Length and Inverse Participation Ratio of Two Dimensional Electron in the Quantized Hall Effect", Progress of Theoretical Physics **76**, 1210–1221 (1986).

[21] J. T. Chalker and P. D. Coddington, "Percolation, quantum tunnelling and the integer Hall effect", Journal of Physics C: Solid State Physics **21**, 2665 (1988).

[22] R. E. Prange, "Quantized hall resistance and the measurement of the fine-structure constant", Phys. Rev. B **23**, 4802–4805 (1981).

[23] D. J. Thouless, M. Kohmoto, M. P. Nightingale, and M. den Nijs, "Quantized Hall Conductance in a Two-Dimensional Periodic Potential", Phys. Rev. Lett. **49**, 405–408 (1982).

[24] R. Kubo, "Statistical-Mechanical Theory of Irreversible Processes. I. General Theory and Simple Applications to Magnetic and Conduction Problems", Journal of the Physical Society of Japan **12**, 570–586 (1957).

[25] M. Berry, "Quantal phase factors accompanying adiabatic changes", en, Proceedings of the Royal Society of London. A. Mathematical and Physical Sciences **392**, 45–57 (1984).

[26] B. Simon, "Berry's Phase, TKNN Integers and All That: My work on Topology in Condensed Matter Physics 1983-1993", IST QM3 - Quantum Matter meets Maths, 2020.

[27] J. E. Avron, R. Seiler, and B. Simon, "Homotopy and Quantization in Condensed Matter Physics", Phys. Rev. Lett. **51**, 51–53 (1983).

[28] B. Simon, "Holonomy, the quantum adiabatic theorem, and berry's phase", Phys. Rev. Lett. **51**, 2167–2170 (1983).

[29] Y. Hatsugai, "Chern number and edge states in the integer quantum Hall effect", Phys. Rev. Lett. **71**, 3697–3700 (1993).

[30] A. Kitaev, "Anyons in an exactly solved model and beyond", en, Annals of Physics, January Special Issue **321**, 2–111 (2006).

[31] A. A. Markov and A. N. Rubtsov, "Local marker for interacting topological insulators", Phys. Rev. B **104**, L081105 (2021).

[32] T. A. Loring, *A guide to the bott index and localizer index*, 2019.

[33] R. Bianco and R. Resta, "Mapping topological order in coordinate space", Phys. Rev. B **84**, 241106 (2011).

[34] C. N. Varney, K. Sun, M. Rigol, and V. Galitski, "Topological phase transitions for interacting finite systems", Phys. Rev. B **84**, 241105 (2011).

[35] J. Richter, J. Schulenburg, and A. Honecker, "Quantum magnetism in two dimensions: from semi-classical néel order to magnetic disorder", in *Quantum magnetism*, edited by U. Schollwöck, J. Richter, D. J. J. Farnell, and R. F. Bishop (Springer Berlin Heidelberg, Berlin, Heidelberg, 2004), pp. 85–153.

[36] D. A. Huse and V. Elser, "Simple variational wave functions for two-dimensional heisenberg spin-$\frac{1}{2}$ antiferromagnets", Phys. Rev. Lett. **60**, 2531–2534 (1988).

[37] R. R. P. Singh and D. A. Huse, "Three-sublattice order in triangular- and kagomé-lattice spin-half antiferromagnets", Phys. Rev. Lett. **68**, 1766–1769 (1992).

[38] S. R. White and A. L. Chernyshev, "Neél order in square and triangular lattice heisenberg models", Phys. Rev. Lett. **99**, 127004 (2007).

[39] J. Richter, J. Schulenburg, A. Honecker, and D. Schmalfuß, "Absence of magnetic order for the spin-half Heisenberg antiferromagnet on the star lattice", Phys. Rev. B **70**, 174454 (2004).

[40] T.-P. Choy and Y. B. Kim, "Classification of quantum phases for the star-lattice antiferromagnet via a projective symmetry group analysis", Phys. Rev. B **80**, 064404 (2009).

[41] B.-J. Yang, A. Paramekanti, and Y. B. Kim, "Competing quantum paramagnetic ground states of the Heisenberg antiferromagnet on the star lattice", Phys. Rev. B **81**, 134418 (2010).

[42] S. S. Jahromi and R. Orús, "Spin-$\frac{1}{2}$ heisenberg antiferromagnet on the star lattice: competing valence-bond-solid phases studied by means of tensor networks", Phys. Rev. B **98**, 155108 (2018).

[43] S. S. Jahromi, R. Orús, M. Kargarian, and A. Langari, "Infinite projected entangled-pair state algorithm for ruby and triangle-honeycomb lattices", Phys. Rev. B **97**, 115161 (2018).

[44] S.-J. Ran et al., "Emergent spin-1 trimerized valence bond crystal in the spin-1 2 Heisenberg model on the star lattice", Phys. Rev. B **97**, 075146 (2018).

[45] A. P. Ramirez, "Strongly geometrically frustrated magnets", Annual Review of Materials Science **24**, 453–480 (1994).

[46] R. Moessner, "Magnets with strong geometric frustration", Canadian Journal of Physics **79**, 1283–1294 (2001).

[47] J. T. Chalker, "Geometrically frustrated antiferromagnets: statistical mechanics and dynamics", in *Introduction to frustrated magnetism: materials, experiments, theory*, edited by C. Lacroix, P. Mendels, and F. Mila (Springer Berlin Heidelberg, Berlin, Heidelberg, 2011), pp. 3–22.

[48] S. Kobe and T. Klotz, "Frustration: how it can be measured", Phys. Rev. E **52**, 5660–5663 (1995).

[49] I. Ritchey, P. Chandra, and P. Coleman, "Spin folding in the two-dimensional heisenberg kagomé antiferromagnet", Phys. Rev. B **47**, 15342–15345 (1993).

[50] J. T. Chalker, P. C. W. Holdsworth, and E. F. Shender, "Hidden order in a frustrated system: properties of the heisenberg kagomé antiferromagnet", Phys. Rev. Lett. **68**, 855–858 (1992).

[51] G. Baskaran, D. Sen, and R. Shankar, "Spin-S kitaev model: classical ground states, order from disorder, and exact correlation functions", Phys. Rev. B **78**, 115116 (2008).

[52] A. M. Samarakoon et al., "Comprehensive study of the dynamics of a classical kitaev spin liquid", Phys. Rev. B **96**, 134408 (2017).

[53] I. Rousochatzakis, Y. Sizyuk, and N. B. Perkins, "Quantum spin liquid in the semiclassical regime", Nature Communications **9**, 1575 (2018).

[54] H. Ma, "$\mathbb{Z}_2$ Spin liquids in the higher spin-S kitaev honeycomb model: an exact deconfined $\mathbb{Z}_2$ gauge structure in a nonintegrable model", Phys. Rev. Lett. **130**, 156701 (2023).

[55] G. H. Wannier, "Antiferromagnetism. the triangular ising net", Phys. Rev. **79**, 357–364 (1950).

[56] P. W. Kasteleyn, "Dimer Statistics and Phase Transitions", Journal of Mathematical Physics **4**, 287–293 (1963).

[57] S. Mugiraneza and A. M. Hallas, "Tutorial: a beginner's guide to interpreting magnetic susceptibility data with the Curie-Weiss law", Communications Physics **5**, 95 (2022).

[58] C. Castelnovo, R. Moessner, and S. L. Sondhi, "Magnetic monopoles in spin ice", Nature **451**, 42–45 (2008).

[59] C. Castelnovo, R. Moessner, and S. Sondhi, "Spin ice, fractionalization, and topological order", Annual Review of Condensed Matter Physics **3**, 35–55 (2012).

[60] M. Udagawa and L. Jaubert, eds., *Spin Ice*, Vol. 197, Springer Series in Solid-State Sciences (Springer International Publishing, Cham, 2021).

[61] J. Knolle and R. Moessner, "A Field Guide to Spin Liquids", Annual Review of Condensed Matter Physics **10**, 451–472 (2019).

[62] L. Savary and L. Balents, "Quantum spin liquids: a review", Reports on Progress in Physics **80**, 016502 (2017).

[63] R. B. Laughlin, "Nobel lecture: fractional quantization", Rev. Mod. Phys. **71**, 863–874 (1999).

[64] R. Peierls, "Zur Theorie des Diamagnetismus von Leitungselektronen", Zeitschrift für Physik **80**, 763–791 (1933).

[65] X. G. Wen, "Mean-field theory of spin-liquid states with finite energy gap and topological orders", Phys. Rev. B **44**, 2664–2672 (1991).

[66] X.-G. Wen, *Quantum Field Theory of Many-Body Systems: From the Origin of Sound to an Origin of Light and Electrons* (Oxford University Press, Sept. 2007).

[67] M. Oshikawa and T. Senthil, "Fractionalization, Topological Order, and Quasiparticle Statistics", en, Phys. Rev. Lett. **96**, 060601 (2006).

[68] S. F. Edwards and P. W. Anderson, "Theory of spin glasses", Journal of Physics F: Metal Physics **5**, 965 (1975).

[69] K. Binder and A. P. Young, "Spin glasses: experimental facts, theoretical concepts, and open questions", Rev. Mod. Phys. **58**, 801–976 (1986).

[70] Y. Singh and P. Gegenwart, "Antiferromagnetic mott insulating state in single crystals of the honeycomb lattice material Na_2IrO_3", Phys. Rev. B **82**, 064412 (2010).

[71] Y. Singh et al., "Relevance of the heisenberg-kitaev model for the honeycomb lattice iridates A_2IrO_3", Phys. Rev. Lett. **108**, 127203 (2012).

[72] A. Revelli et al., "Fingerprints of kitaev physics in the magnetic excitations of honeycomb iridates", Phys. Rev. Res. **2**, 043094 (2020).

[73] L. J. Sandilands et al., "Scattering continuum and possible fractionalized excitations in $\alpha-RuCl_3$", Phys. Rev. Lett. **114**, 147201 (2015).

[74] A. Banerjee et al., "Proximate Kitaev quantum spin liquid behaviour in a honeycomb magnet", Nature Materials **15**, 733–740 (2016).

[75] P. d'Ornellas, R. Barnett, and D. K. K. Lee, "Quantized bulk conductivity as a local Chern marker", Phys. Rev. B **106**, 155124 (2022).

[76] G. Cassella et al., "An exact chiral amorphous spin liquid", Nature Communications **14**, 6663 (2023).

[77] P. d'Ornellas and J. Knolle, "Kitaev-heisenberg model on the star lattice: from chiral majorana fermions to chiral triplons", Phys. Rev. B **109**, 094421 (2024).

[78] P. d'Ornellas, "Forces between kinks in ϕ^8 theory", Journal of Physics Communications **4**, 055014 (2020).

[79] D. Xiao, M.-C. Chang, and Q. Niu, "Berry phase effects on electronic properties", Reviews of Modern Physics **82**, 1959–2007 (2010).

[80] D. Vanderbilt, *Berry phases in electronic structure theory*, English (Cambridge University Press, 2018).

[81] J. K. Asbóth, L. Oroszlány, and A. Pályi, *A Short Course on Topological Insulators: Band Structure and Edge States in One and Two Dimensions*, Lecture Notes in Physics (Springer International Publishing, 2016).

[82] R. Resta, "Geometry and Topology in Electronic Structure Theory", Lecture Notes, 2020.

[83] X. L. Qi, Y. S. Wu, and S. C. Zhang, "Topological quantization of the spin Hall effect in two-dimensional paramagnetic semiconductors", Phys. Rev. B **74**, 085308 (2006).

[84] J. K. Asbóth, L. Oroszlány, and A. Pályi, "Berry Phase, Chern Number", in *A Short Course on Topological Insulators: Band Structure and Edge States in One and Two Dimensions*, Lecture Notes in Physics (Springer International Publishing, Cham, 2016), pp. 23–44.

[85] X.-L. Qi, Y.-S. Wu, and S.-C. Zhang, "General theorem relating the bulk topological number to edge states in two-dimensional insulators", Phys. Rev. B **74**, 045125 (2006).

[86] M. Z. Hasan and C. L. Kane, "Colloquium: Topological insulators", Reviews of Modern Physics **82**, 3045–3067 (2010).

[87] X.-L. Qi and S.-C. Zhang, "Topological insulators and superconductors", Reviews of Modern Physics **83**, 1057–1110 (2011).

[88] F. D. M. Haldane, "Model for a Quantum Hall Effect without Landau Levels: Condensed-Matter Realization of the "Parity Anomaly"", en, Phys. Rev. Lett. **61**, 2015–2018 (1988).

[89] C. K. Chiu, J. C. Y. Teo, A. P. Schnyder, and S. Ryu, "Classification of topological quantum matter with symmetries", Reviews of Modern Physics **88**, 035005 (2016).

[90] P. Delplace, J. B. Marston, and A. Venaille, "Topological origin of equatorial waves", Science **358**, 1075–1077 (2017).

[91] L. M. Nash et al., "Topological mechanics of gyroscopic metamaterials", Proceedings of the National Academy of Sciences **112**, 14495–14500 (2015).

[92] M. Xiao et al., "Geometric phase and band inversion in periodic acoustic systems", Nature Physics **11**, 240–244 (2015).

[93] N. P. Mitchell et al., "Amorphous topological insulators constructed from random point sets", Nature Physics **14**, 380–385 (2018).

[94] R. Resta, "Macroscopic polarization from electronic wave functions", International Journal of Quantum Chemistry **75**, 599–606 (1999).

[95] D. Vanderbilt and R. D. King-Smith, "Electric polarization as a bulk quantity and its relation to surface charge", Phys. Rev. B **48**, 4442–4455 (1993).

[96] S. A. Trugman, "Localization, percolation, and the quantum Hall effect", Phys. Rev. B **27**, 7539–7546 (1983).

[97] Q. Niu, D. J. Thouless, and Y.-S. Wu, "Quantized Hall conductance as a topological invariant", Phys. Rev. B **31**, 3372–3377 (1985).

[98] J. Bellissard, A. van Elst, and H. Schulz-Baldes, "The noncommutative geometry of the quantum Hall effect", Journal of Mathematical Physics **35**, 5373–5451 (1994).

[99] D. Toniolo, "On the equivalence of the Bott index and the Chern number on a torus, and the quantization of the Hall conductivity with a real space Kubo formula", arXiv:1708.05912 [cond-mat, physics:math-ph] (2017).

[100] D. Toniolo, "Time-dependent topological systems: A study of the Bott index", Phys. Rev. B **98**, 235425 (2018).

[101] M. B. Hastings and T. A. Loring, "Almost commuting matrices, localized Wannier functions, and the quantum Hall effect", Journal of Mathematical Physics **51**, 015214 (2010).

[102] D. Toniolo, "On the Bott index of unitary matrices on a finite torus", Letters in Mathematical Physics **112**, 126 (2022).

[103] R. Bianco and R. Resta, "Orbital Magnetization as a Local Property", Phys. Rev. Lett. **110**, 087202 (2013).

[104] R. Fan, P. Zhang, and Y. Gu, *Generalized Real-space Chern Number Formula and Entanglement Hamiltonian*, 2023.

[105] D. Muñoz-Segovia et al., "Structural spillage: an efficient method to identify noncrystalline topological materials", Phys. Rev. Res. **5**, L042011 (2023).

[106] A. Agarwala and V. B. Shenoy, "Topological Insulators in Amorphous Systems", Phys. Rev. Lett. **118**, 236402 (2017).

[107] H. Huang and F. Liu, "Theory of spin Bott index for quantum spin Hall states in nonperiodic systems", Phys. Rev. B **98**, 125130 (2018).

[108] M. D. Caio, G. Möller, N. R. Cooper, and M. J. Bhaseen, "Topological marker currents in Chern insulators", Nature Physics **15**, 257–261 (2019).

[109] D. B. Golovanova, A. R. Yavorsky, A. A. Markov, and A. N. Rubtsov, "Truly local topological dynamics of driven defects in Chern insulator", arXiv Preprint (2021).

[110] A. A. Markov, D. B. Golovanova, A. R. Yavorsky, and A. N. Rubtsov, *Locality of topological dynamics in Chern insulators*, 2023.

[111] M. B. Hastings and T. A. Loring, "Topological insulators and C*-algebras: Theory and numerical practice", Annals of Physics **326**, 1699–1759 (2011).

[112] M. B. Hastings and T. Koma, "Spectral Gap and Exponential Decay of Correlations", en, Communications in Mathematical Physics **265**, 781–804 (2006).

[113] A. Yazdani, Private communication, 2022.

[114] P. Streda, "Theory of quantised Hall conductivity in two dimensions", Journal of Physics C: Solid State Physics **15**, L717 (1982).

[115] T. Rauch, T. Olsen, D. Vanderbilt, and I. Souza, "Geometric and nongeometric contributions to the surface anomalous Hall conductivity", en, Phys. Rev. B **98**, 115108 (2018).

[116] T. Kato, "On the Adiabatic Theorem of Quantum Mechanics", Journal of the Physical Society of Japan **5**, 435–439 (1950).

[117] B. Simon, "Tosio Kato's work on non-relativistic quantum mechanics: part 1", en, Bulletin of Mathematical Sciences **8**, 121–232 (2018).

[118] J. E. Avron, R. Seiler, and L. G. Yaffe, "Adiabatic theorems and applications to the quantum hall effect", en, Communications in Mathematical Physics **110**, 33–49 (1987).

[119] J. E. Avron and A. Elgart, "Adiabatic Theorem without a Gap Condition", en, Communications in Mathematical Physics **203**, 445–463 (1999).

[120] A. Agarwala, V. Juri či ć, and B. Roy, "Higher-order topological insulators in amorphous solids", Phys. Rev. Res. **2**, 012067 (2020).

[121] Q. Marsal, D. Varjas, and A. G. Grushin, "Topological Weaire-Thorpe Models of Amorphous Matter", Proc. Natl. Acad. Sci. U.S.A. **117**, 30260–30265 (2020).

[122] M. Costa et al., "Toward realistic amorphous topological insulators", Nano letters **19**, 8941–8946 (2019).

[123] H. Spring, A. R. Akhmerov, and D. Varjas, "Amorphous topological phases protected by continuous rotation symmetry", SciPost Phys. **11**, 22 (2021).

[124] P. Corbae et al., "Observation of spin-momentum locked surface states in amorphous Bi2Se3", Nature Materials **22**, 200–206 (2023).

[125] W. Buckel and R. Hilsch, "Einfluss der Kondensation bei tiefen Temperaturen auf den elektrischen Widerstand und die Supraleitung für verschiedene Metalle", Zeitschrift für Physik **138**, 109–120 (1954).

[126] W. L. McMillan and J. Mochel, "Electron tunneling experiments on amorphous $Ge_{1-x}Au_x$", Phys. Rev. Lett. **46**, 556–557 (1981).

[127] L. V. Meisel and P. J. Cote, "Eliashberg function in amorphous metals", Phys. Rev. B **23**, 5834–5838 (1981).

[128] G. Bergmann, "Amorphous metals and their superconductivity", Physics Reports **27**, 159–185 (1976).

[129] S. Manna, S. K. Das, and B. Roy, *Noncrystalline topological superconductors*, 2022.

[130] S. Kim, A. Agarwala, and D. Chowdhury, "Fractionalization and Topology in Amorphous Electronic Solids", Phys. Rev. Lett. **130**, 026202 (2023).

[131] A. Aharony, "Critical behavior of amorphous magnets", Phys. Rev. B **12**, 1038 (1975).

[132] G. A. Petrakovskii, "Amorphous magnetic materials", Soviet Physics Uspekhi **24**, 511–525 (1981).

[133] M. Fähnle, "Monte Carlo study of phase transitions in bond-and site-disordered Ising and classical Heisenberg ferromagnets", Journal of magnetism and magnetic materials **45**, 279–287 (1984).

[134] T. Kaneyoshi, *Introduction to amorphous magnets* (World Scientific Publishing Company, 1992).

[135] J. A. Plascak, L. E. Zamora, and G. A. Pérez Alcazar, "Ising model for disordered ferromagnetic Fe − Al alloys", Phys. Rev. B **61**, 3188–3191 (2000).

[136] T. Kaneyoshi, ed., *Amorphous Magnetism*, CRC Revivals (CRC Press, Boca Raton, 2018).

[137] J. Coey, "Amorphous magnetic order", Journal of Applied Physics **49**, 1646–1652 (1978).

[138] F. Barahona, "On the computational complexity of ising spin glass models", Journal of Physics A: Mathematical and General **15**, 3241 (1982).

[139] F. Roma et al., "The ground state energy of the edwards–anderson spin glass model with a parallel tempering monte carlo algorithm", Physica A: Statistical Mechanics and its Applications **388**, 2821–2838 (2009).

[140] W. Wang, J. Machta, and H. G. Katzgraber, "Comparing monte carlo methods for finding ground states of ising spin glasses: population annealing, simulated annealing, and parallel tempering", Phys. Rev. E **92**, 013303 (2015).

[141] C. Fan et al., "Searching for spin glass ground states through deep reinforcement learning", Nature Communications **14**, 725 (2023).

[142] M. Hermanns, I. Kimchi, and J. Knolle, "Physics of the Kitaev Model: Fractionalization, Dynamic Correlations, and Material Connections", Annual Review of Condensed Matter Physics **9**, 17–33 (2018).

[143] S. M. Winter et al., "Models and materials for generalized Kitaev magnetism", Journal of Physics: Condensed Matter **29**, 493002 (2017).

[144] S. Trebst and C. Hickey, "Kitaev materials", Physics Reports **950**, 1–37 (2022).

[145] H. Takagi et al., "Concept and realization of Kitaev quantum spin liquids", Nature Reviews Physics **1**, 264–280 (2019).

[146] G. Jackeli and G. Khaliullin, "Mott insulators in the strong spin-orbit coupling limit: from Heisenberg to a quantum compass and Kitaev models", Phys. Rev. Lett. **102**, 017205 (2009).

[147] S. Y. Lee and Y. J. Park, "Lithia/(Ir, Li2IrO3) nanocomposites for new cathode materials based on pure anionic redox reaction", en, Scientific Reports **9**, 13180 (2019).

[148] R. Zallen, *The physics of amorphous solids* (John Wiley & Sons, 2008).

[149] D. Turnbull, "Under what conditions can a glass be formed?", Contemporary Physics **10**, 473–488 (1969).

[150] J. G. Rau and H.-Y. Kee, *Trigonal distortion in the honeycomb iridates: proximity of zigzag and spiral phases in na2iro3*, 2014.

[151] E. Sela, H.-C. Jiang, M. H. Gerlach, and S. Trebst, "Order-by-disorder and spin-orbital liquids in a distorted heisenberg-kitaev model", Phys. Rev. B **90**, 035113 (2014).

[152] G. Baskaran, S. Mandal, and R. Shankar, "Exact Results for Spin Dynamics and Fractionalization in the Kitaev Model", Phys. Rev. Lett. **98**, 247201 (2007).

[153] G. Baskaran, D. Sen, and R. Shankar, "Spin-S Kitaev model: Classical ground states, order from disorder, and exact correlation functions", Phys. Rev. B **78**, 115116 (2008).

[154] Z. Nussinov and G. Ortiz, "Bond algebras and exact solvability of hamiltonians: spin $S = \frac{1}{2}$ multilayer systems", Phys. Rev. B **79**, 214440 (2009).

[155] K. O'Brien, M. Hermanns, and S. Trebst, "Classification of gapless $\mathbb{Z}_2$ spin liquids in three-dimensional kitaev models", Phys. Rev. B **93**, 085101 (2016).

[156] H. Yao and S. A. Kivelson, "An exact chiral spin liquid with non-Abelian anyons", Phys. Rev. Lett. **99**, 247203 (2007).

[157] M. Hermanns, K. O'Brien, and S. Trebst, "Weyl spin liquids", Phys. Rev. Lett. **114**, 157202 (2015).

[158] E. H. Lieb, "Flux Phase of the Half-Filled Band", Phys. Rev. Lett. **73**, 2158–2161 (1994).

[159] T. Eschmann et al., "Thermodynamics of a gauge-frustrated kitaev spin liquid", Phys. Rev. Res. **1**, 032011 (2019).

[160] V. Peri et al., "Non-Abelian chiral spin liquid on a simple non-Archimedean lattice", Phys. Rev. B **101**, 041114(R) (2020).

[161] C. N. Self, J. Knolle, S. Iblisdir, and J. K. Pachos, "Thermally induced metallic phase in a gapped quantum spin liquid: Monte Carlo study of the Kitaev model with parity projection", Phys. Rev. B **99**, 045142 (2019).

[162] C. R. Laumann, A. W. W. Ludwig, D. A. Huse, and S. Trebst, "Disorder-induced Majorana metal in interacting non-Abelian anyon systems", Phys. Rev. B **85**, 161301(R) (2012).

[163] V. Lahtinen, A. W. W. Ludwig, J. K. Pachos, and S. Trebst, "Topological Liquid Nucleation Induced by Vortex-Vortex Interactions in Kitaev's Honeycomb Model", Phys. Rev. B **86**, 075115 (2012).

[164] V. Chua, H. Yao, and G. A. Fiete, "Exact chiral spin liquid with stable spin Fermi surface on the kagome lattice", Phys. Rev. B **83**, 180412(R) (2011).

[165] V. Chua and G. A. Fiete, "Exactly solvable topological chiral spin liquid with random exchange", Phys. Rev. B **84**, 195129 (2011).

[166] G. A. Fiete et al., "Topological insulators and quantum spin liquids", Physica E: Low-dimensional Systems and Nanostructures **44**, 845–859 (2012).

[167] W. M. H. Natori, E. C. Andrade, E. Miranda, and R. G. Pereira, "Chiral Spin-Orbital Liquids with Nodal Lines", Phys. Rev. Lett. **117**, 017204 (2016).

[168] C. Wu, D. Arovas, and H.-H. Hung, "Γ-matrix generalization of the kitaev model", Phys. Rev. B **79**, 134427 (2009).

[169] H. Wang and A. Principi, "Majorana edge and corner states in square and kagome quantum spin-$\frac{3}{2}$ liquids", Phys. Rev. B **104**, 214422 (2021).

[170] X.-Y. Feng, G.-M. Zhang, and T. Xiang, "Topological Characterization of Quantum Phase Transitions in a Spin-1/2 Model", Phys. Rev. Lett. **98**, 087204 (2007).

[171] H.-D. Chen and J. Hu, "Exact mapping between classical and topological orders in two-dimensional spin systems", Phys. Rev. B **76**, 193101 (2007).

[172] H.-D. Chen and Z. Nussinov, "Exact results of the Kitaev model on a hexagonal lattice: spin states, string and brane correlators, and anyonic excitations", Journal of Physics A: Mathematical and Theoretical **41**, 075001 (2008).

[173] J. Nasu, "Majorana quasiparticles emergent in Kitaev spin liquid", Progress of Theoretical and Experimental Physics, ptad115 (2023).

[174] T. Senthil and M. P. A. Fisher, "Z_2 Gauge theory of electron fractionalization in strongly correlated systems", Phys. Rev. B **62**, 7850–7881 (2000).

[175] X.-G. Wen and P. A. Lee, "Theory of Underdoped Cuprates", Phys. Rev. Lett. **76**, 503–506 (1996).

[176] A. Y. Kitaev, "Fault-tolerant quantum computation by anyons", Annals of Physics **303**, 2–30 (2003).

[177] K. P. Schmidt, S. Dusuel, and J. Vidal, "Emergent Fermions and Anyons in the Kitaev Model", Phys. Rev. Lett. **100**, 057208 (2008).

[178] S. Dusuel, K. P. Schmidt, and J. Vidal, "Creation and Manipulation of Anyons in the Kitaev Model", Phys. Rev. Lett. **100**, 177204 (2008).

[179] J. Vidal, K. P. Schmidt, and S. Dusuel, "Perturbative approach to an exactly solved problem: Kitaev honeycomb model", Phys. Rev. B **78**, 245121 (2008).

[180] R. Jackiw and C. Rebbi, "Solitons with fermion number $\frac{1}{2}$", Phys. Rev. D **13**, 3398–3409 (1976).

[181] P. G. Tait, "Remarks on the Colouring of Maps", Proceedings of the Royal Society of Edinburgh **10**, 501–503 (1880).

[182] K. Appel and W. Haken, *Every Planar Map Is Four Colorable*, Vol. 98, Contemporary Mathematics (American Mathematical Society, 1989).

[183] G. Ringel and J. W. Youngs, "Solution of the heawood map-coloring problem", eng, Proceedings of the National Academy of Sciences of the United States of America **60**, 438–445 (1968).

[184] R. M. Karp, "Reducibility among Combinatorial Problems", in *Complexity of Computer Computations*, edited by R. E. Miller, J. W. Thatcher, and J. D. Bohlinger (Springer US, Boston, MA, 1972), pp. 85–103.

[185] A. Ignatiev, A. Morgado, and J. Marques-Silva, "PySAT: A Python Toolkit for Prototyping with SAT Oracles", in SAT (2018), pp. 428–437.

[186] C. Adiga, R. Balakrishnan, and W. So, "The skew energy of a digraph", en, Linear Algebra and its Applications **432**, 1825–1835 (2010).

[187] M. Cavers et al., "Skew-adjacency matrices of graphs", en, Linear Algebra and its Applications, Special Issue on Matrices Described by Patterns **436**, 4512–4529 (2012).

[188] J. Nasu, M. Udagawa, and Y. Motome, "Thermal fractionalization of quantum spins in a Kitaev model: Temperature-linear specific heat and coherent transport of Majorana fermions", Phys. Rev. B **92**, 115122 (2015).

[189] J. Knolle, *Dynamics of a Quantum Spin Liquid* (Springer, 2016).

[190] J. Knolle, R. Moessner, and N. B. Perkins, "Bond-disordered spin liquid and the honeycomb iridate H 3 LiIr 2 O 6: Abundant low-energy density of states from random Majorana hopping", Phys. Rev. Lett. **122**, 047202 (2019).

[191] A. J. Willans, J. T. Chalker, and R. Moessner, "Disorder in a quantum spin liquid: flux binding and local moment formation", Phys. Rev. Lett. **104**, 237203 (2010).

[192] A. J. Willans, J. T. Chalker, and R. Moessner, "Site dilution in the kitaev honeycomb model", Phys. Rev. B **84**, 115146 (2011).

[193] D. P. Mitchell, "Spectrally Optimal Sampling for Distribution Ray Tracing", in Proceedings of the 18th Annual Conference on Computer Graphics and Interactive Techniques, SIGGRAPH '91 (1991), pp. 157–164.

[194] demofox2, *Generating Blue Noise Sample Points With Mitchell's Best Candidate Algorithm*, Oct. 2017.

[195] S. Lloyd, "Least squares quantization in PCM", IEEE Transactions on Information Theory **28**, 129–137 (1982).

[196] J. ř. Chaloupka, G. Jackeli, and G. Khaliullin, "Kitaev-heisenberg model on a honeycomb lattice: possible exotic phases in iridium oxides A_2IrO_3", Phys. Rev. Lett. **105**, 027204 (2010).

[197] J. G. Rau, E. K.-H. Lee, and H.-Y. Kee, "Generic Spin Model for the Honeycomb Iridates beyond the Kitaev Limit", Phys. Rev. Lett. **112**, 077204 (2014).

[198] J. ř. Chaloupka, G. Jackeli, and G. Khaliullin, "Zigzag magnetic order in the iridium oxide Na_2IrO_3", Phys. Rev. Lett. **110**, 097204 (2013).

[199] J. G. Rau, E. K.-H. Lee, and H.-Y. Kee, "Spin-orbit physics giving rise to novel phases in correlated systems: Iridates and related materials", Annual Review of Condensed Matter Physics **7**, 195–221 (2016).

[200] M. Gohlke, R. Verresen, R. Moessner, and F. Pollmann, "Dynamics of the Kitaev-Heisenberg Model", Phys. Rev. Lett. **119**, 157203 (2017).

[201] P. A. McClarty et al., "Topological magnons in kitaev magnets at high fields", Phys. Rev. B **98**, 060404 (2018).

[202] H. Katsura, N. Nagaosa, and P. A. Lee, "Theory of the Thermal Hall Effect in Quantum Magnets", Phys. Rev. Lett. **104**, 066403 (2010).

[203] L. Zhang, J. Ren, J.-S. Wang, and B. Li, "Topological magnon insulator in insulating ferromagnet", Phys. Rev. B **87**, 144101 (2013).

[204] A. Mook, J. Henk, and I. Mertig, "Edge states in topological magnon insulators", Phys. Rev. B **90**, 024412 (2014).

[205] P. A. McClarty, "Topological magnons: A review", Annual Review of Condensed Matter Physics **13**, 171–190 (2022).

[206] R. Matsumoto and S. Murakami, "Theoretical Prediction of a Rotating Magnon Wave Packet in Ferromagnets", Phys. Rev. Lett. **106**, 197202 (2011).

[207] Y. Kasahara, T. Ohnishi, Y. Mizukami, et al., "Majorana quantization and half-integer thermal quantum Hall effect in a Kitaev spin liquid", Nature **559**, 227–231 (2018).

[208] J. A. N. Bruin et al., "Robustness of the thermal Hall effect close to half-quantization in $\alpha - RuCl_3$", Nature Physics **18**, 401–405 (2022).

[209] P. Czajka et al., "Planar thermal Hall effect of topological bosons in the Kitaev magnet $\alpha - RuCl_3$", en, Nature Materials **22**, 36–41 (2023).

[210] L. E. Chern, E. Z. Zhang, and Y. B. Kim, "Sign structure of thermal hall conductivity and topological magnons for in-plane field polarized kitaev magnets", Phys. Rev. Lett. **126**, 147201 (2021).

[211] M. I. Sorolla et al., "Synthesis of the Elusive S = 1/2 Star Structure: A Possible Quantum Spin Liquid Candidate", Journal of the American Chemical Society **142**, 5013–5016 (2020).

[212] C.-X. Ji et al., "Dielectric and Magnetic Relaxations Exhibited in a 2D Parallel Interpenetrating Frustrated Star Net", Chemistry - A European Journal **28**, e202104503 (2022).

[213] Y.-Z. Zheng et al., "A "star" antiferromagnet: a polymeric iron(iii) acetate that exhibits both spin frustration and long-range magnetic ordering", Angewandte Chemie International Edition **46**, 6076–6080 (2007).

[214] S. Sachdev and R. N. Bhatt, "Bond-operator representation of quantum spins: Mean-field theory of frustrated quantum Heisenberg antiferromagnets", Phys. Rev. B **41**, 9323–9329 (1990).

[215] D. G. Joshi and A. P. Schnyder, "Topological quantum paramagnet in a quantum spin ladder", Phys. Rev. B **96**, 220405 (2017).

[216] J. Romhányi, K. Totsuka, and K. Penc, "Effect of dzyaloshinskii-moriya interactions on the phase diagram and magnetic excitations of $\mathrm{srcu_2(bo_3)_2}$", Phys. Rev. B **83**, 024413 (2011).

[217] J. Romhányi, K. Penc, and R. Ganesh, "Hall effect of triplons in a dimerized quantum magnet", Nature Communications **6**, 6805 (2015).

[218] P. A. McClarty et al., "Topological triplon modes and bound states in a Shastry–Sutherland magnet", Nature Physics **13**, 736–741 (2017).

[219] K. Nawa et al., "Triplon band splitting and topologically protected edge states in the dimerized antiferromagnet", Nature Communications **10**, 2096 (2019).

[220] M. Malki and K. P. Schmidt, "Magnetic Chern bands and triplon Hall effect in an extended Shastry-Sutherland model", Phys. Rev. B **95**, 195137 (2017).

[221] R. Schaffer, S. Bhattacharjee, and Y. B. Kim, "Quantum phase transition in Heisenberg-Kitaev model", en, Phys. Rev. B **86**, 224417 (2012).

[222] I. Kimchi and A. Vishwanath, "Kitaev-heisenberg models for iridates on the triangular, hyperkagome, kagome, fcc, and pyrochlore lattices", Phys. Rev. B **89**, 014414 (2014).

[223] K. Shinjo, S. Sota, and T. Tohyama, "Density-matrix renormalization group study of the extended Kitaev-Heisenberg model", Phys. Rev. B **91**, 054401 (2015).

[224] J. Hauschild and F. Pollmann, "Efficient numerical simulations with Tensor Networks: Tensor Network Python (TeNPy)", SciPost Phys. Lect. Notes, 5 (2018).

[225] J. Knolle, S. Bhattacharjee, and R. Moessner, "Dynamics of a quantum spin liquid beyond integrability: the kitaev-heisenberg-Γ model in an augmented parton mean-field theory", Phys. Rev. B **97**, 134432 (2018).

[226] S. Gopalan, T. M. Rice, and M. Sigrist, "Spin ladders with spin gaps: A description of a class of cuprates", Phys. Rev. B **49**, 8901–8910 (1994).

[227] J.-P. Blaizot and G. Ripka, *Quantum Theory of Finite Systems* (The MIT Press, 1986).

[228] J. M. Luttinger, "Theory of thermal transport coefficients", Phys. Rev. **135**, A1505–A1514 (1964).

[229] S. Ryu, A. P. Schnyder, A. Furusaki, and A. W. W. Ludwig, "Topological insulators and superconductors: tenfold way and dimensional hierarchy", New Journal of Physics **12**, 065010 (2010).

[230] W. P. Su, J. R. Schrieffer, and A. J. Heeger, "Solitons in polyacetylene", Phys. Rev. Lett. **42**, 1698–1701 (1979).

[231] A. Y. Kitaev, "Unpaired majorana fermions in quantum wires", Physics-Uspekhi **44**, 131 (2001).

[232] B. A. Bernevig, T. L. Hughes, and S.-C. Zhang, "Quantum spin hall effect and topological phase transition in hgte quantum wells", Science **314**, 1757–1761 (2006).

[233] W. Chen, "Universal topological marker", Phys. Rev. B **107**, 045111 (2023).

[234] J. Sykes and R. Barnett, "Local topological markers in odd dimensions", Phys. Rev. B **103**, 155134 (2021).

[235] J. D. Hannukainen, M. F. Martinez, J. H. Bardarson, and T. K. Kvorning, "Local topological markers in odd spatial dimensions and their application to amorphous topological matter", Phys. Rev. Lett. **129**, 277601 (2022).

[236] T. Yokoi, S. Ma, Y. Kasahara, et al., "Majorana quantization and half-integer thermal quantum Hall effect in a Kitaev spin liquid", Science **373**, 568–572 (2021).

[237] M. Yamashita et al., "Sample dependence of half-integer quantized thermal hall effect in the kitaev spin-liquid candidate $\alpha-RuCl_3$", Phys. Rev. B **102**, 220404 (2020).

[238] S. K. Kim, H. Ochoa, R. Zarzuela, and Y. Tserkovnyak, "Realization of the Haldane-Kane-Mele Model in a System of Localized Spins", Phys. Rev. Lett. **117**, 227201 (2016).

[239] L.-C. Zhang et al., "Interplay of Dzyaloshinskii-Moriya and Kitaev interactions for magnonic properties of Heisenberg-Kitaev honeycomb ferromagnets", Phys. Rev. B **103**, 134414 (2021).

Appendix A

Voronoi Lattices

In this appendix we detail the methods used to create the random two-dimensional tri-coordinated lattices used in Chapters 2 and 3 to create the amorphous analogue of the QWZ model, and in Chapter 4 to construct the amorphous Kitaev model. This is done using the Voronoi partition [1], which well-known in the physics community as the method used to produce a Wigner-Seitz unit cell [2]. The method allows one – given a set of n points – to partition the plane into a set of n regions. Each of these regions contains the area of the plane that is closer to a given point than any other, with the boundary between two regions always being perpendicular to the line connecting their two respective points.

In practice, fast routines exist for constructing a Voronoi partition, we used a built-in function from the python package `scipy`, namely `scipy.spatial.Voronoi`, which uses the quickhull algorithm [3]. The only complication comes from working in periodic boundary conditions, since the algorithm is designed for open boundaries. This is straightforwardly solved by tiling the system before computing the Voronoi partition. Then, once a Voronoi diagram has been constructed, we restrict back to the unit square, identifying the unit-separated vertices that should equivalent under periodic boundaries. An example is shown in Fig. A.1.

A Voronoi lattice can now be extracted from the Voronoi partition by assigning an edge to the boundary between every pair of cells, and a vertex to the points at which three cells meet. This lattice will always be tri-coordinated, provided that none of the original seed points lie at the corners of a regular m-sided polygon, since this would lead to the formation of an m-coordinated vertex at the centre of that polygon in the Voronoi lattice.

A.1 Lloyd's Algorithm

Typically, lattices generated via Voronoi partition do not resemble real amorphous materials. This is because, when a set of seed points are arranged roughly equidistant from a central point, the Voronoi partition will place a cluster of vertices extremely close to one another at that point. An example is seen in the green-shaded area in Fig. A.2a. In general, physical materials usually have some condition that prevents vertices (or atoms) from becoming extremely close to one another. Thus, in order to generate more physically applicable random lattices, we use Lloyds algorithm to approximately evenly space the vertices in a lattice. The algorithm is straightforward, consisting of three steps which are repeated:

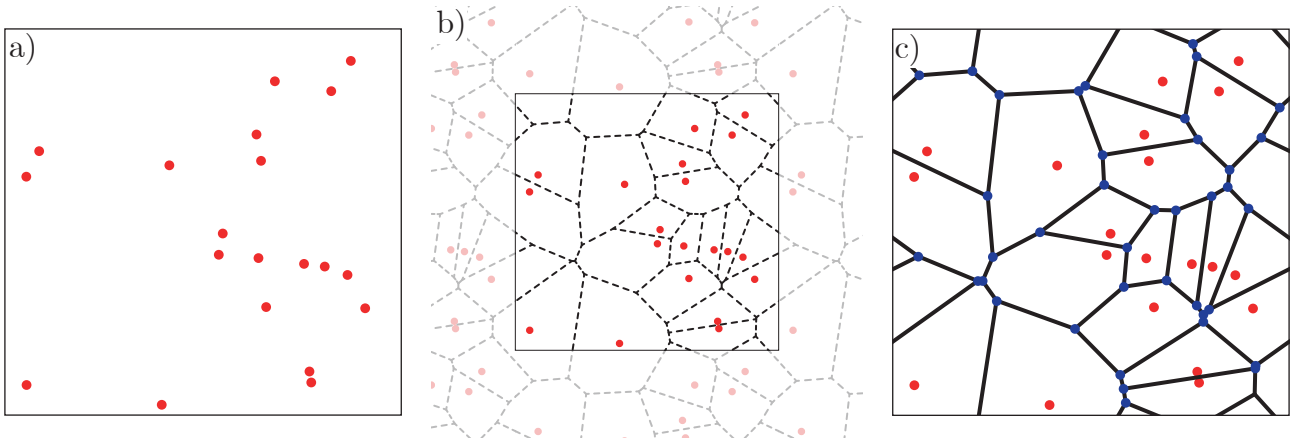


Figure A.1: An example Voronoi partition calculated for a set of 20 points on the unit square in periodic boundaries. **(a)** The initial set of 20 points, sampled uniformly on the square. **(b)** In order to construct a partition consisted with periodic boundary conditions, the initial set of points is tiled, creating eight copies around the central region. Now a Voronoi diagram is calculated for this extended system, corresponding to the dashed lines. **(c)** We restrict back to the unit square, identifying vertices that should be equivalent, resulting in a final, periodic, Voronoi partition. A Voronoi lattice is now identified by the edges and blue vertices, each of which sits at the point of intersection of three Voronoi cells.

1. Given a Voronoi partition, a new set of seed points are generated for each cell, defined as the centre of mass of each cell.
2. The original seed points are then moved to these new centre-of-mass points.
3. Now the Voronoi lattice is recalculated using the new points, producing a new Voronoi diagram that is slightly more regular than the original.

An example of one step in this process is shown in Fig. A.2.

With each successive application of this algorithm, the lattice will become increasingly regular. In Fig. A.3 we show the result of applying 5, 50 and 150 iterations of this process to the Voronoi partition generated in Fig. A.1.

References

[1] G. Voronoi, "Nouvelles applications des paramètres continus a la théorie des formes quadratiques. deuxième mémoire. recherches sur les parallélloèdres primitifs.", Journal für die reine und angewandte Mathematik **134**, 198–287 (1908).

[2] E. Wigner and F. Seitz, "On the constitution of metallic sodium", Phys. Rev. **43**, 804–810 (1933).

[3] C. B. Barber, D. P. Dobkin, and H. Huhdanpaa, "The quickhull algorithm for convex hulls", ACM Trans. Math. Softw. **22**, 469–483 (1996).

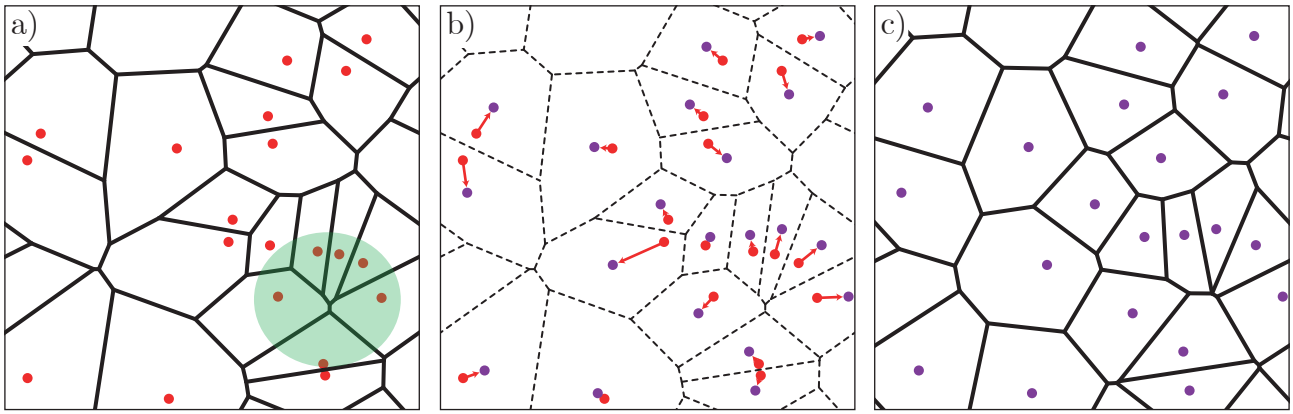


Figure A.2: One step of Lloyd's algorithm is shown. **(a)** The initial Voronoi lattice is shown, with initial seed points shown in red. The green highlighted area shows a series of points that would be unphysical in a physics model, since they are extremely close to one another. **(b)** New seed points are calculated for each cell, positioned at the centre of mass of the cell. The seed points are then moved to these new positions. **(c)** The Voronoi lattice is recalculated, producing a new, more evenly spaced lattice.

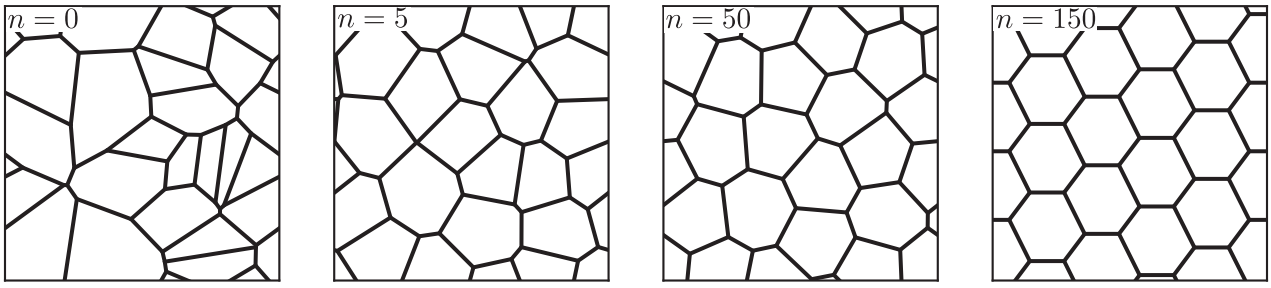


Figure A.3: Four Voronoi lattices are shown, each corresponding to performing n-steps of Lloyd's algorithm to the Voronoi lattice generated in Fig. A.1. After around 150 steps, successive iterations of the algorithm produce no changes.

Appendix B

Time-Evolution and Current Under Kato Dynamics

B.1 Adiabatic Time-Evolution Operator

In this section we will justify the form of the adiabatic Hamiltonian,

$$K(t) = i\left[\partial_t P_I(t), P_I(t)\right], \tag{B.1}$$

as the generator of the correct adiabatic time-evolution for a given initial projector, P_0. We introduce a parameter T that defines the period over which the system evolves, $t \in [0, T]$. Changing variables to $s = tT^{-1}$, we arrive at the scaled Schrödinger equation

$$i\partial_s U_T(s) = TH(s)U_T(s), \tag{B.2}$$

where we can use T to parametrise how slowly the system changes. We will also define the scaled adiabatic Hamiltonian

$$\bar{K}(s) = i[\partial_s P_I(s), P_I(s)]. \tag{B.3}$$

Since $\partial_s = T\partial_t$, so this quantity is related to K by $\bar{K} = TK$.

Our aim will be to show that in the limit of large T, the time-evolved state $P(s) = U_T(s)P_0U_T^\dagger(s)$, can be approximated by the instantaneous projector, $P_I(s) = \sum_{i\in\text{band}} |\psi_i(s)\rangle \langle\psi_i(s)|$, where $|\psi_i(s)\rangle$ are eigenstates of $H(s)$. We wish to define an adiabatic time-evolution operator $U_A(s)$ such that

$$P_I(s) = U_A(s)P_0U_A^\dagger(s). \tag{B.4}$$

We propose an ansatz for U_A that satisfies the following conditions,

$$U_A(0) = \mathbb{1}, \tag{B.5}$$

$$i\partial_s U_A(s) = \left[TH(s) + \bar{K}(s)\right] U_A(s). \tag{B.6}$$

To verify that U_A produces the right dynamics, let us consider the quantity

$$G(s) = U_A(s)^\dagger P_I(s)U_A(s). \tag{B.7}$$

In the interest of keeping equations legible, we will drop explicit s-dependence from our operators. From hereon in it is safe to assume that, unless stated otherwise, all operators are being evaluated at time s. We take the s-derivative of G,

$$\partial_s G = \partial_s \left[(U_A^\dagger P_I)(P_I U_A) \right]. \tag{B.8}$$

Using the identity

$$\partial_s (P_I U_A) = \partial_s P_I U_A - i P_I \left(T H(s) + \bar{K}(s) \right) U_A, \tag{B.9}$$

we can show that

$$\partial_s G = U_A^\dagger \left(iT[H, P_I] + \{P_I, \partial_s P_I\} + i[\bar{K}, P_I] \right) U_A. \tag{B.10}$$

The first term in this expression vanishes, since P and H commute by definition. Next we can use the identities $\partial_s P_I = \{P_I, \partial_s P_I\}$ and $P_I \partial_s P_I P_I = 0$ to show that the second and third terms respectively equal $\partial_s P_I$ and $-\partial_s P_I$, cancelling out. Thus we have shown that $\partial_s G = 0$ for all s. Since $G(0) = P_0$, we see that

$$G(s) = P_0, \ \forall\, s, \tag{B.11}$$

confirming that our definition satisfies Eqn. B.4.

Now all that remains is to show that, as $T \to \infty$, the actual dynamics, U_T, asymptotically approach the adiabatic dynamics described by U_A. We will omit the proof of this result, which is simply a proof of the adiabatic theorem, however a complete justification can be found in [1]. We quote the result, which compares the projector generated by non-adiabatic dynamics, $P(s) = U_T P_0 U_T^\dagger$ compared to that generated by the adiabatic time evolution $P_I(s) = U_A P_0 U_A^\dagger$. The result states that

$$|P(s) - P_I(s)| = \mathcal{O}(T^{-1}) \tag{B.12}$$

Thus we can see that in the limit of large T, U_T generates the correct time evolution.

B.2 Adiabatic Current Operators

In this section we will expand our justification for the form of the adiabatic current presented in §3.3.3.2. The argument splits into two parts. First we introduce an operator that describes the direct flow of particles between a pair of individual sites $\mathbf{r}_i$ and $\mathbf{r}_j$ in the system, $f_{\mathbf{r}_i,\mathbf{r}_j}$. Then we will show how, in the adiabatic limit, the flow between a pair of sites is determined by the adiabatic Hamiltonian K, introduced in §3.3.3. Bulk current can always be written as the sum over the flow between individual sites, thus all the properties of $f_{\mathbf{r}_i,\mathbf{r}_j}$ naturally extend to the currents defined in §3.3.2.

B.2.1 Two-Point Flow Operator

The flow between individual sites can be extracted from the continuity equation for electron density. We start by looking at the change in occupation number at a single site, $\delta_{\mathbf{r}} = |\mathbf{r}\rangle \langle \mathbf{r}|$,

for a projector onto a set of occupied states P,

$$\partial_t \langle \delta_{\mathbf{r}} \rangle = \mathrm{Tr}\left(\partial_t P \delta_{\mathbf{r}}\right). \tag{B.13}$$

We use the Von-Neumann equation to express $\partial_t P$ in terms of the Hamiltonian, cycling the terms in the trace to arrive at

$$\partial_t \langle \delta_{\mathbf{r}} \rangle = \mathrm{Tr}\left(P i[H, \delta_{\mathbf{r}}]\right). \tag{B.14}$$

Inserting a complete set of position eigenstates $\mathbb{1} = \sum_j \delta_{\mathbf{r}_j}$, we may re-express this in the form of a continuity equation,

$$\partial_t \langle \delta_{\mathbf{r}} \rangle = \sum_j \mathrm{Tr}\left[P(i\delta_{\mathbf{r}_j} H \delta_{\mathbf{r}} - i\delta_{\mathbf{r}} H \delta_{\mathbf{r}_j})\right]. \tag{B.15}$$

This describes the change of number density at site $\mathbf{r}$ as a sum of the flow from every other site $\mathbf{r}_j$ in the system. Thus we can interpret the operator

$$f_{\mathbf{r}_i,\mathbf{r}_j} = i\left(\delta_{\mathbf{r}_j} H \delta_{\mathbf{r}_i} - \delta_{\mathbf{r}_i} H \delta_{\mathbf{r}_j}\right), \tag{B.16}$$

as quantifying the flow of electrons from the site at $\mathbf{r}_i$ to $\mathbf{r}_j$. Note that it is antisymmetric in $\mathbf{r}_i \leftrightarrow \mathbf{r}_j$.

In the next section we will work in the adiabatic limit, thus let us find the current per unit of scaled time s. Using the substitution $t = sT$, we define the scaled flow operator

$$\bar{f}_{\mathbf{r}_i,\mathbf{r}_j} = iT\left(\delta_{\mathbf{r}_j} H \delta_{\mathbf{r}_i} - \delta_{\mathbf{r}_i} H \delta_{\mathbf{r}_j}\right), \tag{B.17}$$

which satisfies the scaled continuity equation $\partial_s \langle \delta_{\mathbf{r}} \rangle = \sum_j \mathrm{Tr}(P \bar{f}_{\mathbf{r}_i,\mathbf{r}_j})$.

Both current operators described in §3.3.2 can be written as a sum of individual flows. The operator in def. 3.86, representing the total current between the two halves of the system, is the sum of all two-point currents where $\mathbf{r}_i \to \mathbf{r}_j$ crosses $x = R_x$,

$$J_{R_x} = \sum_{\substack{x_i > R_x \\ x_j < R_x}} f_{\mathbf{r}_i,\mathbf{r}_j}, \tag{B.18}$$

whereas def. 3.87 may be written as the sum of all two-point currents that cross $x = R_x$ and either start or finish at $\mathbf{r}$,

$$J_{R_x}(\mathbf{r}) = \sum_{x_i > R_x} f_{\mathbf{r},\mathbf{r}_i}, \tag{B.19}$$

where we have assumed that $\mathbf{r}$ has $x < R_x$.

B.2.2 Adiabatic Current

Here we show that the scaled flow operator may be replaced with the adiabatic equivalent up to small corrections in T^{-1}:

$$\bar{f}_{\mathbf{r}_i,\mathbf{r}_j} = \bar{f}^A_{\mathbf{r}_i,\mathbf{r}_j} + \mathcal{O}\left(\frac{1}{T}\right), \tag{B.20}$$

with f^A defined according to

$$\bar{f}^A_{\mathbf{r}_i,\mathbf{r}_j} = i\delta_{\mathbf{r}_j}\bar{K}\delta_{\mathbf{r}_i} - i\delta_{\mathbf{r}_i}\bar{K}\delta_{\mathbf{r}_j}, \tag{B.21}$$

and $\bar{K} = i[\partial_s P_I, P_I]$ in analogy to the definition in §3.3.3. Note that the flow in Eqn. B.16 is always valid regardless of what state it is acted on. Since K is defined for a choice of P_I, the adiabatic flow is only correct when evaluated with an occupied band consisting of the states in P_I.

Our argument has two parts. We shall first decompose the Hamiltonian into a term that commutes with P and a term that does not. Only the non-commuting term contributes to measurable change in the system. Finally, we show that this term has a straightforward expression in the near-adiabatic limit, and defines the adiabatic flow.

As shown in Appendix B.1, the time-evolution of our system is determined by the scaled Von-Neumann equation,

$$\partial_s P = -iT[H, P], \tag{B.22}$$

where we treat T as a tunable parameter. Clearly, any component in H that commutes with P will vanish in this expression. Thus, let us split H into a commuting and non-commuting part,

$$H = (PHP + QHQ) + (PHQ + QHP), \tag{B.23}$$

where we define $Q = \mathbb{1} - P$ as the projector onto unoccupied states. We will label the two terms in brackets $H_\parallel$ and $H_\perp$ respectively. $H_\parallel$ commutes with P, vanishing in the Von-Neumann equation and thus does not effect any change in P whatsoever. Furthermore, any Hamiltonian that differs from H only by a term that commutes with P (e.g. $H' = H + PMP + QMQ$ for some arbitrary operator M) will still produce the exact same dynamics for P.

Using these two components of H, we can split the flow operator into two components according to

$$\begin{aligned}\bar{f}_{\mathbf{r}_i,\mathbf{r}_j} = &(iT\delta_{\mathbf{r}_j}H_\parallel\delta_{\mathbf{r}_i} + h.c.)\\ &+ (iT\delta_{\mathbf{r}_j}H_\perp\delta_{\mathbf{r}_i} + h.c.),\end{aligned} \tag{B.24}$$

and label these two terms as $\bar{f}^\parallel_{\mathbf{r}_i,\mathbf{r}_j}$ and $\bar{f}^\perp_{\mathbf{r}_i,\mathbf{r}_j}$ respectively. Let us examine the contribution of each term to the continuity equation B.15,

$$\partial_s\langle\delta_{\mathbf{r}}\rangle = \sum_j \mathrm{Tr}\left[P\left(\bar{f}^\parallel_{\mathbf{r},\mathbf{r}_j} + \bar{f}^\perp_{\mathbf{r},\mathbf{r}_j}\right)\right]. \tag{B.25}$$

Writing out the $\bar{f}^\parallel$ term explicitly, we see that it vanishes

$$\begin{aligned}\sum_j \mathrm{Tr}\left[P\bar{f}^\parallel_{\mathbf{r},\mathbf{r}_j}\right] &= \sum_j \mathrm{Tr}\left(iTP\delta_{\mathbf{r}_j}H_\parallel\delta_{\mathbf{r}}\right) + h.c.\\ &= \mathrm{Tr}\left(iTPHP\delta_{\mathbf{r}}\right) + h.c.\\ &= 0.\end{aligned} \tag{B.26}$$

Thus, the only term that contributes to the continuity equation is $\bar{f}^\perp_{\mathbf{r}_i,\mathbf{r}_j}$. We can interpret $\bar{f}^\parallel_{\mathbf{r}_i,\mathbf{r}_j}$ as a circulating current, representing the flow between occupied states in P. As it vanishes in

the continuity equation, it is not possible for this term to change the number density at any site in the system.

Now, let us examine $\bar{f}^{\perp}_{\mathbf{r}_i,\mathbf{r}_j}$ in the near-adiabatic limit. As we have seen in appendix B.1, the projector is equal to the instantaneous projector P_I up to order T^{-1}. Thus, treating T as a tunable parameter, let us expand the dynamics around the limit $T \to \infty$,

$$P = P_I + \frac{1}{T}\delta P + \mathcal{O}\left(\frac{1}{T^2}\right), \tag{B.27}$$

where δP is the first-order perturbation away from the exact adiabatic result. Inserting this into eqn B.22, we get

$$\partial_s P_I + \frac{1}{T}\partial_s \delta P = -iT[H, P_I] - i[H, \delta P] + ... \tag{B.28}$$

The terms omitted are at least of order T^{-1}. The first term on the right vanishes, since P_I and H commute by definition. Thus, collecting the next lowest order in T, we get

$$\partial_s P_I = -i[H, \delta P]. \tag{B.29}$$

Time evolution of P_I is determined by $\bar{K}$, thus we arrive at the identity

$$[H, \delta P] = [\bar{K}, P_I]. \tag{B.30}$$

Let us consider $H_\perp$ in this limit. It is straightforward to show that

$$\begin{aligned} H_\perp &= PHQ + QHP \\ &= \big[[H, P], P\big]. \end{aligned} \tag{B.31}$$

H commutes with P_I, so we can set

$$[H, P] = [H, \frac{1}{T}\delta P] + \mathcal{O}\left(\frac{1}{T^2}\right), \tag{B.32}$$

and use identity B.30 to get this in the form.

$$H_\perp = \frac{1}{T}\big[[\bar{K}, P_I], P_I\big] + \mathcal{O}\left(\frac{1}{T^2}\right), \tag{B.33}$$

where we have also expanded the second P according to Eqn. B.27. Finally we use the identities $\partial_s P_I = -i[\bar{K}, P_I]$ and $\bar{K} = i[\partial_s P_I, P_I]$ to show that

$$H_\perp = \frac{1}{T}\bar{K} + \mathcal{O}\left(\frac{1}{T^2}\right). \tag{B.34}$$

Thus, in the near-adiabatic regime, we have shown that the flow operator separates into two terms

$$\bar{f}_{\mathbf{r}_i,\mathbf{r}_j} = \bar{f}^{\parallel}_{\mathbf{r}_i,\mathbf{r}_j} + \bar{f}^{\perp}_{\mathbf{r}_i,\mathbf{r}_j} \tag{B.35}$$

The first represents a circulating current that does not effect a change in P whatsoever. In

any sum of current into or out of a region, we expect any $f^{\parallel}$ terms to vanish, since the total flow from this term into any individual site vanishes according to Eqn. B.26. Additionally, it is worth noting that the term,

$$\bar{f}^{\parallel}_{\mathbf{r}_i,\mathbf{r}_j} = iT\delta_{\mathbf{r}_j} H_{\parallel} \delta_{\mathbf{r}_i} + h.c. \tag{B.36}$$

is linearly dependent on T, since $H^{\parallel}$ has nonzero components of order T^0. Thus it diverges as $T \to \infty$. Any constant current scaled over an infinitely large time period will diverge. In what follows, we shall omit these terms, meaning that our current operator will not account for persistent or *frozen in* current in the bulk at any point in the adiabatic evolution.

The second term, given by

$$\bar{f}^{\perp}_{\mathbf{r}_i,\mathbf{r}_j} = i\delta_{\mathbf{r}_j} \bar{K} \delta_{\mathbf{r}_i} - i\delta_{\mathbf{r}_i} \bar{K} \delta_{\mathbf{r}_j}, \tag{B.37}$$

represents the current generated over the course of the adiabatic evolution by the change in the electronic arrangements of states in the band, P. Thus, we see that in the adiabatic limit, in the absence of persistent current, the flow in the system can be approximated by the adiabatic flow operator,

$$\bar{f}_{\mathbf{r}_i,\mathbf{r}_j} = i\delta_{\mathbf{r}_j} \bar{K} \delta_{\mathbf{r}_i} - i\delta_{\mathbf{r}_i} \bar{K} \delta_{\mathbf{r}_j} + \mathcal{O}\left(\frac{1}{T}\right). \tag{B.38}$$

Finally, we may rescale from s back to t, making the substitutions $\bar{f} = fT$ and $\bar{K} = KT$ to arrive at

$$f_{\mathbf{r}_i,\mathbf{r}_j} = i\delta_{\mathbf{r}_j} K \delta_{\mathbf{r}_i} - i\delta_{\mathbf{r}_i} K \delta_{\mathbf{r}_j} + \mathcal{O}\left(\frac{1}{T^2}\right). \tag{B.39}$$

Since the current operators used in §3.3.2 and §3.3.4 can be expressed as a sum over individual flows, this property naturally extends to the current, and we see that

$$J_{R_x} \to J^A_{R_x} + \mathcal{O}\left(\frac{1}{T^2}\right) \tag{B.40}$$

$$J_{R_x}(\mathbf{r}) \to J^A_{R_x}(\mathbf{r}) + \mathcal{O}\left(\frac{1}{T^2}\right), \tag{B.41}$$

where in each case, the adiabatic version is found by substituting $H \to K$ in the definition.

References

[1] J. E. Avron, R. Seiler, and L. G. Yaffe, "Adiabatic theorems and applications to the quantum hall effect", en, Communications in Mathematical Physics **110**, 33–49 (1987).

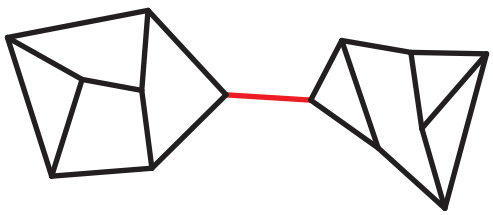
Appendix C

Tait Colourings and the Four-Colour Theorem

In this appendix we will discuss a very old theorem first proposed by Scottish physicist Peter Tait, who in the late 1800s was working towards a proof of the four-colour theorem. In his attempt to simplify the problem, Tait found a correspondence between the problem of four-colouring the faces of a graph and three-colouring the edges [1, 2]. Tait used this result to construct an incorrect proof of the four-colour theorem, which stood unchallenged for 11 years until a counterexample was provided by Julius Petersen [3, 4]. Here we will provide a simple proof of Tait's original correspondence, which states that:

Every bridge-free cubic planar graph can be face-coloured with four colours if and only if it can be edge-coloured with 3 colours.

Let us start by making a few definitions. We will be working only with fully connected cubic graphs, consisting of a set of vertices v_i, edges e_i and faces f_i – where every vertex connects to three edges. Furthermore, a bridge is an edge where, if it were removed the graph would be divided into two connected components. For example in the following graph, the red edge is a bridge, so the graph is considered illegal.



Let us construct a labelling system for our faces and edges. Rather than using an integer from 0-4, we will label them using a binary representation of these integers,

$$\mathfrak{l} \in \mathrm{IF}_2^2 = \{(0,0),\ (0,1),\ (1,0),\ (1,1)\}, \tag{C.1}$$

where IF_2^2 is a 2d vector space over the finite field of order 2. Note we always denote a label with $\mathfrak{fraktur}$. On this space, let us define a 'subtraction' operator as the bitwise XOR of two labels. Note that this operator is associative, commutative, and has an identity element which we label $\mathbf{0} = (0,0)$. We refer to this as a 'subtraction' because it satisfies the following property

$$\mathfrak{l}_1 \oplus \mathfrak{l}_2 = (0,0) \implies \mathfrak{l}_1 = \mathfrak{l}_2, \tag{C.2}$$

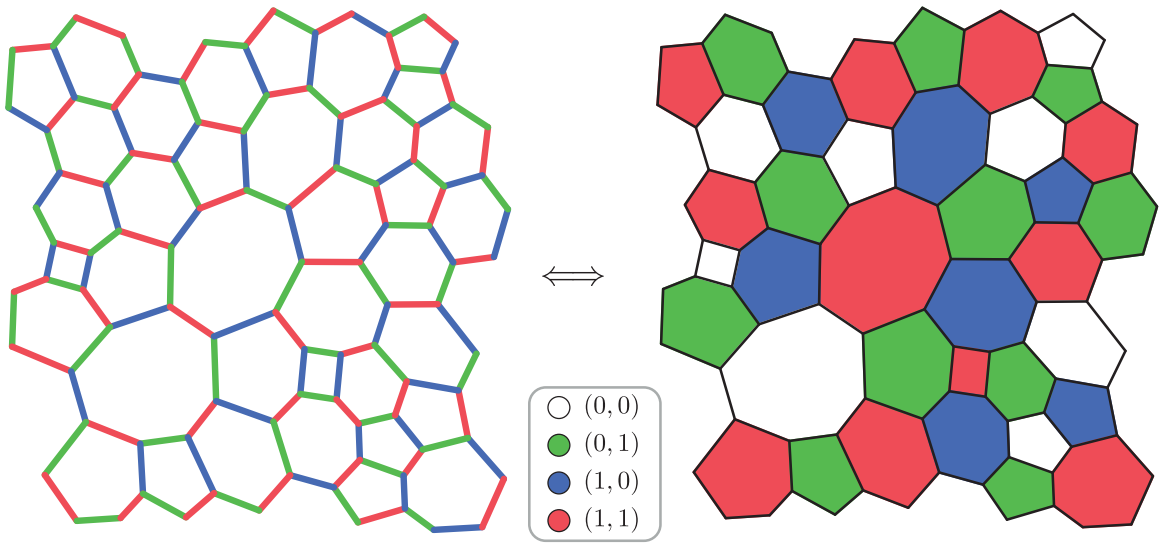


Figure C.1: An example of a 3-edge colouring on a graph with coordination number $z \leq 3$, along with the corresponding 4-face colouring, related according to Eqn. C.5.

although it does fail to satisfy some other properties one might expect of subtraction such as having $\mathfrak{l}_1 \oplus \mathfrak{l}_2 = \mathfrak{l}_2 \oplus \mathfrak{l}_1$.

We shall define a 4-face colouring by assigning one of these four labels $\mathfrak{f}$ to each of the faces in the graph, with the condition that no two adjacent faces share the same label.

$$\mathfrak{f} : f_i \to \mathfrak{f}_i \in \mathrm{IF}_2^2 \tag{C.3}$$

Similarly, we define a 3-edge colouring by assigning an edge label $\mathfrak{e}$ from the three nonzero labels such that no vertex touches two edges with the same label.

$$\mathfrak{e} : e_i \to \mathfrak{e}_i \in \mathrm{IF}_2^2/\mathbf{0} \tag{C.4}$$

Now let us suppose that we have two labelled faces, f_1 and f_2, which are separated by an edge e. We assert that a valid edge colouring can be found by taking the difference of the two adjacent face colours

$$\mathfrak{e} = \mathfrak{f}_1 \oplus \mathfrak{f}_2. \tag{C.5}$$

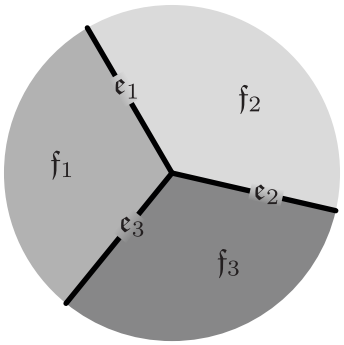
Thus, we may visualise the face colours as behaving something like a 'height' or 'position' coordinate, and the edge colours as acting more like a 'difference' coordinate. Now let us prove that the relation above provides a direct mapping from any valid 4-face colouring to a 3-edge colouring and vice versa, see Fig. C.1.

C.1 4-Face Colouring to a 3-Edge Colouring

Suppose we start with a valid 4-face colouring. Let us show that the relation in Eqn. C.5 always allows us to transform this into a valid edge colouring. Firstly, note that, provided that no adjacent faces have the same colour, we are guaranteed to have only three colours in our edge

colouring. This is because an edge will only have colour $\mathbf{0}$ if the two faces it borders have the same colour, however this is prohibited for the face colouring to be valid.

Now we must show that it is not possible for any vertex to touch two edges of the same colour. Let us consider a single vertex between three faces. Each face has a distinct colour $\mathfrak{f}_i$ and each edge that meets this vertex has a colouring $\mathfrak{e}_i$ as shown below:



Now let us consider the quantity

$$\mathfrak{m} = \mathfrak{e}_1 \oplus \mathfrak{e}_2 \oplus \mathfrak{e}_3 \tag{C.6}$$

Using Eqn. C.5 we may rewrite this in terms of the face colours as

$$\mathfrak{m} = (\mathfrak{f}_1 \oplus \mathfrak{f}_2) \oplus (\mathfrak{f}_2 \oplus \mathfrak{f}_3) \oplus (\mathfrak{f}_3 \oplus \mathfrak{f}_1) = \mathbf{0}, \tag{C.7}$$

since every term appears twice in this sum. No edge can have $\mathfrak{e}_i = \mathbf{0}$, so the only way for $\mathfrak{e}_i$ to satisfy Eqn. C.6 is to have one $\mathfrak{e}_i$ of each nonzero type. Thus, we see that $\mathfrak{e}_i$ represents a valid edge colouring around the vertex. In general this means that a valid face colouring will always generate a valid face colouring.

C.2 3-Edge Colouring to a 4-Face Colouring

Suppose we start with a valid 3-edge colouring and are instructed to transform it into a valid 4-face colouring. To do this, let us pick an arbitrary face of the graph – labelled f_0 – and assign it an arbitrary colour, say $(0, 0)$. Now, given an arbitrary face, f_j, we may determine its colour $\mathfrak{f}_j$ by traversing from f_0 to f_j, and taking the sum of the edge colours $\mathfrak{e}_k$ for every edge that crosses on the path p,

$$\mathfrak{f}_j = \mathfrak{f}_0 \bigoplus_{k \in p} \mathfrak{e}_k. \tag{C.8}$$

The colour of $\mathfrak{f}_j$ is uniquely defined provided that this process is invariant to the choice of path taken. If we consider two paths p and p', from f_0 to f_j, shown in Fig. C.2 we require that

$$\mathfrak{f}_j = \mathfrak{f}'_j \implies \mathfrak{f}_j \oplus \mathfrak{f}'_j = \mathbf{0}. \tag{C.9}$$

Inserting Eqn. C.8 into this expression, we arrive at the condition

$$\mathbf{0} = \left(\bigoplus_{k \in p} \mathfrak{e}_k \right) \oplus \left(\bigoplus_{k \in p'} \mathfrak{e}_k \right) \tag{C.10}$$

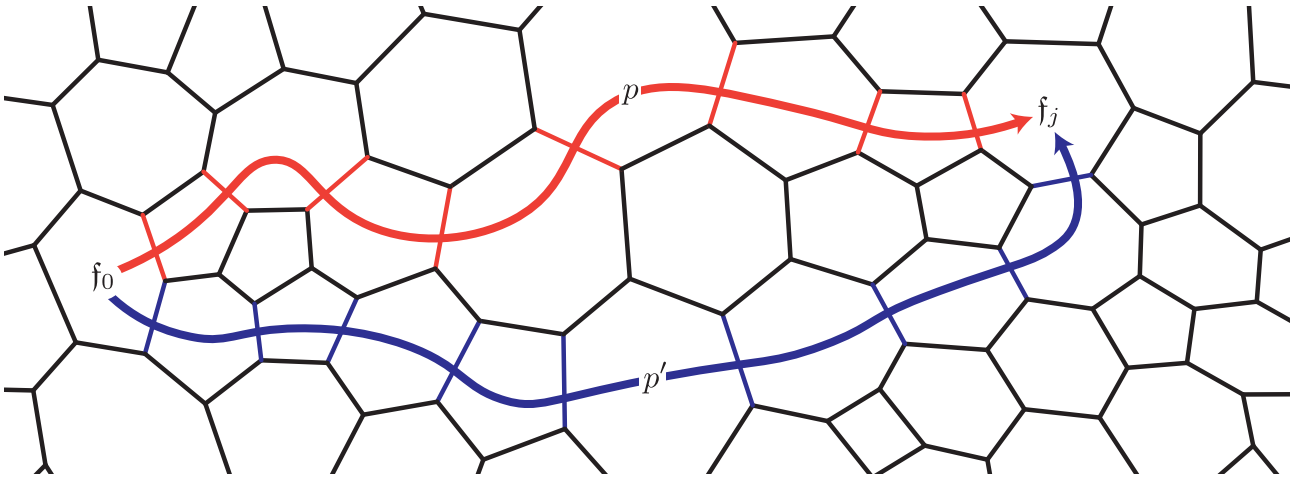


Figure C.2: Two distinct paths from f_0 to f_j. The combination of both paths forms a closed loop, where the value of $\mathfrak{f}_j$ is uniquely determined provided that $\bigoplus \mathfrak{e}$ around this loop vanishes.

Since the composition of the two paths is a closed loop, this amounts to the condition that the integral of $\mathfrak{e}_k$ around any closed loop in the system must vanish.

In order to show this condition holds, let us first notice that – as we saw in the previous section – the sum of $\mathfrak{e}_k$ around any single vertex must vanish if we have a valid 3-edge colouring. Similarly, a path that encloses two vertices is also guaranteed to vanish, since it can be decomposed as a sum of the paths that encircle each vertex individually. Thus, we see that a general closed loop that encircles some set of vertices can always be decomposed into a sum of loops around each individual vertex, which then all vanish individually.

This argument completes the proof, any path from f_0 to f_j will give an identical value for $\mathfrak{f}_j$. Furthermore, the 4-colouring obtained is guaranteed to always satisfy the condition of no adjacent faces having the same colour, since any two adjacent faces $\mathfrak{f}_1$ and $\mathfrak{f}_2$ separated by $\mathfrak{e}$ must satisfy

$$\mathfrak{f}_1 \oplus \mathfrak{e} = \mathfrak{f}_2 \neq \mathfrak{f}_1 \text{ for } \mathfrak{e} \neq \mathbf{0}. \tag{C.11}$$

What about periodic boundaries? — The eagle-eyed reader might have noticed an omission in the argument presented. We showed that all closed loops that encircle a set of vertices are guaranteed to have $\bigoplus e = \mathbf{0}$. However not all closed loops have a defined inside and outside. If we construct such a system on a manifold with genus g, then in general there will be $2g$ topologically distinct non-contractible loops. Since these have no inside and outside, the argument above fails, and it is possible for such non-contractible loops to have $\bigoplus e \neq \mathbf{0}$. In such a case, a valid 3-edge colouring does not imply a 4-face colouring.

Thus, on a manifold that is not simply connected, a 4-face colouring implies a 3-edge colouring however a 3-edge colouring *does not* imply a 4-face colouring!

References

[1] P. G. Tait, "Remarks on the Colouring of Maps", Proceedings of the Royal Society of Edinburgh **10**, 501–503 (1880).

[2] K. Appel and W. Haken, *Every Planar Map Is Four Colorable*, Vol. 98, Contemporary Mathematics (American Mathematical Society, 1989).

[3] J. Petersen, "Die Theorie der regulären graphs", Acta Mathematica **15**, 193–220 (1891).

[4] H. M. Mulder, "Julius Petersen's theory of regular graphs", Discrete Mathematics **100**, 157–175 (1992).

Appendix D

Diagonalising Quadratic Hamiltonians

In this appendix we shall present the details of the methods used to diagonalise the quadratic Hamiltonians encountered in Chapters 4 and 5. In each of these cases, the problem amounts to expressing some Hamiltonian in the form

$$H \sim \Psi^\dagger M \Psi, \tag{D.1}$$

where Ψ is some arbitrary column vector consisting of either Majorana fermionic of bosonic creation operators. Let us start with the Majorana fermion case, followed by the bosonic case.

D.1 The Majorana Case

Here we shall provide a detailed explanation of the methods used to solve the Majorana mean field Hamiltonian in momentum space, as well as the methods for calculating mean field expectation values and Chern number. Finally, we shall discuss the detailed results obtained from this method.

We start by defining a maximally generic Majorana free fermion system:

$$H = \sum_{jk} iA_{jk} c_j c_k. \tag{D.2}$$

Here, A is a real skew-symmetric matrix, ensuring that the overall operator is Hermitian. The matrix iA is pure imaginary, so has particle hole symmetry, so we have a guarantee that the eigenstates come in conjugate pairs, with opposite energy. Thus, we may diagonalise iA according to

$$iA_{jk} = R^\dagger \begin{pmatrix} \varepsilon_1 & 0 & & & \\ 0 & -\varepsilon_1 & & & \\ & & \varepsilon_2 & 0 & \\ & & 0 & -\varepsilon_2 & \\ & & & & \ddots \end{pmatrix} R, \tag{D.3}$$

with R being a row matrix of eigenstates of iA,

$$R = \begin{pmatrix} — & \psi_1 & — \\ — & \psi_1^* & — \\ — & \psi_2 & — \\ — & \psi_2^* & — \\ & \vdots & \end{pmatrix}. \tag{D.4}$$

Of course, none of these eigenstates ψ_i represent a valid Majorana mode, which must take the form $b_j = Q_{jk}c_k$ with Q a real orthogonal matrix. Thus, let us perform a further rotation on each subspace containing conjugate pair of eigenstates to find a pair of real Majorana modes ϕ and ϕ' corresponding to the real and imaginary parts of ψ_i,

$$\begin{pmatrix} \phi \\ \phi' \end{pmatrix} = \frac{1}{\sqrt{2}} \begin{pmatrix} 1 & 1 \\ -i & i \end{pmatrix} \begin{pmatrix} \psi \\ \psi^* \end{pmatrix}. \tag{D.5}$$

Thus, we may define a real orthogonal transformation

$$Q = \begin{pmatrix} — & \phi_1 & — \\ — & \phi_1' & — \\ — & \phi_2 & — \\ — & \phi_2' & — \\ & \vdots & \end{pmatrix}, \tag{D.6}$$

that skew-diagonalises the matrix iA according to

$$iA_{jk} = Q^T \begin{pmatrix} 0 & i\varepsilon_1 & & & \\ -i\varepsilon_1 & 0 & & & \\ & & 0 & i\varepsilon_2 & \\ & & -i\varepsilon_2 & 0 & \\ & & & & \ddots \end{pmatrix} Q, \tag{D.7}$$

with Q calculated according to

$$Q = \frac{1}{\sqrt{2}} \begin{pmatrix} 1 & 1 & & & \\ -i & i & & & \\ & & 1 & 1 & \\ & & -i & i & \\ & & & & \ddots \end{pmatrix} R \tag{D.8}$$

The Hamiltonian can now be written in terms of a new basis of Majorana fermions $b_n = Q_{(2n-1)k}c_k$ and $b_n' = Q_{(2n)k}c_k$ as

$$H = \sum_j i\varepsilon_j b_j b_j' - i\varepsilon_j b_j' b_j, \tag{D.9}$$

which can be re-expressed in terms of fermions using the identity $ib_j b'_j = 2f_j^\dagger f_j - 1$

$$H = \sum_j 2\left(2f_j^\dagger f_j - 1\right). \tag{D.10}$$

Thus, we see that the ground state $|\Psi\rangle$ contains no f-type fermions, and has energy

$$E_{g.s.} = -2\sum_j \varepsilon_j \tag{D.11}$$

D.1.1 Correlation Values

Now let us derive the expression for the ground state expectation value of a two-Majorana operator $\langle\Psi|ic_i c_j|\Psi\rangle$. We start by transforming to the 'diagonalising' Majorana basis, according to $c_j = Q^T_{jk} b_k$ to get

$$\langle ic_j c_k\rangle = \langle\Psi|ib_\alpha b_\beta|\Psi\rangle\, Q_{\alpha j} Q^T_{k\beta}, \tag{D.12}$$

We know that the ground state contains no fermions as defined in Eqn. D.10, thus we can derive the following four relations for the diagonalising b-Majorana modes:

$$\langle ib_j b_j\rangle = \langle ib'_j b'_j\rangle = i, \tag{D.13}$$
$$\langle ib_j b'_j\rangle = -1, \tag{D.14}$$
$$\langle ib'_j b_j\rangle = +1, \tag{D.15}$$
$$\langle ib_j b_k\rangle = 0 \quad \forall j \neq k. \tag{D.16}$$

From this we can calculate the matrix element

$$\langle\Psi|ib_\alpha b_\beta|\Psi\rangle = M_{\alpha\beta} = \begin{pmatrix} i & -1 & & & \\ +1 & i & & & \\ & & i & -1 & \\ & & +1 & i & \\ & & & & \ddots \end{pmatrix}_{\alpha\beta}. \tag{D.17}$$

Therefore, Eqn. D.12 becomes

$$\sum_{\alpha\beta} \langle\Psi|ib_\alpha b_\beta|\Psi\rangle\, Q^T_{j\alpha} Q_{\beta k} = \left[Q^T M Q\right]_{jk}. \tag{D.18}$$

Finally, using Eqn. D.8, we see that this expression becomes

$$\langle\Psi|ic_j c_k|\Psi\rangle = \left[R^\dagger \begin{pmatrix} 2i & 0 & & & \\ 0 & 0 & & & \\ & & 2i & 0 & \\ & & 0 & 0 & \\ & & & & \ddots \end{pmatrix} R \right]_{jk}. \tag{D.19}$$

Therefore, we arrive at the final expression

$$\langle\Psi|ic_jc_k|\Psi\rangle = -2iP_{jk}, \tag{D.20}$$

where P_{jk} is the projector onto the negative energy eigenstates of iA.

D.2 Triplons and the Bosonic Case

In this section we shall provide a detailed explanation of the methods used for solving the triplon Hamiltonian presented in §5.3 using bosonic triplon MFT. This section has three parts: First we discuss the momentum space construction of the Hamiltonian, next we shall explain the methods used to solve this Hamiltonian for the bosonic eigenstates. Finally, we derive the form of the Chern number for a bosonic system.

D.2.1 Construction of the Hamiltonian

Let us start by restating the Hamiltonian given in Eqn. 5.29, given by

$$H = H_0 + H_2 + H_4, \tag{D.21}$$

where

$$H_0 = N\left[\bar{s}^2(K+2J-\mu)+\mu\right], \tag{D.22}$$

$$\begin{aligned} H_2 = &\sum_{j\in\mathcal{D}}(K-2J-\mu)t^\dagger_{\alpha j}t_{\alpha j} - (K+\mu)t^\dagger_{\bar{\alpha}j}t_{\bar{\alpha}j} \\ &+ h_\alpha 2i\varepsilon_{\alpha\beta\gamma}t^\dagger_\beta t_\gamma \\ &- \sum_{jk\in\mathcal{D},\alpha} J^\alpha_{jk}\bar{s}^2\left(t^\dagger_{\alpha k}t_{\alpha j} - t_{\alpha j}t_{\alpha k} + h.c.\right). \end{aligned} \tag{D.23}$$

The four-boson Hamiltonian is decoupled using the mean fields,

$$P^\alpha_{jk} = \langle t^\dagger_{j\alpha}t_{k\alpha}\rangle \tag{D.24}$$

$$Q^\alpha_{jk} = \langle t_{j\alpha}t_{k\alpha}\rangle, \tag{D.25}$$

taking the following form

$$\begin{aligned} H_4 = &-\sum_{jk\in\mathcal{D},\alpha} J^\alpha_{jk}\Big(P^b_{jk}t^\dagger_{cj}t_{ck} + t^\dagger_{bj}t_{bk}P^{c*}_{jk} + h.c. \\ &\quad - t^\dagger_{bj}t^\dagger_{bk}Q^c_{jk} - Q^{b*}_{jk}t_{cj}t_{ck} + h.c.\Big) \\ &+ \sum_{jk\in\mathcal{D},\alpha} J^\alpha_{jk}\Big(P^b_{jk}P^{c*}_{jk} - Q^{b*}_{jk}Q^c_{jk} + h.c.\Big). \end{aligned} \tag{D.26}$$

Note that here, the indices b and c denote the two subscripts that are not equal to α for each term in the sum. Since we are working in a translationally invariant system, we transform to momentum space. We replace every position index j, with a pair $\mathbf{r}, j$, where $\mathbf{r}$ labels the

unit cell position and j now labels the site within the unit cell. Momentum-space annihilation operators are defined as

$$t_{j\mathbf{r},\alpha} = \frac{1}{\sqrt{N}} \sum_{\mathbf{q}} e^{-i\mathbf{r}\cdot\mathbf{q}} t_{j\mathbf{q},\alpha}. \tag{D.27}$$

Under this, terms in the Hamiltonian containing triplet operators are transformed according to

$$\sum_{\mathbf{r}} t^\dagger_{j\mathbf{r}+\boldsymbol{\Delta},\alpha} t_{k\mathbf{r},\alpha} = \sum_{\mathbf{q}} e^{i\mathbf{q}\boldsymbol{\Delta}} t^\dagger_{j\mathbf{q},\alpha} t_{k\mathbf{q},\alpha}, \tag{D.28}$$

$$\begin{aligned}\sum_{\mathbf{r}} t_{j\mathbf{r}+\boldsymbol{\Delta},\alpha} t_{k\mathbf{r},\alpha} = \frac{1}{2} \sum_{\mathbf{q}} \Big(& e^{i\mathbf{q}\boldsymbol{\Delta}} t_{j-\mathbf{q},\alpha} t_{k\mathbf{q},\alpha} \\ & + e^{-i\mathbf{q}\boldsymbol{\Delta}} t_{k-\mathbf{q},\alpha} t_{j\mathbf{q},\alpha} \Big).\end{aligned} \tag{D.29}$$

Thus, we get a full Hamiltonian containing the following seven sets of terms:

$$\text{Constant shift: } 3\bar{s}^2 \left(K + 2J - \mu\right) + 3\mu \tag{D.30}$$

$$\text{On-colouring on-site potential: } \left(K - 2J - \mu\right) \sum_{\mathbf{q},j} t^\dagger_{j\mathbf{q},\alpha} t_{j\mathbf{q},\alpha} \tag{D.31}$$

$$\text{Off-colouring on-site potential: } \left(-K - \mu\right) \sum_{\mathbf{q},j} t^\dagger_{j\mathbf{q},\alpha} t_{j\mathbf{q},\alpha} \tag{D.32}$$

$$\text{Magnetic Field: } 2ih_\alpha \sum_{\mathbf{q},j} \varepsilon_{\alpha\beta\gamma} t^\dagger_{j\mathbf{q},\beta} t_{j\mathbf{q},\gamma} \tag{D.33}$$

$$\begin{aligned}\text{Hopping: } & - \sum_{\langle j,k\rangle,\alpha} J^\alpha_{jk} \bar{s}^2 \sum_{\mathbf{q}} e^{i\mathbf{q}\cdot\boldsymbol{\Delta}} t^\dagger_{j\mathbf{q},\alpha} t_{k\mathbf{q},\alpha} + h.c. \\ & + \sum_{\langle j,k\rangle,\alpha} \frac{1}{2} J^\alpha_{jk} \bar{s}^2 \sum_{\mathbf{q},j,k} e^{i\mathbf{q}\cdot\boldsymbol{\Delta}} t_{j-\mathbf{q},\alpha} t_{k\mathbf{q},\alpha} + e^{-i\mathbf{q}\cdot\boldsymbol{\Delta}} t_{k-\mathbf{q},\alpha} t_{j\mathbf{q},\alpha} + h.c.\end{aligned} \tag{D.34}$$

Adding in the mean fields (i.e. the quartic interactions) we get a few additional terms:

$$\text{Constant shift: } \sum_{\text{bonds}} \sum_{\alpha} J^\alpha_{jk} \left(P^b_{jk} P^{c*}_{jk} - Q^b_{jk} Q^{c*}_{jk} + h.c. \right) \tag{D.35}$$

$$\begin{aligned}\text{Hopping: } & - \sum_{\mathbf{q},\alpha} J^\alpha_{jk} e^{i\mathbf{q}\cdot\boldsymbol{\Delta}} \left(P^{b*}_{jk} t^\dagger_{j\mathbf{q},c} t_{k\mathbf{q},c} + P^{c*}_{jk} t^\dagger_{j\mathbf{q},b} t_{k\mathbf{q},b} \right) + h.c. \\ & + \sum_{\mathbf{q},\alpha} \frac{1}{2} J^\alpha_{jk} Q^{b*}_{jk} \left(e^{i\mathbf{q}\cdot\boldsymbol{\Delta}} t_{j-\mathbf{q},c}\, t_{k\mathbf{q},c} + e^{-i\mathbf{q}\cdot\boldsymbol{\Delta}} t_{k-\mathbf{q},c}\, t_{j\mathbf{q},c} \right) + h.c. \\ & + \sum_{\mathbf{q},\alpha} \frac{1}{2} J^\alpha_{jk} Q^{c*}_{jk} \left(e^{i\mathbf{q}\cdot\boldsymbol{\Delta}} t_{j-\mathbf{q},b}\, t_{k\mathbf{q},b} + e^{-i\mathbf{q}\cdot\boldsymbol{\Delta}} t_{k-\mathbf{q},b}\, t_{j\mathbf{q},b} \right) + h.c.\end{aligned} \tag{D.36}$$

D.2.2 Bosonic Bogoliubov-de Gennes Method

In order to solve this Hamiltonian, we shall use the bosonic Bogoliubov-de Gennes (BDG) method, detailed in [1]. This method is well-understood, however for the sake of completeness, and to introduce the notation used to derive the Chern number in §D.2.3, we discuss the method here. Let us work with a generic set of momentum-space bosonic annihilation operators, $b_{\mathbf{q}j}$, satisfying the bosonic commutation relations $[b_{\mathbf{q}j}, b^\dagger_{\mathbf{p}k}] = \delta(\mathbf{q}-\mathbf{p})\delta_{jk}$, where the Hamiltonian is given by

$$\begin{aligned} H_{\mathbf{q}} &= h_{jk}(\mathbf{q}) b^\dagger_{\mathbf{q}j} b_{\mathbf{q}k} \\ &\quad + \frac{1}{2}\left(\Delta_{jk}(\mathbf{q}) b^\dagger_{\mathbf{q}j} b^\dagger_{-\mathbf{q}k} + \Delta^\dagger_{jk}(\mathbf{q}) b_{-\mathbf{q}j} b_{\mathbf{q}k}\right), \end{aligned} \tag{D.37}$$

where h is a hermitian matrix. We assume that h satisfies the relation $h^*(\mathbf{q}) = h(-\mathbf{q})$, with the same for Δ. Using the bosonic commutation relations, we may rewrite the first term in the following form,

$$\begin{aligned} h_{jk}(\mathbf{q}) b^\dagger_{\mathbf{q}j} b_{\mathbf{q}k} =& \frac{1}{2}\left(h_{jk}(\mathbf{q}) b^\dagger_{\mathbf{q}j} b_{\mathbf{q}k} + h^T_{jk}(\mathbf{q}) b_{\mathbf{q}j} b^\dagger_{\mathbf{q}k}\right) \\ & - \frac{1}{2}\mathrm{Tr}h. \end{aligned} \tag{D.38}$$

Thus, the Hamiltonian can be written in a generic BdG form as

$$H_{\mathbf{q}} = \frac{1}{2}\Psi^\dagger_{\mathbf{q}} M(\mathbf{q}) \Psi_{\mathbf{q}} - \frac{1}{2}\mathrm{Tr}h, \tag{D.39}$$

where we have introduced the bosonic vector of creation/annihilation operators

$$\Psi_{\mathbf{q}} = (b_{\mathbf{q}0}, b_{\mathbf{q}1}, ..., b^\dagger_{-\mathbf{q}0}, b^\dagger_{-\mathbf{q}1}, ...)^T \tag{D.40}$$

and defined the BdG matrix

$$M(\mathbf{q}) = \begin{pmatrix} h(\mathbf{q}) & \Delta(\mathbf{q}) \\ \Delta^\dagger(\mathbf{q}) & h(\mathbf{q}) \end{pmatrix}. \tag{D.41}$$

To diagonalise this, let us consider the time-dependence of $\Psi_{\mathbf{q}}$, given by

$$\partial_t \Psi_{\mathbf{q}} = i\left[H_{\mathbf{q}}, \Psi_{\mathbf{q}}\right]. \tag{D.42}$$

Applying the bosonic commutation relations, we arrive at the following expression,

$$\partial_t \Psi_{\mathbf{q}} = i\eta M_{\mathbf{q}} \Psi_{\mathbf{q}}, \tag{D.43}$$

where the 'metric' η is defined as

$$\eta := \begin{pmatrix} \mathbb{1} & \\ & -\mathbb{1} \end{pmatrix} \tag{D.44}$$

We now define a rotated set of bosonic operators $\boldsymbol{\alpha}_{\mathbf{q}}$, with $\Phi_{\mathbf{q}} = (\boldsymbol{\alpha}_{\mathbf{q}0}, ..., \boldsymbol{\alpha}^{\dagger}_{-\mathbf{q}0}, ...)^T$, according to

$$b_{\mathbf{q}j} = \mathbf{u}_j \cdot \boldsymbol{\alpha}_{\mathbf{q}} + \mathbf{v}_j \cdot \boldsymbol{\alpha}^{\dagger}_{-\mathbf{q}}, \tag{D.45}$$

$$b^{\dagger}_{-\mathbf{q}j} = \bar{\mathbf{v}}_j \cdot \boldsymbol{\alpha}_{\mathbf{q}} + \bar{\mathbf{u}}_j \cdot \boldsymbol{\alpha}^{\dagger}_{-\mathbf{q}}, \tag{D.46}$$

$$\implies \Psi_q = R_{\mathbf{q}}\Phi_{\mathbf{q}}, \text{ for } R_{\mathbf{q}} = \begin{pmatrix} U & V \\ \bar{V} & \bar{U} \end{pmatrix}. \tag{D.47}$$

Here $R_{\mathbf{q}}$ is a rotation matrix that must be determined. In order to preserve bosonic commutation relations for $\boldsymbol{\alpha}$, we require that $R_{\mathbf{q}}$ satisfies

$$R\eta R^{\dagger} = \eta, \tag{D.48}$$

$$R^{\dagger}\eta R = \eta. \tag{D.49}$$

After applying this transformation to our equation of motion D.43, we arrive at

$$i\partial_t \Phi_{\mathbf{q}} = R^{-1}\eta M(\mathbf{q}) R \Phi_{\mathbf{q}}. \tag{D.50}$$

Thus, eigenstates of the Hamiltonian are found by choosing a transformation R that diagonalises the operator $\eta M(\mathbf{q})$, which we write in the form

$$R^{-1}\eta M_{\mathbf{q}} R = \eta D \tag{D.51}$$

where D should have only positive eigenvalues, ensuring that the bosonic modes all have positive energy. In practice, this can be done by diagonalising the matrix ηM and adjusting the normalisation of the eigenstates such that they satisfy Eqns. D.48 and D.49.

Now, let us rewrite the original Hamiltonian as

$$H_{\mathbf{q}} = \frac{1}{2}\begin{pmatrix} \boldsymbol{\alpha}^{\dagger}_{\mathbf{q}} & \boldsymbol{\alpha}_{-\mathbf{q}} \end{pmatrix} R^{\dagger} M_{\mathbf{q}} R \begin{pmatrix} \boldsymbol{\alpha}_{\mathbf{q}} \\ \boldsymbol{\alpha}^{\dagger}_{-\mathbf{q}} \end{pmatrix} - \frac{1}{2}\mathrm{Tr}h. \tag{D.52}$$

By rearranging Eqn. D.49 to get the identity $R^{\dagger} = \eta R^{-1}\eta$, and inserting it into the above, we can show that $R^{\dagger} M_{\mathbf{q}} R = D$ and the Hamiltonian takes the form

$$H_{\mathbf{q}} = \frac{1}{2}\sum_j \left(\omega_j \alpha^{\dagger}_{\mathbf{q}j}\alpha_{\mathbf{q}j} + \omega'_j \alpha_{-\mathbf{q}j}\alpha^{\dagger}_{-\mathbf{q}j}\right) - \frac{1}{2}\mathrm{Tr}h, \tag{D.53}$$

where we have labelled the positive eigenvalues of ηM as ω_j and the negative eigenvalues of ηM determine ω'_j (which are positive – negative energies would indicate an instability, where the system can infinitely populate the negative energy states). We rearrange the second set of bosonic operators to get

$$\begin{aligned} H_{\mathbf{q}} =& \frac{1}{2}\sum_j \left(\omega_j \alpha^{\dagger}_{\mathbf{q}j}\alpha_{\mathbf{q}j} + \omega'_j \alpha^{\dagger}_{-\mathbf{q}j}\alpha_{-\mathbf{q}j}\right) \\ & - \frac{1}{2}\mathrm{Tr}h + \frac{1}{2}\sum \omega' \end{aligned} \tag{D.54}$$

Of course, in order to implement the full mean field theory, one needs not only the bosonic spectrum but also the ground state expectation values for the mean fields, $\langle 0|b^{\dagger}_{\mathbf{q}j} b_{\mathbf{q}'k}|0\rangle$ and

$\langle 0|b_{\mathbf{q}j}b_{\mathbf{q}'k}|0\rangle$. These can be extracted from the rotation matrix $R_{\mathbf{q}}$ by transforming the expectation value to our diagonalising basis $\{\boldsymbol{\alpha}\}$:

$$\begin{aligned}\langle 0|b^{\dagger}_{\mathbf{q}j}b_{\mathbf{q}k}|0\rangle = \langle 0|(\mathbf{u}^{*}_{j}\cdot\boldsymbol{\alpha}^{\dagger}_{\mathbf{q}} + \mathbf{v}^{*}_{j}\cdot\boldsymbol{\alpha}_{-\mathbf{q}}) \\ \times(\mathbf{u}_{k}\cdot\boldsymbol{\alpha}_{\mathbf{q}} + \mathbf{v}_{k}\cdot\boldsymbol{\alpha}^{\dagger}_{-\mathbf{q}})\,|0\rangle\,.\end{aligned} \tag{D.55}$$

Since the ground state contains no bosons, the only term here that does not vanish is

$$\langle 0|b^{\dagger}_{\mathbf{q}j}b_{\mathbf{q}k}|0\rangle = \langle 0|(\mathbf{v}^{*}_{j}\cdot\boldsymbol{\alpha}_{-\mathbf{q}})(\mathbf{v}_{k}\cdot\boldsymbol{\alpha}^{\dagger}_{-\mathbf{q}})|0\rangle \tag{D.56}$$

$$= \langle 0|V^{*}_{jm}V_{km}|0\rangle \tag{D.57}$$

$$= (VV^{\dagger})_{kj}. \tag{D.58}$$

Equally, we can repeat the process for the other correlation function of interest,

$$\langle 0|b_{-\mathbf{q}j}b_{\mathbf{q}k}|0\rangle = (V\bar{U}^{\dagger})_{kj}. \tag{D.59}$$

D.2.3 Bosonic Chern Number

In order to define a bosonic version of the Chern number, let us start by restating the results of the previous section. We have a BdG matrix given by $M(\mathbf{q})$ – assumed to be positive definite (defined in Eqn. D.41), with a set of eigenstates $|\psi_j(\mathbf{q})\rangle$ which satisfy

$$\eta M(\mathbf{q})\,|\psi_j(\mathbf{q})\rangle = \lambda_j(\mathbf{q})\,|\psi_j(\mathbf{q})\rangle\,. \tag{D.60}$$

For a physical solution, we make the assumption that all eigenstates are real, i.e. there is no dynamical instability. Then we can show that if $|\psi_j(\mathbf{q})\rangle$ is a right eigenstate of $\eta M(\mathbf{q})$, from the hermiticity of $M_{\mathbf{q}}$, we must have a corresponding left eigenvector defined as

$$\langle\overline{\psi_j}(\mathbf{q})| = \langle\psi_j(\mathbf{q})|\,\eta, \tag{D.61}$$

with the same eigenvalue. Now, let's assume that the eigenstates of ηM are all either positive or negative, then we can calculate the quantity

$$\langle\overline{\psi_j}|\eta M|\psi_j\rangle = \lambda_j\,\langle\overline{\psi_j}|\psi_j\rangle \tag{D.62}$$

$$\implies \langle\psi_j|M|\psi_j\rangle = \lambda_j\,\langle\overline{\psi_j}|\psi_j\rangle\,. \tag{D.63}$$

The left-hand side here is always positive due to the positive definiteness of M. This implies that positive eigenstates of ηM have positive norm, and the negative eigenstates of ηM have negative norm. Thus, we see that (in agreement with condition D.49) the states can be split into two sets and normalised, which we will label with ϕ^{+}_{i} and ϕ^{-}_{i} with the following norms

$$\langle\phi^{+}_{i}|\eta|\phi^{+}_{i}\rangle = +1 \tag{D.64}$$

$$\langle\phi^{-}_{i}|\eta|\phi^{-}_{i}\rangle = -1. \tag{D.65}$$

In this context, let us look now at finding relative phases between adjacent eigenstates in k-space. We can define the phase between two states as

$$\gamma = \arg\left[\pm\,\langle\phi^{\pm}_{i}(\mathbf{k})|\eta|\phi^{\pm}_{i}(\mathbf{q})\rangle\right]. \tag{D.66}$$

In analogy with the standard discussion around Berry phase, this quantity is not gauge invariant for a local gauge $|\phi_i(\mathbf{q})\rangle \to e^{i\alpha(\mathbf{q})}|\phi_i(\mathbf{q})\rangle$. Thus, let us define a gauge-invariant quantity – the Berry phase around a plaquette in k-space,

$$\begin{aligned}\gamma_B(\mathbf{q}) = \arg\big[&\langle\phi_i^{\pm}(\mathbf{q})|\eta|\phi_i^{\pm}(\mathbf{q}+\boldsymbol{\delta}_x)\rangle \\ &\langle\phi_i^{\pm}(\mathbf{q}+\boldsymbol{\delta}_x)|\eta|\phi_i^{\pm}(\mathbf{q}+\boldsymbol{\delta}_x+\boldsymbol{\delta}_y)\rangle \\ &\langle\phi_i^{\pm}(\mathbf{q}+\boldsymbol{\delta}_x+\boldsymbol{\delta}_y)|\eta|\phi_i^{\pm}(\mathbf{q}+\boldsymbol{\delta}_y)\rangle \\ &\langle\phi_i^{\pm}(\mathbf{q}+\boldsymbol{\delta}_y)|\eta|\phi_i^{\pm}(\mathbf{q})\rangle\big],\end{aligned} \tag{D.67}$$

where δ_x and δ_y represent a translation in momentum space by $2\pi/L$ in either the x or y direction, L being the system size. Here the factor of $(\pm 1)^4$ from state normalisation clearly vanishes. Let us simplify this expression by defining the symplectic projector onto a single eigenstate,

$$\hat{\phi}_i^{\pm}(\mathbf{q}) = |\phi_i^{\pm}(\mathbf{q})\rangle\langle\phi_i^{\pm}(\mathbf{q})|\,\eta, \tag{D.68}$$

which is identical to a standard density matrix aside from the extra factor of η. Using this expression we can rewrite the Berry phase in the following form:

$$\begin{aligned}\gamma_B(\mathbf{q}) = \arg\mathrm{Tr}\Big[&\hat{\phi}_i^{\pm}(\mathbf{q})\hat{\phi}_i^{\pm}(\mathbf{q}+\boldsymbol{\delta}_x) \\ &\hat{\phi}_i^{\pm}(\mathbf{q}+\boldsymbol{\delta}_x+\boldsymbol{\delta}_y)\hat{\phi}_i^{\pm}(\mathbf{q}+\boldsymbol{\delta}_y)\Big].\end{aligned} \tag{D.69}$$

Finally, the Chern number is calculated using the usual expression

$$\begin{aligned}C = \frac{1}{2\pi}\sum_{\mathbf{q}}\arg\mathrm{Tr}\Big[&\hat{\phi}_i^{\pm}(\mathbf{q})\hat{\phi}_i^{\pm}(\mathbf{q}+\boldsymbol{\delta}_x) \\ &\hat{\phi}_i^{\pm}(\mathbf{q}+\boldsymbol{\delta}_x+\boldsymbol{\delta}_y)\hat{\phi}_i^{\pm}(\mathbf{q}+\boldsymbol{\delta}_y)\Big].\end{aligned} \tag{D.70}$$

References

[1] J.-P. Blaizot and G. Ripka, *Quantum Theory of Finite Systems* (The MIT Press, 1986).

American Physical Society
Reuse and Permissions License

22-Jan-2024

This license agreement between the American Physical Society ("APS") and Peru d'Ornellas ("You") consists of your license details and the terms and conditions provided by the American Physical Society and SciPris.

Licensed Content Information

License Number:	**RNP/24/JAN/074360**
License date:	22-Jan-2024
DOI:	10.1103/PhysRevB.106.155124
Title:	Quantized bulk conductivity as a local Chern marker
Author:	Peru d'Ornellas, Ryan Barnett, and Derek K. K. Lee
Publication:	Physical Review B
Publisher:	American Physical Society
Cost:	USD $ 0.00

Request Details

Does your reuse require significant modifications: Yes

Modification Details:

It has been edited to fit the thesis

Specify intended distribution locations:	UK & Commonwealth (excluding Canada)
Reuse Category:	Reuse in a thesis/dissertation
Requestor Type:	Author of requested content
Items for Reuse:	Whole Article
Format for Reuse:	Print
Total number of print copies:	Up to 1000

Information about New Publication:

University/Publisher:	Imperial College London
Title of dissertation/thesis:	Topology on Almost Any Lattice
Author(s):	Peru d'Ornellas
Expected completion date:	Jan. 2024

License Requestor Information

Name:	Peru d'Ornellas
Affiliation:	Individual
Email Id:	
Country:	

American Physical Society
Reuse and Permissions License

TERMS AND CONDITIONS

The American Physical Society (APS) is pleased to grant the Requestor of this license a non-exclusive, non-transferable permission, limited to Print format, provided all criteria outlined below are followed.

1. You must also obtain permission from at least one of the lead authors for each separate work, if you haven't done so already. The author's name and affiliation can be found on the first page of the published Article.
2. For electronic format permissions, Requestor agrees to provide a hyperlink from the reprinted APS material using the source material's DOI on the web page where the work appears. The hyperlink should use the standard DOI resolution URL, http://dx.doi.org/{DOI}. The hyperlink may be embedded in the copyright credit line.
3. For print format permissions, Requestor agrees to print the required copyright credit line on the first page where the material appears: "Reprinted (abstract/excerpt/figure) with permission from [(FULL REFERENCE CITATION) as follows: Author's Names, APS Journal Title, Volume Number, Page Number and Year of Publication.] Copyright (YEAR) by the American Physical Society."
4. Permission granted in this license is for a one-time use and does not include permission for any future editions, updates, databases, formats or other matters. Permission must be sought for any additional use.
5. Use of the material does not and must not imply any endorsement by APS.
6. APS does not imply, purport or intend to grant permission to reuse materials to which it does not hold copyright. It is the requestor's sole responsibility to ensure the licensed material is original to APS and does not contain the copyright of another entity, and that the copyright notice of the figure, photograph, cover or table does not indicate it was reprinted by APS with permission from another source.
7. The permission granted herein is personal to the Requestor for the use specified and is not transferable or assignable without express written permission of APS. This license may not be amended except in writing by APS.
8. You may not alter, edit or modify the material in any manner.
9. You may translate the materials only when translation rights have been granted.
10. APS is not responsible for any errors or omissions due to translation.
11. You may not use the material for promotional, sales, advertising or marketing purposes.
12. The foregoing license shall not take effect unless and until APS or its agent, Aptara, receives payment in full in accordance with Aptara Billing and Payment Terms and Conditions, which are incorporated herein by reference.
13. Should the terms of this license be violated at any time, APS or Aptara may revoke the license with no refund to you and seek relief to the fullest extent of the laws of the USA. Official written notice will be made using the contact information provided with the permission request. Failure to receive such notice will not nullify revocation of the permission.
14. APS reserves all rights not specifically granted herein.
15. This document, including the Aptara Billing and Payment Terms and Conditions, shall be the entire agreement between the parties relating to the subject matter hereof.